UNIVERSITY OF GENOVA

POLYTECHNIC SCHOOL

Department of Mechanical, Energy, Management and Transportation Engineering

DOCTORAL THESIS

Optimal Design of Beam-Based Compliant Mechanisms via Integrated Modeling Frameworks

Supervisor:
Prof. Giovanni Berselli
Co-supervisor:
Prof. Larry L. Howell

Candidate:
Pietro Bilancia

April 2020

Optimal Design of Beam-Based Compliant Mechanisms via Integrated Modeling Frameworks

Pietro Bilancia

A dissertation submitted to the faculty of
University of Genova
in partial fulfillment of the requirements for the degree of

Doctor of Philosophy

Department of Mechanical, Energy, Management
and Transportation Engineering

University of Genova

April 2020

Abstract

Beam-based Compliant Mechanisms (CMs) are increasingly studied and implemented in precision engineering due to their advantages over the classic rigid-body mechanisms, such as scalability and reduced need for maintenance. Straight beams with uniform cross section are the basic modules in several concepts, and can be analyzed with a large variety of techniques, such as Euler-Bernoulli beam theory, Pseudo-Rigid Body (PRB) method, chain algorithms (e.g. the Chained Beam-Constraint Model, CBCM) and Finite Element Analysis (FEA). This variety is unquestionably reduced for problems involving special geometries, such as curved or spline beams, variable section beams, nontrivial shapes and, eventually, contacts between bodies. 3D FEA (solid elements) can provide excellent results but the solutions require high computational times. This work compares the characteristics of modern and computationally efficient modeling techniques (1D FEA, PRB method and CBCM), focusing on their applicability in nonstandard problems. In parallel, as an attempt to provide an easy-to-use environment for CM analysis and design, a multi-purpose tool comprising Matlab and modern Computer-Aided Design/Engineering (CAD/CAE) packages is presented. The framework can implement different solvers depending on the adopted behavioral models. Summary tables are reported to guide the designers in the selection of the most appropriate technique and software architecture. The second part of this work reports demonstrative case studies involving either complex shapes of the flexible members or contacts between the members. To improve the clarity, each example has been accurately defined so as to present a specific set of features, which leads in the choice of a technique rather than others. When available, theoretical models are provided for supporting the design studies, which are solved using optimization approaches. Software implementations are discussed throughout the thesis. Starting from previous works found in the literature, this research introduces novel concepts in the fields of constant force CMs and statically balanced CMs. Finally, it provides a first formulation for modeling mutual contacts with the CBCM. For validation purposes, the majority of the computed behaviors are compared with experimental data, obtained from purposely designed test rigs.

Related Publications

Journal Papers:

1. **Bilancia, P.**, Berselli, G., Bruzzone, L. and Fanghella, P., 2019. "A CAD/CAE integration framework for analyzing and designing spatial compliant mechanisms via pseudo-rigid-body methods". *Robotics and Computer-Integrated Manufacturing*, **56**, pp. 287-302.

2. **Bilancia, P.**, Berselli, G., Magleby, S. and Howell, L., 2020. "On the modeling of a contact-aided cross-axis flexural pivot". *Mechanism and Machine Theory*, **143**, p. 103618.

3. **Bilancia, P.** and Berselli, G., 2020. "Design and testing of a monolithic compliant constant force mechanism". *Smart Material and Structures*, **29**(4), p. 044001.

4. Pehrson, N., **Bilancia, P.**, Magleby, S. and Howell, L., 2020. "Load-displacement characterization in three degrees of freedom for general lamina emergent torsion arrays". *Journal of Mechanical Design*, **142**(9), pp. 093301-11.

5. **Bilancia, P.**, Berselli, G. and Palli, G., 2020. "Virtual and physical prototyping of a beam-based variable stiffness actuator for safe human-machine interaction". *Robotics and Computer-Integrated Manufacturing*. (Accepted)

6. **Bilancia, P.**, Smith, S., Berselli, G., Magleby, S. and Howell, L., 2020. "Zero torque compliant mechanisms employing pre-buckled beams". *Journal of Mechanical Design*. (Accepted)

7. **Bilancia, P.**, Baggetta, M., Berselli, G., Bruzzone, L. and Fanghella, P., 2020. "Design of a bio-inspired contact-aided compliant wrist". *Robotics and Computer-Integrated Manufacturing*. (Under Review)

Conference Papers:

1. **Bilancia, P.**, Berselli, G., Bruzzone, L. and Fanghella, P., 2017. "A Practical method for determining the pseudo-rigid-body parameters of spatial compliant mechanisms via CAE tools". *Procedia Manufacturing*, **11**, pp. 1709-1717.

2. Vaschieri, V., Gadaleta, M., **Bilancia, P.**, Berselli, G. and Razzoli, R., 2017. "Virtual prototyping of a flexure-based RCC device for automated assembly". *Procedia Manufacturing*, **11**, pp. 380-388.

3. **Bilancia, P.**, Berselli, G., Scarcia, U. and Palli, G., 2018. "Design of a beam-based variable stiffness actuator via shape optimization in a CAD/CAE environment". *ASME SMASIS Conference on Smart Materials, Adaptive Structures and Intelligent Systems*, V001T03A013.

4. **Bilancia, P.**, Geraci, A. and Berselli, G., 2019. "On the design of a long-stroke beam-based compliant mechanism providing quasi-constant force". *ASME SMASIS Conference on Smart Materials, Adaptive Structures and Intelligent Systems*, V001T03A001.

5. Seymour, K., **Bilancia, P.**, Magleby, S. and Howell, L., 2020. "Hinges and curved lamina emergent torsional joints in cylindrical developable mechanisms". *ASME IDETC International Design Engineering Technical Conferences & Computers and Information in Engineering Conference*. (Accepted)

Acknowledgements

I would like to express my sincere gratitude to my supervisor Prof. Giovanni Berselli, for the constant support of my PhD study and research, for his motivation, kindness and immense knowledge. His guidance helped me in my work and in my life.

My sincere thank also goes to Prof. Larry L. Howell for accepting me into the CMR group, supervising my activity during the last semester and sharing with me many ideas and projects. His work inspired me from the beginning of my PhD.

I am particularly grateful for the support I received during the collaborations with the colleagues from the MCAE Lab and the CMR group. Their contributions have been essential for my research.

An immense heartfelt thank goes to Roxana, who always finds time and energy to support me and my dreams.

Last but not the least, I would like to thank my family and friends for always believing in me.

Pietro Bilancia

Genova
April 2020

Contents

Abstract **I**

Related Publications **II**

Acknowledgements **IV**

List of Figures **VIII**

List of Tables **X**

List of Abbreviations **XI**

1 Introduction and Thesis Outline **1**
1.1 General Concepts and Terminology 1
1.2 Problem Statement 2
1.3 Contribution of the Thesis 4
1.4 Research Methods 5
1.5 Collaboration 6
1.6 Thesis Outline 6

2 Design of Beam-Based Compliant Mechanisms **8**
2.1 Introduction 8
2.2 Modeling Techniques: A Literature Review 10
2.3 A Demonstrative Case Study 14
2.3.1 Cross-Axis Flexural Pivot 14
2.3.2 Kinetostatic Large Deflections Modeling of the Pivot 16
2.4 General Guidelines: How to Proceed in Design Problems 19
2.5 Optimization Approaches 23
2.6 Integrated Design Tool 24
2.7 Final Considerations 26

3 Hybrid Flexures Synthesis in a Compliant Four-Bar Linkage **29**
3.1 System Description and Aim of the Study 29
3.2 Overview of the Design Approach 30
3.3 PRB Modeling: Background Theory and Practical Procedure 32
3.3.1 Planar Assumption: Fixed-Guided Flexible Segment 32
3.3.2 Spatial Case Study 37
3.4 #Step 1: Quick Evaluation of Design Alternatives 38
3.4.1 Performance Indexes Estimation 39
3.4.2 Design Tool - Framework B 40
3.4.3 Numerical Results - Performance Maps 43
3.5 #Step 2: Shape Optimization 43

3.5.1 Problem Formulation . . . 44
3.5.2 Design Tool - Framework G . . . 45
3.5.3 Numerical Results - Optimal Configuration . . . 47
3.6 Summary . . . 50

4 Design of a Linear Constant Force Compliant Crank Mechanism 51
4.1 Constant Force Compliant Mechanisms . . . 51
4.2 System Description and Aim of the Study . . . 52
4.3 Overview of the Design Approach . . . 53
4.4 #Step 1a: Optimal PRB Model Derivation . . . 54
4.4.1 Eccentric Crank-Slider Mechanism: Analytical PRB Model . . . 55
4.4.2 Problem Formulation . . . 57
4.4.3 Design Tool - Framework A . . . 57
4.4.4 Numerical Results - Optimal Configuration . . . 57
4.5 #Step 1b: Flexural Hinges Dimensioning . . . 58
4.5.1 Theoretical Formulation and Practical Procedure . . . 58
4.5.2 Final Dimensions and FEA Validation . . . 60
4.6 #Step 2: FEA Shape Optimization . . . 62
4.6.1 Parametric FE Model . . . 62
4.6.2 Problem Formulation . . . 64
4.6.3 Design Tool - Framework D . . . 64
4.6.4 Numerical Results - Optimal Configuration and Final Tests . . . 66
4.7 Experimental Validation . . . 68
4.8 Summary . . . 69

5 Design of Special-Purpose Torsional Compliant Springs 72
5.1 Compliant Mechanisms with Nonlinear Prescribed Load-Displacement Behavior . . . 72
5.2 Aim of the Study . . . 73
5.3 #Case Study I - Quadratic Compliant Mechanisms in Variable Stiffness Actuators . . . 73
5.3.1 Antagonistic Variable Stiffness Actuators . . . 73
5.3.2 Embodiment Design of the Actuator . . . 74
5.3.3 Actuator Theoretical Static Model . . . 76
5.3.4 CTE Reference Quadratic Behavior . . . 78
5.4 #Case Study II - Nonlinear Compensation Springs in Zero Torque Compliant Mechanisms . . . 79
5.4.1 Zero Torque Compliant Mechanisms . . . 79
5.4.2 Design Configuration in Annular Domain . . . 81
5.4.3 Analytical Modeling of Pinned-Pinned Pre-Buckled Beams . . . 82
5.4.4 Negator Trend and Reference Behavior . . . 84
5.5 Overview of the Design Approach . . . 86
5.6 General Problem Formulation . . . 87
5.7 Numerical Results - Optimal Configurations . . . 89
5.8 Experimental Validations . . . 89
5.8.1 #Case Study I - Dynamic Test . . . 89
5.8.2 #Case Study II - Static Test . . . 92

5.9 Summary . . . 93

6 Performance Study of a Contact-Aided Cross-Axis Flexural Pivot 97
6.1 Contact-Aided Pivots as Asymmetrical Compliant Transmission Elements . 97
6.2 Pivot Geometrical Configurations . . . 99
6.3 Overview of the Performance Study . . . 100
6.4 CBCM Formulation . . . 101
6.4.1 Static Modeling Under Planar Loads . . . 101
6.4.2 Contact Force . . . 106
6.4.3 Performance Indexes Estimation . . . 108
6.5 Design Tool - Frameworks C and D . . . 109
6.5.1 Software Architecture . . . 109
6.5.2 Parametric FE model . . . 111
6.6 Results - Numerical Characterization of the Pivot . . . 112
6.7 Experimental Validations . . . 114
6.7.1 Rotational setup . . . 114
6.7.2 Vertical setup . . . 117
6.8 Summary . . . 118

7 Conclusions 120

Bibliography 122

Appendix 137
A ProcessNet Code Used for the Automatic Model Generation (Chap. 3) . . . 137
A.1 Main Function . . . 137
A.2 Batch File . . . 141
B Matlab Code Used for the PRB Optimization and the Flexural Hinges Dimensioning (Chap. 4) . . . 141
B.1 Main Matlab Script . . . 141
B.2 Objective Function (Behavioral Model) . . . 144
B.3 Optimization Constraint . . . 145
C ANSYS Code Used for the Analysis of the Beam-Based Constant Force CM (Chap. 4) . . . 145
D ANSYS Code Used for the Analysis of the Torsional Springs (Chap. 5) . . . 151
E ANSYS Code Used for the Analysis of the Zero Torque CM (Chap. 5) . . . 155
F Code Used for the Analysis of the Contact-Aided CAFP (Chap. 6) . . . 159
F.1 Main Matlab Script . . . 159
F.2 Matlab Script for the CBCM Equations . . . 168
F.3 Matlab Script for the Shift Evaluation . . . 171
F.4 Matlab Script for the Stress Evaluation . . . 172
F.5 ANSYS Script . . . 173
F.6 Batch File . . . 179

List of Figures

1.1 Compliant configurations. 2
1.2 Flexible systems modeled with the open source design tools. 4

2.1 Examples of configurations with nonstandard geometry. 13
2.2 Standard CAFP - geometrical parameters. 16
2.3 CAFP modeling. 18
2.4 Comparison of results achieved on the standard CAFP with different modeling techniques for an imposed rotation $\theta = 0.7$ rad. 19
2.5 Demonstrative case studies. 27

3.1 Spatial crank mechanism. 31
3.2 Multi-step design flow. 32
3.3 Planar compliant four-bar linkage. 33
3.4 Fixed-guided flexible beam. 34
3.5 Cantilever flexible beam subjected to out-of-plane loads. 38
3.6 Spatial four-bar linkage: adopted PRB model. 39
3.7 Framework B used for the #Step 1. 41
3.8 Performance maps for the evaluation of design alternatives. 42
3.9 Parametric hybrid flexure. 45
3.10 Framework G used for the #Step 2. 46
3.10 Optimal solution and comparison between PRB model and CM behaviors. 49
3.11 Final platform trajectory. 49

4.1 Constant force mechanism in robot end-effector. 52
4.2 Multi-Step design flow. 53
4.3 Eccentric crank-slider mechanism - PRB model. 55
4.4 Framework A used for the #Step 1a. 58
4.5 PRB behavioral analysis. 59
4.6 Optimal results on the small-length configuration. 61
4.7 Schematic showing the correlation between the mechanisms. 63
4.8 Framework D used for the #Step 2. 65
4.9 Optimal results on the beam-based configuration. 67
4.10 Experimental setup. 69
4.11 Experimental force-deflection relationships. 70

5.1 Functional schematic of the antagonistic VSA. 74
5.2 VSA CAD overview. 75
5.3 Conceptual schematic of the zero torque CM. 80
5.4 Pinned-pinned pre-buckled negators in the annular frame. 82
5.5 Principle schematic of the pre-buckled negator. 83
5.6 Negator Testing. 85
5.7 Parametric FE model used for the optimizations. 87

5.8 Graphical representation of the error evaluation principle. 88
5.9 Optimal FE models. 90
5.10 Performance of the optimal configurations. 92
5.11 CTE physical prototype and experimental rotational setup. 93
5.12 CTE experimental results. 94
5.13 Zero torque CM - static balancing in different angular positions. 95
5.14 Experimental rotational setup for the static test. 95
5.15 Comparison between predicted and measured behaviors. 95

6.1 Conceptual design of a bio-inspired wrist employing the contact-aided CAFP. 98
6.2 Contact-aided parametric CAFP. 100
6.3 Effect of the contact member on the pivot deflection. 101
6.4 CBCM - details about the model. 103
6.5 CAFP global equilibrium. 105
6.6 Framework C-D used for the parametric studies. 110
6.7 DOE results for $\beta = \pi/4$ rad in a pure rotation $\theta = 0.7$ rad. 112
6.8 DOE results for $L = 50$ mm in a pure rotation $\theta = 0.7$ rad. 113
6.9 Experimental setup for stiffness evaluation. 115
6.10 Experimental and numerical results with an imposed rotation $\theta = 0.52$ rad. 116
6.11 Vertical experimental setup for parasitic shift evaluation. 117
6.12 Experimental and numerical results with a pure force $F_x = 3.92$ N. 118

List of Tables

2.1 Modeling techniques: time required to build and solve the single model. . . 20
2.2 A comparison of modeling techniques for the study of nonstandard problems. 22
2.3 Selection of the appropriate framework architecture and solver. 25

3.1 Main dimensions of the system. 30
3.2 Hybrid flexures - additional parameters. 44
3.3 Optimal hybrid flexure - numerical solution. 47

4.1 Optimal PRB model - characteristic parameters. 58
4.2 Flexure dimensions. 60
4.3 Reference points coordinates. 63
4.4 Optimal beam-based CM parameters. 66

5.1 Optimal dimensions of the nonlinear torsional CMs. 91

6.1 CAFP parameters considered in this work. 111

List of Abbreviations

BCM	Beam-Constraint Model
CAD	Computer Aided Design
CAE	Computer Aided Engineering
CAFP	Cross-Axis Flexural Pivot
CBCM	Chained Beam-Constraint Model
CBDA	Constraint-Based Design Approach
CM	Compliant Mechanism
CTE	Compliant Transmission Element
DOE	Design of Experiments
DOF	Degree of Freedom
FACT	Freedom And Constraint Topology
FEA	Finite Element Analysis
GA	Genetic Algorithm
MBD	Multibody Dynamics
PRB	Pseudo-Rigid Body
RMS	Root Mean Square
RSM	Response Surface Modeling
SLFP	Small Length Flexural Pivot
VSA	Variable Stiffness Actuator

Chapter 1

Introduction and Thesis Outline

1.1. General Concepts and Terminology

Differently from rigid-body mechanisms, which transfer forces and displacements employing traditional kinematic pairs based on conjugate surfaces, Compliant Mechanisms (CMs) gain at least some of their mobility from the deflection of elastic members [1]. Potential advantages over traditional mechanisms can be outlined into cost reduction and increased performance. In fact, CMs require fewer components to achieve the desired mobility with consequent reduction of time/cost for device manufacturing. For what concerns possible performance improvement, the absence of rigid kinematic pairs reduces wear, need of lubrication and possible backlash, which might be beneficiary in terms of mechanism precision. Also, CMs can be scaled and miniaturized. Some CMs' application areas include constant force and nonlinear springs [2, 3], compliant actuators [4], monolithic cardan/-spherical joints [5, 6], micro-manipulators [7, 8] and micro-grippers for precision assembly [9]. Moreover, the development of new materials, production technologies (e.g. additive manufacturing [10]) and fields of application (see, e.g., medical [11, 12] or origami-inspired devices [13, 14]) largely justifies the increased studies in this area during the last twenty years of research.

From a terminology standpoint, generic CMs may be classified into two main categories: lumped CMs and distributed CMs. As for lumped CMs, they are characterized by compliant structures whose elastic deformation is localized in "small regions", i.e. the so-called Small Length Flexural Pivots (SLFPs) [15], as shown in Fig. 1.1(a). These are usually obtained by machining one or two cutouts in a blank material with constant width, making it possible to obtain (if desired) monolithic solutions. On the contrary, in distributed CMs the deformation occurs along a large part of the elements, which are usually identified by beam-like segments (also referred to as beam-based CMs) or shells, as depicted in Figs. 1.1(b) and 1.1(c). Beam-

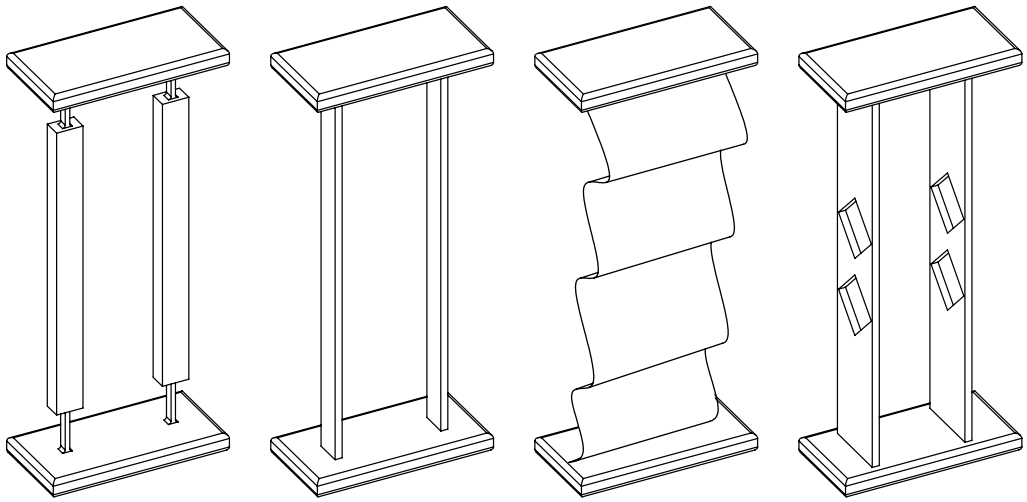

(a) Lumped CM. (b) Beam-based CM. (c) Compliant shell. (d) Hybrid flexure.

Figure 1.1: Compliant configurations.

based CMs may comprise both flexible and rigid links connected with traditional kinematic pairs [1], whereas compliant shells are open, thin-walled, discretely corrugated structures, with flat facets or curved regions [16].

According to [17], in this thesis, the term "hybrid flexures" is adopted for describing distributed CMs with complex topology, seen as a combination of eyelets, holes, rounds or, in general, as a pattern of geometrical attributes. Figure 1.1(d) shows an example of a hybrid flexure in a beam-based CM. A similar concept is reported in [18], which introduces the "lattice flexures" as a new flexure type that has an envelope similar to a standard flexure but has dramatically reduced motion-direction bending stiffness.

1.2. Problem Statement

Beyond the above-mentioned advantages, a series of challenging issues arise when dealing with CMs. In particular, it should be considered that: a) the motion of a flexible member is limited to the elastic deflection range; b) a certain amount of strain energy is stored during the deflection; c) fatigue life of the flexible members requires special attention in case of cyclical loads; d) stress relaxation can occur if the flexible members are loaded for long periods of time. These aspects make the design of CMs more complex if compared to traditional mechanisms, since analysis and synthesis methods must be integrated with accurate models describing the deflections of the flexible members. As long as CMs undergo large deflections,

simple linearized equations are not valid and geometric nonlinearities must be taken into account. Starting from the Euler-Bernoulli beam theory, several advances have been made over recent decades regarding the modeling of large deflections. Many researchers developed new algorithms for improving the computation or proposed innovative techniques for including even more complex scenarios, such as nonstandard geometries and contacts between bodies. Aside from the general and well established Finite Element Analysis (FEA), some specific examples in the CM area are the elliptic integrals solution [19], the Pseudo-Rigid Body (PRB) method [1], the circle arc method [20], the Beam-Constraint Model (BCM) [21] and the Chained Beam-Constraint Model (CBCM) [22]. In the following, 1D FEA and 3D FEA will be used to indicate the mono-dimensional or three-dimensional element types within the FEA. A detailed overview of the modeling techniques will be given in Chap. 2.

As specified in the previous section, CMs may be categorized on the basis of the relative size of the deflecting "portion". Lumped CMs have been largely described and analyzed from the research community. Concepts and design methods are well summarized in [15]. As for beam-based CMs, their macroscopic deflections have been modeled via different approaches, each of them usable under certain conditions. Overall, the large variety of modeling techniques may be quite confusing for designers that have to face nonstandard problems and challenging requirements. These circumstances usually need an optimization study, where several simulations must be performed. Therefore, the selection of the appropriate modeling technique becomes essential to achieve fast and accurate solutions. At the current state-of-the-art, despite a wide literature dealing with the theories behind any modeling technique is available, neither comparative studies between the techniques nor practical guidelines that show the applicability of such theories are provided.

In parallel, there is an evident lack of specific CM design tools. The existent solutions are limited to SPACAR [23] and DAS 2D/3D [24], namely open source environments capable of accurately solving problems involving CMs with both rigid and flexible parts. These packages may be useful during the preliminary design steps. They provide simple modeling features that help in exploring new concepts. Also, the high computational efficiency allows to quickly compute the properties of the conceived design. However, as the main drawback, complex geometries of the flexible members as well as contacts cannot be natively included in the simulations. Consequently, these environments are successful only for case studies

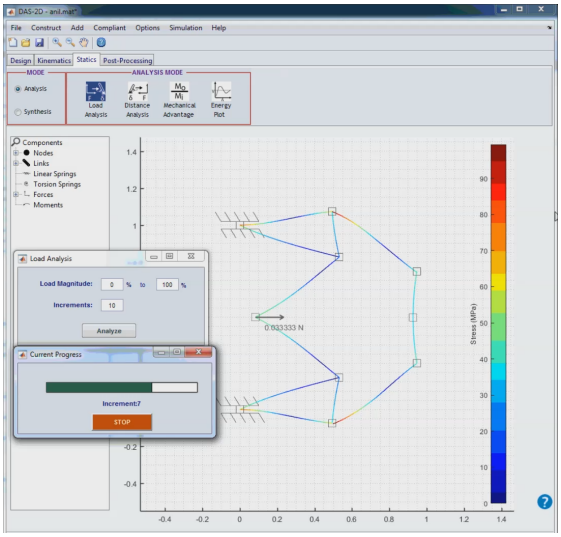

(a) Example of DAS 2D/3D post-processing.

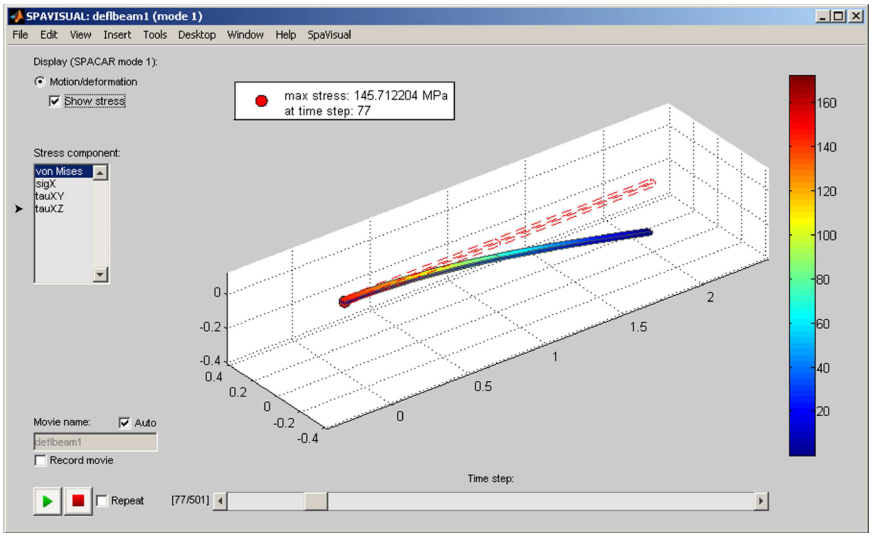

(b) Example of SPACAR post-processing.

Figure 1.2: Flexible systems modeled with the open source design tools.

involving "standard" compliant elements, as the ones visible in Figs. 1.2(a) and 1.2(b).

1.3. Contribution of the Thesis

This research reports on advances in the design of beam-based CMs. The main contributions of the thesis are as follows:

- a structured study concerning the advantages and the limits of the most used modeling techniques for the analysis/design of complex scenarios (1D FEA, 3D FEA, PRB method and CBCM). Comparative tables are presented to help designers in the selec-

tion of the appropriate technique(s) on the basis of the defined design intents.

- a set of possible software frameworks that combine commercial packages in an integrated design environment. The frameworks are guided from Matlab and can be customized by the user to solve optimization problems with one or more modeling techniques. Technical details about the codes as well as discussions about the selection of the solver are given throughout the chapters.

- practical examples that support the previous comparison and illustrate how to face design problems of different natures by combining the capabilities of the modeling techniques and the software frameworks. For each case study, theoretical models are reported and discussed in order to show their applicability. In most of the reported examples, physical experiments are used to validate the numerical results and to prove the suitability of the proposed approaches.

- new concepts in the field of constant force CMs and statically balanced CMs.

- an exploratory study showing the CBCM capabilities for modeling contact-aided CMs. Numerical results achieved on a demonstrative case study are validated through FEA and experiments.

1.4. Research Methods

The research work proceeded along the following general steps:

1. Survey of literature for design methods and modeling techniques regarding beam-based CMs;

2. Study of special-purpose beam-based CMs focusing on their design procedures;

3. Development of accurate and efficient behavioral models by exploiting different techniques;

4. Numerical validations of the models through rapid comparisons between the outputs from different techniques;

5. Production and testing of physical prototypes.

1.5. Collaboration

The majority of this work has been performed at the University of Genova, but will also include important results achieved during the visiting period at Brigham Young University - Compliant Mechanisms Research Group (Provo, Utah).

1.6. Thesis Outline

This thesis is composed of chapters that are conceived as "stand alone" contributions. Therefore, each chapter contains its introduction and final remarks. It must be specified that the mathematical notation is consistent within each chapter, whereas the terminology is kept general to facilitate the reading.

The manuscript is organized as follows:

- **Chapter 1** introduces the motivation for studying the modeling techniques of beam-based CMs in case of nonstandard scenarios and the need to develop dedicated design tools.

- **Chapter 2** reviews the background and literature concerning the design methods and behavioral modeling of beam-based CMs. The limits of each techniques are highlighted and discussed. Practical considerations are given to help the designers in the selection of the most convenient/efficient modeling technique(s) in case of nontrivial shapes of the flexible members or contacts. The chapter also presents possible software framework architectures that can be implemented in design optimization problems.

- **Chapter 3** reports the shape optimization process carried out on custom shaped hybrid flexures and provides details about the software implementations. Such flexures are used as compliant elements in a four-bar linkage and are subjected to out-of-plane motions. The design problem is solved in two sequential steps. At first, a PRB model is employed to investigate the behavior of the system by varying different geometrical parameters. Performance maps are produced and then used to select the most promising configuration. By adopting the optimal PRB configuration as reference, the second step provides the final flexures' configuration through a FEA optimization.

- **Chapter 4** illustrates a multi-step procedure for the structural optimization of CMs that combines analytical and numerical modeling techniques. The method is tested on a constant force linear mechanism based on the slider-crank concept. At first, the PRB approximation is used to synthesize the optimal lumped compliance configuration. Then, a variable thickness beam is adopted to smooth the shape of the CM where the cross section presents discontinuities. The final shape is achieved by means of a FEA optimization. At last, the predicted behaviors are validated with experiments on 3D printed specimens.

- **Chapter 5** reports the optimal design of nonlinear torsional springs with prescribed load-deflection relationships. Two case studies are discussed, namely a Compliant Transmission Element (CTE) to be used in an antagonistic Variable Stiffness Actuator (VSA), and a compensation spring integrated in the design of statically balanced CMs. Theoretical models of the overall systems are discussed to prove the need of specific nonlinear torque-deflection relationships. The prescribed behaviors are obtained using spline beams as connection elements between the inner and outer rings. A FEA optimization is performed to obtain the final shapes. Lastly, data acquired by means of two custom test rigs are used to validate the numerical results.

- **Chapter 6** presents the modeling of a contact-aided Cross-Axis Flexural Pivot (CAFP), namely a system comprising a standard CAFP and a purposely shaped contact member that acts on a single flexure. The behavior of the pivot is numerically investigated by introducing a penalty-based contact algorithm in the CBCM formulation. The obtained results are compared to the ones achieved with FEA in order to evaluate the CBCM efficiency in case of contact analysis. The accuracy of the results is finally validated via experimental investigations for different planar loads.

- **Chapter 7** summarizes the main contributions of this thesis and reports on the methods and tools used to achieve the presented results.

- **Appendix** includes a group of codes used in this research.

Chapter 2

Design of Beam-Based Compliant Mechanisms

2.1. Introduction

CM design is more complex when compared to traditional mechanisms. In rigid-body mechanisms, the motion and the transmitted forces can be singularly analyzed (i.e. in two sequential steps, if necessary). On the contrary, in CMs, forces are required to produce deformations, which are related to the mechanism configuration and geometry, as well as on the adopted material. Therefore, CMs are more sensitive to the geometrical parameters. CM design is primarily made difficult by the presence of finite deflections of the flexible members, possibly causing undesired deformations (i.e. cross-axis and parasitic error motions [21, 25]), whose effects are usually more pronounced in beam-based CMs than in lumped compliance CMs. Specific requirements in terms of motion and load-displacement functions must be satisfied by designing a mechanism capable of achieving large deflections within the elastic range. Consequently, the stress arising in the mechanism has to be monitored and it represents a crucial aspect during the design. Continuous rotational motions cannot be obtained and, as it may be evident, CMs' resistance to buckling and fatigue must be carefully addressed via either experimental characterization (see e.g. [26]) or dedicated simulation tools (such as ANSYS, see, e.g., [27, 28]). The necessity to provide the engineering community with effective strategies for CM analysis and synthesis has led to the development of several design approaches and modeling techniques. An overview of the design approaches is given in the following, whereas Sec. 2.2 provides a description of the techniques commonly used for CM modeling.

Once the mechanism requirements and constraints are defined, the design procedure focuses on the research of the correct topology, shape and size of the flexible parts. In the last decades, many planar and spatial CMs have been introduced, analyzed and optimized. Thus, for a given kinematic and force deflection need, plenty of configurations can be adopted

within the existing devices (a comprehensive library can be found in [29]). In most situations (see Chaps. 4 and 6), the synthesis process starts from the selection of a consolidated concept, namely a system well described and discussed in the previous literature. This system may be a compliant device or a rigid-body mechanism performing a desired function (in this case the rigid-body replacement method [29] is employed for the transition into compliant mechanisms). Recommended actions, behavioral models and performance maps are usually available and guide the designers in the definition of new prototypes. Note that rigid-body kinematic methods are particularly useful for the analysis and design of lumped compliance mechanism, but are not longer applicable if a large portion of the structures deforms, i.e. in case of beam-based CMs.

As it may be evident, to fulfill strict requirements or achieve high levels of accuracy, the designer may choose to synthesize a new concept instead of selecting, combining and modifying previous configurations. This approach leads to innovative solutions that can match precise design requirements, however, it needs the use of more advanced and sophisticated design methods. For instance, the conceptual design of beam-based CMs has been tackled by means of the Constraint-Based Design Approach (CBDA), which is described in [30]. The CBDA leverages on the evidence that any motion of a rigid body is basically determined by the constraints' position and orientation (i.e. the constraint topology). Also, a mathematical formulation of the CBDA, based on the screw theory formalism, has been addressed in [31]. In parallel, the Freedom And Constraint Topology (FACT) method, described in [32, 33], combines qualitative information about the flexure system's degrees of freedom and its constraint topology, in order to investigate the relationships between all possible flexure designs and related displacements. Then, the shapes of the deformable members, which allow realizing a desired motion of a point of interest, are selected on a map in which all known shape combinations are distributed over the design space. On the other hand, quoting [34], when the FACT method is used for designing multi-degree-of-freedom CMs, the quantitative modeling of the motion characteristics is not involved. Therefore, FACT-based CM design can be improved by employing the so-called position-space-based reconfiguration approach, which allows to reconfigure a CM designed for a specific task, with the aim of minimizing its parasitic motions [34–36].

Another alternative method for generating viable initial solutions directly from problem

specifications leverages on the concept of basic compliant building blocks, which are well described in [37]. However, whenever strict tolerances on the desired displacement are required, a further optimization procedure is necessary after the preliminary study. Shape optimization [38] and topology optimization [39–43] (or, more generally, continuum structure optimization approaches [44]) are applicable for the synthesis of distributed CMs with irregular or complex shapes (see e.g. [45]). Topology optimization can result in novel solutions that the designer might not have arrived at by combining standard compliant elements. It is intended to predict the best topology, or structural layout, for a specific design problem. From a practical standpoint, once the spatial domain as well as the connection element type, the constraints and the external loads acting on the solid are defined, this method is used to find the best pattern of connectivity (or spatial sequence of elements in the structure), i.e. the one that provides a specified output displacement in response to the input force. The topology optimization problem has been formulated in a number of alternative ways and a dense literature is available (see [46] for a survey). Nonetheless, a well-known drawback of this method is the possibility to generate design solutions comprising singularities (like punctual flexural structures). For a more detailed overview about the design approaches, the interested reader may refer to [1, 29, 44].

2.2. Modeling Techniques: A Literature Review

Once a concept is chosen, behavioral models need to be defined in order to characterize the CM under investigation, understand the influence of the design variables (such as thickness and length of flexible parts) on the required outputs (motion, forces and stresses), and then finalize the design. As previously stated, systems employing SLFPs may be modeled resorting to common theories for rigid-body mechanisms both for analysis and synthesis purposes [1, 4]. A case study employing the principle of virtual works is discussed in Chap. 3.

Simple, parametric and accurate analytical models are always desirable for designing flexible parts since they require limited computational resources. However, when modeling beam-based CMs, the use of analytical approaches, such as the Euler-Bernoulli beam theory, is restricted to regular geometries, i.e. flexible beams with constant cross sectional area along the main axis. Large deflections introduce additional limits in the problem, since geometric nonlinearities must be taken into account and a closed-form solution is no longer available.

The elliptic integral approach has been extensively used for modeling large deflections of slender beams in which the elongation and the shear are negligible, showing accurate results [19, 47]. However, its implementation is quite intricate and the solution is straightforward only when the end slope of the deflected beam is in a certain range. Practically speaking, these expressions must comply with some strict limitations in order to work properly and are convenient only when relative simple geometries and loading scenarios are considered.

Given that initially straight beams are largely used in the field of CMs, building upon the above-mentioned limits, several model improvements have been developed to either incorporate even more features or to simplify the derivation process. A numerical integration technique, based on the Gauss-Chebyshev quadrature formulae, is proposed in [48] with the aim of simplifying the procedure and limit the computational time. As an attempt to further facilitate the computation, an incremental linearization approach to turn the nonlinear problem into a sequence of linear problems is presented in [49]. In [50], the Adomian decomposition method is used to obtain a semi-analytical solution that is particularly suitable for optimization purposes.

Many researches focused on the need to extend the applicability of the Euler-Bernoulli formulation to more complicated case studies. A complete model that incorporates the axial deflection of the beam to correct for the inextensible assumption made in the bending model is reported in [51], whereas a comprehensive elliptic integral approach capable to solve beams of any end angle and with multiple inflection points is proposed in [52], showing accurate results for complex deflection modes.

In this context, another powerful method for CM analysis/synthesis is the PRB approach [1], which describes a CM by a series of rigid links connected through spring-loaded kinematic pairs, such as spherical, prismatic or revolute joints (also called characteristic pivots). Once a PRB topology has been selected (namely, number and type of kinematic pairs), specific optimization routines, such as gradient-based [53] or nongradient based methods [54], are employed in order to assess the values of both springs' stiffness and pivots' location allowing a PRB-based mechanism to replicate the CM kinetostatic behavior as close as possible. In general, it may happen that the chosen PRB representation does not capture the deformations of the compliant elements up to a level of accuracy that is deemed sufficient for the application at hand, thus forcing the designer to increase the PRB model's degrees of

freedom. A detailed discussion of this issue can be found in [55], where a spring-loaded 3R chain is used to approximate the deflection of a cantilever beam subjected to a general tip load. The obtained performances are compared with the ones achievable through a simple 1R PRB model.

In practice, PRB techniques basically offer two advantages: i) enhanced computational efficiency during CM simulation; ii) possibility to employ well established methods and software tools, such as common Multibody Dynamics (MBD) environments, specifically conceived for analyzing rigid-link mechanisms. On the other hand, PRB limitations, whose acceptability has to be evaluated on a case by case basis, may be listed as follows: i) possibility for the PRB parameters to become load dependent in case of insufficient mobility of the chosen PRB topology (refer to [56] for an overview and a comparison of several PRB topologies); ii) incapability to capture nonlinear effects arising during large deflections, such as material nonlinearity, geometric nonlinearity and load-stiffening effects [21]. Henceforth, CM architectures computed via the PRB method are usually validated by means of FEA or experiments at the end of any design process. Despite these limitations, PRB techniques have been successfully used for the preliminary design of beam-based CMs [57], for evaluating CM workspaces [58], for comparing compliant joints morphologies [59], for modeling contacts [60], bi-stability [61] and dynamics [62] in CMs, and for model-based control of compliant mechatronic devices [63]. Examples of applications of the PRB method are reported in Chaps. 3 and 4.

There are also a few discretization-based techniques available for the modeling of CMs. They provide accurate prediction of very large deflections and may be very efficient and useful in certain situations, such as for describing irregular (curved) geometries of the flexible members. Also, they represent a valid approach for simulating the effect of contacts between members or their buckling instability. This class of methods divides the beam being modeled into elements and analyzes each contribute in succession in order to obtain the overall behavior. A chain algorithm has been initially proposed in [64], where each element is modeled as a small-deflection beam cantilevered at the end of the previous element. The response is computed by inverting the elements' stiffness matrices. An alternative procedure is described in [20], where the beam is discretized using a low number of elements, each of them assumed to deform into a circle arc when loaded. The algorithm can be easily programmed

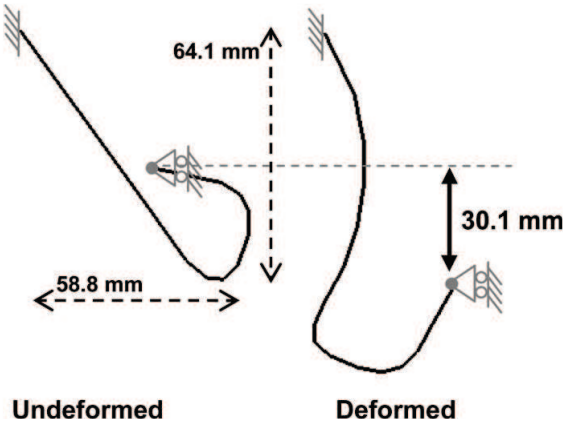

(a) Spline beam [38].

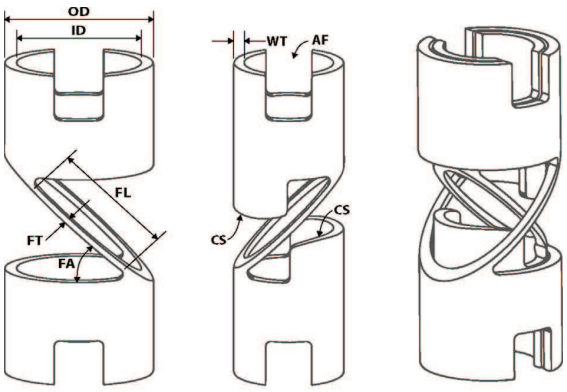

(b) Cylindrical CAFP [67].

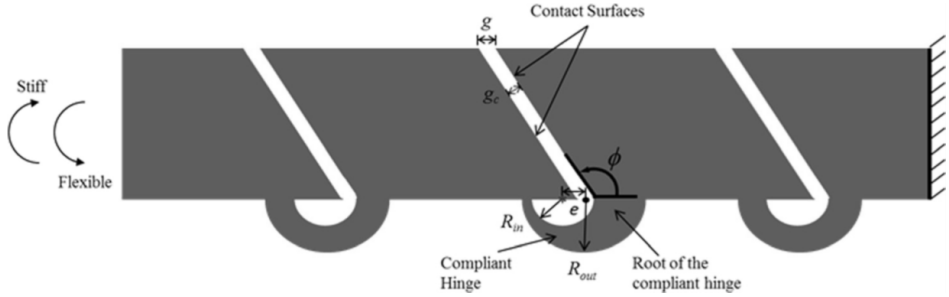

(c) Contact-aided CM for passive bending [68].

Figure 2.1: Examples of configurations with nonstandard geometry.

due to its simple formulation and it is well suitable for optimization procedures. The main limit is that the beam is treated as inextensible.

Recently, by leveraging the closed-form BCM reported in [21], which include the axial deflection and accurately capture the relevant nonlinearities when deflections are within 10-15% of the beam length, an efficient chain algorithm has been defined. The CBCM [22] divides the flexure into elements and models each element via BCM equations. Because of the higher accuracy of the single element model, the CBCM requires much fewer elements than other discretization-based techniques utilizing linear elements to obtain the desired accuracy in large deflection problems. Other important advantages are the closed-form nature of the overall system (which leads to evident advantages from a computational point of view), and the possibility of analyzing initially curved beams [65], spatial deflections [66] and contacts (see Chap. 6). Generally, the CBCM outperforms all the methods that ignore the axial strain. A detailed explanation of the CBCM equations is included in Chap. 6.

At last, a powerful technique for the CM modeling is the FEA due to its wide library

of element types, modeling features and options. Modern commercial environments allow to easily manage nontrivial geometry (such as hybrid flexures) and to analyze systems comprising large numbers of parts. On the contrary, the previously discussed techniques are best used for modeling single elements due to their complex formulation. FEA provides accurate algorithms for the modeling of contacts and other nonlinearities, such as specific material properties (plasticity, superelasticity, creep, etc.) or buckling instability. For this reason, most of the works dealing with the CM analysis/design make final performance checks using FEA. Properly defined FE models can be an excellent way to demonstrate the potentiality of a concept and validate the study [67, 69].

As demonstrated by [38, 70, 71], 1D FEA (beam elements) may be a strategic tool for designing beam-based CMs when irregular shapes, as the one in Fig. 2.1(a), or systems composed of several beams in series and parallel are considered. A single parametric 1D FE model can be solved in few seconds, promoting the use of optimization routines.

The use of 3D FEA becomes essential for systems comprising custom shaped geometries, defined and subsequently exported from a parametric Computer Aided Design (CAD) environment. Examples of configurations that need 3D FE models are visible in Figs. 2.1(b) and 2.1(c). In such cases, none of the other techniques can be used for achieving accurate results.

2.3. A Demonstrative Case Study

This section aims at comparing the primary outputs of a typical CM analysis (force-deflection relationship and maximum stress) obtained with four modeling techniques among the most used and described. The large deflections study is performed on a standard CAFP by considering regular beam geometries and by excluding contacts, buckling and other additional nonlinearities. More complex case studies will be discussed in the next chapters.

The first part of the section introduces and describes the CAFP concept, whereas the second part reports the results of the comparative study.

2.3.1. Cross-Axis Flexural Pivot

The CAFP is a planar beam-based CM formed by two symmetric beams, that are connected at both ends to a pair of shared rigid blocks [72], hereafter referred to as ground

and output links. Two different configurations have been conceived in literature: in the first one, the crossing beams are completely independent, whereas in the second one, usually referred as cartwheel pivot, the beams are connected to each other where they cross, producing a single structure. As highlighted in [73], the resulting elasto-kinematic behavior shows remarkable differences based on the selected configuration. In particular, the first configuration is characterized by an increasing nonlinear trend of the equivalent stiffness for very large deflections, whereas the second configuration presents the typical trend of circular and elliptical flexural hinges, namely a reduction of the equivalent stiffness as the angle of rotation increases.

From a kinematic standpoint, the CAFP's maximum deflection is naturally limited by the stress field arising within the flexures [74] and it is usually constrained in the range $[0, \pi/2]$, depending on the employed material. This aspect restricts the use of the CAFP to applications that need a limited well-defined deflection range. Also, the relative rotation between the ground and output links entails a parasitic shift from the initial center of rotation, i.e. the intersection point between the flexures in the undeflected configuration [70, 75–78].

When employed in place of a revolute joint, the CAFP morphology enables a highly selective compliant behavior [15, 25], namely a low stiffness for in-plane motion and high stiffness along other directions. Due to potential advantages over common rigid kinematic pairs, such as the absence of backlash and friction, the high positioning accuracy, and the reduced number of components (thus, the simplified manufacturing process), the CAFP concept is commonly implemented in precision engineering applications [79]. Examples include measurement systems [80], precision mechanisms [67, 81–83], optical instruments [84], bio-inspired devices [85] and space systems [86]. The relatively simple CAFP topology allows to easily form arrays [87] or to combine the mechanism with additional structural elements to synthesize static-balanced mechanisms [88–91]. As a result of the advent of efficient additive manufacturing technologies, even more complex shapes can be produced [18, 67, 90]. Furthermore, by combining typical origami principles and two-dimensional machining processes, folded CAFP joints can be manufactured [13].

However, as a CM, the CAFP analysis/design is more complex and some critical structural issues have to be considered. In the literature, several works are focused on the CAFP performance analysis. Apart from the fatigue life [92], which has to be carefully investigated

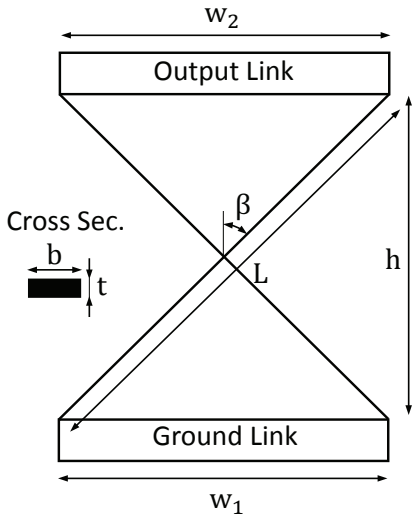

Figure 2.2: Standard CAFP - geometrical parameters.

in case of dynamic operative conditions, the CAFP's beams can fail due to buckling in case of compressive loads acting on the ground and output rigid links [72].

The CAFP analysis and design have been addressed via various approaches. For example, models employing the linear Euler-Bernoulli beam theory for small angles of deflections are reported in [72, 79]. In [72], the large deflection problem is solved by means of elliptic integrals for a pure moment load case. In [93], the CAFP is studied resorting to two PRB models. In [74, 76], the CAFP under the effect of both forces and moment is modeled resorting to the BCM [21, 94], which can accurately capture the intermediate deflection range. Very Large deflections can be correctly described via the CBCM, as proven in [22].

2.3.2. Kinetostatic Large Deflections Modeling of the Pivot

As specified in the previous section, the CAFP modeling can be approached through different numerical techniques. The current comparative study comprises a group of general purpose techniques among the most used and described in the recent literature about CMs, namely the PRB method, the 1D and 3D FEA and the CBCM. Generally, each technique allows to solve problems of different nature, and with specific sets of boundary conditions, material models and simulation settings. Also, the required level of expertise varies depending on the adopted approach and increases when commercial tools cannot be used for solving the problem.

A standard CAFP consisting of two independent beams with constant rectangular cross section along the axis is considered in order to evaluate the results accuracy, the modeling time (i.e. the total time required to build a single model) and the simulation time for each of the above-mentioned techniques. In fact, by excluding complex scenarios, such as complex beam's geometries (i.e. nontrivial shapes) and contact analysis, all the considered approaches can be applied to solve the CAFP's large deflection problem.

With reference to Fig. 2.2, the CAFP geometry is completely defined by w_1, w_2, β, b and t, namely the lower and upper width, the angle between the crossing beams and the cross section dimensions. The pivot height, h, and the flexure length, L, can be easily found as:

$$h = \frac{w_1 + w_2}{2\tan(\beta)} \tag{2.1}$$

$$L = \frac{w_1 + w_2}{2\sin(\beta)} \tag{2.2}$$

Four behavioral models are developed by considering an isotropic material with Young's modulus and Poisson's ratio equal to $E = 1400$ MPa and $\nu = 0.4$ respectively, and by adopting $w_1 = w_2 = 30$ mm, $\beta = \pi/4$, $b = 5$ mm and $t = 1.6$ mm. In particular:

1. a 3D CAD of the system is drawn and meshed with brick elements to build the 3D FE model (see Fig. 2.3(a));

2. two simple lines are drawn, meshed with beam elements and connected each other with a rigid body element to build the 1D FE model (see Fig. 2.3(b));

3. an anti-parallel symmetric four-bar-linkage, as the one proposed and described in [93], is adopted as PRB model (see Fig. 2.3(c));

4. the closed-form procedure reported in [22] is used to define the CBCM model (shown in Fig. 2.3(d)).

Detailed descriptions of the numerical models are beyond of the scope of the current section and will be given in the next chapters (see also the Appendix for code implementations). By applying a rotation $\theta = 0.7$ rad to the outer link and recording the reaction torque, the static load-deflection relationship has been obtained in a series of substeps. The models also output the maximum stress occurred during the deflection. Figure 2.4 shows a comparison between

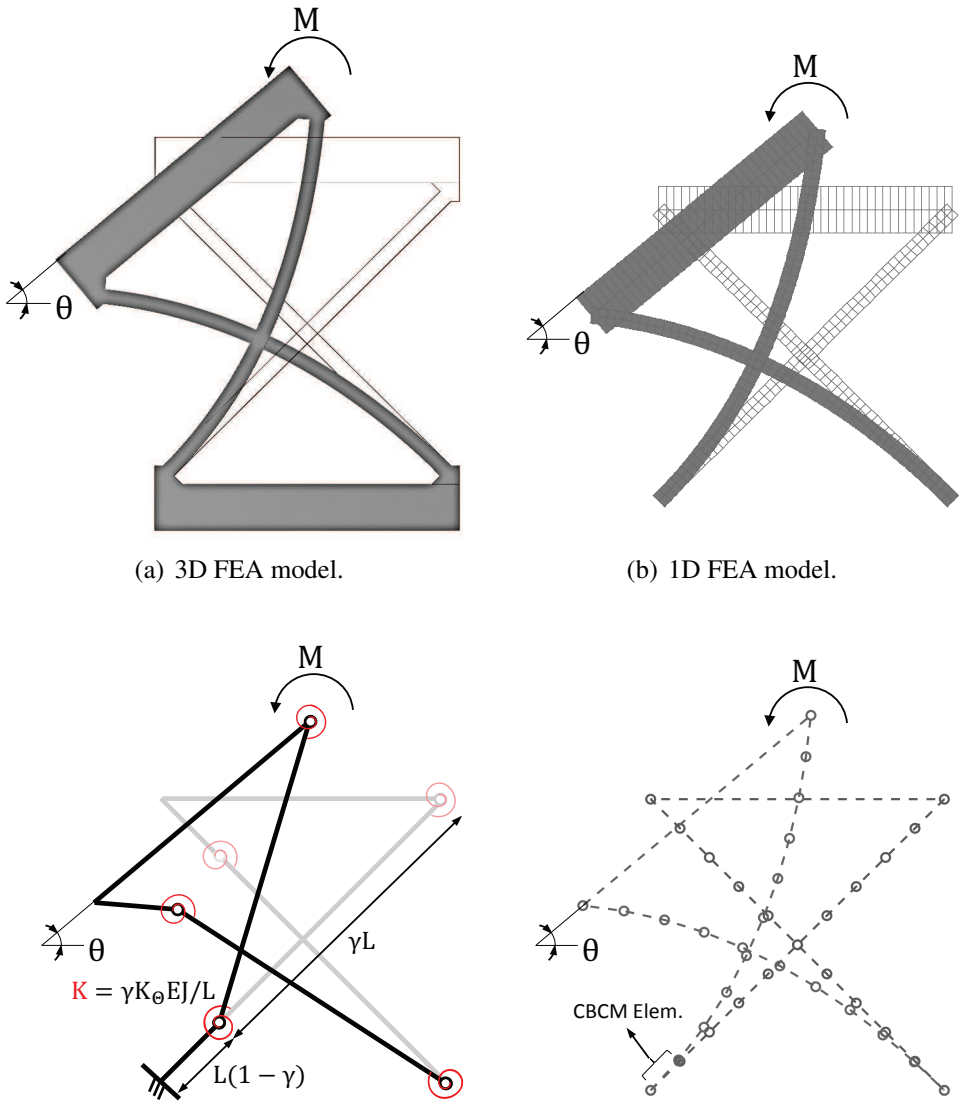

(a) 3D FEA model.

(b) 1D FEA model.

(c) 4R PRB model with $\gamma = 0.785$ and $K_\Theta = 2.311$ (taken from [93]).

(d) CBCM with 10 elements for each beam.

Figure 2.3: CAFP modeling.

the numerical results. Overall, there is acceptable agreement between the data, confirming the suitability of the techniques for studying beam-based CMs in large deflections problems. Taking the 3D FEA as the reference load-displacement behavior, the discrepancy may be quantified with a Root Mean Square (RMS) error equal to 0.36 Nmm, 2.42 Nmm and 1.09 Nmm for the 1D FEA, PRB method and CBCM respectively. Modeling and simulation times are listed for each technique in Tab. 2.1. While the former values are related the user's skills, the latter may vary depending on the employed software as well as on the workstation characteristics. In this research work, all the simulations are performed on a workstation

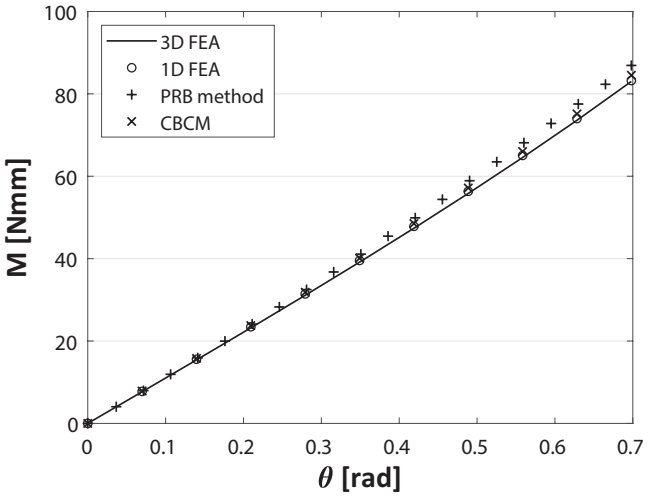

(a) Torque-deflection relationship.

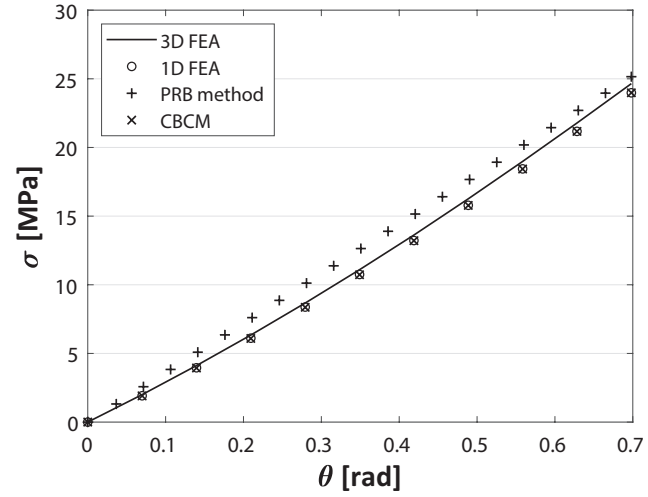

(b) Maximum flexural stress.

Figure 2.4: Comparison of results achieved on the standard CAFP with different modeling techniques for an imposed rotation $\theta = 0.7$ rad.

with an Intel Intel(R) Xeon(R) CPU E3-1270 v5 @ 3.6 GHz and 32GB RAM.

2.4. General Guidelines: How to Proceed in Design Problems

This section focuses on the selection of the appropriate modeling technique(s) in the design of nonstandard scenarios, namely specific case studies where purely analytical methods fail to provide useful information. As highlighted in the previous state-of-the-art overview (see Sec. 2.2), the large deflection problem has been studied extensively in the field of CMs.

Table 2.1: Modeling techniques: time required to build and solve the single model.

Modeling Technique	Modeling Time	Solving Time
3D FEA	45 min	300 s
1D FEA	30 min	2.5 s
PRB method	60 min	0.2 s
CBCM	180 min	1.5 s

Many techniques can be selected for general problems, as visible from the discussion reported in the previous section (note, once again, that more than four techniques can be employed for modeling the standard CAFP). When available, analytical approaches are always suggested since they provide accurate outputs and require limited resources. Moreover, several codes can be found in the literature, allowing a relatively simple implementation of the proposed methods.

In addition to the large deflections, which are commonly experienced in design problems involving beam-based CMs, designers may need to model specific features or conditions arising within the beams. Typical situations involve irregular geometries, for example spline beams [38], variable section beams [95] or hybrid flexures [17], as an efficient way for increasing the range of motion or configuring the mechanism selective compliant behavior [15]. Other examples may be contact-aided CMs, which are particularly effective for limiting the CM operative range or the stress level [67, 68], for avoiding buckling phenomena [96] and for achieving nonlinear torque-deflection behaviors [97].

To include these features in the behavioral models, designers may refer to the 3D FEA. It is the most general and comprehensive approach and it provides a large variety of outputs. However, as visible from Tab. 2.1, its computational cost is much higher than the other techniques. The time required to solve the simulation depends on several aspects, such as number and type of elements, simulation settings, contact algorithm and options set in the model. Even though the designer can easily adopt simplifications in the model (causing a lost of quality regarding the achievable results), the 3D FEA is not particularly suitable for optimization studies, i.e. when several simulations must be performed in order to assess the final configuration. In fact, as discussed in the next section and implemented in the following chapters, problems involving special geometries of the flexible members and/or

contacts are usually approached with meta-models or Genetic Algorithms (GAs) [98], since a direct correlation between the design variables and the performance indexes is not available at the proof-of-concept step. Two more issues make the 3D FEA not the best choice for optimization purpose:

1. the limited user's control in the mesh definition during a batch analysis. At each iteration of the optimization process, the geometry must be updated and thus re-meshed. User's mesh options may be appropriate for a certain configuration and completely incorrect for the others. This may be solved using a free mesher and general options (element size and type, shape functions order and constraint on the numbers of tetrahedral). However, the quality of the numerical results would surely decrease.

2. the necessity to perform a mesh convergence check in order to evaluate the influence of the element size on the simulation outputs. This can be done very quickly in case of a single analysis (e.g. for the final configuration). On the contrary, checking each candidate during the optimization routine would significantly increase the total number of simulations.

This proves the necessity of making important considerations before proceeding with the modeling. The selection of a technique rather than others can offer a considerable reduction in the overall computational cost (in the order of 150-200 times), while still preserving high accuracy concerning the obtained results.

In the following, three computationally efficient techniques (1D FEA, PRB method and CBCM) are considered as possible alternatives of the well established 3D FEA. Each technique describes accurately a specific set of conditions but may result inappropriate in other scenarios. To simplify the selection of the most convenient technique, a comparison is reported in Tab. 2.2. A score is assigned to the techniques for each category of problems: "$-$" means unavailability, "0" is to indicate that the use is discouraged, "1" is assigned when examples can be found in the literature, whereas "2" implies full availability for a certain problem.

As visible in Tab. 2.2, 1D FEA can be used as behavioral unit as long as hybrid flexures are excluded from the analysis. The beams are defined by polynomial functions that interpolate or approximate a set of control points. Thus, by parametrizing the location of the

Table 2.2: A comparison of modeling techniques for the study of nonstandard problems.

Modeling Technique	Curve/Spline Beams	Variable Sections	Nontrivial Shapes	Contact Pairs	Computational Efficiency
3D FEA	2 / 2	2	2	2	0
1D FEA	2 / 2	2	–	1	1
PRB method	1 / –	1	1	1	2
CBCM	1 / –	–	–	1	2

control points, very complex shapes can be defined and tested [38]. Also, the designer can adopt one or more cross sectional areas along the beam's axis. Nontrivial beam's shape, as the one shown in Fig. 2.1(b), cannot be accurately described with beam elements (even with tapered cross sections) and must be drawn in a CAD environment. Contact analysis can be performed but it is limited to the line-to-line type, which is preferably used in planar problems [99]. The contact is detected around a radius for the line contact elements, so proper use would be for beams with regular geometry. For this reason, complex interactions between convoluted surfaces require the use of surface-to-surface contacts from the 3D FEA library.

The PRB method makes the CMs much easier and is applicable to the most of the considered scenarios, including contact-aided CMs [60, 100]. Initially curved beams are well captured with a simple 2R PRB model [101], whereas spline configurations require much more complex chains with remarkable increments in the number of parameters. Therefore, the inherent lost of simplicity excludes the use of the PRB method when spline geometries are involved. At last, as it will be demonstrated in Chap. 3, a well defined PRB model can accurately describe the spatial deflections of hybrid flexures, even though theoretical models describing the correlation between the systems are not obtainable.

From a rapid overview of Tab. 2.2, the designer may feel dissuaded to implement the CBCM. However, it must be remarked that it has been introduced recently and it is still under investigations. As a discretization method, many researches focus on the development of more accurate element models. An example may be found in [65], where the circular-arc segments are introduced for studying initially curved beams of uniform cross section. Models employing variable thickness segments are not available, though impressive BCM equations are presented in [102]. Also the modeling of contacts has not yet been treated in the literature, and will be addressed in Chap. 6. In line with the 1D FEA, customized beams

(holes, eyelets, rounds, etc.) cannot be described with BCM elements.

2.5. Optimization Approaches

Optimization has been extensively used in the field of CMs. Ready examples are constant torque CMs [103], joints for assistive devices [104], microgrippers [105], rotational springs [106], positioning stages [107] and balancing systems [108]. Depending on the nature of the problem, on the number of design variables and on the computational cost related to each simulation, the optimizations are usually performed resorting to deterministic algorithms, meta-models [109] or GAs [110].

Generally, deterministic algorithms are directly applied to analytical models and provide very efficient responses. On the contrary, meta-modeling techniques become useful when it is impossible or too complex to define analytical correlations between the objective function and the design variables. They provide a suitable approximation of the real objective function, whose construction is based on two essential steps: Design Of Experiments (DOE), where the design space is sampled in a discrete number of points, and Response Surface Modeling (RSM), which refers to all those techniques employed to create an interpolating or approximating n-dimensional hypersurface in the $(n+1)$-dimensional space given by the n design variables plus the objective function. Considering the objective function, Y, and a set of design variables, $X = p_1, .., p_n$, the selected DOE+RSM procedure provides an approximation, $\hat{Y}$, such that:

$$Y = \hat{Y} + \varepsilon \tag{2.3}$$

where ε is the approximation error, that can be minimized with a careful compromise between the number of samples and the choice of the discretization technique (e.g. full factorial, fractional factorial, central composite, Tagughi, latin hypercube, etc.). As it always happens in optimization, there is no general role and the choice depends on the problem to be investigated. The designers may refer to [98] for assistance in the selection of the best technique.

The benefit of this approach is that, once the meta-model has been obtained, very quick gradient-based algorithms [98] can be used to determine the stationary points on the response

surface. However, the total number of samples increases with the number of design variables, n, and with the allowed levels for each of these variables, k. For instance, adopting the full factorial discretization technique (very common in design optimization problems), the total number of samples (i.e. simulations) is $n_{sim} = k^n$. Consequently, the DOE+RSM is not particularly suitable for problems with a large number of design variables and/or levels for each variable, since a high value of n_{sim} would increment the total elapsed time, especially if 3D FEA is employed (see, once again, Tab. 2.1). On the contrary, GAs do not provide as an output the complete representation of the objective function over the domain but they can manage a very large number of design variables and converge after a relatively limited number of iterations [98].

2.6. Integrated Design Tool

In terms of computer-aided design of mechanisms, there has been a number of numerical solvers developed throughout the years (see [24] for a review), comprising nonlinear FEA and MBD packages. Nonetheless, practical methods, which take advantage of the capabilities of integrated Computer Aided Engineering (CAE) environments, when specifically applied for CM analysis/design, have been scarcely described and should be further investigated. As for the latter point, for what concerns specific CM design tools, a first example is represented by SPACAR [23], an open-source code that can simulate the motion of 3D flexible devices. More recently, a Matlab-based, object-oriented software tool called DAS-2D [24] has been released for the same purpose. Possible drawbacks of the above-mentioned tools are the rather basic graphic interface (see Fig. 1.2) and the restricted element and contact libraries. Therefore, by using either SPACAR or DAS-2D, it is currently impossible to manage compliant members with nonconventional shape or undergoing self and mutual contacts. In addition, DAS-2D is limited to planar case studies, although a 3D version (i.e. DAS-3D) is announced in development.

In practice, nowadays, despite several impressive modeling techniques are largely employed and refined, an integrated environment easily allowing for CM design optimization in case of nonstandard scenarios, such as the ones reported in Tab. 2.2, is nonexistent. Therefore, similarly to [111], the only viable strategy seems to be the integration of multiple platforms, namely a CAE solver for model solution and an external optimizer. A parametric

Table 2.3: Selection of the appropriate framework architecture and solver.

Scenario		PRB method	CBCM	1D FEA	3D FEA
CM	Simple or Built-in Geom.	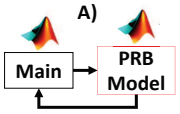	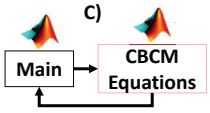	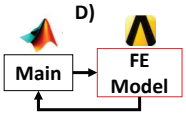	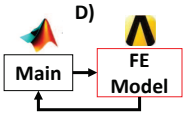
	External CAD	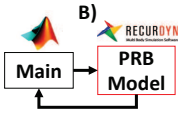	–	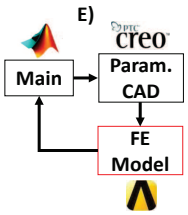	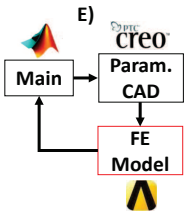
CM + RIGID	Simple or Built-in Geom.	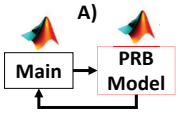	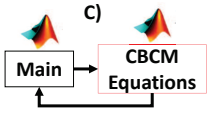	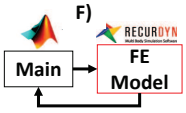	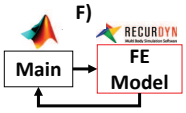
	External CAD	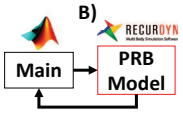	–	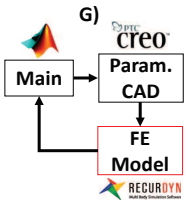	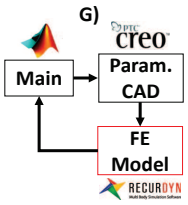

CAD for shape modeling may also be considered in case of hybrid flexures. Many CAE tools provide an internal CAD for the modeling of 3D shapes and also an optimizer. Even so, in case the shape of the compliant members needs to be optimized on the basis of a user-defined cost function, the designer may rapidly face the intrinsic limits of all the above-mentioned packages.

Owing to these considerations, the purpose of this section is to propose possible software frameworks specifically conceived for analyzing and designing beam-based CMs by means of the above-discussed modeling techniques. Such frameworks, shown in Tab. 2.3, are guided by Matlab, which manages the optimization process, along with all the simulations and the data exchange activities. In Tab. 2.3, "CM" means that the system is composed of only flexible members, whereas "CM+RIGID" indicates the presence of both flexible and rigid bodies.

Depending on the adopted modeling technique (see Tab. 2.2), the single framework adopts specific commercial tools, such as:

- ANSYS as nonlinear FEA solver;
- RecurDyn as interdisciplinary tool that simulates both rigid and flexible body dynamics by combining traditional rigid MBD and nonlinear FEA solvers;
- PTC Creo as parametric CAD.

By entering in Tab. 2.3 with the information regarding the mechanical model, the designer can evaluate the most appropriate framework architecture. At first sight, the use of two commercial solvers may be confusing. This point can be clarified by looking at the system under investigation. In fact, while ANSYS may be the best choice for analyzing individual elements or systems composed of flexible members only, RecurDyn allows to easily combine rigid and flexible bodies in a single simulation environment. This potentiality leads to remarkable reductions of the computational cost since meshing operations are not required for the rigid bodies in RecurDyn. By exploiting its MBD solver, RecurDyn can be also employed for solving complex PRB models, for example systems composed of several bodies undergoing out-of-plane motions. As previously stated, the use of PTC Creo becomes necessary only for including nonconventional geometries of the flexible members.

All the proposed frameworks can be modified based on the available tools. Same results can be obtained with other commercial programming (Fortran, Python, etc.), FEA (Abaqus, Nastran, etc.), MBD (Adams, LMS Virtual.Lab, etc.) and CAD (Solidworks, Catia, etc.) packages.

2.7. Final Considerations

This chapter is intended to orient the designer in the solution of nonstandard problems and provides general guidelines for assisting in the selection of the most appropriate modeling technique and software framework. Detailed descriptions of the theory behind the techniques as well as of the software implementations will be given in the next chapters. In particular, each chapter solves a case study in the field of beam-based CMs by combining the information of Tabs. 2.2 and 2.3:

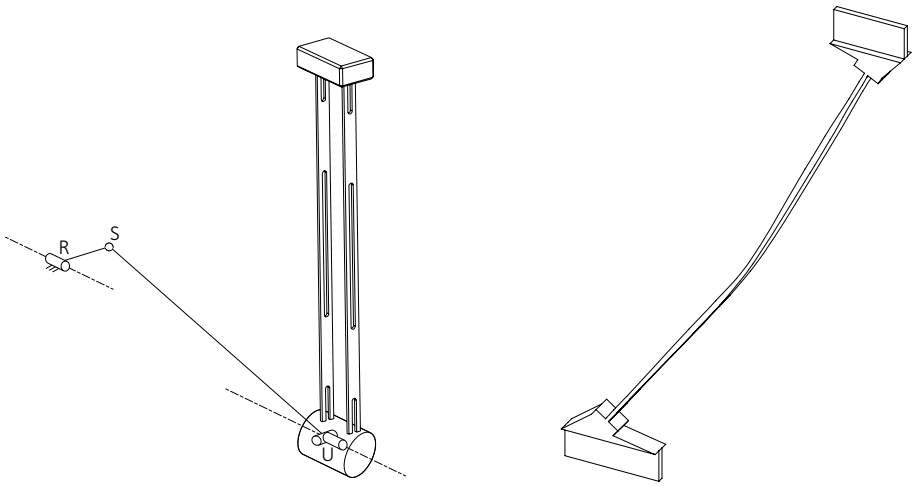

(a) Hybrid flexures in a four-bar linkage.

(b) variable section beam.

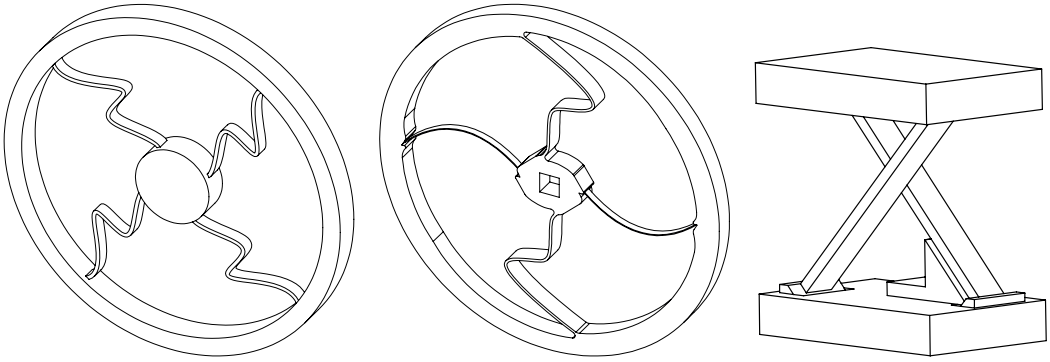

(c) Nonlinear torsional spring with spline beams.

(d) Statically balanced CM.

(e) Contact-aided CAFP.

Figure 2.5: Demonstrative case studies.

1. Chapter 3 analyzes a system composed of a rigid slider-crank mechanism and a compliant four-bar linkage utilizing hybrid flexures (see Fig. 2.5(a)). The aim is to optimize the shape of such flexible parts to fulfill strict requirements in terms slider's trajectory. According Tabs. 2.2 and 2.3, the system is modeled resorting to the PRB method and the 3D FEA by adopting the frameworks B and G respectively. Meta-models are used to study the influence of the design variables on the output performances and then to finalize the design.

2. Chapter 4 explores the use of variable section beams for the design of a linear constant force CM, depicted in Fig. 2.5(b). The proposed device is based on the compliant crank-slider concept and is initially studied with the PRB method through the framework A. The 1D FEA is used in the final design step to accurately model the flexible

beam with multiple parametric sections along the axis. To solve the shape optimization problem, aiming at finding a beam configuration that ensures a precise constant output force, a GA is set within the framework D.

3. Chapter 5 shows the design procedure for obtaining torsional CMs with prescribed torque-deflection relationships. The considered CMs, shown in Figs. 2.5(c) and 2.5(d), are implemented in antagonistic VSAs and statically balanced mechanisms. The nonlinear behavior is obtained by employing spline beams, whose shapes are optimized with 1D FEA by adopting the framework D and a GA.

4. Chapter 6 deals with a contact-aided CAFP, namely a system that combines a standard CAFP and a contact member, which affects one of the CAFP's beams (as visible in Fig. 2.5(e)). The CM behavior is investigated for various load cases with both the CBCM and the 1D FEA techniques. Frameworks C and D are combined together and meta-models are used to map the design domain.

To facilitate the reproduction of the results, the used codes are reported in the Appendix.

Chapter 3

Hybrid Flexures Synthesis in a Compliant Four-Bar Linkage

3.1. System Description and Aim of the Study

In this chapter, an industrial case study consisting of a spatial CM with hybrid flexures is discussed. Let one first consider a particular linkage system, namely a spatial slider-crank mechanism (see Fig. 3.1(a)), which transforms a rotational motion of an input crank into a purely translational motion of a slider (hereafter also referred to as platform). Such mechanism is composed of a revolute, a spherical, an universal and a prismatic pairs. An eccentricity along y-axis, namely an offset between the crank rotational axis and the platform translational axis is introduced (see the distance e in Fig. 3.1).

To reduce friction, the prismatic joint may be substituted by parallel leaf-spring flexures (i.e. a fully compliant four-bar linkage), which can provide approximate straight line guiding [112]. The CAD model of such partially CM is depicted in Fig. 3.1(b). The system is composed of three moving rigid bodies (crank, rod and platform), two rigid bodies fixed to the ground (motor and frame), and two hybrid flexures [17] with nonstandard shape. These flexures, made of spring steel, are designed as slender beams that comprise a set of eyelets. It is evident that, due to the mechanism topology and the absence of a prismatic joint guiding the platform (as in Fig. 3.1(a)), a spatial motion of the platform itself may occur during functioning. This crucial aspect is highlighted in Fig. 3.1(b), where the platform spatial trajectory is shown in red. The main dimensions of the system are reported in Tab. 3.1.

In the following sections, the shape optimization carried out on the hybrid flexures with the specific aim of reducing the undesired out-of plane motion is reported and described. The design target could be achieved by simply considering flexures with constant rectangular cross section and by increasing the beams width. In any case, it shall be remarked that the main purpose of the study is to show that custom flexures with defined in-plane and out-

Table 3.1: Main dimensions of the system.

Dimension	Value
l	400 mm
d	59 mm
r	70 mm
s	345 mm
e	93 mm

of-plane stiffness characteristics can be obtained according to complex design goals via the proposed design frameworks.

3.2. Overview of the Design Approach

The behavior of custom shaped hybrid flexures cannot be modeled with theoretical approaches, especially when the topology of such flexures is subjected to functional or practical constrains (as in the industrial scenario, where fabrication processes play an important role in the design). Given a parametric CAD file, 3D FEA is the most appropriate modeling approach. However, as previously discussed, the computational cost may be an important issue for optimization purposes, i.e. when a large number of simulations must be performed. As visible in Tab. 2.2, the presence of holes and/or eyelets does not limit the use of the PRB approach if straight beams are considered. Building upon on these considerations, in this study, a PRB model is initially employed to study the behavior of the spatial compliant four-bar linkage in a very quick and efficient way. The 3D FEA is then used to finalize the design.

A conceptual schematic of the adopted design flow is depicted in Fig. 3.2. The two main steps can be described as follows:

- #Step 1: several design alternatives can be tested by means of a PRB model, the only limit being that the initial mechanism topology shall be maintained. Naturally, the PRB representation allows to simulate each design variant in a limited computational time (reduced of three order of magnitude as compared to 3D FEA, as shown in Tab. 2.1);

- #Step 2: once the most promising solution (still based on a PRB representation) is found, the final shape of the flexible members is determined by leveraging on a CAD/-

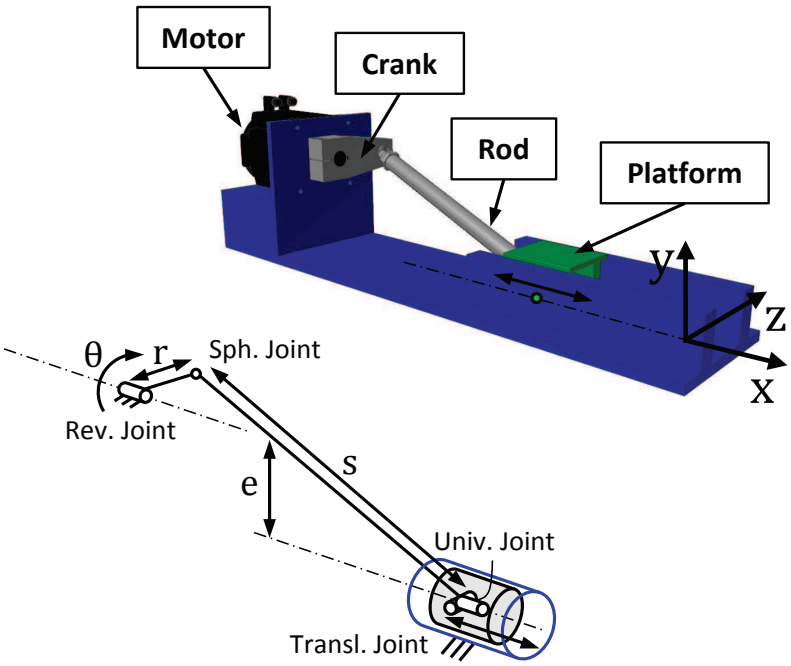

(a) Standard rigid configuration.

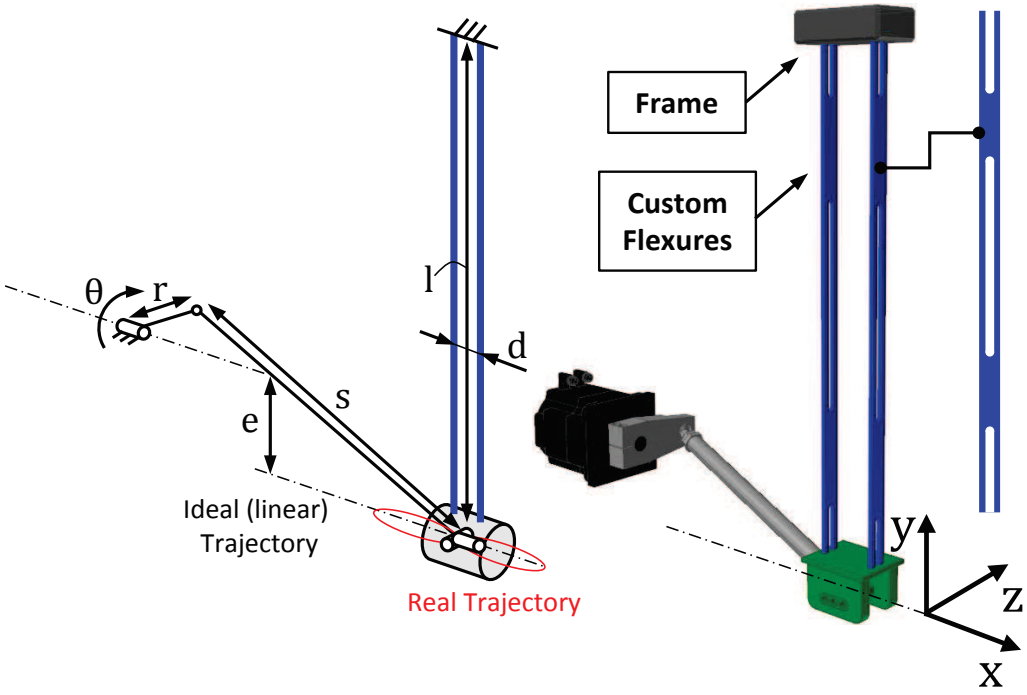

(b) Compliant configuration - four-bar linkage with hybrid flexures.

Figure 3.1: Spatial crank mechanism.

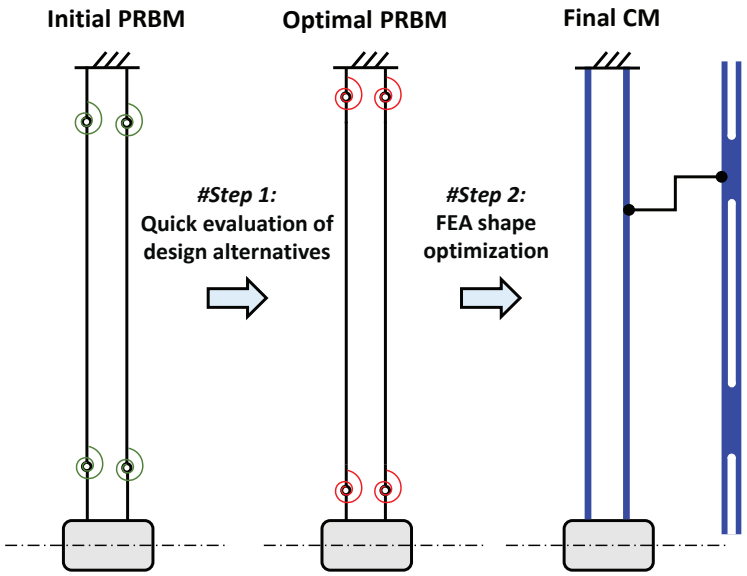

Figure 3.2: Multi-step design flow.

CAE optimization framework (see Tab. 2.3). Note that the final CM design fully replicates the behavior of its PRB counterpart. In the following, this last step will be referred to as FEA shape optimization.

If the computed accuracy is envisaged as sufficient for the considered application, the obtained hybrid flexure represents the final solution. In any other case, a design iteration will be necessary, based on an increment of the number of Degrees of Freedom (DOFs) as compared to the initial PRB model.

3.3. PRB Modeling: Background Theory and Practical Procedure

The adopted compliant four-bar linkage presents out-of-plane motions and thus its PRB counterpart must implement spherical spring-loaded joints. Before dealing with spatial PRB modeling, a simple beam subjected to planar boundary conditions is discussed. In fact, by neglecting all the out-of-plane forces and motions, the considered CM may be described by a pair of fixed-guided flexible segments, as shown in Fig. 3.3.

3.3.1. Planar Assumption: Fixed-Guided Flexible Segment

This section recalls the modeling of the fixed-guided flexible segment, visible in Fig. 3.4, and provides formulas to derive the dimensions of a simple flexure on the basis of the op-

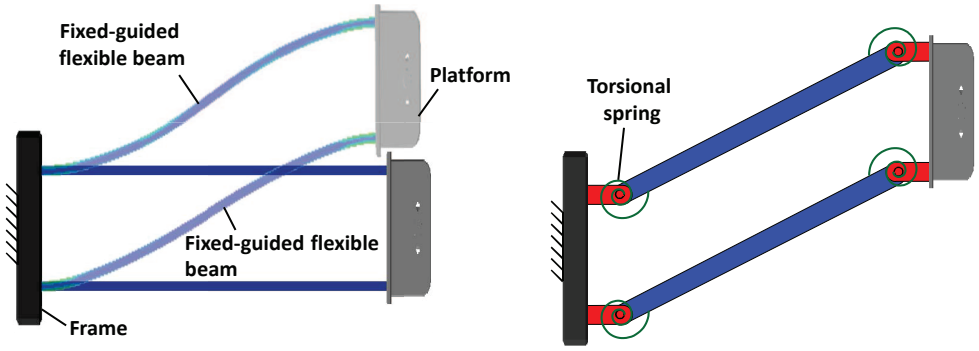

(a) CM model (undeflected + deflected configurations).

(b) PRB representation.

Figure 3.3: Planar compliant four-bar linkage.

timal PRB model (i.e. the one obtained after #Step 1 with desired stiffness characteristics). The schematic layout and the boundary conditions of such slender beam flexure are depicted in Fig. 3.4(a), the related 2R PRB model is shown in Fig. 3.4(c), whereas the free-body diagram of one half of the beam and its 1R PRB model are reported in Figs. 3.4(b) and 3.4(d). In particular, one end of the flexure is fixed to the ground, whereas the other end is guided to maintain absence of rotation. In order to obtain this configuration, a resultant clockwise moment M must be applied at the beam end point, in addition to the vertical force F. The resulting deflected shape is antisymmetric at its centerline (as shown in Fig. 3.4(a)), the angular deflection of the beam (θ) reaching its maximum for $\theta_{y=a_c/2} = \theta_0$ where the curvature is zero. Being directly related to the beam curvature, the moment at $y = a_c/2$ is null. Consequently, a single half-beam subjected to the only vertical force F can be considered. Summing moments at either ends of the free-body diagram in Fig. 3.4(b) yields to the following relation:

$$Fa_c - M = \frac{Fa_c}{2} \rightarrow M = \frac{Fa_c}{2} \tag{3.1}$$

where a_c is the horizontal distance between beam free and fixed ends (see Fig. 3.4(a)). Following the theory reported in [1], a system consisting of three rigid links connected by two symmetrically-disposed revolute pairs, as the one in Fig. 3.4(c), is used as a PRB model. Two torsional springs with same stiffness are located over the revolute joints in order to approximate the beam compliance. Therefore, such 2R PRB model requires two characteristic parameters to describe the kinematic and the force-deflection behavior of the related CM. By

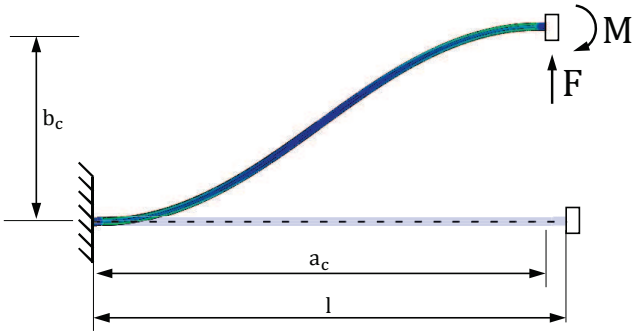

(a) CM model (undeflected + deflected configurations).

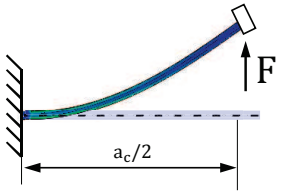

(b) Half-beam schematic subjected to end force.

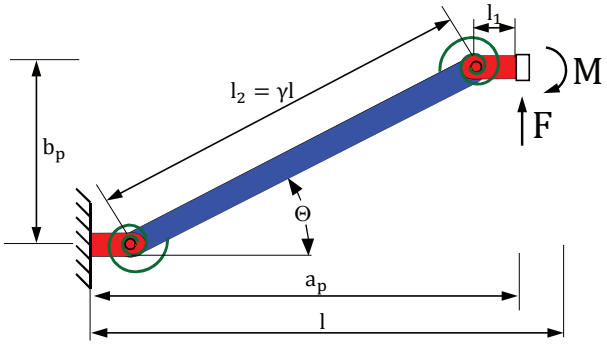

(c) 2R PRB model.

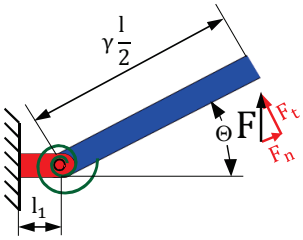

(d) Half-beam PRB model.

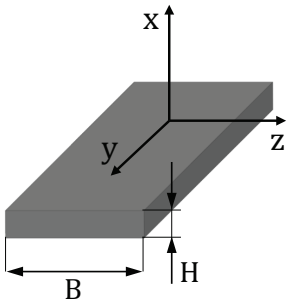

(e) Beam cross section.

Figure 3.4: Fixed-guided flexible beam.

employing the same notations suggested in [1], the PRB parameters are indeed the characteristic radius factor (γ) and the stiffness coefficient (K_Θ). Within the PRB approximation, the length of the links (i.e. l_1 and l_2, see Fig. 3.4(c)) and, consequently, the horizontal, a_p, and vertical, b_p, positions of the PRB model end point can be defined as function of γ. The

following relations hold:

$$l_1 = \frac{(1-\gamma)l}{2} \qquad l_2 = \gamma l \tag{3.2}$$

$$a_p = l(1-\gamma(1-\cos(\Theta))) \qquad b_p = \gamma l \sin(\Theta) \tag{3.3}$$

In parallel, the stiffness of the torsional springs can be expressed considering the half-beam and the related PRB model (see Fig. 3.4(d)). The PRB angle Θ is proportional (with K constant) to the torque at the revolute joint, given by $T = F_t \gamma l/2$. Combining the equations, the force can be expressed as follows:

$$F_t = \frac{2K\Theta}{\gamma l} \tag{3.4}$$

where F_t is the transverse component of the vertical force F. Moreover, by considering also the nondimensional transverse load index [1], defined as:

$$\alpha_t = \sqrt{\frac{F_t l^2}{EJ_{zz}}} \tag{3.5}$$

where E is the Young's modulus of the beam material and J_{zz} is the moment of inertia of the beam cross section with respect to the z-axis (perpendicular to the motion plane), the force-deflection relationships may be written as:

$$\alpha_t^2 = \frac{F_t l^2}{EJ_{zz}} = K_\Theta \Theta \tag{3.6}$$

where K_Θ is, as previously introduced, the stiffness coefficient. Then, by means of Eqs. 3.4 and 3.6, the constant spring stiffness of each revolute joint of the half-PRB model can be formulated as:

$$K = \gamma K_\Theta \frac{EJ_{zz}}{2l} \tag{3.7}$$

Equation 3.7 has to be adapted in order to comply with the complete PRB model, that involves two revolute pairs and a total length equal to l. In this case, Eq. 3.6 becomes

$\alpha_t^2 = 2K_\Theta\Theta$, and the final stiffness value is given by:

$$K = 2\gamma K_\Theta \frac{EJ_{zz}}{l} = \tau \frac{EJ_{zz}}{l} \tag{3.8}$$

where $\tau = 2\gamma K_\Theta$. The numerical values of γ and K_Θ and, as a consequence, of τ can be assessed via optimization techniques aiming at providing PRB models which can fulfill pre-defined functional requirements (#Step 1 in Fig. 3.2).

For what concerns the determination of the flexure geometric parameters starting from a PRB model (i.e. #Step 2 in Fig. 3.2), some additional assumptions are needed, namely cross section type and flexure material properties. Let one then consider a slender beam with rectangular cross section, as the one shown in Fig. 3.4(e). The moment of inertia of the beam cross section is:

$$J_{zz} = \frac{BH^3}{12} \tag{3.9}$$

As previously said, it is also necessary to consider the maximum stress associated to the load condition. Considering bending as the predominant loading mode, the associated stress is given by:

$$\sigma_{max} = \frac{M_{max}}{W} = \frac{6M_{max}}{BH^2} \tag{3.10}$$

where W is the cross section's modulus, whereas B and H are, respectively, the cross section's width and thickness. Since the maximum bending moment $|M_{max}|$ is placed, for this configuration, at each beam end, Eq. 3.10 evolves in:

$$\sigma_{max} = \frac{3Fa_c}{BH^2} \tag{3.11}$$

In order to avoid failures, the maximum stress σ_{max} shall be always lower than the material yield strength, σ_s. In conclusion, the cross section width, B, and thickness, H, can be determined by solving a system of equations, in which the reference PRB model is completely

defined. The first system includes Eqs. 3.8 and 3.9:

$$\begin{cases} K = \tau \frac{EJ_{zz}}{l} \\ J_{zz} = \frac{BH^3}{12} \end{cases} \rightarrow BH^3 = \frac{12Kl}{E\tau} \tag{3.12}$$

The final system also considers Eq. 3.11, having selected a maximum stress σ_{max} and having imposed $a_p = a_c$ (namely, the compliant system to be designed replicates the reference PRB model). The cross section dimensions are finally determined as follows:

$$\begin{cases} BH^3 = \frac{12Kl}{E\tau} \\ \sigma_{max} = \frac{3Fa_p}{BH^2} \end{cases} \rightarrow \begin{cases} H = \frac{4kl\sigma_{max}}{E\tau Fa_p} \\ B = \frac{3Fa_p}{\sigma_{max}H^2} \end{cases} \tag{3.13}$$

3.3.2. Spatial Case Study

Note that the above-mentioned theoretical procedure is quite straightforward, although based on simplifying assumptions (e.g. bending stress only) and only applicable to the design of slender beam-like segments with uniform cross section subjected to planar deformations. For what concerns flexures subjected to out-of-plane deformations (i.e. spatial motions), the above-mentioned theoretical procedure is rather complex [113], and a numerical approach seems preferable. Let consider a slender flexible beam subjected to out-of-plane loads, as the one shown in Fig. 3.5(a). In this particular situation, the compliant system can be approximate via a 2S PRB model consisting of three links connected by two spring-loaded S pairs, as shown in Fig. 3.5(b). Considering the rectangular cross section depicted in Fig. 3.4(e), along with a reference frame in which the principal beam axis is directed in the y-direction, the x-axis and the z-axis respectively defining the direction of the higher (primary) and smaller (secondary) beam cross-section moments of inertia (also shown in Fig. 3.4(e)), the values for the PRB rotational stiffness can be formulated as follows [114, 115]:

$$K_{\theta_x} = \mu \frac{EJ_{xx}}{l} = \mu \frac{EHB^3}{12l} \tag{3.14}$$

$$K_{\theta_y} = \epsilon \frac{2G(J_{xx} + J_{zz})}{l} = \epsilon \frac{2GBH(B^2 + H^2)}{12l} = K_{\theta_x} \frac{\epsilon}{\mu} \frac{2G(B^2 + H^2)}{EB^2} \tag{3.15}$$

$$K_{\theta_z} = \tau \frac{EJ_{zz}}{l} = \tau \frac{EBH^3}{12l} = K_{\theta_x} \frac{\tau}{\mu} \frac{H^2}{B^2} \tag{3.16}$$

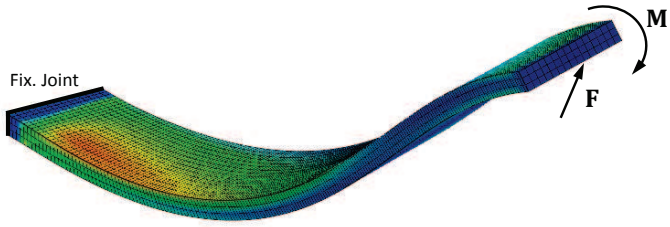

(a) CM model.

(b) Related 2S PRB.

Figure 3.5: Cantilever flexible beam subjected to out-of-plane loads.

where K_{θ_x}, K_{θ_y} and K_{θ_z} are, respectively, the stiffness related to the rotations around the x-, y-, and z-axis, J_{xx} is the moment of inertia of the beam cross section along x-axis, G is the shear modulus of the material and μ, ϵ and τ are specific constants. In practice, in case of planar CMs, the PRB model derivation process requires the determination of the revolute joints location and a single stiffness coefficient, $K_{\theta_z} = K$, for each rotational pair (or, in turn, the values of γ and τ, see Eqs. 3.2, 3.3 and 3.8). On the other hand, when dealing with spatial CMs and spring-loaded spherical joints, two additional rotational stiffness, namely K_{θ_x}, K_{θ_y} shall be determined (or, in turn, the values of μ and ϵ, see Eqs. 3.14, 3.15 and 3.16). In such case, the numerical optimization procedure presented hereafter can provide reliable results in an efficient manner.

3.4. #Step 1: Quick Evaluation of Design Alternatives

To allow the spatial motion of the platform, the adopted PRB system (shown in Fig. 3.6(a)) is formed by four equally-spaced spherical joints, each having a generalized rotational spring mounted in parallel. These four springs are characterized by the same rotational stiffness constants (K_{θ_x}, K_{θ_y} and K_{θ_z}). Such PRB model replicates the behavior of a simple spatial system composed of two flexures with rectangular cross section, defined by width $B = 15$ mm and thickness $H = 5$ mm, as shown in Fig. 3.6(b). The relation between these mechan-

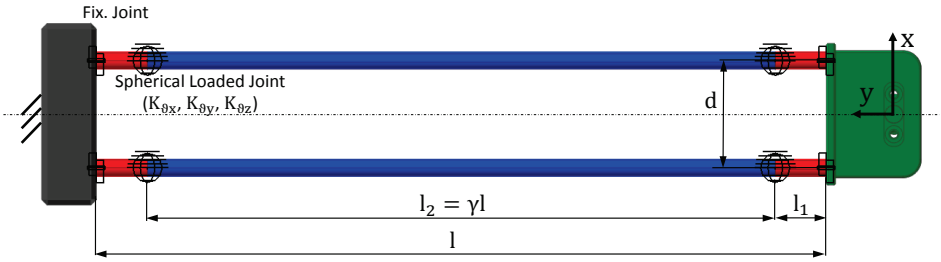

(a) 2S PRB model.

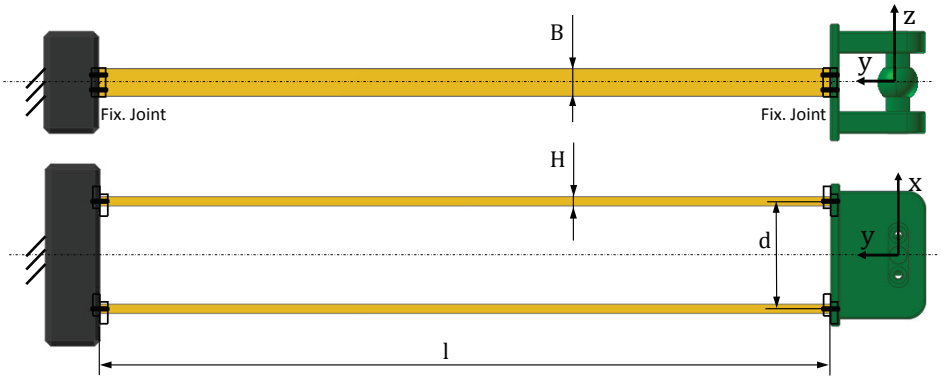

(b) Compliant four-bar linkage with standard beams.

Figure 3.6: Spatial four-bar linkage: adopted PRB model.

ical systems is expressed by Eqs. 3.14, 3.15 and 3.16 with $\gamma = 0.86$, $\mu = 0.47$, $\epsilon = 0.12$ and $\tau = 2.40$ (details about the PRB derivation process can be found in the published paper related to this work, [116]). #Step 1 allows to quickly evaluate several design alternatives resorting to a computationally efficient PRB model.

3.4.1. Performance Indexes Estimation

Three measures of the CM performance, evaluated on its PRB implementation, will be evaluated hereafter, namely:

- trajectory tracking of an ideal path;
- required actuation torque (measured on the motor shaft);
- maximum bending stress arising in the flexures.

Regarding the first measure, since parallel leaf-spring flexures are employed to replace a prismatic joint acting on the platform (along x-direction), the kinematic performance of the PRB model may be evaluated by computing the actual platform trajectory (green body

in Fig. 3.6) and comparing it to a pure platform translation (ideal motion) that would be obtained by the rigid slider-crank mechanism in Fig 3.1(a). The tracking error e_{lin} between the platform's trajectory and the ideal profile (i.e. a straight line along the x-axis) can be evaluated in a series of Q simulation steps as follows:

$$e_{lin}(K_{\theta_x}, K_{\theta_y}, K_{\theta_z}, d) = e_{lin}(l, B, H, d) = \sqrt{\frac{1}{Q}\sum_{i=1}^{Q}\left[\sum_{j=1}^{2}\left|x_j^P\right|\right]_i^2} \tag{3.17}$$

where x_1^P and x_2^P are the displacements of the platform along y-direction and z-direction. As highlighted in Eq. 3.17, the trajectory tracking error is function of the flexure distance, d (see Fig. 3.6), along with the parameters K_{θ_x}, K_{θ_y} and K_{θ_z}. These latter stiffness values are, in turn, function of the flexure geometry via the parameters l, B and H (see Eqs. 3.14, 3.15 and 3.16), which respectively represent flexure length and cross section's width and thickness. As for the actuation torque, it can be directly measured within the MBD environment, whereas the maximum bending stress (which is mainly function of the beam thickness H [115]), is computed via Eq. 3.11 by neglecting the out-of-plane deformations.

3.4.2. Design Tool - Framework B

The multi-DOFs nature of the system as well as the use of dedicated CAD files suggests the implementation of the framework B in Tab. 2.3, which exploits Matlab as a multi-tasks programming environment and RecurDyn as a MBD solver. Based on the schematic depicted in Fig. 3.7, the framework is guided by Matlab and leverages on RecurDyn's interfacing capabilities, which allow the use of batch simulation execution: RecurDyn's solver can be run in batch mode through a set of command files set up by Matlab. In particular, the following file types are employed in the framework:

- **Scenario File** (*MBD_Scenario.rss*), that contains information about the simulation to be performed (e.g. the simulation type and the number of simulation steps);
- **RecurDyn Design Parameter Files**, which provide all the parametric data to be set in the model. In particular, the mathematical relations between the parameters are stored in *MBD_Parameters.rdp*, whereas the numerical values of l, B, H and d are stored into *MBD_Input.rpv*, that can be created and modified via a Matlab function.

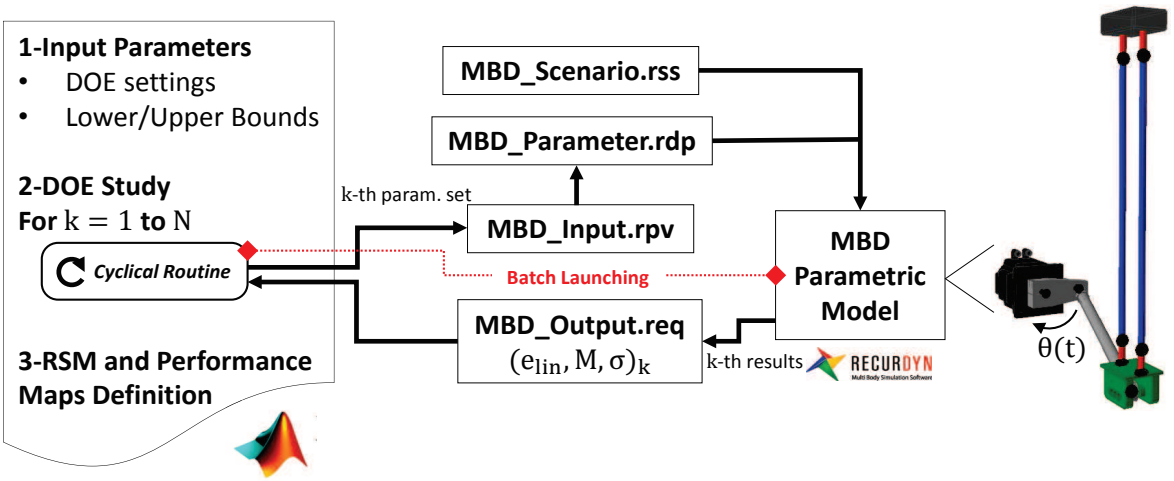

Figure 3.7: Framework B used for the #Step 1.

To generate the performance maps, the full factorial criterion and the radial basis function (Multi-Quadratic) technique are respectively adopted for the DOE+RSM phase [98, 117]. With 2-dimensional design domains, the full factorial provides an uniform grid of points over the plane, being the samples given by every possible combination of the design variables. To complete the DOE+RSM, the following operations are performed through a sequence of Matlab functions:

- **Creation of the design space and sampling points**
- **For** $k = 1$ **to** $Number\ of\ Sampling\ Points$
  - Update the RecurDyn design parameter file (*MBD_Input.rpv*) with the k-th set of values;
  - Batch RecurDyn execution of the k-th PRB model
  - Extraction of the k-th results set from *MBD_Output.req* and evaluation of $e_{lin,k}$, M_k and $\sigma_{max,k}$;

  end
- **Data fitting**

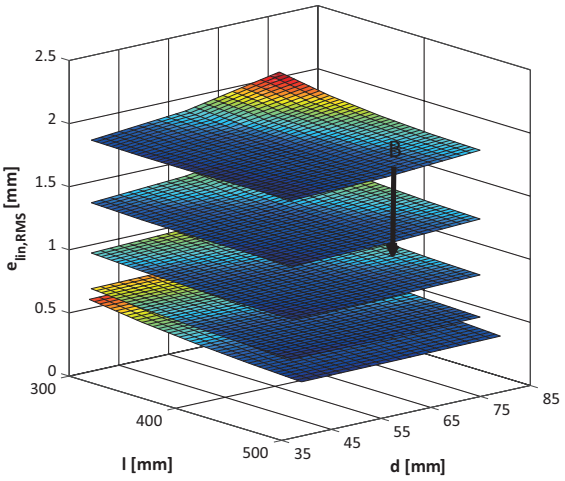

(a) e_{lin} RMS with $H = 5$ mm.

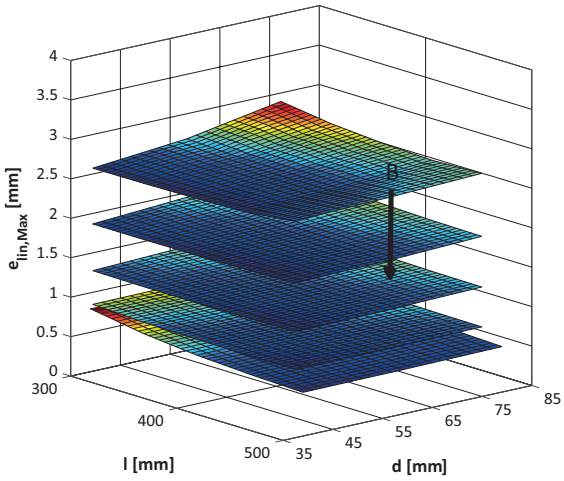

(b) e_{lin} max with $H = 5$ mm.

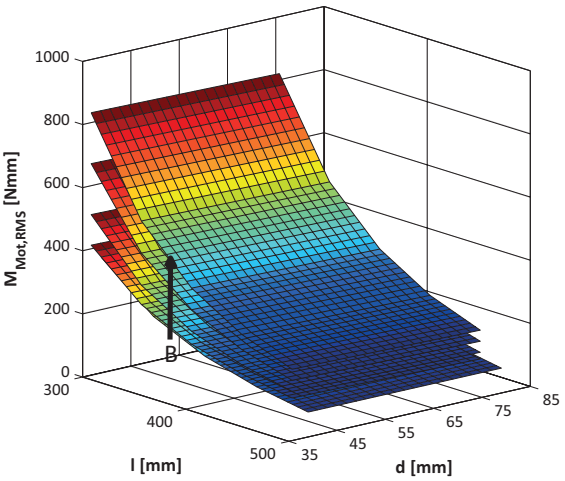

(c) Torque RMS with $H = 5$ mm.

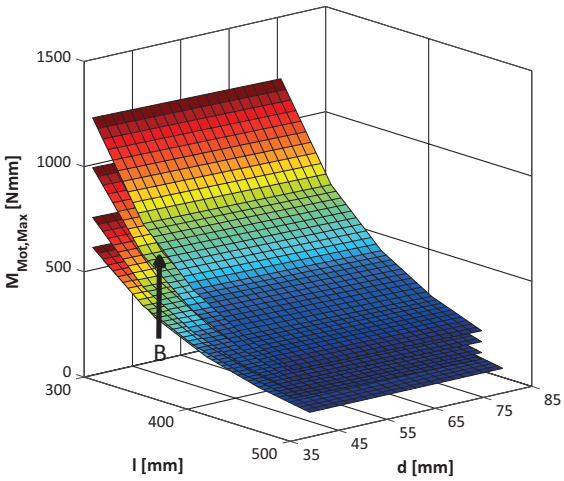

(d) Torque max with $H = 5$ mm.

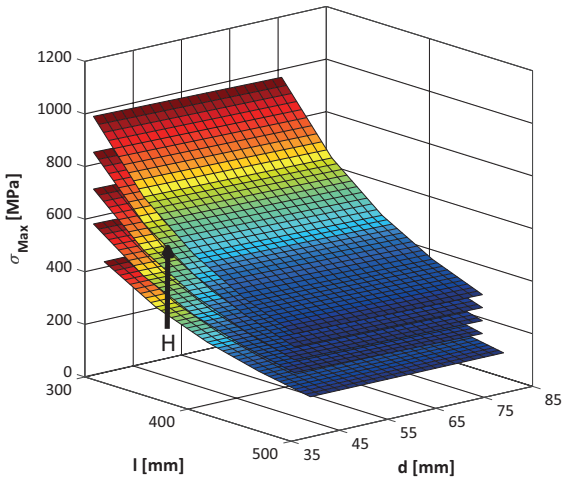

(e) Stress max with $B = 20$ mm.

Figure 3.8: Performance maps for the evaluation of design alternatives.

3.4.3. Numerical Results - Performance Maps

Several DOE+RSM investigations have been performed by considering different variables intervals. As an example, the following discrete intervals are hereinafter examined to build the performance maps: $l \in \{300, 350, 400, 450, 500\}$ mm, $d \in \{9, 49, 59, 69, 79\}$ mm, $B \in \{10, 12, 15, 18, 25\}$ mm, and $H \in \{3, 4, 5, 6, 7\}$ mm. To consider the quasi-static behavior of the system, a rotation at low constant velocity is enforced along the rotation axis of the crank (0.25 rev/s) for each simulation in RecurDyn. The obtained results are reported in Fig. 3.8, allowing to easily evaluate a design solution that is suited to the functional requirements of the system in terms of the above-mentioned quantities, i.e. maximum and RMS trajectory tracking and actuation torques, and maximum stress. As a result of the study, the selected PRB model is characterized by a length $l = 500$ mm, a width $B = 18$ mm, a thickness $H = 4$ mm, and a distance $d = 59$ mm. Note that, as visible in Figs. 3.8(a) and 3.8(b), the trajectory tracking performance reasonably increases as the flexures' length, l, and width, B, increase. However, in order to limit the maximum and RMS actuation torques, the beam width should not exceed a certain threshold (as visible in Figs. 3.8(c) and 3.8(d)). Regarding the maximum stress, the adopted spring steel is characterized by a Young's Modulus $E = 207000$ MPa, a Poisson's ratio, $\nu = 0.33$, and a yield strength $\sigma_s = 950$ MPa. Therefore, by adopting a flexure thickness $H = 4$ mm, the designer is enforcing a safety coefficient slightly higher than 2, as visible in Fig. 3.8(e).

3.5. #Step 2: Shape Optimization

To obtain the hybrid flexure design (see Fig. 3.1(b)) based on the PRB model evaluated in the previous section, no general analytic solution is available. Systems composed of both flexible and rigid parts may be analyzed via the RecurDyn software, as suggested in Tab. 2.3 (framework G). In this case, the problem can be tackled resorting to a software tool (i.e. RecurDyn) enabling an effective search of a CM optimal design starting from a parametric CAD/CAE model. Essentially, such tool aims at solving a shape optimization problem, having defined an objective function, lower and upper bounds for a set of design variables in the CAE environment, and a set of constraints.

Table 3.2: Hybrid flexures - additional parameters.

Dimension	Value
l_β	500 mm
l_γ	45 mm
B_β	7 mm
B_γ	$B_\alpha - 2B_\beta$

3.5.1. Problem Formulation

In the final design, custom shaped hybrid flexures are optimized to replicate the spatial load-displacement behavior of the optimal PRB model. Practically speaking, by imposing an input motion to the crank, the platform's trajectory (shown in red in Fig. 3.1(b)) can be used as a performance index in the optimization. The overview of the adopted hybrid flexure is shown in Fig. 3.9, together with the user-defined set of geometric dimensions setup within the parametric CAD. The design variables considered in the study are l_α, B_α and H_α. The remaining principal dimensions are reported in Tab. 3.2. The optimization problem, whose objective function will be hereafter referred to as trajectory error, e_{tra}, can be formulated as follows:

$$\textbf{Min.} \;\; e_{tra}(l_\alpha, B_\alpha, H_\alpha) = \sqrt{\frac{1}{Q}\sum_{i=1}^{Q}\left[\sum_{j=1}^{3}\left|\frac{x_j^P - x_j^C}{l}\right| + \sum_{k=1}^{3}|\theta_k^P - \theta_k^C|\right]_i^2} \tag{3.18}$$

$$\textbf{Constraint} \rightarrow \quad \sigma < \sigma_s \tag{3.19}$$

where x_j^C, x_j^P, θ_k^C, θ_k^P are, respectively, translations and rotations (defined, for instance, via the Euler angles convention) of the chosen reference frame fixed to the platform (green body in Fig. 3.6) of the CM (superscript C) and of the PRB (superscript P), and l is the flexure length (as in Fig. 3.6). The objective function e_{tra}, namely the RMS value of the trajectory error, is then evaluated through a series of Q simulation steps from the undeformed configuration to the maximum imposed deflection. The constraint expressed by Eq. 3.19 allows to respect the yield strength (950 MPa) during the optimization study.

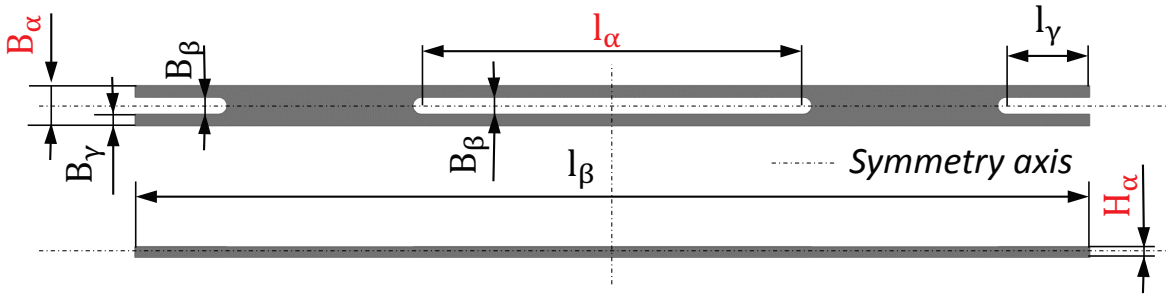

Figure 3.9: Parametric hybrid flexure.

3.5.2. Design Tool - Framework G

Given that the explicit relationship between design variables (l_α, B_α and H_α) and the objective function (e_{tra}) is not available, similarly to the performance study carried out in Sec. 3.4, the DOE+RSM technique is used in #Step 2 to investigate the design domain. A deterministic algorithm is then used to find the minimum, namely the optimal hybrid flexure configuration.

Concerning the software architecture, important changes have to be made when flexible members are included in the analysis. With reference to Tab. 2.3, custom shaped 3D flexures can be managed via the software framework G. In #Step 1, parametrization and calculations are performed by leveraging only on Matlab functions managing the MBD environment (i.e. framework B in Tab. 2.3). In case of CM shape optimization two additional tools are needed, as visible in the conceptual schematic in Fig. 3.10(a). This is due to the necessity to vary the flexure parametric dimensions at each iteration of the DOE, to regenerate the actual 3D shapes of the beams and, consequently, to re-mesh them, to re-set their boundary conditions (connections with other bodies of the system) and to specify material properties. Automatic execution of re-meshing and boundary condition definition are not natively provided by RecurDyn, but it is possible to implement them by leveraging on ProcessNet, a macro development toolkit integrated within RecurDyn and based on C# programming language. A ProcessNet script, executing re-meshing, boundary conditions re-settings and material properties definition, can be automatically run when RecurDyn is launched in batch mode. By implementing the framework G, the procedure involves Matlab (main environment), PTC Creo, RecurDyn and ProcessNet.

As mentioned, the need to change the flexure geometry at every iteration involves the use

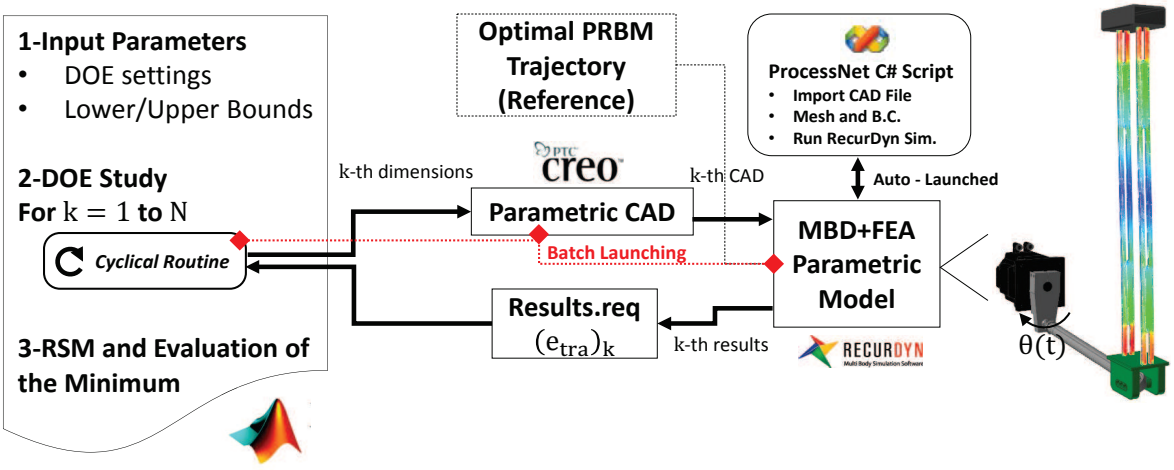

(a) Schematic of the framework.

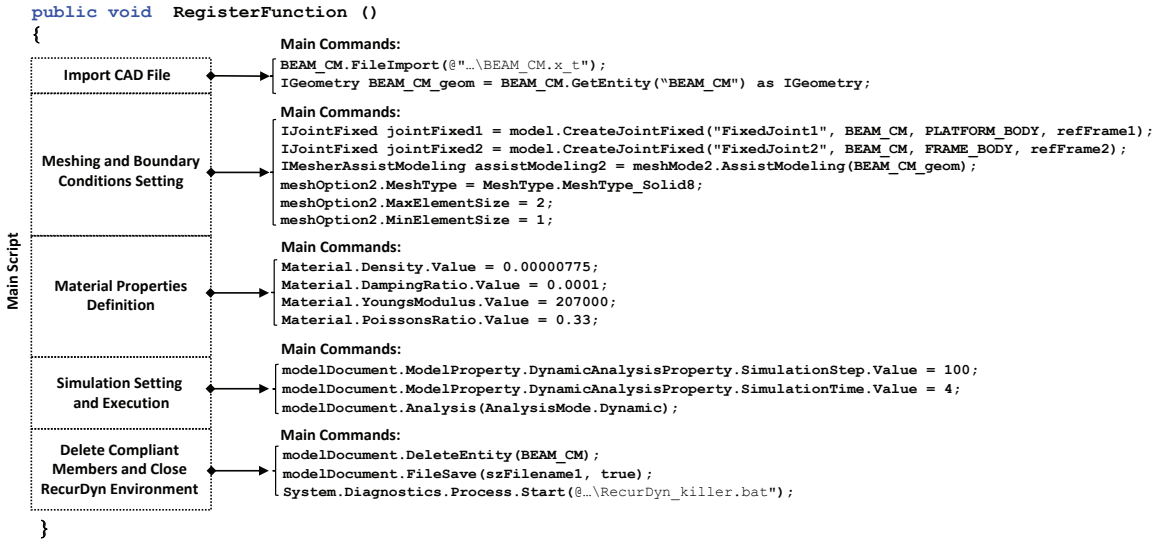

(b) Main sections of the ProcessNet script.

Figure 3.10: Framework G used for the #Step 2.

of a parametric CAD (i.e. PTC Creo) that can be controlled by using a text file, in which geometrical features and dimension parameters are defined. Such text file is modified by Matlab and overwritten for every k-th sampling of the design space. In this way, the k-th geometry is automatically generated and exported. Then, a specific ProcessNet script updates the RecurDyn model with the k-th CAD file. The structure of the ProcessNet script considered in this routine is represented in Fig. 3.10(b), which provides an overview of the main sections of the code. The complete code is reported in Appendix A. For a detailed explanation of each command/action, the interested reader may refer to the ProcessNet manual [118].

To obtain the mathematical expression of the objective function via the DOE+RSM (full

Table 3.3: Optimal hybrid flexure - numerical solution.

Design Var.	Range	Opt. Value
$l_\alpha \in$	$[100, 250]$ mm	200 mm
$B_\alpha \in$	$[18, 24]$ mm	19 mm
$H_\alpha \in$	$[3.5, 6]$ mm	4 mm

factorial criterion combined with radial basis function), the following operations are performed through a sequence of Matlab functions:

- **Creation of the design space and sampling points**
- **For** $k = 1$ **to** $Number\ of\ Sampling\ Points$
  - Batch PTC Creo execution to create the k-th hybrid flexure geometry;
  - Batch RecurDyn execution of the k-th CM configuration. The model is managed by a ProcessNet Script (launched automatically from RecurDyn), that imports the k-th flexible model and enforces joints, mesh (first order brick elements) and material properties definition. Subsequently, the k-th simulation starts upon the execution of a ProcessNet command.
  - Extraction of the k-th results set from *Results.req* and evaluation of $e_{tra,k}$;

  end
- **Data fitting**

A deterministic algorithm within Matlab (*fmincon* routine) is then used to find the minimum of the response surface (e_{tra}) and thus identify the optimum (i.e. $l_{\alpha,opt}$, $B_{\alpha,opt}$ and $H_{\alpha,opt}$). Since the definition of an initial value (from which the algorithm starts the optimum search) is usually required, in order to avoid local minima, several initial values are tested. Those values are selected among the discrete minima found during the DOE step, as suggested in [98].

3.5.3. Numerical Results - Optimal Configuration

The results of the shape optimization process are plotted in Fig. 3.11(a), where the function $e_{tra}(l_\alpha, B_\alpha, H_\alpha)$ and its minimum value are shown over the explored design space (by

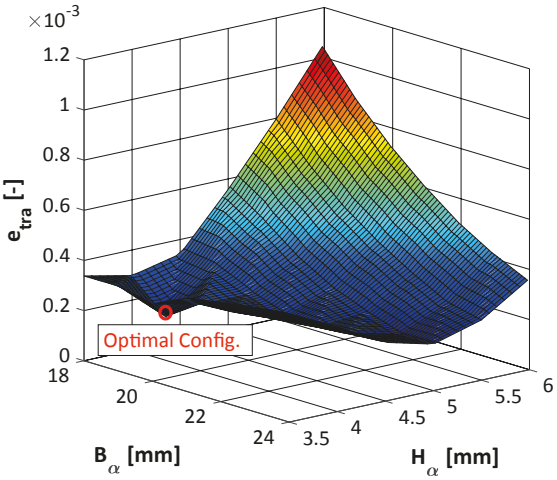

(a) Optimal solution for $l_\alpha = 200$ mm.

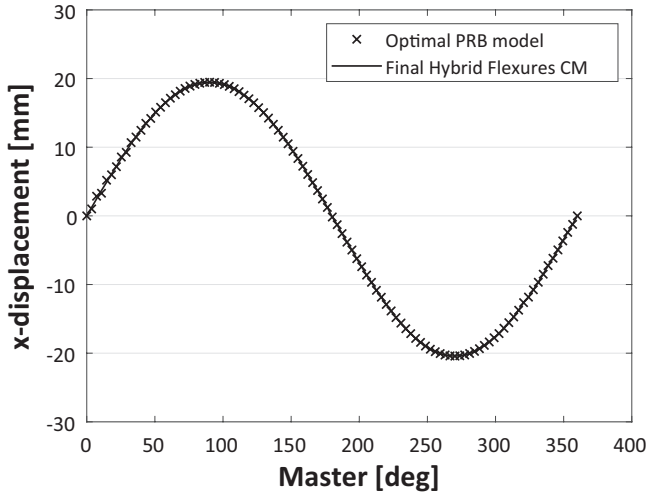

(b) Displacement along the x-direction.

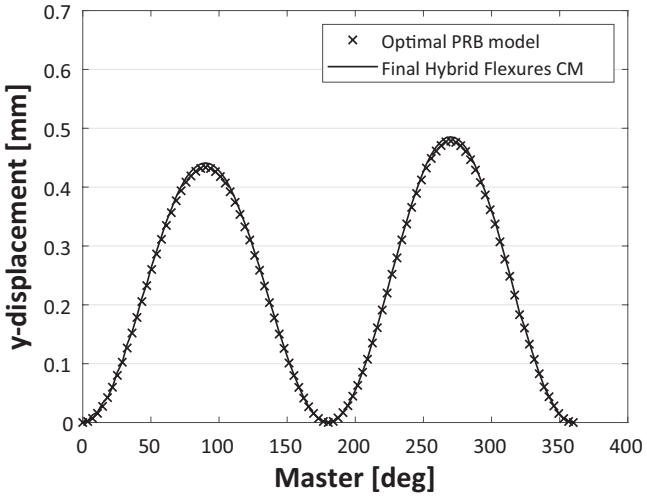

(c) Displacement along the y-direction.

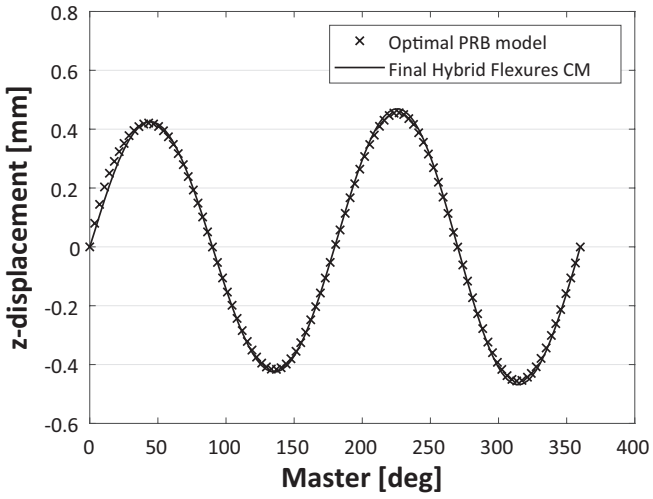

(d) Displacement along the z-direction.

Figure 3.10: Optimal solution and comparison between PRB model and CM behaviors.

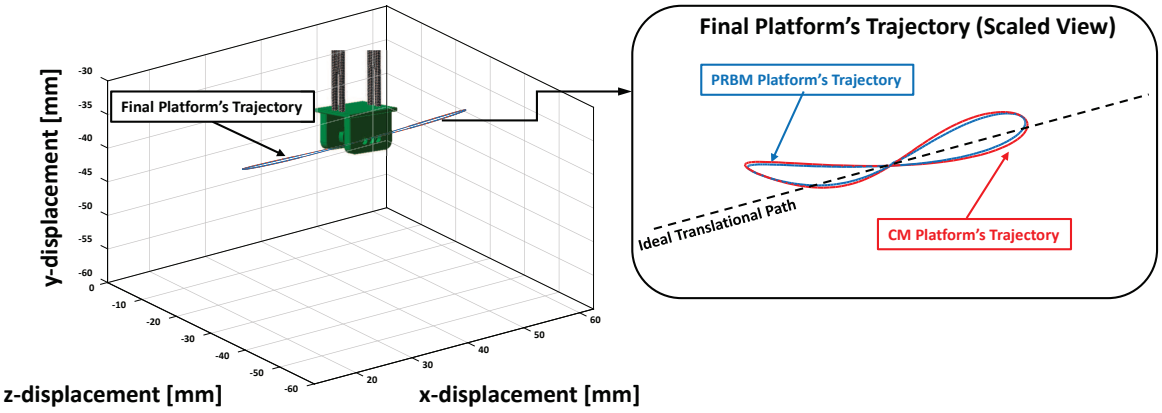

Figure 3.11: Final platform trajectory.

fixing $l_\alpha = 200$ mm for visualization purposes). The optimal solution, summarized in Tab. 3.3, represents the final flexure geometry. To confirm the accuracy of the procedure a comparison between the optimized PRB model and the final CM is presented in Figs. 3.11(b), 3.11(c) and 3.11(d), which provide the position profiles of the two systems (PRB model and hybrid flexure CM) along the x-, y-, and z-axis. Also, the path followed by the platform in the 3D space is provided in Fig. 3.11. As desired, the final CM design closely follows the behavior established by the PRB model, also confirming that the choice of the PRB topology is acceptable for the considered application. After the shape optimization routine, a final

simulation test has been performed to verify the maximum Von Mises stress and the actuation torque at the motor shaft, that are, respectively, 580 MPa, 590 Nmm (maximum torque) and 397 Nmm (RMS torque). These values are compatible with the design constraints.

3.6. Summary

In this chapter, a general method for optimizing the shape of spatial CMs with nonstandard custom geometry has been presented. The compliant system under investigation is a spatial slider-crank mechanism connected to a compliant four-bar linkage. The overall procedure consists of two main steps, each of them addressed via a specific design tool (selected on the basis of Tab. 2.3). In #Step 1 several design alternatives are evaluated on a parametric PRB model so as to produce several performance maps and select the most promising solution with a limited computational cost. Then, in #Step 2, the final CM design (composed of two hybrid flexures) is derived, confirming the practical usability of the proposed multi-software frameworks. For what concerns computational times, every CM model is solved in RecurDyn in 200 s (mean value, having defined ≈ 2500 first order brick elements for each flexure), whereas the PRB models are simulated in 0.35 s, further highlighting the advantage of the PRB method in the initial design step.

Chapter 4

Design of a Linear Constant Force Compliant Crank Mechanism

4.1. Constant Force Compliant Mechanisms

Constant force CMs provide a reaction force at the output port that does not change for a specific range of input motion [2]. These devices are useful in a large variety of applications, including mechatronic systems designed to interact with humans or to manipulate sensitive parts/interfaces. Ready examples are grippers [119], surgical tools [11], robot end-effectors [120], energy absorption devices [121], small-scale electrical contacts [122] and exercise machines [123].

One of the reasons is that, adopting a CM, a constant force can be exerted on the manipulated part with an open loop work-cycle [124], removing the need of force sensing and control. Nowadays, due to the rapid development of advanced manipulation technologies, a precise force regulation becomes essential, especially when dealing with flexible and/or delicate objects that are particularly sensitive to the change of the contact force [125]. Generally, robots operating in unknown environments are equipped with an adequate controller [126] and specific sensors [127, 128]. By implementing a closed loop algorithm the manipulation force can be maintained at a precise value [129]. However, the presence of the sensory apparatus may be inappropriate in harsh industrial environments or in small-scale applications [11], where clearances must be accurately defined. In this context, the implementation of a well designed CM would simplify the overall system, even thought the force level would be constrained to a single value [125, 130, 131] or to a limited range of values [11, 57, 120].

Focusing on the recent literature in the field of linear constant force CMs, the intrinsic zero-stiffness condition can be obtained resorting to two different methods [2]. The first method combines a typical positive stiffness structures, i.e. a system characterized by a direct proportionality between the applied force and the resulted displacement, with a negative

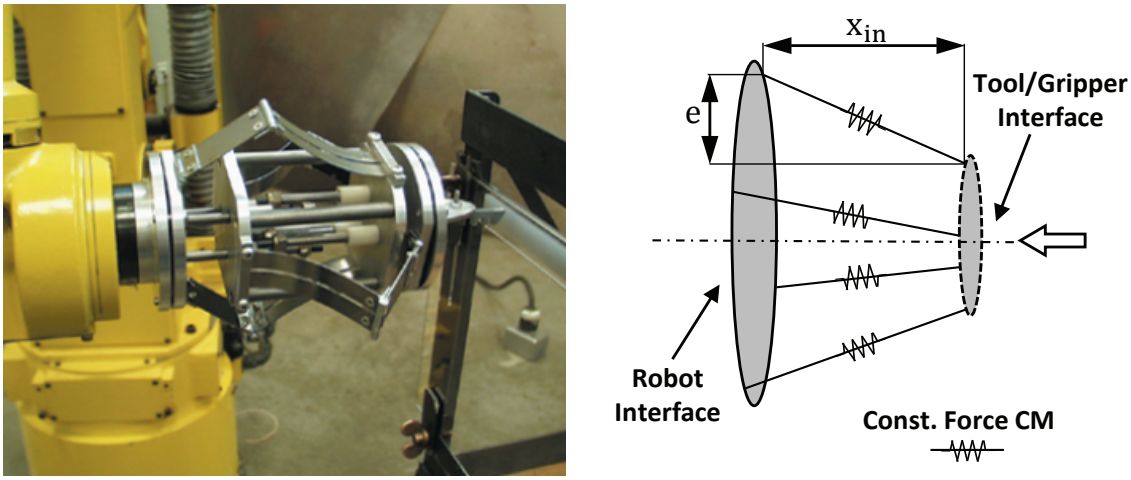

(a) Prototype taken from [137].

(b) Principle schematic of the system.

Figure 4.1: Constant force mechanism in robot end-effector.

stiffness structure, usually identified by a bi-stable beam [130, 132–135]. The second method refers to a single member, whose shape has to be accurately designed with the specific aim of providing a constant response. The result is a monolithic compliant solution (see [136] as an example), usually characterized by a larger available stroke. However, the complex shape of the resulting structure leads to possible machining error, which can affect the output force. For a more detailed review about constant force CMs, the interested reader may refer to [2].

4.2. System Description and Aim of the Study

In the following sections, the design of a linear monolithic long-stroke constant force CM to be used in robot end-effectors is reported. A possible application of the proposed scalable device is shown in Fig. 4.1, which refers to the work described in [62]. Four parallel springs are connected to a movable interface, while a linear guide ensures a purely translational motion during the operations. Following the results described in [1, 124], in this work, the compliant slider-crank concept is used as a module for the spring system shown in Fig. 4.1(b) due to its simplicity and to evident advantages from the analysis/design standpoint, such as the possibility to employ the PRB approximation. An additional eccentricity (i.e. an offset between the slider axis and the crank pin) is added to connect the robot interface with the tool/gripper interface, as shown in Fig. 4.1(b).

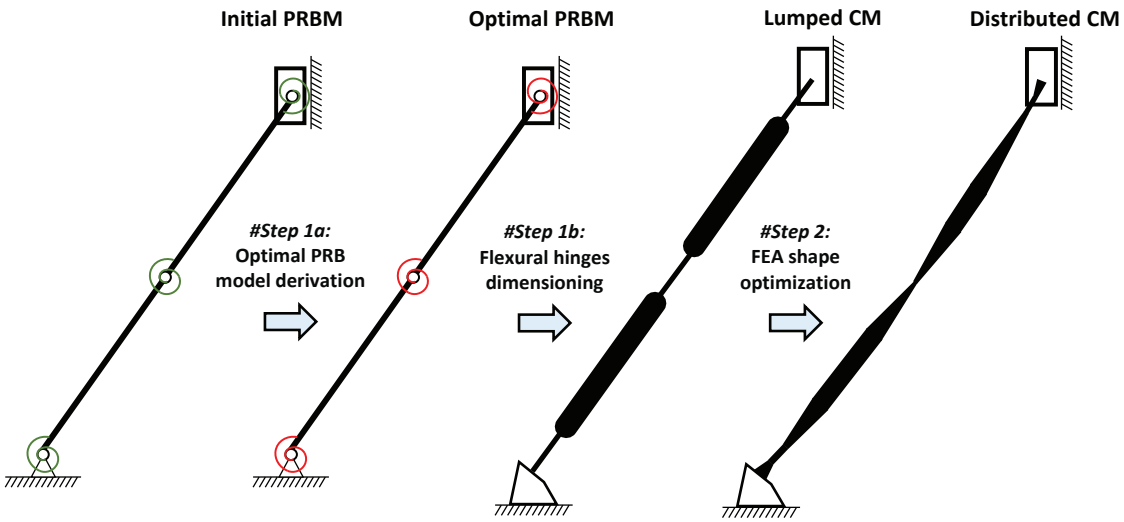

Figure 4.2: Multi-Step design flow.

4.3. Overview of the Design Approach

The CM design is divided in two main steps, as visible in Fig. 4.2. With reference to previous works in the literature dealing with the crank-slider concept [1, 124, 138], the PRB method is adopted in #Step 1a to synthesize the optimal lumped compliance configuration with good accuracy and reduced computational costs. In particular, the kinetostatic behavior of the 1-DOF rigid mechanism is studied with the principle of virtual work. A simple analytical model describing the output force at the slider is derived and subsequently used to optimize the PRB characteristic parameters (length of links and stiffness coefficients) with the aim of achieving a constant output force, equal to 1.5 N, over a large range of linear displacements.

Then, by replacing the spring-loaded revolute joints with equivalent SLFPs [1, 15, 139], in #Step 1b the lumped compliance constant force mechanism is obtained, as shown in Fig. 4.2. The system is tested with 1D and 3D FEA, resulting in a constant force-deflection behavior available for a limited displacement range (in the order of few millimeters). To reduce the stress concentration areas and thus extend the available operative stroke of the mechanism, a shape optimization is performed in #Step 2 by taking the sub-optimal lumped compliance configuration as a reference. The new embodiment, depicted in Fig. 4.2, consists of a flexible beam with variable thickness along the main axis. Continuously variable thickness beams cannot be easily modeled via analytical formulations, especially when subjected

to very large deflections. Consequently, the explicit relationship between input variables and the objective function (i.e. the force error with respect of the target force, 1.5 N) is not available.

The behavior of the proposed beam-based CM can be analyzed resorting to the CBCM. Optimization studies may benefit from its high computational efficiency. Given that at the current state-of-the-art the CBCM implementation is limited to cases involving constant cross sections along the beam's axis (see Tab. 2.2), variable cross sections, as the ones considered in the current application, may be analyzed by dividing the beam into several elements and by modeling each element as a constant cross section segment. However, following this method, the benefits in terms of computational efficiency would be limited by the large number of elements (and parameters) required in order to approximate linearly variable segments. Based on these considerations, 1D FEA (beam elements with tapered cross sections) have been chosen as an attempt to compromise between result accuracy and computational costs [38, 71]. In fact, compared to 3D FEA, 1D FEA requires limited computational resources (and time) to generate, mesh and solve a complex-shaped structure. The design space is parametrized by variables describing the shape and size of the beam-based CM. The best variable set is determined via a Matlab GA. In line with the lumped compliance design, the optimal solution has been verified through a 3D FEA simulation.

Finally, physical prototypes are fabricated via 3D printing technology and tested by means of a special purpose test rig. The aim of the test is to verify the constant behavior of the mechanisms as well as the absence of structural failures in the whole design stroke.

4.4. #Step 1a: Optimal PRB Model Derivation

The analysis/design is focused on a single module of the spring system shown in Fig. 4.1(b). A PRB model is used to determine the stiffness of the SLFPs on the basis of a pre-defined target output force, so that the system behaves as a nonlinear compression spring. To comply with the difference in terms of diameter between the robot interface and the tool/gripper interface, the eccentric slider-crank mechanism is adopted as architecture. In particular, $x_{in} = 100$ mm and $e = 60$ mm (i.e. the required encumbrance, see Fig. 4.1(b)) are considered as design requirements.

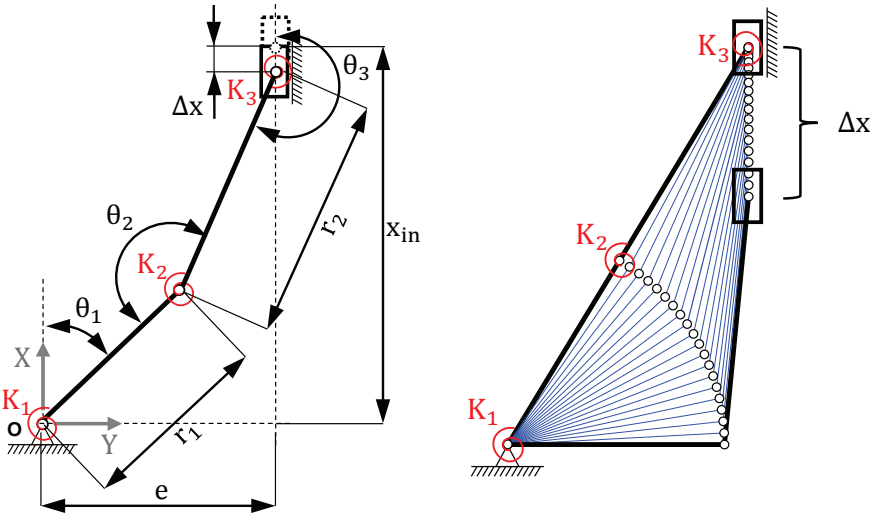

(a) Characteristic parameters.

(b) Static analysis at different slider positions.

Figure 4.3: Eccentric crank-slider mechanism - PRB model.

4.4.1. Eccentric Crank-Slider Mechanism: Analytical PRB Model

This section reports the analytical formulation of the output force provided by the slider with an imposed linear displacement. Referring to Fig. 4.3(a), r_1 and r_2 are the crank and the connecting rod lengths respectively, e is the mechanism eccentricity, x_{in} is the initial slider position, θ_1 and θ_3 are the crank angle and connecting rod angular position. The torques due to the presence of each spring-loaded revolute joint are given by:

$$T_i = -K_i \Psi_i \tag{4.1}$$

where K_i, $i = 1, 2, 3$ are the spring stiffness values, and Ψ_1, Ψ_2, Ψ_3 are defined as:

$$\Psi_1 = \theta_1 - \theta_{10} \tag{4.2}$$

$$\Psi_2 = \theta_2 - \theta_{20} = \theta_3 - \theta_{30} - \theta_1 + \theta_{10} \tag{4.3}$$

$$\Psi_3 = \theta_3 - \theta_{30} \tag{4.4}$$

being θ_{10}, θ_{20} and θ_{30} the initial joint angles, measured in the undeflected state. Considering ideal frictionless joints, the static behavior of the system, i.e. the vertical output force transmitted by the slider for an imposed displacement Δ_x, may be derived by applying the

principle of virtual work. From a practical standpoint, θ_1 is used as kinematic input instead of Δ_x in this work. By defining $\alpha = \arctan(e/x)$, where x is the slider position along the working direction with respect to the fixed coordinate system, and resorting to the superposition principle, the total output force may be written as:

$$F = F_1 + F_2 + F_3 \tag{4.5}$$

where

$$F_1 = K_1 \Psi_1 \cos(\theta_3) \Big/ r_1 \sin(\theta_3 - \theta_1) \tag{4.6}$$

$$F_2 = K_2 \Psi_2 \cos(\alpha) \Big/ r_1 \sin(\theta_1 - \alpha) \tag{4.7}$$

$$F_3 = K_3 \Psi_3 \cos(\theta_1) \Big/ \left(x \, \sin(\theta_1) - e \, \cos(\theta_1)\right) \tag{4.8}$$

are the contributes related to each single rotational spring. To calculate F for different slider positions (imposed by increasing θ_1), the values of e, r_1, x and θ_3 as well as K_1, K_2 and K_3 are needed, as visible in Eqs. 4.6, 4.7 and 4.8. Resorting to the mechanism position analysis, the following relations hold:

$$r_2 = \sqrt{x_{in}^2 + e^2} - r_1 \tag{4.9}$$

$$\vartheta_3 = \pi + \arcsin\left(\frac{e - r_1 \sin(\theta_1)}{r_2}\right) \tag{4.10}$$

$$x = r_1 \cos(\theta_1) - r_2 \cos(\theta_3) \tag{4.11}$$

By considering θ_1 as the Lagrangian coordinate and (x_{in}, e) as known parameters (design inputs), and by taking into account Eqs. 4.9 and 4.10, the remaining set of variables is composed of r_1, θ_{10}, K_1, K_2 and K_3. Note that (x_{in}, e) may be added to the design variables vector whenever no strict requirements in terms of encumbrance are specified.

4.4.2. Problem Formulation

To obtain the constant force behavior, the optimization problem can be formulated as follows:

$$\textbf{Min.}\ \ e_F = e_F(r_1, \theta_{10}, K_1, K_2, K_3) = \sqrt{\frac{1}{Q}\sum_{i=1}^{Q}\left[F_i - F_t\right]^2} \tag{4.12}$$

where e_F represents the RMS value of the error, namely the difference between the target force $F_t = 1.5$ N and the one derived by means of Eq. 4.5, evaluated for a single design candidate in a series of Q simulation steps.

4.4.3. Design Tool - Framework A

From a practical standpoint, the following aspects shall be taken into consideration:

- a simple mathematical formulation correlating the design variables vector (r_1, θ_{10}, K_1, K_2, K_3) and the objective function (e_F) is available (see Secs. 4.4.1 and 4.4.2);
- no information about the geometry of the parts (i.e. special CAD files) are needed to complete the study;
- being all the dynamics effects (e.g. inertias, dampings, frictions, etc.) neglected in the current scenario, to perform the kinetostatic behavioral analysis no special purpose solvers are required.

As suggested by Tab. 2.3, the study can be easily conducted in Matlab by means of the framework A. As shown in Fig. 4.4, the optimization is managed in the main environment, whereas the behavioral model is stored in an external function. A computationally efficient gradient-based algorithm (*fmnincon* routine) is used to solve the problem. For each of the candidate,a *for* loop structure with a total number of Q increments on the Lagrangian coordinate θ_1 allows to analyze the whole linear stroke, $\Delta_x = 35$ mm, and thus compute the corresponding value of e_F. See Appendix B for Matlab code used in this work.

4.4.4. Numerical Results - Optimal Configuration

The optimal variable set is summarized in Tab. 4.1. The PRB model is characterized by a RMS error equal to 0.01 N with respect to the ideal constant force solution. To validate the

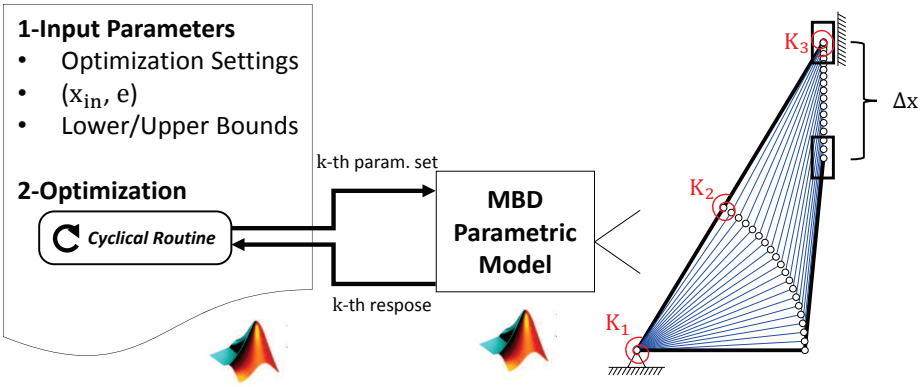

Figure 4.4: Framework A used for the #Step 1a.

Table 4.1: Optimal PRB model - characteristic parameters.

Design Var.	Range	Opt. Value
r_1	$[e/5, (9/10)e]$ mm	54.00 mm
θ_{10}	$\left[\arcsin\left(\frac{e}{\sqrt{e^2+x_{in}^2}}\right), \pi/2\right]$ rad	0.54 rad
K_1	$[0, 100]$ Nmm/rad	28.30 Nmm/rad
K_2	$[0, 100]$ Nmm/rad	35.38 Nmm/rad
K_3	$[0, 100]$ Nmm/rad	35.38 Nmm/rad

results, a MBD simulation is performed in RecurDyn. The model, depicted in Fig. 4.5(a), is analyzed by imposing a linear displacement $\Delta_x = 35$ mm to the slider and by measuring the resulting reaction force during the motion. To exclude dynamics effects, a quasi-null material density is set for the rigid bodies and a total simulation time of 4 s is imposed. Figure 4.5(b) shows the performance of the optimal PRB configuration and, in particular, the comparison between the results achieved with the theoretical model and the final MBD simulation in RecurDyn. The plot highlights a precise matching between the data, being the discrepancy quantifiable with a RMS error equal to 0.0035 N.

4.5. #Step 1b: Flexural Hinges Dimensioning

4.5.1. Theoretical Formulation and Practical Procedure

From the values of K_i, $i = 1, 2, 3$ listed in Tab. 4.1, the dimensions of the SLFPs can be derived. Supposing the SLFPs are straight beam hinges with rectangular cross section, the

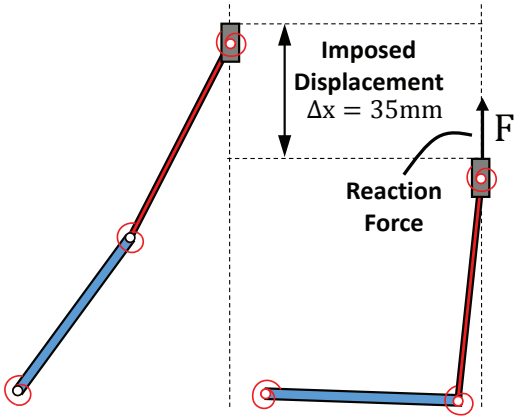

(a) Schematic of the MBD model in RecurDyn.

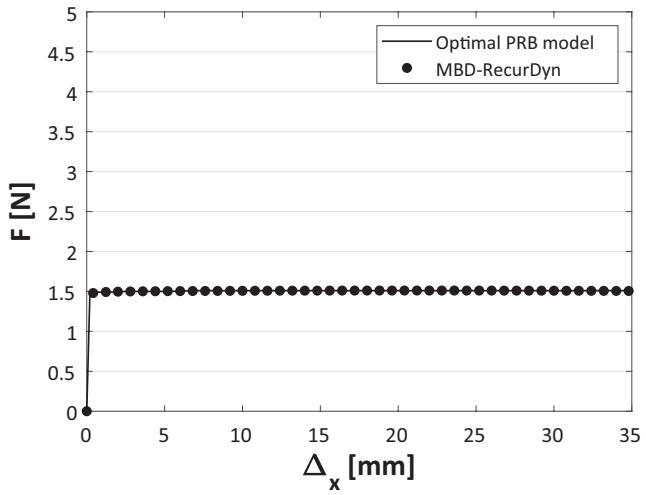

(b) Optimal PRB model - force-deflection relationship.

Figure 4.5: PRB behavioral analysis.

following relation holds [1]:

$$K_i = \frac{EJ_i}{L_i} \tag{4.13}$$

where E is the Young's modulus, L_i is the SLFP length, and $J_i = b_i {h_i}^3/12$ is the moment of inertia of the cross sectional area with respect to the barycentric axis (parallel to the width), b_i and h_i being the hinge width and thickness respectively. By adopting ABS plastic as the CM material, Young's modulus, Poisson's ratio and flexural yield strength are respectively equal to $E = 1800$ MPa, $\nu = 0.4$ and $\sigma_s = 42.5$ MPa. Starting from the optimal PRB model and assuming bending as the predominant behavior, the SLFPs dimensions are determined by considering that:

Table 4.2: Flexure dimensions.

Dimension	b_i	h_i	L_i
Joint K_1	2.72 mm	0.91 mm	10.80 mm
Joint K_2	2.88 mm	0.96 mm	10.80 mm
Joint K_3	2.88 mm	0.96 mm	10.80 mm

- to behave as a SLFP, L_i, $i = 1, 2, 3$ must be significantly lower than the length of the shortest rigid body (i.e. the crank);
- to minimize out-of-plane deflections, b_i, $i = 1, 2, 3$ must be larger than h_i, $i = 1, 2, 3$.

On the basis of these considerations and similarly to previous literature dealing with SLFP design [15, 139], $L_i = r_1/5 = 10.8$ mm and $b_i = 3h_i$, $i = 1, 2, 3$ are imposed in the model. Therefore, by knowing K_i, E and L_i, the value of h_i can be obtained as:

$$h_i = \sqrt[4]{\frac{4L_iK_i}{E}} \tag{4.14}$$

The value of b_i is then easily calculated as $b_i = h_i/3$, $i = 1, 2, 3$. Each PRB rigid pair is located at the center of the related SLFP [1].

4.5.2. Final Dimensions and FEA Validation

To compute the hinges dimensions, the above-discussed formulas are added to the main file of the framework A (after the PRB optimization section). The obtained values are reported in Tab. 4.2, whereas Fig. 4.6(a) shows the CAD model of the lumped compliance configuration. The CM is numerically analyzed via 1D and 3D nonlinear (NLGEOM option) FEA simulations in ANSYS. Regarding the FE models, *Beam 188* elements are used for the 1D analysis, whereas a free Hexa-dominant mesh has been defined (0.5 mm as max element size on the SLFPs) for the 3D analysis. As for the boundary conditions, the base of the system is fixed to the ground and the upper interface is guided along the x-axis and constrained along the y-axis, as visible in Fig. 4.6(a).

The FEA results are shown in Figs. 4.6(b), 4.6(c) and 4.6(d), where both the force-deflection characteristic and the 1D and 3D stress fields are reported. As clearly depicted in Fig. 4.6(b), both the 1D and 3D FEA outputs show good agreement with the behavior pre-

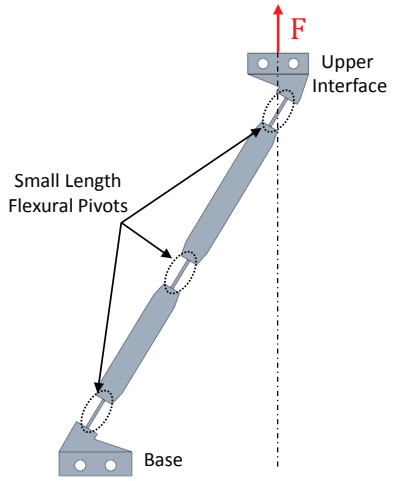

(a) Optimal lumped compliance constant force mechanism.

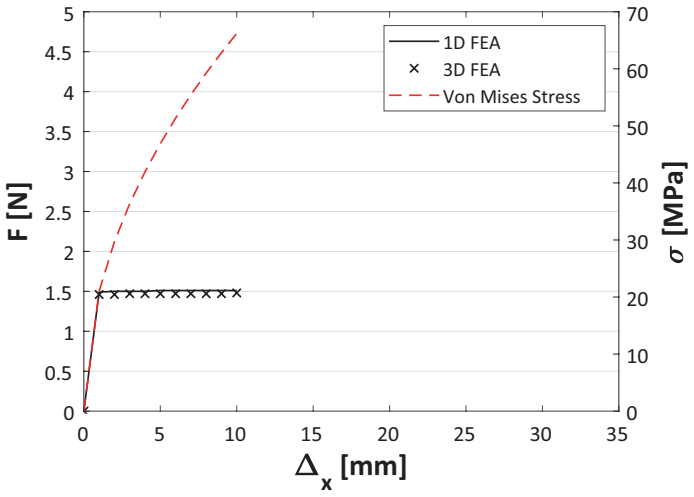

(b) Force-deflection relationship.

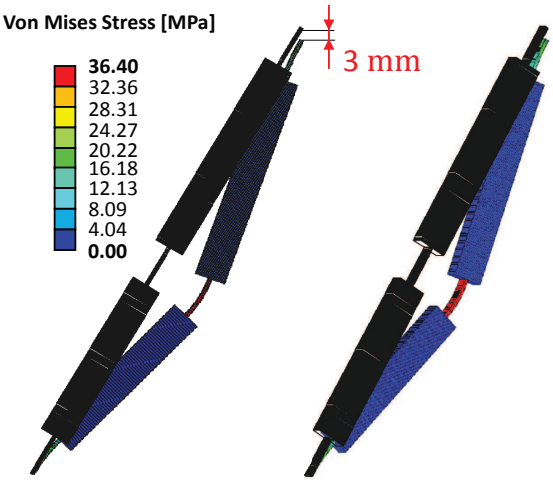

(c) 1D FEA stress field at maximum available stroke.

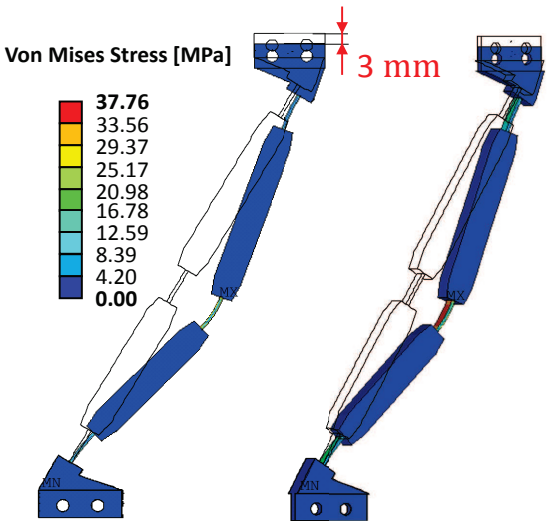

(d) Validation with 3D FEA.

Figure 4.6: Optimal results on the small-length configuration.

dicted by the PRB model, confirming the validity of the previous assumption ($L_i = r_1/5 = 10.8$ mm, $i = 1, 2, 3$). However, the assessed stress field limits the use of the lumped compliance configuration to the deflection range $0 < \Delta_x < 4$ mm. Accepting a RMS force error of 0.01 N, the constant reaction force becomes available after an initial deflection equalling 1 mm, thus resulting in an useful available stroke equalling 3 mm.

4.6. #Step 2: FEA Shape Optimization

This section describes a shape optimization process aiming at extending the operative stroke Δ_x of the constant force CM, limited to about 3 mm in the previous design. The new CM solution is composed of a series of variable thickness straight segments. The idea is to smooth the shape of the lumped compliance solution where the cross section undergoes remarkable variations (see Fig. 4.2). As previously said, continuously variable thickness beams cannot be easily modeled via analytical approaches. Consequently, 1D FEA is selected from Tab. 2.2 as the most efficient way to analyze the nonlinear beam-based CM. ANSYS is adopted as solver to accurately model the single parametric flexible beam (see Tab. 2.3). The script-based approach allows to avoid the graphical user interface if the simulations are run in batch mode.

4.6.1. Parametric FE Model

To keep consistency with the lumped CM and its related PRB system, the extremities of each SLFP are taken as fixed reference points for the new design (blue points S_i, $i = 1, .., 6$ in Fig. 4.7). In fact, as specified in Sec. 4.5.1, each revolute joint is located in the center of the related SLFP. The coordinates of the fixed reference points are listed in Tab. 4.3. To vary the shape of the overall CM, a set of two movable design points (red points p_j, $j = 1, .., 10$ in Fig. 4.7) is added to every interval defined by two fixed reference points. From a practical standpoint, these intervals ($S_1 - S_2$, $S_2 - S_3$, $S_3 - S_4$, $S_4 - S_5$ and $S_5 - S_6$) correspond to the SLPFs and to the rigid bodies in the lumped compliance configuration (see Fig. 4.6(a)). Each design (red) point identifies a parametric rectangular cross section and it is free to move in the interval between two consecutive fixed reference (blue) points.

The overall CM is a chain of straight segments, whose extremities are defined by the design points p_j, $j = 1, .., 10$, except for the initial and final segments, which are also connected to S_1 and S_6 respectively (see Fig. 4.7). Each design point, p_j, is located at a precise distance from the closest inferior fixed reference point, S_i. Taking as an example the design point p_3 (detailed view in Fig. 4.7), its position in the work-space can vary in the interval

Table 4.3: Reference points coordinates.

Reference Point	x**-coordinate**	y**-coordinate**
S_1	0.00 mm	0.00 mm
S_2	8.37 mm	6.36 mm
S_3	43.64 mm	31.78 mm
S_4	52.85 mm	37.41 mm
S_5	99.10 mm	60.75 mm
S_6	108.74 mm	65.61 mm

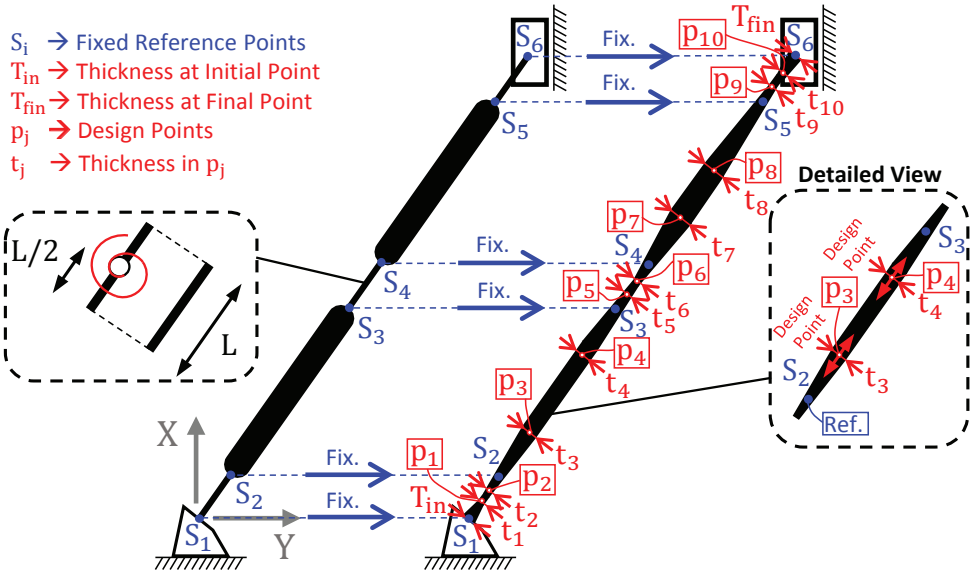

Figure 4.7: Schematic showing the correlation between the mechanisms.

S_2-S_3 as follows:

$$p_3 \rightarrow \begin{cases} x_{p_3} = x_{S_2} + a_3(x_{S_3} - x_{S_2}) \\ y_{p_3} = y_{S_2} + a_3(y_{S_3} - y_{S_2}) \end{cases} \tag{4.15}$$

where a_3 is the position coefficient taken into account during the optimization, along with the cross section width B_3 and thickness t_3 related to the point p_3. Hence, in the segment defined between p_3 and p_4, the thickness is linearly varied from t_3 to t_4.

Concerning the FE model, all the straight segments are discretized with *Beam 188* elements (quadratic shape functions), that allow tapered cross sections. The first node, located in S_1) is fixed to the ground, whereas the upper node, located in S_6, is guided by a remote displacement $\Delta_x = 20$ mm along the x-axis and constrained along the y-axis.

4.6.2. Problem Formulation

By imposing an equal out-of-plane width B for all the segments of the beam-based CM, the design variables vector is be composed of 23 entities:

- a_j, $j = 1, .., 10$ (design point location);
- t_j, $j = 1, .., 10$ (thickness at p_j);
- T_1, T_6 (thickness at CM's extremities, i.e. S_1 and S_6);
- B; (CM's out-of-plane width).

The optimization problem can be formalized as follows:

$$\textbf{Min.} \;\; e_F = \sqrt{\frac{1}{r}\sum_{i=1}^{r}\left[F_{FEA_i} - F_t\right]^2} \tag{4.16}$$

$$\textbf{Constraint} \rightarrow \;\; \sigma < \sigma_s = 42.5MPa \tag{4.17}$$

where F_{FEA} is the output force evaluated for the single FE model by imposing the displacement $\Delta_x = 20$ mm in a series of $r = 10$ simulation substeps. The constraint expressed in Eq. 4.17 is used to respect the material yield strength.

4.6.3. Design Tool - Framework D

Differently from the #Step 1a, the absence of an explicit correlation between the objective function and the related design variables suggests the use of DOE or GA [98]. By adopting a full factorial discretization in the design space, the DOE method can provide an excellent approximation of the objective function, allowing the use of a gradient-based algorithm for the subsequent research of the optimum (see Chap. 3). However, a large number of design variables (such as 23) leads to a remarkable increment in the total amount of simulations to be performed. For instance, by considering only 3 levels, namely 3 possible values for each design variable within its range, the total number of simulations would be equal to $n_{sim} = 3^{23} = 9.4\ 10^{10}$. Therefore, to limit the total computational cost, the optimization is solved by using the Matlab GA, particularly suitable for studies characterized by a very large number of design variables [38].

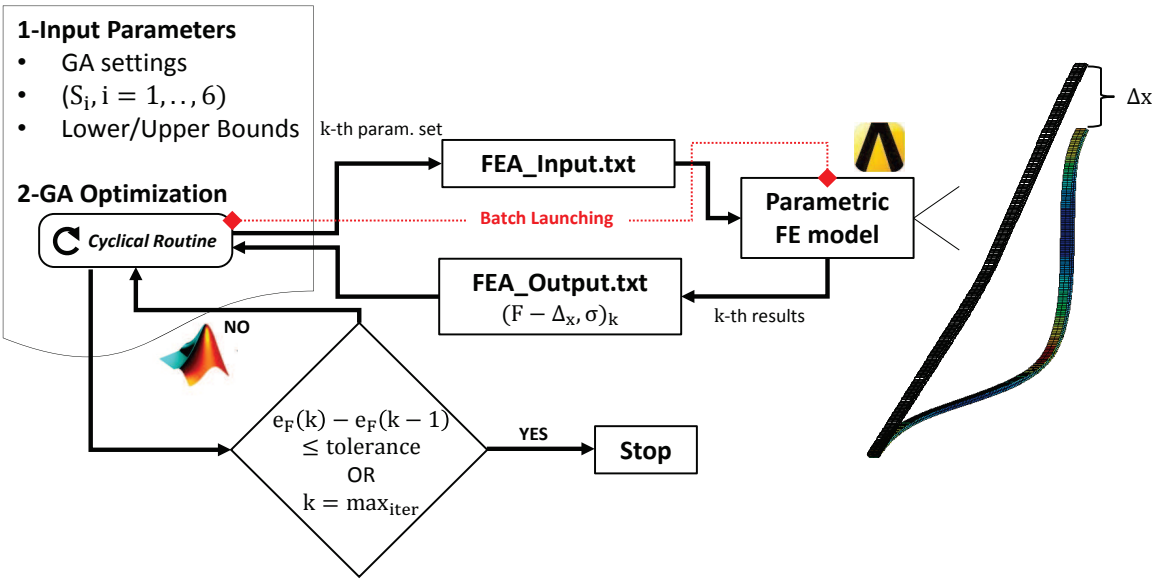

Figure 4.8: Framework D used for the #Step 2.

In the adopted software architecture (i.e. framework D from Tab. 2.3), Matlab manages the optimization process and the data exchange activities whereas ANSYS APDL performs the behavioral analysis. Following the schematic depicted in Fig. 4.8, for each candidate Matlab defines the design variables vector, which is then stored into an external *FEA_Input.txt* file and imported in ANSYS environment to update the FE model. ANSYS is automatically run by Matlab and provides, as a response of the nonlinear FEA simulation, the force-deflection behavior of the CM as well as the maximum Von Mises stress. These outputs are stored into another external *FEA_Output.txt* file, which is then automatically imported and processed by Matlab, allowing the evaluation of the error e_F. The GA is run with 100 generations and a population size of 30 candidates for each generation. The Matlab solver stops either when the average relative change in the value of e_F is less than or equal to the function tolerance (10^{-2} N) or if the maximum number of iterations exceeds 3000. To avoid issues due to possible unconverged FEA simulations, a Matlab subroutine capable of recognizing the lack of results from ANSYS has been setup. In particular, the subroutine returns a result of $e_F = 5$ N for all the unconverged candidates. Consequently, once the optimization study is concluded, the resulted configuration is a feasible solution. However, the accuracy of its behavior, defined by e_F, depends on the allowed range of variation of each design variable as well as on the algorithm settings. An APDL code that simulates the optimal configuration can be found in Appendix C.

Table 4.4: Optimal beam-based CM parameters.

Design Variable	Range	Opt. Value
a_1	$[0.125, 0.500]$	0.285
a_2	$[0.625, 0.875]$	0.803
a_3	$[0.500, 0.625]$	0.582
a_4	$[0.750, 0.875]$	0.851
a_5	$[0.125, 0.375]$	0.254
a_6	$[0.625, 0.875]$	0.842
a_7	$[0.375, 0.625]$	0.578
a_8	$[0.750, 0.875]$	0.798
a_9	$[0.125, 0.375]$	0.231
a_{10}	$[0.750, 0.875]$	0.765
t_1	$[0.850, 1.100]$ mm	0.997 mm
t_2	$[0.850, 1.100]$ mm	0.929 mm
t_3	$[1.200, 1.400]$ mm	1.356 mm
t_4	$[1.200, 1.400]$ mm	1.339 mm
t_5	$[0.800, 1.150]$ mm	0.996 mm
t_6	$[0.800, 1.150]$ mm	0.920 mm
t_7	$[1.300, 1.600]$ mm	1.440 mm
t_8	$[1.300, 1.600]$ mm	1.434 mm
t_9	$[0.900, 1.100]$ mm	0.968 mm
t_{10}	$[0.900, 1.100]$ mm	1.046 mm
T_{in}	$[0.850, 1.100]$ mm	0.927 mm
T_{fin}	$[0.900, 1.100]$ mm	0.947 mm
B	$[5.000, 8.000]$ mm	5.138 mm

4.6.4. Numerical Results - Optimal Configuration and Final Tests

The code has been run several times to test the repeatability of the framework. The GA always converged to a vector whose differences have been registered on the third decimal number, after 82 ± 3 iterations. Overall, these differences do not affect the fabrication process if 3D printing is employed. Imposed range of variation for each design parameter, evaluated after a limited number of initial FEA simulations, and optimal values are summarized in Tab. 4.4. Figure 4.9(a) shows the optimal configurations of the proposed beam-based CM. Similarly to the previous lumped compliance solution, a 3D FEA simulation is performed on the optimal CM. The force-deflection characteristic and the maximum registered Von Mises stresses along the stroke are plotted in Fig. 4.9(b). It is possible to see the matching between the desired target force (i.e. 1.5 N), the behavior obtained by means of the automatic design procedure (i.e. FEA-1D) and the one resulted from the last simulations (i.e. FEA-3D).

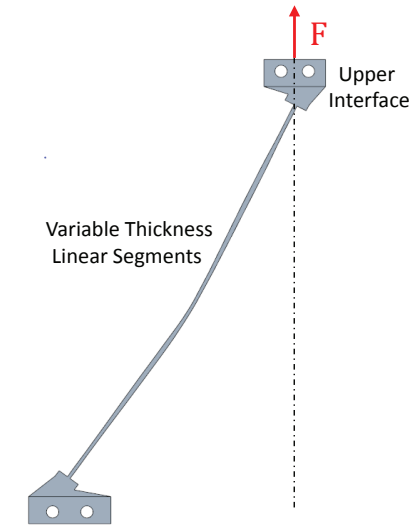

(a) Optimal distributed compliance constant force mechanism.

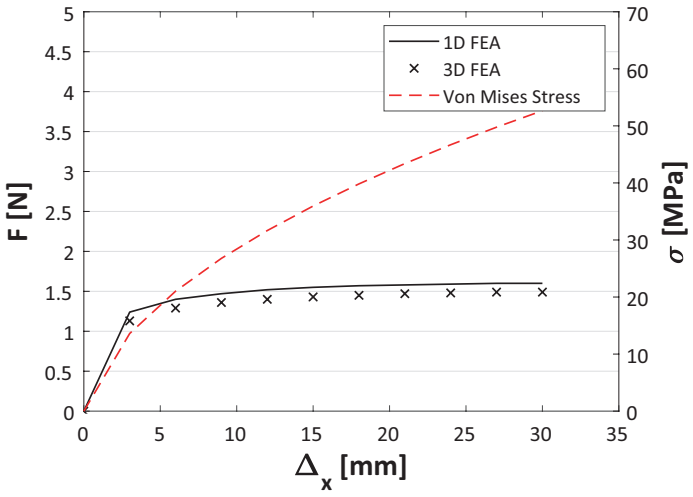

(b) Force-deflection relationship.

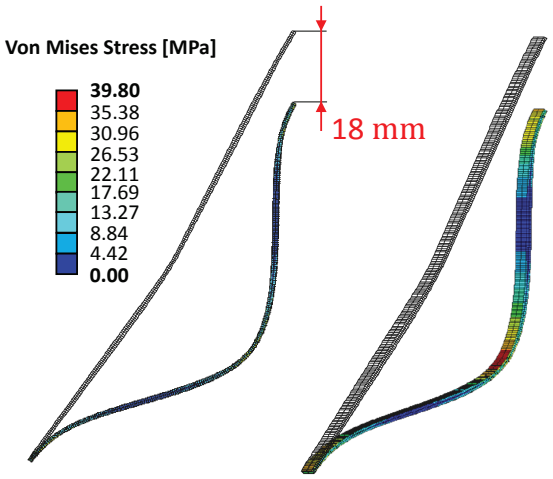

(c) 1D FEA stress field at maximum available stroke.

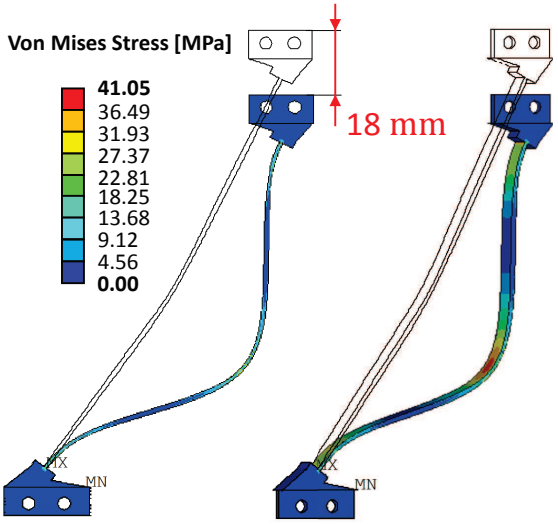

(d) Validation with 3D FEA.

Figure 4.9: Optimal results on the beam-based configuration.

The overall deflection range is equal to 18 mm. With reference to Fig. 4.9(b), accepting a RMS force error (computed by means of Eq. 4.17) equal to 0.075 N, the constant force behavior is achieved in the range $4 < \Delta_x < 18$ mm (i.e. overall useful stroke of 14 mm). Therefore, considering the lumped compliance mechanism as the reference solution, namely the behavior reported in Fig. 4.6, the available useful stroke is increased of an amount equal to 467% (i.e. from 3 mm to 14 mm).

It must be remarked that the optimal beam-based design can be modified in case of a different target force by simply changing the material, by scaling the out-of-plane thickness B,

or by employing systems composed of several beams placed in parallel spring configuration (as in Fig. 4.1).

4.7. Experimental Validation

To confirm the modeled results experimentally, the synthesized constant force CMs have been fabricated by employing a 3D printer capable of extruding ABS with a layer height of 0.100 mm. The specimens have been printed by aligning the 3D printer's z-axis with the out-of-plane width (i.e. B) direction. Experimental tests have been carried out on the CMs resorting to a purposely designed test rig. The test aims at verifying output force of the prototypes and the absence of failures for a deflection range equal to $\Delta_x = 4$ mm for the lumped compliance solution, and to $\Delta_x = 18$ mm for the distributed compliance solution. The experimental setup, shown in Fig. 4.10, is equipped with a linear motor (LinMot PS02-23x80-F), a 1-axis load cell (characterized by a structural stiffness of 242.000 N/mm, an overall weight of 11 g and an accuracy of 0.1 N), and a series of 3D printed connection members. Two specimens are tested simultaneously, as shown in Fig. 4.10, in order to maintain the symmetry and to exclude undesired disturbance forces (e.g. friction or other out-of-axis contributes). Moreover, the considered configuration (a couple of parallel linear springs) ensures to keep consistency with the schematic depicted in Fig. 4.1. The specimens are fixed to the ground from one end and guided in a linear motion by means of the LinMot slider on the other end. The 1-axis load cell is mounted on the LinMot slider and provides the overall reaction force. A LabView interface is used to acquire the data from the LinMot integrated linear encoder and the load cell. With the aim of investigating the static behavior of the system, a velocity of 2 mm/s has been assigned to the slider, neglecting the major dynamic contributes.

As depicted in Fig. 4.11, which reports the contribute of a single beam for all the tested configurations, the experimental results show good agreement with the behavior predicted during the previous design steps. The differences between FEA and experimental force-displacement relationships are mainly due to:

- manufacturing errors in the deposition of the filament, causing uncertainties in the thickness effectively obtained along the path of the beams;
- technical limits of the 3D printer, such as the layer height equal to 0.100 mm, that does

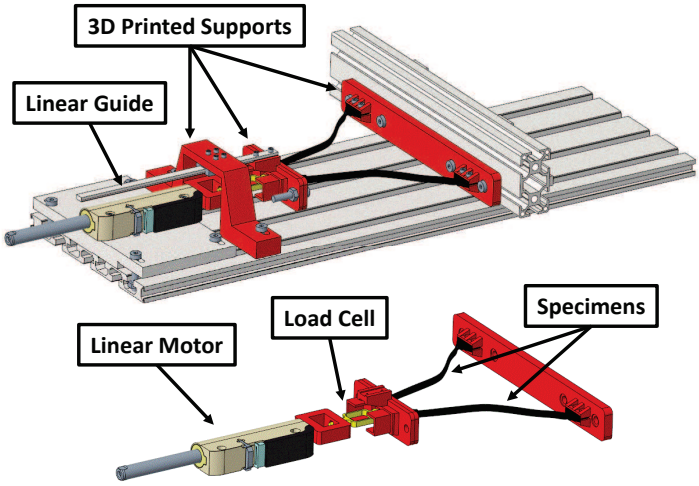

(a) CAD drawings of the main components.

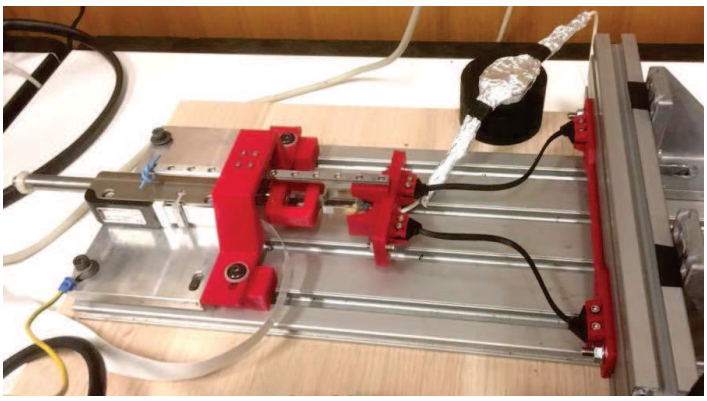

(b) Test on the beam-based configuration.

Figure 4.10: Experimental setup.

not allow to respect the optimal values of B, i.e. the one reported in Tab. 4.4;

- nonideal linear guides, affected by friction (see Fig. 4.10).

Different from the FEA results, the lumped compliance solution failed at $\Delta_x = 6.5$ mm, and the straight segments solution presented irreversible structural damages at $\Delta_x = 22$ mm.

4.8. Summary

This chapter describes a computationally efficient two-steps procedure for the structural optimization of CMs, by combining analytical and numerical modeling techniques. The method can be applied to a large number of beam-based CMs, starting from their PRB counterpart. Each of the design steps is implemented and solved using an integrated design tool

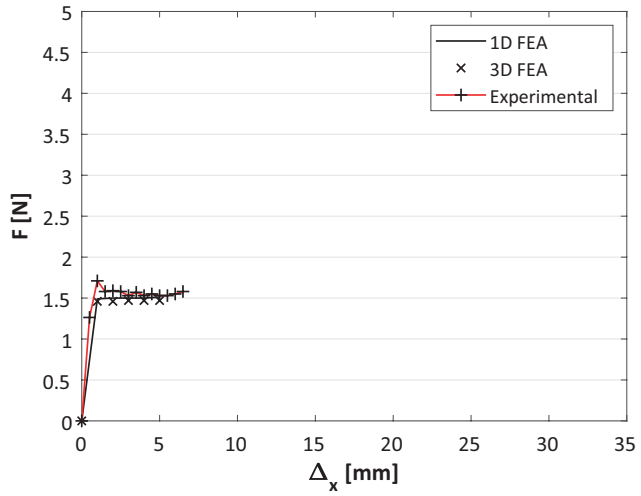

(a) Small-length configuration.

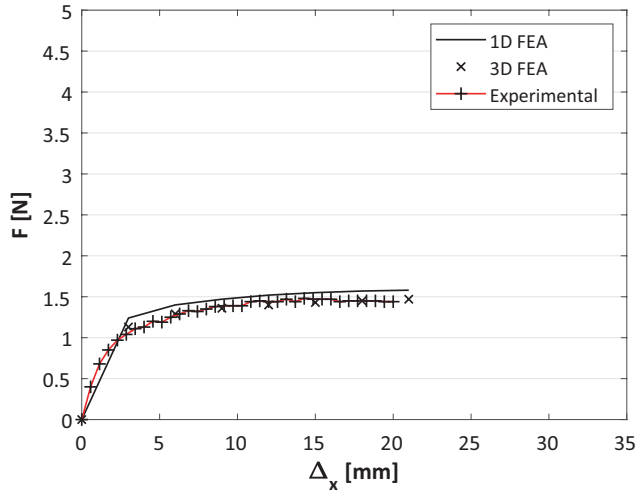

(b) Beam-based configuration.

Figure 4.11: Experimental force-deflection relationships.

(selected among the configurations in Tab. 2.3). The method is tested on a monolithic constant force CM based on the slider-crank architecture. In #Step 1, a fast optimization routine is performed on the equivalent PRB model to synthesize three SLFPs. FEA results verified the validity of the solution and highlighted a critical stress condition after a rather limited linear displacement. To overcome this drawback, in #Step 2, the CM's shape is optimized by combining the Matlab GA and the ANSYS solver. The resulted configuration is composed of a series of variable thickness flexible segments. The stress concentrations have been drastically reduced, as proved by a remarkable increment of the available stroke, approximately

about 467%.

As for the computational efficiency, the PRB optimization process takes 25 to be completed, whereas a single batch FEA simulation is solved in $3 - 4$ s with 250 1D elements distributed along the beam.

The designed CMs have been produced by means of 3D printing technologies and experimentally verified. The acquired data show good consistency with the numerical results, confirming the suitability of the proposed multi-step design approach.

Chapter 5

Design of Special-Purpose Torsional Compliant Springs

5.1. Compliant Mechanisms with Nonlinear Prescribed Load-Displacement Behavior

Many special-purpose CMs present, for a certain working condition, a defined nonlinear relation between the deflection and the applied force/torque. Examples include constant force CMs (see Sec. 4.1), constant torque CMs [103] (i.e. the rotational counterpart of the constant force CMs), quadratic CMs [4] and bistable CMs [140]. Several applications benefit from the use of nonlinear CMs. In particular:

- constant force CMs may reduce the number of sensors and the complexity of the control law in mechatronic systems (see Chap. 4);
- constant torque CMs are useful for rehabilitative and assisting devices [103], medical tools [11], aerospace devices [141] and counterbalancing systems in robotic arms [142];
- quadratic CMs are commonly implemented in antagonistic VSAs to obtain a decoupled regulation of joint position and stiffness [4, 143–145];
- bistable CMs can be used as compensation modules in statically balanced mechanisms [2, 146].

Each application requires a prescribed load-displacement behavior. Therefore, the CM configuration must be tailored to match unique requirements. Apart from bistable CMs, which usually exploit the post-buckling behavior of straight beams [2, 146–149], the design of nonlinear CMs is typically achieved via the use of self and mutual contacts [67, 68, 97, 150, 151] (see also Chap. 6) or curvilinear/spline beams [38, 106]. The former solution leads to an increment in the number of parts, whereas the latter allows monolithic designs. Spline

beams offer greater effective lengths that enable larger deformations (and lower stresses) within relatively compact footprints. Several works exploited the benefits of spline beams in shape optimization [11, 71, 103, 152, 153]. Given that theoretical approaches, such as elliptic integrals [1], are quite knotty for the modeling of spline beams, the optimal design can be addressed through FEA (see Tab. 2.2).

5.2. Aim of the Study

This chapter reports a procedure for the shape optimization of special-purpose torsional CMs exploiting spline beams. Two case studies are discussed and analyzed among the previous classification, namely a quadratic torsional CM to be used in antagonistic VSAs and a statically balanced CM (hereinafter referred as to zero torque CM, as explained in Sec. 5.4). Before dealing with the compliant parts, a general overview of the mechanical systems is given to clarify the design requirements and the overall working principles. Afterwards, a single design procedure is reported, allowing the definition of the final torsional CMs. Lastly, physical prototypes of both torsional springs are manufactured and their performance tested with two rotational setups.

5.3. #Case Study I - Quadratic Compliant Mechanisms in Variable Stiffness Actuators

5.3.1. Antagonistic Variable Stiffness Actuators

As for the first case study, a VSA is considered, namely a mechatronic system capable of actively varying the compliance of a joint [144]. Numerous configurations of VSAs have been developed in the last two decades to address specific demands in terms of functionality and performance (overviews are reported in [154, 155]). These electromechanical devices are implemented in many applications, resulting particularly useful in entertainment robots [156], rehabilitative prostheses [157] and for increasing the safety in robotic arms that interact with humans in a work environment [158].

In fact, industrial robots are usually realized extremely fast and stiff in order to increase positioning accuracy, thus leveraging on mechanical structures characterized by very rigid links and aiming at minimizing the joint elasticity. Such design paradigms, especially in

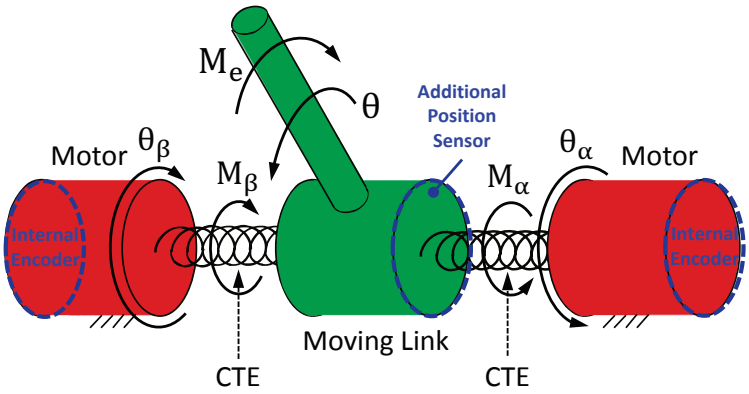

Figure 5.1: Functional schematic of the antagonistic VSA.

.

industrial applications, lead to devices that may be rather unsafe in case of physical interaction with humans. As proven by [158], an effective way to enhance the safety in robotics arms is the introduction of a programmable compliance in the mechanical chain, which can be actively varied during the robot functioning. Such functional feature can be achieved by implementing VSAs on the robot joints [4, 143, 154, 159–161]. The aim of the VSAs is to increase safety while maintaining at the same time an adequate level of accuracy. This type of solution allows to change both mechanical stiffness and angular position of the robot joints. A conceptual schematic of a VSA with antagonistic architecture [4, 143] is depicted in Fig. 5.1: a moving link, i.e the actuator output, is controlled, both in terms of angular position and rotational stiffness, via two separate electrical motors and a pair of nonlinear CTEs [144, 145]. If such nonlinear behavior is achieved via a quadratic torque-deflection relationship, both design and control may be simplified, as properly explained in Sec. 5.3.3. By actively acting on the CTEs pre-load, the stiffness of the joint can be varied in both static and dynamic conditions. Referring to such concept, plenty of different design solutions have been developed in the literature [143, 160, 162, 163]. The VSA principle as well as the guidelines for the selection of the appropriate CTE profile (i.e. the torque deflection relationship) are described in the following sections.

5.3.2. Embodiment Design of the Actuator

In this section the embodiment design of a VSA, which implements the antagonistic principle depicted in Fig. 5.1, is introduced and described. The VSA CAD drawings are

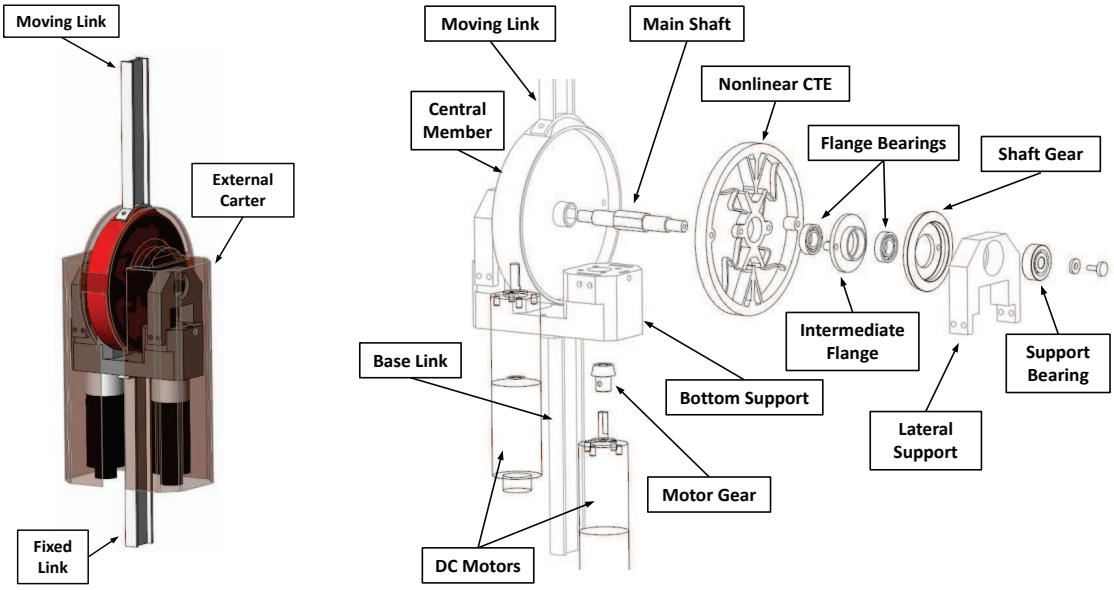

(a) VSA prototype.

(b) CAD exploded view.

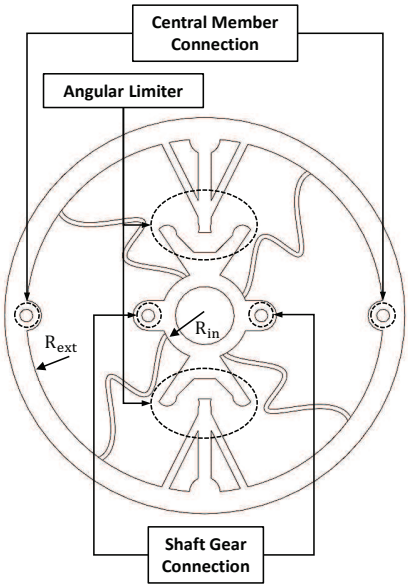

(c) Nonlinear CTE.

Figure 5.2: VSA CAD overview.

shown in Fig. 5.2. By observing the exploded view of Fig. 5.2(b), the main parts of the device can be listed as follows:

- a *Moving Link*, fixed to the *Central Member* and to the *Main Shaft*, which is supported at both extremities by a couple of *Support Bearings*;
- a set of two *DC Motors*, equipped with an optical encoder and a gearbox with reduction ratio of 23:1;

- a pair of conic transmissions (i.e. *Motor Gear* and *Shaft Gear*) with ratio 3.5:1, that allows to arrange the *DC Motors* perpendicular to the VSA *Main Shaft* and, as a consequence, to reduce the lateral encumbrance of the VSA;
- a pair of identical *Nonlinear CTE*s, connecting the *Moving Link* to each *Shaft Gear* and, as a consequence, to the *DC Motors*;
- a set of additional bearings (i.e. *Flange Bearings*) for supporting and decoupling each *Shaft Gear* from the *Main Shaft*. In this way, *DC Motors* can deflect the *Nonlinear CTE*s without directly acting on the *Moving Link*;
- a *Base Link* (composed of *Bottom Support* and two *Lateral Supports*) that acts as a common frame for the *DC Motors* and the joint.

At last, Fig. 5.2(c) shows the *Nonlinear CTE*. As said, this planar spring is designed to match a pre-defined quadratic torque-deflection behavior. In particular, spline beams are used to realize the connection between the inner and the outer rings, being $R_{in} = 10$ mm and $R_{ext} = 41$ mm input parameters, defined by the physical encumbrances. The inner rings are rigidly guided by the *DC Motors*, whereas the outer rings are fixed to the *Moving Link*.

5.3.3. Actuator Theoretical Static Model

As previously stated, the antagonistic VSA employs two independent motors, mounted on a single fixed frame, that act on a pair of nonlinear CTEs, as shown in Fig. 5.1. These CTEs are connected to the moving link, namely the VSA output member. The torques M_α and M_β applied by the motors are given by:

$$M_\alpha = \tau_\alpha(\epsilon_\alpha) + \cancel{I_m \ddot{\theta}_\alpha} \qquad\qquad M_\beta = \tau_\beta(\epsilon_\beta) + \cancel{I_m \ddot{\theta}_\beta} \tag{5.1}$$

where

$$\epsilon_\alpha = \theta_\alpha - \theta \qquad\qquad \epsilon_\beta = \theta_\beta + \theta \tag{5.2}$$

having defined I_m as the motors' inertia (assumed identical for both motors), $\tau_\alpha = \tau_\alpha(\epsilon_\alpha) = \tau_\alpha(\theta, \theta_\alpha)$ and $\tau_\beta = \tau_\beta(\epsilon_\beta) = \tau_\beta(\theta, \theta_\beta)$ as the coupling torques between the moving link

and the actuators generated by the CTEs deformations, θ_α and θ_β as the motors' positions, θ as the angular position of the moving link, ϵ_α and ϵ_β as the angular deflection of the CTEs. Since a static model is now being considered, as shown in Eq. 5.1, the angular accelerations $\ddot{\theta}_\alpha$ and $\ddot{\theta}_\beta$ are null. The total torque M_J applied to the joint by the two motors is then:

$$M_J = M_\beta - M_\alpha = \tau_\beta - \tau_\alpha \tag{5.3}$$

and the joint stiffness is given by:

$$k = \frac{\partial M_J}{\partial \theta} \tag{5.4}$$

If τ_α and τ_β are chosen to be nonlinear functions of the angular deflections ϵ_α and ϵ_β, both joint position, θ, and stiffness, k, can be independently modulated via a precise control of the motors' angular positions, θ_α and θ_β [164]. The joint stiffness profile, defined by Eq. 5.4 and its range of variation, $[k_{min}, k_{max}]$, depend on the VSA technological implementation.

The only strict requirement for the CTEs is to provide a nonlinear characteristic $\tau_\alpha = \tau_\alpha(\epsilon_\alpha)$ (note that $\tau_\alpha = \tau_\beta$ since identical CTEs are considered). The CTE's torque-deflection relationship, $\tau_\alpha(\epsilon_\alpha)$, can be defined by ensuring some advantages for the VSA controller. It is possible to prove that only if τ_α is designed to be a quadratic functions of ϵ_α, the joint stiffness k is not related to the joint position θ. Consequently, k can be precisely modulated with no actual information about the value of θ. Hence, practically speaking, a position sensor on the moving link, schematized in Fig. 5.1 and implemented in [162, 165, 166], as well as its cabling and interface can be avoided, allowing a more compact and simple design. The stiffness can be controlled by knowing the values of θ_α and θ_β from the motors' integrated encoders. Generally, the dependence of the joint stiffness from its position can be compensated by control within its bandwidth [167]. However, a quadratic CTE enables the joint stiffness to be independent from the joint position disregarding the controller bandwidth. Therefore, the joint stiffness will be preserved also in case of abrupt change of the external torque M_e applied to the joint.

Let one then suppose that τ_α and τ_β can be written as:

$$\tau_\alpha = a_2\epsilon_\alpha^2 + a_1\epsilon_\alpha \qquad\qquad \tau_\beta = a_2\epsilon_\beta^2 + a_1\epsilon_\beta \tag{5.5}$$

where the parameters a_1, a_2 are user-selected constants of the quadratic CTE's torque-deflection profile. Then, recalling all the previous equations, the following relations hold for the total torque and for the joint stiffness:

$$M_J = [a_2(\theta_\alpha + \theta_\beta) + a_1][\theta_\beta - \theta_\alpha + 2\theta] \tag{5.6}$$

$$k = \frac{\partial M_J}{\partial \theta} = 2[a_2(\theta_\alpha + \theta_\beta) + a_1] \tag{5.7}$$

Note that, in static conditions, i.e. when $\theta(t) = const$, M_J is equal and opposite to the total external load M_e, if present. From Eq. 5.7 the following concepts can be easily verified:

1. a nonlinear CTE is necessary for achieving stiffness modulation capabilities. In fact, by employing a linear CTE (i.e. with stiffness coefficient a_1, as in Eq. 5.5 if $a_2 = 0$), the resulting joint stiffness will always be constant, i.e. equal to $k = 2a_1$;

2. if a quadratic CTE is selected, the joint stiffness can be varied by a suitable selection of the actuators configuration, i.e. by changing θ_α and θ_β, since k does not depend to θ. This concept can be further demonstrated by considering an exponential profile for the CTEs [167], i.e $\tau_\alpha = a_1 e^{\epsilon_\alpha} - 1$ and $\tau_\beta = a_1 e^{\epsilon_\beta} - 1$. In this case, the joint stiffness can be expressed as $k = a_1 e^{\epsilon_\alpha} + a_1 e^{\epsilon_\beta} = a_1 e^{\theta_\alpha - \theta} + a_1 e^{\theta_\beta + \theta}$ and thus a sensor that provides the value of θ is required for control purpose.

From Eqs. 5.6 and 5.7, the equilibrium position of the moving link can be derived as:

$$\theta = \frac{1}{2}\left(\theta_\alpha - \theta_\beta + \frac{M_J}{a_2(\theta_\alpha + \theta_\beta) + a_1}\right) = \frac{\theta_\alpha - \theta_\beta}{2} + \frac{M_J}{k} \tag{5.8}$$

The first term in Eq. 5.8, i.e. $(\theta_\alpha - \theta_\beta)/2$, is the joint position in absence of an external load, whereas the second term, i.e. M_J/k, describes the effect of the external load, highlighting the decoupling of θ from k. On the basis of these considerations, a quadratic profile for the CTEs is selected in this work for the VSA design.

5.3.4. CTE Reference Quadratic Behavior

In the current work the CTE torque-deflection relationship, described by a_1 and a_2 (see Eq. 5.5), has been defined by considering:

1. a variation in the actuator stiffness in the order of 1000 Nmm/rad between the minimum (i.e. k_{min}) and the maximum (i.e. k_{max}) conditions (see Eq. 5.7);

2. a deflection range $\theta_{\alpha,\beta} = [-0.26, 0.26]$ rad for the CTEs;

3. the selected material for the CTE, i.e. ABS plastic. Considering a layer height equal to 0.1 mm, the Young's modulus, Poisson's ratio and flexural yield strength adopted for the current work are, respectively, $E_b = 1800$ MPa, $\nu_b = 0.4$ and $\sigma_{s,b} = 42.5$ MPa.

The resulting coefficients are $a_1 = 630.25$ Nmm/rad and $a_2 = 510.66$ Nmm/rad^2, allowing a stiffness modulation in the range $[726, 1795]$ Nmm/rad.

5.4. #Case Study II - Nonlinear Compensation Springs in Zero Torque Compliant Mechanisms

5.4.1. Zero Torque Compliant Mechanisms

As the rotational version of the constant force CMs (described in Chap. 4), constant torque CMs are devices that provide a near constant output torque for a certain range of angular inputs [11, 71, 103, 152, 168, 169]. Different than the constant torque springs presented in [170], the constant torque CMs are characterized by a single common axis of rotation between the input and output frames. Despite their stiffness is null for a definite range of angular displacements, constant torque CMs require external actuation to deflect the flexible members and to maintain the deformed state. In particular, employing the same terminology of [89], the spring-back behavior can be avoided by designing hereby called zero torque CMs, namely a special class of statically balanced mechanisms [88, 171–174] characterized by a single pure rotational DOF. Referring to Fig. 5.3, a zero torque CM is composed of two concentric rings, one fixed and one movable. If a pure rotation is applied to the movable ring and other external disturbances (parasitic loads [25]) are neglected, the system will react with a negligible torque and a null axis shift. However, differently from e.g. C-Flex bearings [175], also referred to as tubular CAFP in [29], the zero torque CMs cannot support radial loads, unless a properly defined constraint set is provided to the rings (as it will be shown in the following sections). Such devices can drastically reduce actuation effort, allowing for smaller actuators [88]. Practically speaking, they combine the benefits of CMs

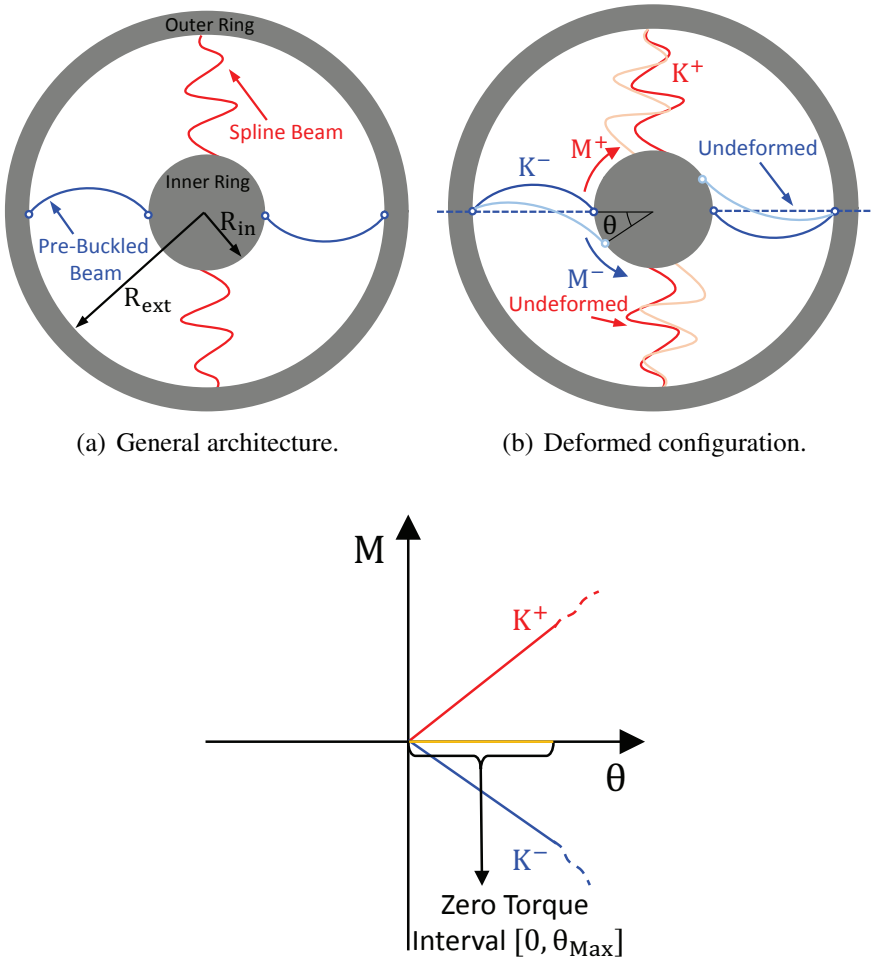

(a) General architecture.

(b) Deformed configuration.

(c) Stiffness compensation.

Figure 5.3: Conceptual schematic of the zero torque CM.

with some benefits of conventional rigid mechanisms, namely absence of a preferential equilibrium position and absence of undesired energy storage [89]. Due to their compactness and scalability, zero torque CMs may be used as substitutes for traditional rotational joints in mechanical systems that need reduced part number or reduced friction. For instance, they may be considered during the initial CM design phase when applying the rigid-body replacement method [176]. Envisaged applications concern small manipulators, such as tendon driven robotic fingers [25].

A zero torque CM can be realized by means of the stiffness compensation method [177, 178], i.e. by adding additional elements to store and release potential energy during the motion of the system, as shown in Fig. 5.3. The overall mechanism is then composed by positive stiffness members (red springs in Fig. 5.3) and by negative stiffness members (blue springs

in Fig. 5.3, hereinafter referred to as negators). Differently from the above-mentioned constant force/torque CMs, the negators are pre-loaded and thus the stiffness compensation is achieved without the initial force/torque offset. In fact, as shown in [148, 149], initially straight beams behave as positive stiffness springs in the first range of deflections. In the recent literature, plenty of architectures for statically balanced CMs employing the CAFP concept have been presented [89–91]. Many of them achieve significant angular deflections (see [89], where the null output is available for 1.4 rad of rotation), however, these mechanisms are rarely implemented due to their large size. Moreover, the CAFP is subjected to an axis shift during the deflection (as it will be shown in Chap. 6).

5.4.2. Design Configuration in Annular Domain

On the basis of the conceptual schematic reported in Fig. 5.3, a new design of an extremely compact zero torque CM, which can be used in small-scale applications that require limited encumbrances, is reported. The proposed device, realized in an annular design domain, can be miniaturized to a large extent. Based on the results reported in [147, 179], pinned-pinned pre-buckled beams are adopted as negators.

If the negators are equally spaced in the angular domain, defined by inner/outer ring radii (R_{in} and R_{ext}), their number, n_N, can be arbitrarily selected while still preserving equilibrium in the initial configuration and thus during assembly. Except for $n_N = 1$, which requires a central pin to constrain the translation along the x-axis, the equally spaced parallel configurations ensure force and torque balancing in the initial state ($\theta = 0$ rad). In practice, the central pin is adopted also for $n_N = 2$, as visible in Fig. 5.4, in order to avoid instability along the vertical axis. To ensure compactness and avoid mutual contact between flexible elements, the proposed device comprises a set of two negators and two connection spline beams arranged in a parallel spring configuration. To achieve a complete balancing, the shape and size of such spline beams are optimized via 1D FEA to match a pre-defined behavior, obtained by reversing the negator's characteristic in the positive plane.

To facilitate machining, $R_{in} = 10$ mm and $R_{ext} = 50$ mm are considered in this work. Much smaller designs necessitate the use of special tools/machines for manufacture. As for the materials, polypropylene and 1095 spring steel are adopted for the spline beams and for the negators respectively. The Young's moduli are $E_b = 1450$ MPa and $E_N = 190000$ MPa,

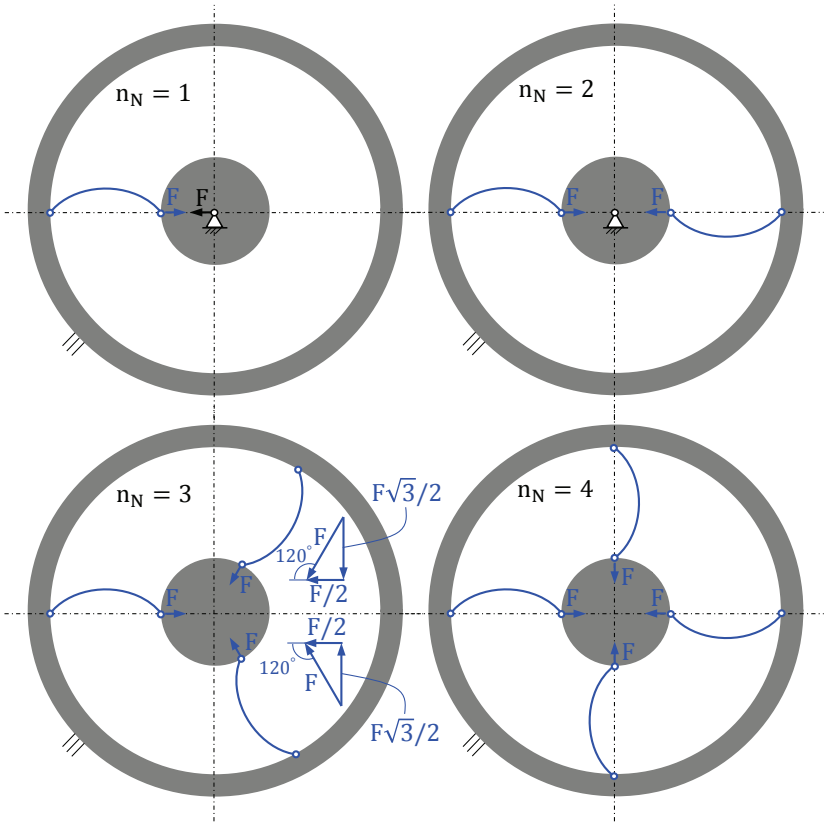

Figure 5.4: Pinned-pinned pre-buckled negators in the annular frame.

the Poisson's ratios are $\nu_b = 0.4$ and $\nu_N = 0.33$ whereas the yield strengths are $\sigma_{s,b} = 50$ MPa and $\sigma_{s,N} = 950$ MPa.

5.4.3. Analytical Modeling of Pinned-Pinned Pre-Buckled Beams

In this section, the behavior of a single pre-buckled beam in the annular domain is analyzed, as visible in the principle schematic of Fig. 5.5. The negator is simply a pinned-pinned straight beam with a constant rectangular cross section along the main axis. Its geometry is defined by length L_N, width b_N and thickness t_N, as shown in Figs. 5.5(a) and 5.5(b). Referencing Fig. 5.5(b) as well as the theory reported in [147], the behavioral modeling of the beam under axial loads beyond the buckling load, $F_{cr} = \pi^2 E_N J_N / L_N^2$, E_N being the material Young's modulus and $J_N = b_N t_N^3/12$ the cross section's moment of inertia, can be solved in closed-form resulting in the following relations:

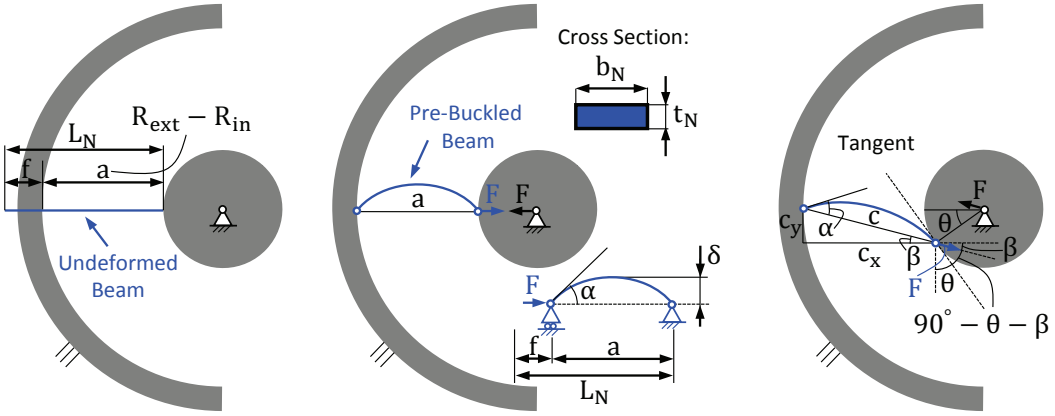

(a) Initial configuration. (b) Pre-loaded condition. (c) Working condition.

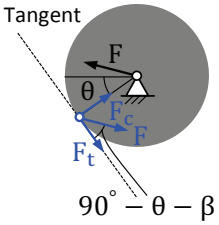

(d) Detailed view: resulting forces.

Figure 5.5: Principle schematic of the pre-buckled negator.

$$\frac{f}{L_N} = \frac{L_N - a}{L_N} = 2\left(1 - \frac{E(\alpha)}{K(\alpha)}\right) \tag{5.9}$$

$$\frac{F}{F_{cr}} = \frac{4K(\alpha)^2}{\pi^2} \tag{5.10}$$

$$\frac{\delta}{L_N} = \frac{\sin(\alpha/2)}{K(\alpha)} \tag{5.11}$$

where f is the axial displacement of the movable pin, $a = R_{ext} - R_{in}$ is the distance between the pins in the deformed configuration, δ is the maximum transversal displacement of the beam, M_{fmax} is the maximum bending moment acting on the beam, and α is the end rotation of the beam under load. The quadratic functions $E(\alpha) = \pi/2 - 0.1\alpha^2$ and $K(\alpha) = \pi/2 + 0.1\alpha^2$ are used in place of the complete elliptic integrals of the first and second kind [180] to ensure the closed-form of the problem. By imposing a rotation θ to the inner ring (see

Fig. 5.5(c)), the distance between the pins can be expressed as:

$$c = \sqrt{c_x^2 + c_y^2} = \sqrt{\left(a - R_{in}\left(\cos(\theta) - 1\right)\right)^2 + R_{in}^2 \sin^2(\theta)} \tag{5.12}$$

By introducing Eq. 5.12 in Eq. 5.9 (where a becomes c), it is possible to derive the following expression for α:

$$\alpha = \pm\sqrt{5\pi}\sqrt{\frac{L_N - c}{3L_N + c}} = \pm\sqrt{5\pi}\sqrt{\frac{L_N - \sqrt{\left(a - R_{in}\left(\cos(\theta) - 1\right)\right)^2 + R_{in}^2 \sin^2(\theta)}}{3L_N + \sqrt{\left(a - R_{in}\left(\cos(\theta) - 1\right)\right)^2 + R_{in}^2 \sin^2(\theta)}}} \tag{5.13}$$

Equation 5.13 can be substituted in $K(\alpha)$ and thus entered in Eq. 5.10 to find the following solution for F:

$$F = \frac{16 E_N I_N \pi^2}{(3L_N + c)^2} = \frac{16 E_N I_N \pi^2}{\left(3L_N + \sqrt{\left(a - R_{in}\left(\cos(\theta) - 1\right)\right)^2 + R_{in}^2 \sin^2(\theta)}\right)^2} \tag{5.14}$$

Referring to Fig. 5.5(d), the torque generated by the negator can be written as:

$$M_N = F_t R_{in} = F \cos(\pi/2 - \theta - \beta) R_{in} \tag{5.15}$$

where

$$\beta = \arctan\left(\frac{R_{in}\sin(\theta)}{a + R_{in} - R_{in}\cos(\theta)}\right) \tag{5.16}$$

5.4.4. Negator Trend and Reference Behavior

To realize the negators in spring steel, it may be convenient to cut a commercial sheet with a pre-defined size instead of trying to machine a precise thickness. In this work the adopted strips are characterized by $b_N = 2.12$ mm, $t_N = 0.26$ mm and $L_N = a + f = 40 + 6.5 = 46.50$ mm. The effect of the single negator for an imposed rotation $\theta = 0.7$ rad can be computed from Eq. 5.15 and then verified through 1D FEA in ANSYS.

To analyze pre-buckled beams starting from their initial undeformed state, a multi-step

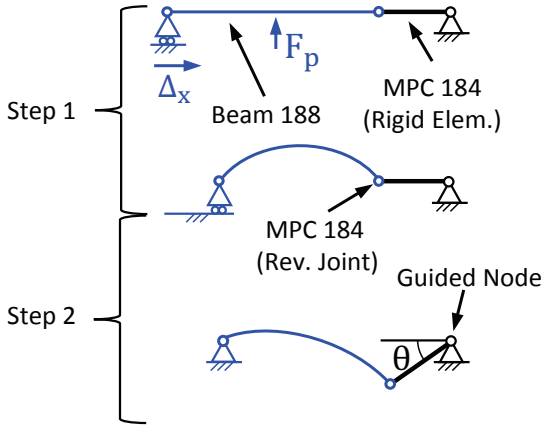

(a) Negator FE model - multi-step analysis.

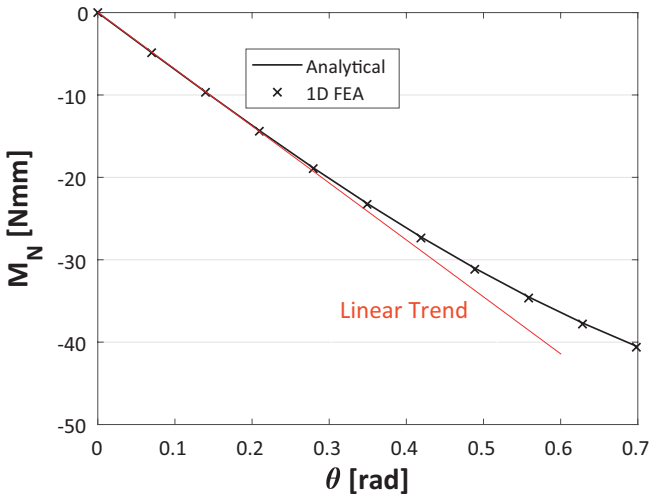

(b) Comparison between analytical and FEA results ($n_N = 2$).

Figure 5.6: Negator Testing.

FEA simulation is needed: i) in the first load-step a displacement $\Delta_x = f$ and a perturbation force F_p are applied to the beam, as in Fig. 5.6(a), to obtain the pre-buckled state with a limited number of numerical iterations (substeps); ii) in the second load-step, F_p is removed and the central node is guided in a rotation θ. All the beams are meshed with *Beam 188* elements (quadratic shape functions). *MPC 184* rigid elements are used both to model the rigid inner ring and, by setting *Key-opt(1)=6*, to create the revolute joint between the negator and the inner ring (see Fig. 5.6(a)).

A comparison between analytical and FEA data, scaled on the basis of $n_N = 2$, is reported in Fig. 5.6(b). The following considerations can be made:

- the analytical and FEA results match very well, as visible in Fig. 5.6(b). The RMS

error between the functions is equal to 0.05 Nmm;

- the load-deflection law shows a remarkable loss in linearity for $\theta > 0.28$ rad.

Therefore, the negators can be balanced with a linear positive stiffness structure, such as the Archimedean Spiral [181–184], for $\theta \leq 0.28$ rad. The dimensional synthesis can be performed with simple analytical models in a limited time. For Larger deflection range, i.e. $\theta > 0.28$ rad, a customized torsional spring may be the best option for achieving a complete balancing. In the following, the behavior in Fig. 5.6(b) is reversed in the positive plane and then used as reference for the shape optimization. Adopting the same notation as in Eq. 5.5, the resulting coefficients are $a_1 = 75.32$ Nmm/rad and $a_2 = -23.94$ Nmm/rad^2.

5.5. Overview of the Design Approach

The design of the nonlinear torsional CMs is addressed through 1D FEA shape optimizations. The aim is to design a spring that generates a desired nonlinear load-displacement behavior, defined by coefficients a_1 and a_2 (see Secs. 5.3.4 and 5.4.4). Both the springs are formed by inner and outer rings and employ spline beams as connection elements between the rings. A system of n_b flexible beams in parallel spring configuration facilitates the designer since each spring experiences an equal part of the total applied load. Therefore, n_b can be selected according to encumbrances, material properties and torque magnitude. Considering a deflection range of $[-0.26, 0.26]$ rad and the presence of physical limiters (see Fig. 5.2(c)), the first CM is composed of four identical spline beams in order to avoid contacts between bodies. As for the second CM, the negators limit the available space, thus only two spline beams are adopted for compensating the system in the range $[0, 0.7]$ rad.

To limit the computational cost, a single spline beam is modeled in FEA and the results of each simulation are then scaled on the basis of $n_b = 4$ and $n_b = 2$ in the first and second case study respectively.

During the optimization, each spring candidate is subjected to the same angular displacement (equivalent to the specified angular range). The simulations are conducted in ANSYS (framework D), as indicated in Tab. 2.3, due the absence of rigid parts and/or particular dynamic conditions. In line with Sec. 4.6, to solve optimization problems with a large number of design variables (see Sec. 5.6), a Matlab GA and a parametric ANSYS APDL script are

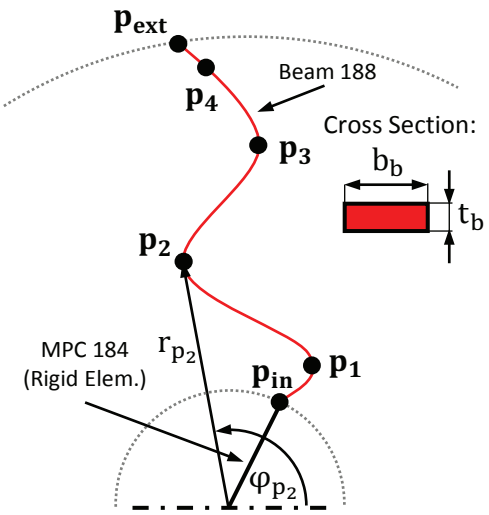

Figure 5.7: Parametric FE model used for the optimizations.

linked together. Given as input a desired torque-deflection law, the framework will output an appropriate CM configuration. Details about the optimization flowchart and the convergence criteria can be found in Sec. 4.6.3.

5.6. General Problem Formulation

Referring to Fig. 5.7, the neutral axis of the flexible beams is defined by a cubic spline [71] and by a set of four interpolation (red) points, p_i, $i = 1, ..4$), in addition to the extreme (black) points p_{in} and p_{ext}, placed on the inner (R_{in}) and outer (R_{ext}) rigid rings. The number of interpolation points has been selected after a series of preliminary design studies, aimed at finding the simplest configuration that matches the functional requirements for the applications.

The shape optimization is performed by varying the position of the control points and the cross section's size. Therefore, by adopting a rectangular constant cross section along the path of the beams, the total number of design variables is 12:

- r_{p_i}, $i = 1, .., 4$ (parametric points radius);
- φ_{p_i}, $i = 1, .., 4$ (parametric points angle);
- $\varphi_{p_{in}}$, $\varphi_{p_{ext}}$ (extreme points angle);
- b_b and t_b (beam's cross section dimensions).

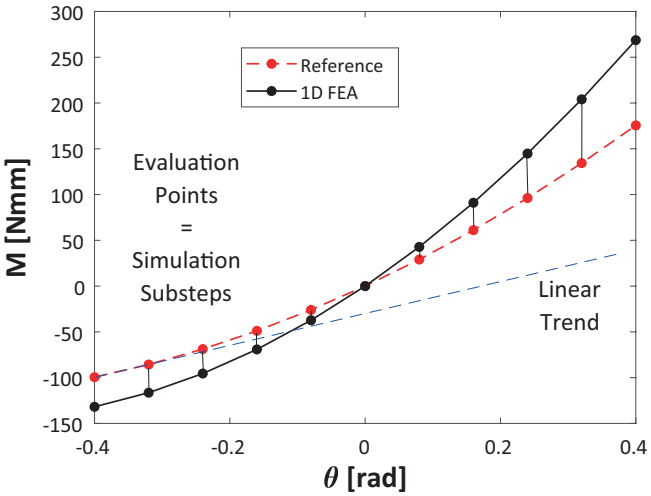

Figure 5.8: Graphical representation of the error evaluation principle.

Therefore, the optimization problem is defined as follows:

$$\textbf{Min.} \quad e_M = \sqrt{\frac{1}{r}\sum_{i=1}^{r}\left[M_{FEA_i} - M_{t_i}\right]^2} \tag{5.17}$$

$$\textbf{Constraint} \rightarrow \quad \sigma < \sigma_s \tag{5.18}$$

where e_M is the RMS value of the error between the single FEA response (i.e. M_{FEA}) and target behavior (i.e. M_t, defined by coefficients a_1 and a_2), computed in a series of $r = 10$ simulation substeps. Instead of evaluating the error over the entire load-displacement function, the behaviors are compared in r discrete points, as shown in Fig. 5.8. The constraint on the maximum stress is added to the algorithm to exclude all the candidates that exceed the yield strength during the simulation. The GA is run with 100 generations and a population size of 30 candidates for each generation. The Matlab solver stops either when the average relative change in the value of e_M is less than or equal to the function tolerance (10^{-4} Nmm) or if the maximum number of iterations exceeds 3000. Regarding the FE model, BSPLIN command is used to define the geometry, which is then discretized by *Beam 188* elements as shown in Fig. 5.7. The beam is fully constrained at one node (the upper extremity, i.e. p_{ext}) and guided in a pure rotation thanks to a rigid body element (*MPC 184*) between the the lower extremity, p_{in}, and a master node placed in the center of the spring. See Appendix D for APDL code used in this work.

5.7. Numerical Results - Optimal Configurations

The GA converged after 96 ± 2 and 90 ± 4 iterations in the first and second case study respectively. Allowed range of variation for each design variable and optimal values are summarized in Tab. 5.1. Figure 5.9 shows the FEA stress fields on the deformed shape of both the torsional CMs. The optimal torque-deflection relationships are shown in Figs. 5.10(a) and 5.10(b), where the matching with the reference behaviors can be easily verified. With reference to Eq. 5.18, the final configurations are affected by a RMS error equal to 2.16 Nmm and 0.21 Nmm. This variance is justified by the evident difference in the torque levels reached in the CMs (200 Nmm vs 40 Nmm).

The behaviors can be scaled with respect to $E_b J_b / L_b$, where $J = b_b t_b^3/12$ and L_b represents the length of each spline beam.

5.8. Experimental Validations

Physical prototypes have been fabricated and tested to validate the predicted torque-deflection behaviors. The CTE has been tested in dynamic conditions to underline the effect of the material damping and thus facilitate the development of a proper controller for the overall VSA. Concerning the compensation spring, the experiment has been performed by considering the overall zero torque CM to verify the accuracy of the designed part.

According to the calculations, the quadratic CTE is made of 3D printed ABS. To obtain high precision, the compensation spring is manufactured by means of a 3-axis Haas DM1 CNC machine using polypropylene, whereas the negators are cut from a commercial spring steel sheet (0.26 mm thick). The negator pins are realized by direct contact of the thin beam against "V" sockets cut into the inner and outer rings.

5.8.1. #Case Study I - Dynamic Test

The optimal configuration is tested by means of the experimental setup shown in Fig. 5.11. The system is composed of a Dynamixel MX-28AR servo, an ATI commercial torque sensor, and a set of rigid 3D printed connection members. The CTE is fixed to the ATI sensor by means of the red flange, whereas the inner ring is actuated by the servo thanks to the connection (gray) member in Fig. 5.11. A LabView interface have been exploited to control the

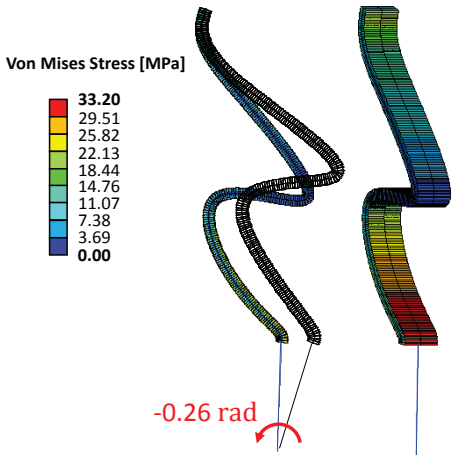

(a) Quadratic CTE: 1D FEA deformed shape and stress for $\theta = -0.26$ rad.

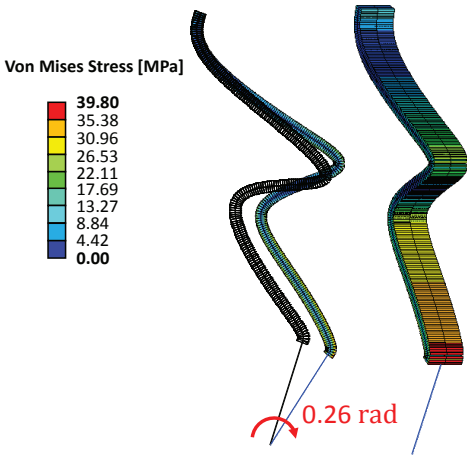

(b) Quadratic CTE: 1D FEA deformed shape and stress for $\theta = 0.26$ rad.

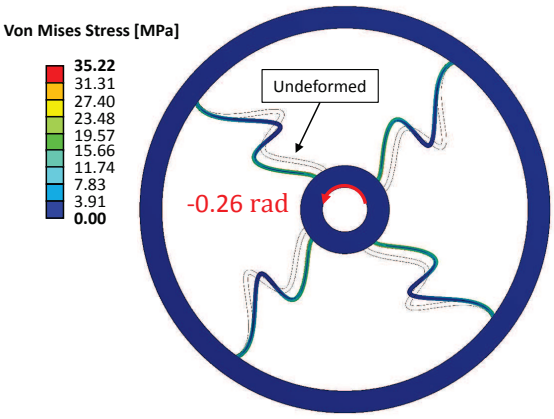

(c) Quadratic CTE: validation with 3D FEA for $\theta = -0.26$ rad.

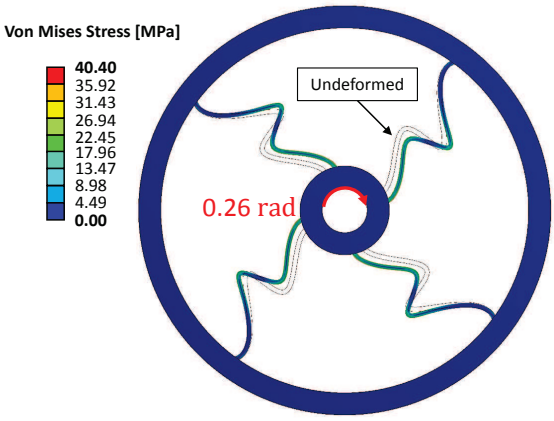

(d) Quadratic CTE: validation with 3D FEA for $\theta = 0.26$ rad.

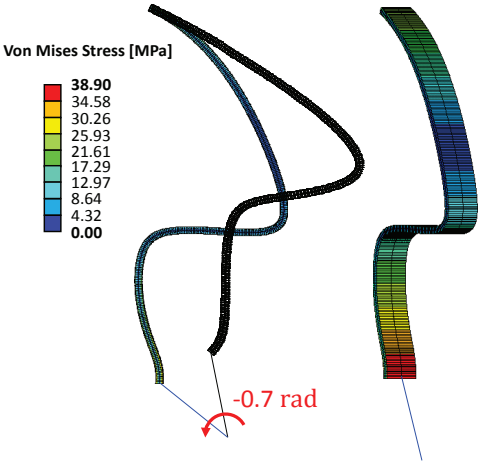

(e) Compensation spring: 1D FEA deformed shape and stress for $\theta = -0.7$ rad.

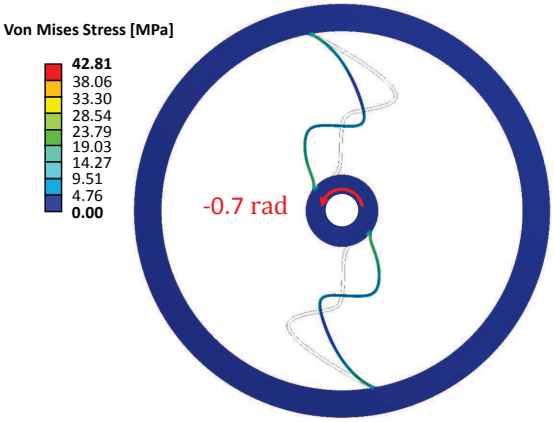

(f) Compensation spring: 3D FEA validation for $\theta = -0.7$ rad.

Figure 5.9: Optimal FE models.

Table 5.1: Optimal dimensions of the nonlinear torsional CMs.

Design Variable	Range	Opt. Value
	Quadratic CTE	
b_b	$[2.5, 7]$ mm	3.41 mm
t_b	$[0.8, 5]$ mm	1.00 mm
r_{p_1}	$[10.5, 13]$ mm	11.33 mm
r_{p_2}	$[1.5, 4.5]$ mm	23.19 mm
r_{p_3}	$[3, 7]$ mm	25.50 mm
r_{p_4}	$[3, 6.5]$ mm	35.36 mm
φ_{p_1}	$[0.8, 2.5]$ rad	1.33 rad
φ_{p_2}	$[0.8, 2.5]$rad	1.70 rad
φ_{p_3}	$[0.8, 2.5]$ rad	1.37 rad
φ_{p_4}	$[0.8, 2.5]$ rad	1.71 rad
$\varphi_{p_{in}}$	$[0.8, 2.5]$ rad	1.27 rad
$\varphi_{p_{ext}}$	$[0.8, 2.5]$ rad	1.73 rad
	Compensation Spring	
b_b	$[1, 10]$ mm	3.81 mm
t_b	$[0.5, 5]$ mm	0.80 mm
r_{p_1}	$[11, 21]$ mm	13.29 mm
r_{p_2}	$[22, 26]$ mm	25.00 mm
r_{p_3}	$[27, 32]$ mm	28.21 mm
r_{p_4}	$[33, 49]$ mm	35.00 mm
φ_{p_1}	$[1, 2.5]$ rad	1.61 rad
φ_{p_2}	$[1, 2.5]$ rad	1.56 rad
φ_{p_3}	$[1, 2.5]$ rad	1.40 rad
φ_{p_4}	$[1, 2.5]$ rad	1.13 rad
$\varphi_{p_{in}}$	$[1, 2.5]$ rad	1.77 rad
$\varphi_{p_{ext}}$	$[1, 2.5]$ rad	1.75 rad

servo position and to acquire the data (i.e. reaction torque) from the sensor. A sinusoidal motion is imposed with the aim of investigating the dynamic response of the nonlinear CTE in the operative range. The results of the dynamic test are shown in Fig. 5.12, with an imposed sinusoidal motion with frequency equaling, respectively, to 1 Hz and 5 Hz. The experimental torque-deflection relationship is visible in Fig. 5.12(c), confirming the reliability of the FEA output. The operative range, $[-0.26, 0.26]$ rad, is reached without failure, which occurred with an angular deflection of 0.32 rad. The differences between numerical and experimental results are mainly due to error in the 3D printing process, causing imperfection on the beam's cross section (b_b and t_b). In addition, the dynamic conditions adopted for the experimental characterization allow to register the effect related to the material damping, as it is clearly

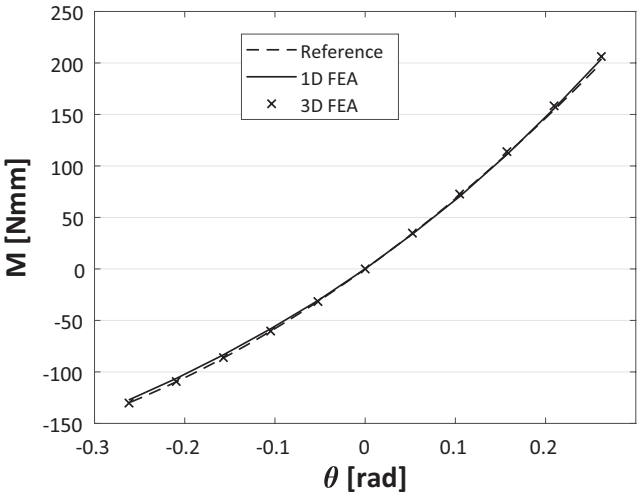

(a) Quadratic CTE torque-deflection relationship.

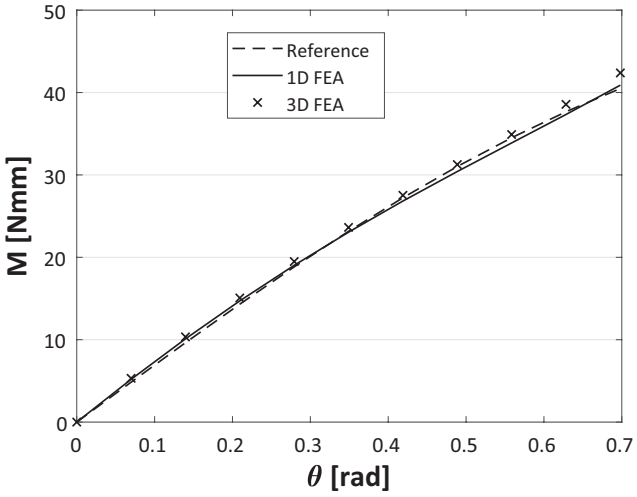

(b) Compensation spring torque-deflection relationship.

Figure 5.10: Performance of the optimal configurations.

highlighted in Fig. 5.12(c), where the hysteresis effect during loading/unloading cycles is visible. This issue must be properly managed via the VSA controller during the functioning.

5.8.2. #Case Study II - Static Test

The accuracy of the machined parts can be seen in Fig. 5.13, which shows a complete balancing of the zero torque CM for different angular positions in the range $[0, 0.7]$ rad. The CM is tested with the experimental setup shown in Fig. 5.14. The system is composed of a worm-wheel gearset that acts on a shaft, an Omega TQ103-50 torque sensor and a US Dig-

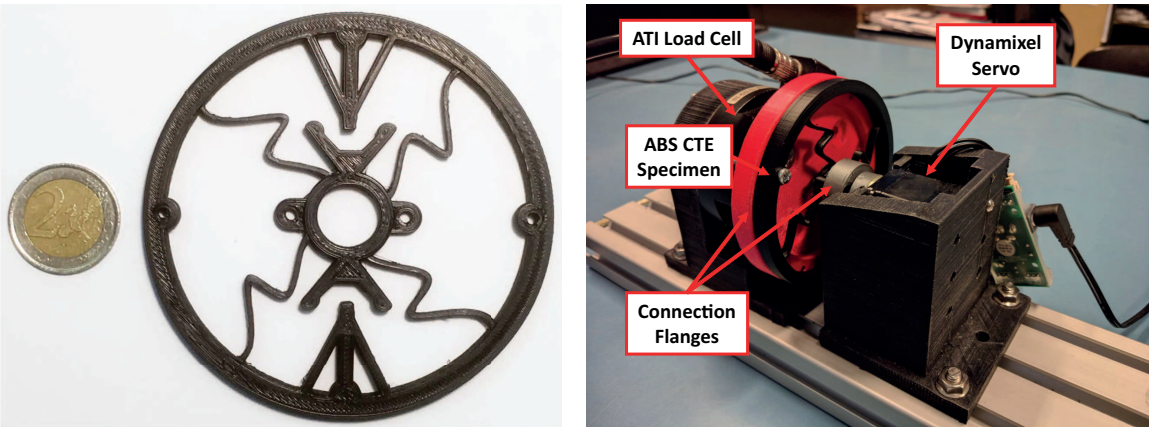

(a) Phtsical 3D printed prototype. (b) Dynamic test.

Figure 5.11: CTE physical prototype and experimental rotational setup.

ital E2-500-375-IE-H-D-B optical encoder. A shape coupling is used to connect the shaft extremity with the inner ring. The outer ring is then fixed to the ground through a connection member (shown in blue in Fig. 5.14). The shaft is manually actuated and both angular position and reaction torque are acquired using a LabView interface. The results of the test are plotted in Fig. 5.15, together with the FEA output obtained from a final simulation on the overall zero torque CM (see Appendix E for the APDL code). FEA and experimental torque-deflection relationships show good agreement, confirming the accuracy of the proposed modeling approach. The discrepancy between the data is due to:

- small defects in the machined parts;
- uncertainties in the material properties;
- the nonideal pins (contact between the negators and the "V" sockets);
- the user's irregular action during the manual deflection of the inner ring.

5.9. Summary

This chapter presents a general efficient method for the design of torsional CMs characterized by a pre-defined torque-deflection law. Spline beams are used as building blocks to achieve large deflections and introduce the nonlinear behavior. According to Tab. 2.2, 1D FEA is selected to solve compliant curved beams in a limited time. In line with Chap. 3, a

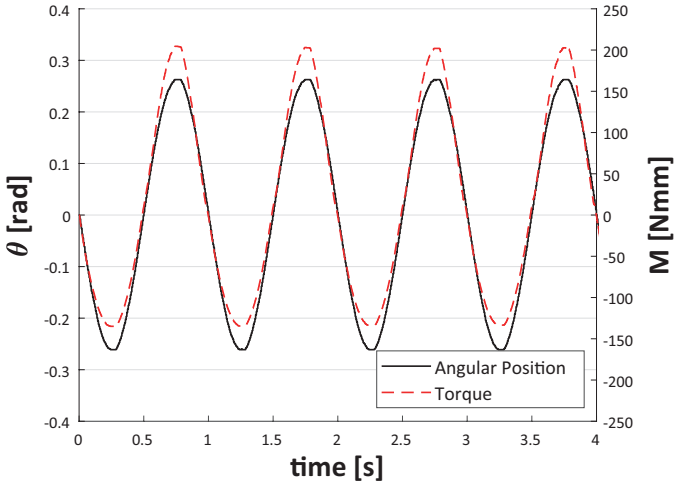

(a) Dynamic response at $f = 1$ Hz.

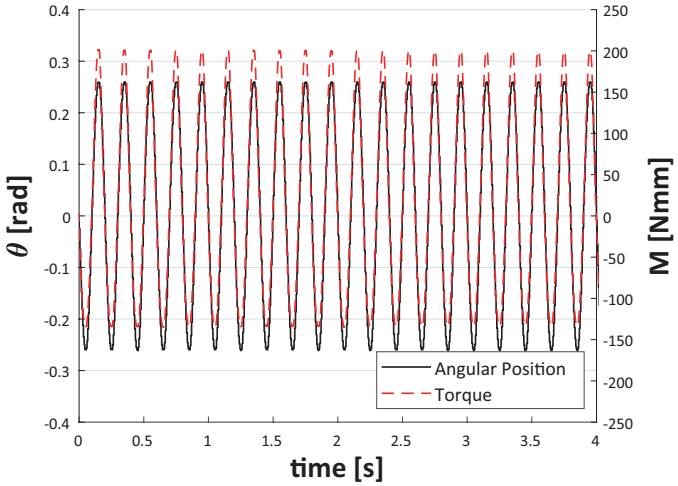

(b) Dynamic response at $f = 5$ Hz.

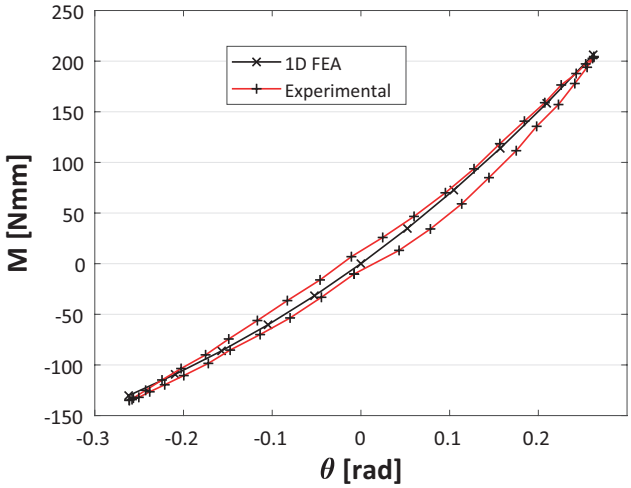

(c) Torque-deflection relationship.

Figure 5.12: CTE experimental results.

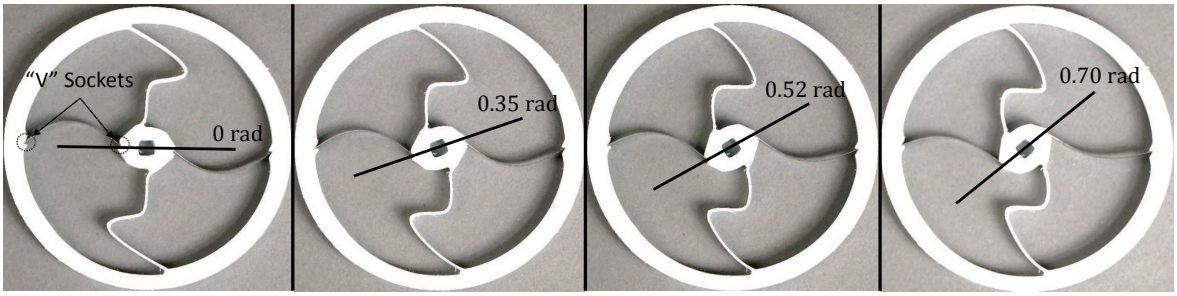

Figure 5.13: Zero torque CM - static balancing in different angular positions.

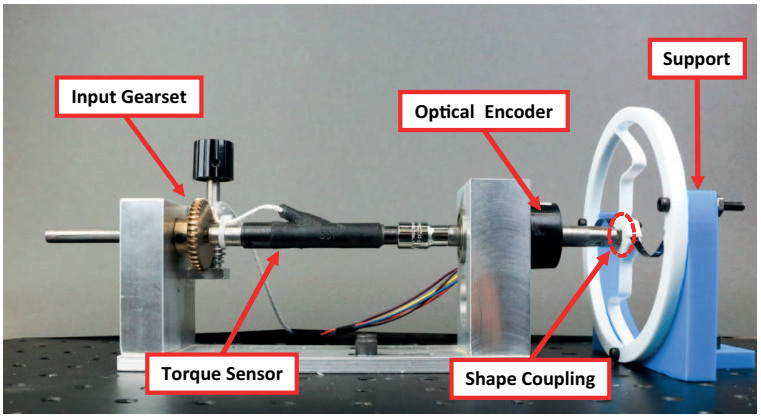

Figure 5.14: Experimental rotational setup for the static test.

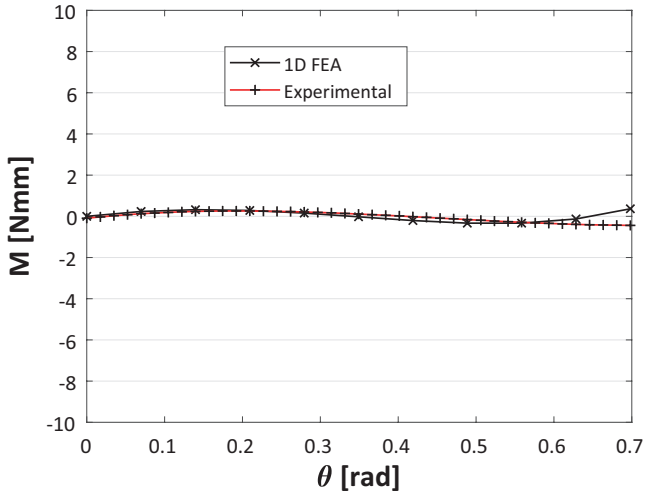

Figure 5.15: Comparison between predicted and measured behaviors.

framework comprising Matlab and ANSYS APDL is developed to solve the shape optimization problem.

To test the validity of the approach, two special-purpose torsional CMs are designed

resorting to a GA linked to a parametric FE model. The first case study deals with a quadratic CTE to be implemented in antagonistic VSAs, whereas the second case study focuses on the synthesis of a nonlinear CM capable of balancing the torsional contributes of pre-buckled straight beams.

After preliminary discussions about the design targets, the chapter reports the results obtained via the framework D. Both the optimizations converged in a limited computational time, being 1.5 s the mean value required to solve the single candidate (with 220 *Beam 188* elements).

Physical prototypes of the torsional CMs are fabricated via 3D printing and CNC machining, and subsequently tested for validation purpose. Generally, the experimental results confirm that the systems behave as expected. Concerning the CTE, the operative conditions imposed for the test highlighted a nonnegligible hysteresis due to the material damping.

Chapter 6

Performance Study of a Contact-Aided Cross-Axis Flexural Pivot

6.1. Contact-Aided Pivots as Asymmetrical Compliant Transmission Elements

This chapter reports the study of a planar CAFP comprising an additional contact pair. The proposed device may be useful for applications requiring a revolute joint that behaves differently when deflecting clockwise/anti-clockwise. In particular, the presence of the contact pair reduces the free length of one flexures, resulting in a considerable increment of the overall joint stiffness. Note that, as specified in [185], referring to contact-aided CMs, contacts can occur between:

1. different regions of the same flexible member (self-contact);
2. parts of different flexible members;
3. part(s) of a flexible member and rigid obstacle(s);
4. parts of different rigid bodies.

Depending on the application, contacts can be exploited for different purposes, such as to limit the operating range of the system or to achieve a specific path of the end-effector by guiding the deflection of the flexible members [68, 186]. In the current case study, the adopted contact-aided solution falls within the third category.

The contact-aided CAFP concept may be employed to design bio-inspired robotic wrists [188], namely joints mimicking the natural asymmetry of the human counterpart. The osteokinematics of the human wrist are limited to 2 DOFs, i.e. the ulnar-radial deviations and the flexion-extension, respectively on the frontal and sagittal planes, as shown in Fig. 6.1(a) (taken from [187]). It can be easily noted that the maximal ulnar-deviation (about 0.52 rad)

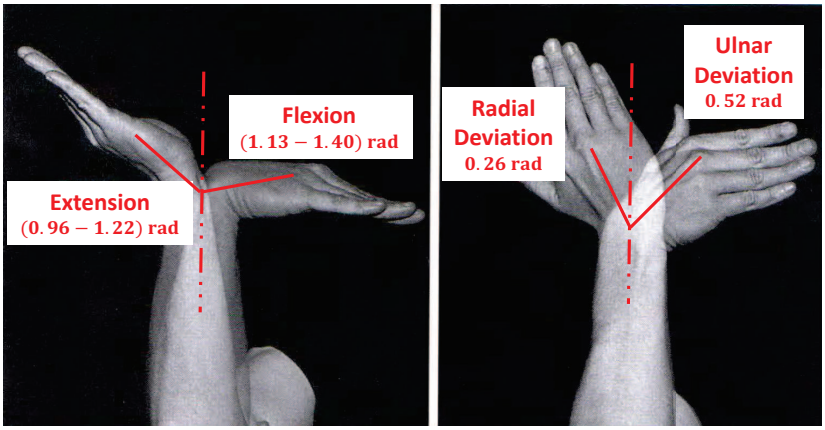

(a) Osteokinematics of the wrist: flexion and extension, ulnar and radial deviations [187].

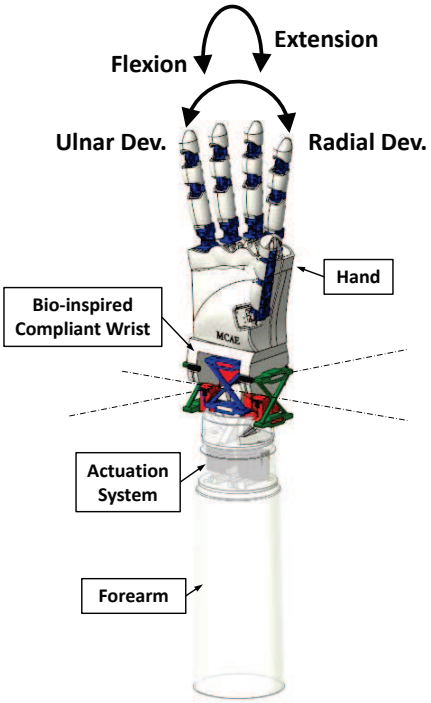

(b) CAD of the bio-inspired wrist.

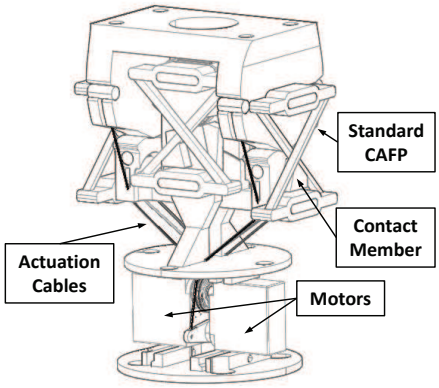

(c) Detailed view of the wrist.

Figure 6.1: Conceptual design of a bio-inspired wrist employing the contact-aided CAFP.

normally is double that of the radial deviation (about 0.26 rad). Also the flexion-extension module presents a nonnegligible asymmetric motion (i.e. from $1.13 - 1.40$ rad to $0.96 - 1.22$ rad), as clearly highlighted in Fig. 6.1(a). Furthermore, as specified in [189] and experimentally proved in [189], the human wrist exhibits evident differences in terms of passive stiffness (i.e. the contribute due to the presence of the muscles in the forearm) between the ulnar and radial deviation and the flexion and extension movements. The proposed contact-aided CAFP offers the required asymmetry and ensures limited encumbrances, thus high

adaptability to complex mechanical systems. An example of possible design embodiment of a robotic wrist with the contact-aided CAFP is shown in Figs. 6.1(b) and 6.1(c).

By stepping back to the preliminary design step, this chapter aims at characterizing the contact-aided pivot under different load cases. The study is performed with the CBCM technique and the results are compared to the ones achieved via 1D FEA. Treating contact analysis in CMs using the CBCM is a new contribution to the field and this work seeks to prove its efficiency, both in terms of results accuracy and computational cost. Two practical aspects guided this research:

- the CBCM closed-form formulation allows to accurately capture the large deflections behavior of beam-based CMs (several examples may be found in [22]), resulting in a computational efficiency higher than the 1D FEA, as it can be seen in Sec. 2.3;
- as a discretization-based approach, the CBCM can be combined with several penalty-based contact algorithms [190]. The mathematical formulation is defined by the user and additional features can be coded.

In the following sections, frameworks C and D (see Tab. 2.3) are combined for testing the CAFP performances in terms of rotational stiffness, parasitic shift and maximum stress, with different combinations of geometrical aspect ratios and contact extensions. Numerical results are then compared to experiments for validation purpose. As an output of the parametric studies, different performance maps are produced to enable designers to visualize the advantages/limits of the joint.

6.2. Pivot Geometrical Configurations

The proposed device, whose principle schematic is represented in Fig. 6.2, is composed of two disconnected independent beams located in parallel planes. Such beams are modeled with constant rectangular cross section in order to respect the CBCM requirements (see Tab. 2.2). Therefore, the pivot geometry is completely defined by h, L, w_1, w_2, b and t, namely the pivot height, the flexure length, the lower and upper width, and the cross section dimensions. The semi-angle between flexures is given by the following trigonometric formula:

$$\beta = \arcsin((w_1 + w_2)/2L) \tag{6.1}$$

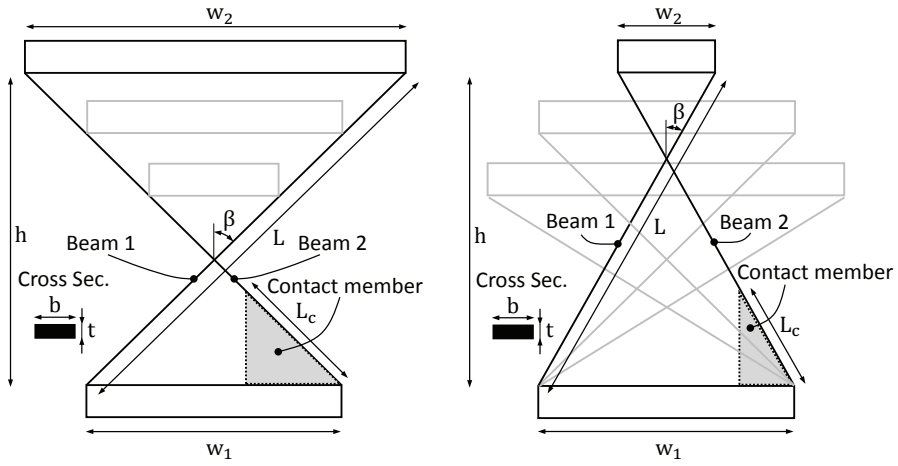

(a) Configurations with $\beta = \text{const}$. (b) Configurations with $L = \text{const}$.

Figure 6.2: Contact-aided parametric CAFP.

According to Figs. 6.2(a) and 6.2(b), and to Eq. 6.1, given w_1, the aspect ratio, defined as $AR = w_2/w_1$, can be varied by assuming a constant angle (i.e. $\beta = \text{const}$) or a constant flexure length (i.e. $L = \text{const}$). As evident from Fig. 6.2(b), the second option is characterized by a minor variation range.

To include the contact in the analysis, a purposely shaped contact member [191], shown in Figs. 6.2 and 6.3, is introduced at the base of the pivot. The primary effect is the increment of the total CAFP stiffness. As visible in Figs. 6.3(a) and 6.3(b), a pure moment M applied on the upper rigid body provides a deflection $\theta^{'} < \theta$ whenever the contact is considered, due to an evident reduction, in the order of L_c, of the flexure *(Beam 2)* free length. Also the parasitic shift, identified by module $s = \overline{PP_0}$ and phase ϕ, as in Fig. 6.3, is influenced by the presence of the contact.

6.3. Overview of the Performance Study

The behavior of the contact-aided pivot is investigated for different combinations of AR (by considering $\beta = \text{const}$ or $L = \text{const}$) and L_c. The DOE+RSM techniques are used to map the design domain with a limited number of sampling points. Three load conditions are tested:

1. a pure rotation applied to the output link;

2. a horizontal force applied to the output link;

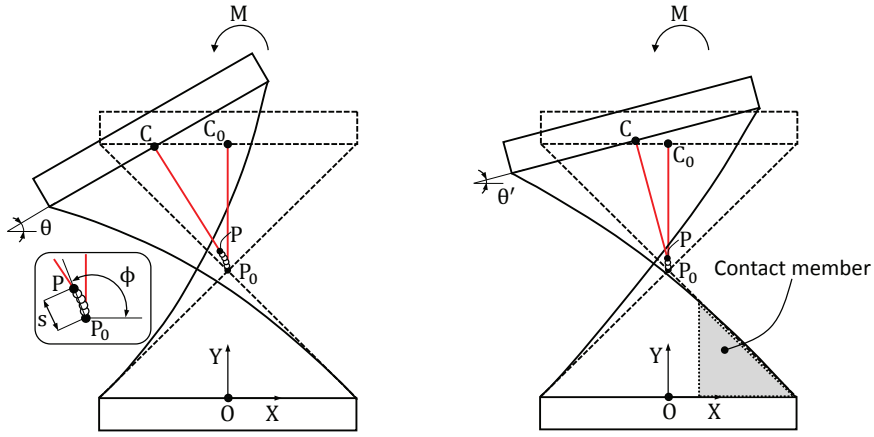

(a) Standard CAFP - deflected configuration.

(b) Contact-aided CAFP - deflected configuration.

Figure 6.3: Effect of the contact member on the pivot deflection.

3. a rotation applied to a constrained point placed in the initial intersection between the flexures (i.e. P_0 in Fig. 6.3).

As a result of the parametric studies, different performance maps for joint stiffness, parasitic shift and maximum stress are provided. As previously introduced, the numerical data are obtained via the frameworks C and D allowing the use of CBCM and 1D FEA. To ensure consistency between the data, the ANSYS penalty-based contact formulation is used to analyze the interaction between the bodies in both the models. To validate the numerical methods, two experimental setups are implemented, providing the rotational stiffness and the parasitic shift respectively.

6.4. CBCM Formulation

6.4.1. Static Modeling Under Planar Loads

Following the work reported in [22], a CAFP's flexure can be discretized into N elements of equal length $L_{el} = L/N$, each of them locally described by BCM equations [21, 94]. Assuming a constant rectangular cross section, defined by b and t, the load-deflection char-

acteristic of the i-th element, shown in Fig. 6.4, is given by the following relations:

$$\begin{bmatrix} f_i \\ m_i \end{bmatrix} = \begin{bmatrix} 12 & -6 \\ -6 & 4 \end{bmatrix} \begin{bmatrix} \delta_{yi} \\ \alpha_i \end{bmatrix} + p_i \begin{bmatrix} 6/5 & -1/10 \\ -1/10 & 2/15 \end{bmatrix} \begin{bmatrix} \delta_{yi} \\ \alpha_i \end{bmatrix} + p_i^2 \begin{bmatrix} -1/700 & 1/1400 \\ 1/1400 & -11/6300 \end{bmatrix} \begin{bmatrix} \delta_{yi} \\ \alpha_i \end{bmatrix} \tag{6.2}$$

$$\delta_{xi} = \frac{t^2 p_i}{12 L_{el}} - 0.5 \begin{bmatrix} \delta_{yi} & \alpha_i \end{bmatrix} \begin{bmatrix} 6/5 & -1/10 \\ -1/10 & 2/15 \end{bmatrix} \begin{bmatrix} \delta_{yi} \\ \alpha_i \end{bmatrix} - p_i \begin{bmatrix} \delta_{yi} & \alpha_i \end{bmatrix} \begin{bmatrix} -1/700 & 1/1400 \\ 1/1400 & -11/6300 \end{bmatrix} \begin{bmatrix} \delta_{yi} \\ \alpha_i \end{bmatrix} \tag{6.3}$$

where δ_{xi}, δ_{yi} and α_i are the displacements and rotation of the i-th element at node i (referred to the local i-th coordinate system, placed in the node i-1 as shown in Fig. 6.4(b)) normalized with respect to L_{el}, and p_i, f_i and m_i are the forces and moment normalized with respect to EJ/L_{el}^2 and EJ/L_{el}, where E is the material Young's modulus and $J = bt^3/12$ is the cross section moment of inertia. The first terms of Eqs. 6.2 and 6.3 define the linear approximation, which is valid for describing the behavior of a cantilever beam under tip loads in case of small deflections. The CAFP's behavior is well captured in the middle range of deflections by applying the BCM equations on the flexures, i.e. by using a unique element $L_{el} = L$ for each of the beams, as proved by [74, 76]. The modeling of two series of N elements for the whole CAFP's structure leads to a remarkable increment in the number of variables. With reference to Fig. 6.4(a), being known any combination of three parameters among the global external loads (i.e. F_x, F_y and M) and the global displacements (i.e. Δ_x, Δ_y and θ), the total number of variables to be determined for solving the CBCM problem is $12N$+7, namely:

- δ_{xi}, δ_{yi}, α_i, p_i, f_i, m_i, for $i = 1, .., 2N$ ($12N$ entities);
- the remaining set containing the undefined global loads and/or displacements (3 entities);
- the coordinate of point A (x_A, y_A) and point B (x_B, y_B) with respect to the coordinate systems $O_{N+1}x_{N+1}y_{N+1}$ and $O_1x_1y_1$ respectively (4 entities).

Therefore, to ensure a closed-form solution for the problem, $12N$+7 relations between the

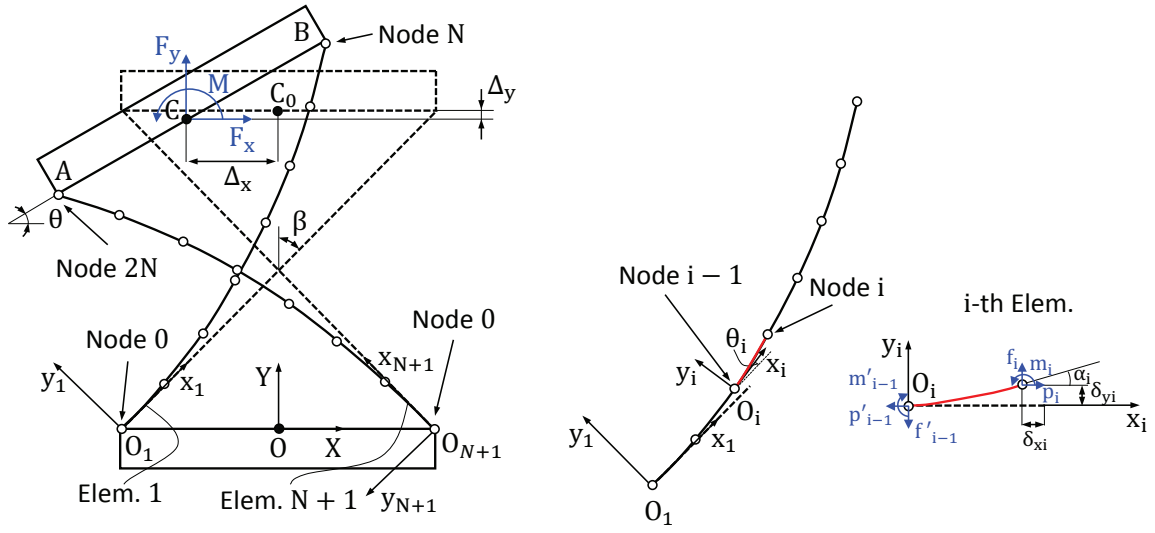

(a) CAFP schematic: global loads and displacements.

(b) Analysis of the i-th element.

Figure 6.4: CBCM - details about the model.

aforementioned variables have to be defined. Besides the $6N$ BCM load-deflection characteristics (3 for each of the $2N$ CAFP elements), expressed by Eqs. 6.2 and 6.3, the remaining relations refer to the local and global equilibrium and to the geometrical constraints.

By analyzing the free-body diagram proposed in Fig. 6.4(b), the following local static equilibrium equations for the i-th element hold:

$$\begin{bmatrix} f'_{i-1} \\ p'_{i-1} \\ m'_{i-1} \end{bmatrix} = \begin{bmatrix} 1 & 0 & 0 \\ 0 & 1 & 0 \\ (1+\delta_{xi}) & -\delta_{yi} & 1 \end{bmatrix} \begin{bmatrix} f_i \\ p_i \\ m_i \end{bmatrix} \tag{6.4}$$

where p'_{i-1}, f'_{i-1}, m'_{i-1} are the loads applied by the (i-1)-th element to the i-th element at node i-1, mathematically obtained by applying a vectorial rotation of α_{i-1} (i.e. the angle between $O_i x_i y_i$ and $O_{i-1} x_{i-1} y_{i-1}$) to the tip loads p_{i-1}, f_{i-1} and m_{i-1}:

$$\begin{bmatrix} f_{i-1} \\ p_{i-1} \\ m_{i-1} \end{bmatrix} = \begin{bmatrix} \cos\alpha_{i-1} & -\sin\alpha_{i-1} & 0 \\ \sin\alpha_{i-1} & \cos\alpha_{i-1} & 0 \\ 0 & 0 & 1 \end{bmatrix} \begin{bmatrix} f'_{i-1} \\ p'_{i-1} \\ m'_{i-1} \end{bmatrix} \tag{6.5}$$

By considering the angle $\theta_i = \sum_1^{i-1} \alpha_i$ between $O_i x_i y_i$ and $O_1 x_1 y_1$, the equilibrium equation

of the i-th element can be re-written as follows:

$$\begin{bmatrix} f_1 \\ p_1 \\ m_{i-1} \end{bmatrix} = \begin{bmatrix} \cos\theta_i & -\sin\theta_i & 0 \\ \sin\theta_i & \cos\theta_i & 0 \\ (1+\delta_{xi}) & -\delta_{yi} & 1 \end{bmatrix} \begin{bmatrix} f_i \\ p_i \\ m_i \end{bmatrix} \quad i = 2, .., N \tag{6.6}$$

and, for the second CAFP's flexure, which refers to $O_{N+1}x_{N+1}y_{N+1}$ as visible in Fig. 6.4(a), the following relation holds:

$$\begin{bmatrix} f_{N+1} \\ p_{N+1} \\ m_{i-1} \end{bmatrix} = \begin{bmatrix} \cos\theta_i & -\sin\theta_i & 0 \\ \sin\theta_i & \cos\theta_i & 0 \\ (1+\delta_{xi}) & -\delta_{yi} & 1 \end{bmatrix} \begin{bmatrix} f_i \\ p_i \\ m_i \end{bmatrix} \quad i = N+2, .., 2N \tag{6.7}$$

Equations 6.6 and 6.7 form 6(N-1) relations of the CBCM system. The global equilibrium can be defined by taking into account the external loads F_x, F_y and M applied at point C, as well as the tip loads of the elements N and $2N$, which can be expressed in the coordinate system $O_1x_1y_1$ and $O_{N+1}x_{N+1}y_{N+1}$ respectively, being:

$$\begin{bmatrix} f_N^* \\ p_N^* \\ m_N^* \end{bmatrix} = \begin{bmatrix} f_1 \\ p_1 \\ m_N \end{bmatrix} = \begin{bmatrix} \cos\theta_N & -\sin\theta_N & 0 \\ \sin\theta_N & \cos\theta_N & 0 \\ 0 & 0 & 1 \end{bmatrix} \begin{bmatrix} f_N \\ p_N \\ m_N \end{bmatrix} \tag{6.8}$$

$$\begin{bmatrix} f_{2N}^* \\ p_{2N}^* \\ m_{2N}^* \end{bmatrix} = \begin{bmatrix} f_{N+1} \\ p_{N+1} \\ m_{2N} \end{bmatrix} = \begin{bmatrix} \cos\theta_{2N} & -\sin\theta_{2N} & 0 \\ \sin\theta_{2N} & \cos\theta_{2N} & 0 \\ 0 & 0 & 1 \end{bmatrix} \begin{bmatrix} f_{2N} \\ p_{2N} \\ m_{2N} \end{bmatrix} \tag{6.9}$$

Therefore, with reference to Fig. 6.5, by rotating $O_1x_1y_1$ and $O_{N+1}x_{N+1}y_{N+1}$ of $-(\pi/2-\beta)$ and $-(\pi/2+\beta)$ respectively, the following 3 equilibrium relations can be added to the

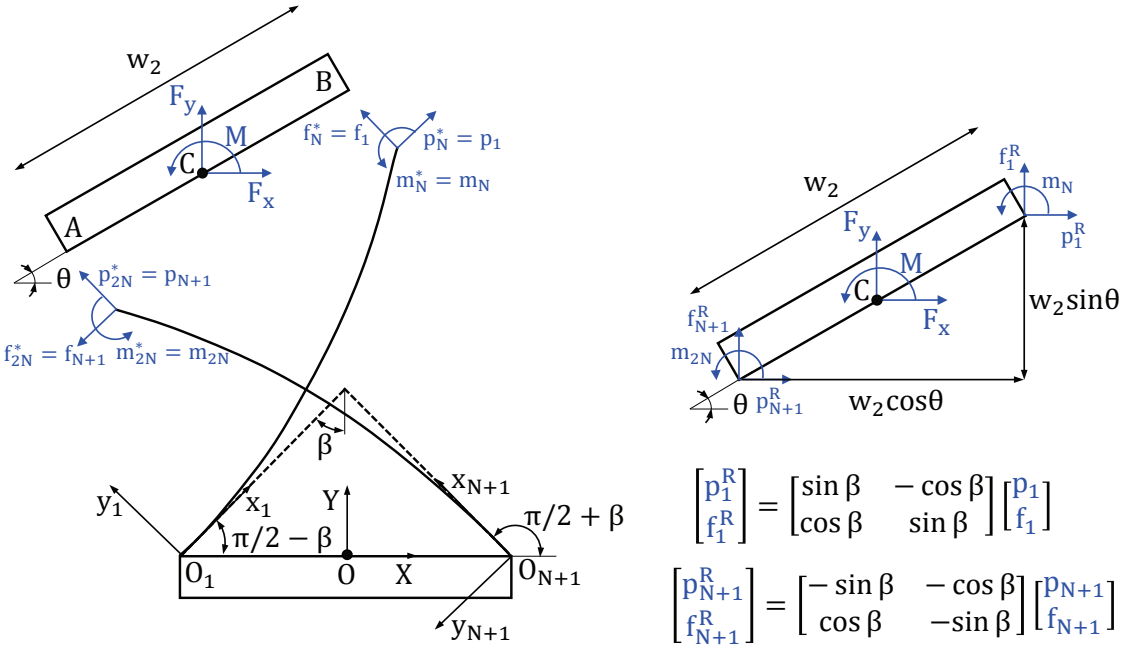

(a) Free-body diagram of the overall CAFP. (b) Detailed view.

Figure 6.5: CAFP global equilibrium.

system:

$$\begin{bmatrix} F_x \\ F_y \end{bmatrix} = \frac{EJ}{L_{el}^2} \begin{bmatrix} \sin\beta & -\cos\beta \\ \cos\beta & \sin\beta \end{bmatrix} \begin{bmatrix} p_1 \\ f_1 \end{bmatrix} + \frac{EJ}{L_{el}^2} \begin{bmatrix} -\sin\beta & -\cos\beta \\ \cos\beta & -\sin\beta \end{bmatrix} \begin{bmatrix} p_{N+1} \\ f_{N+1} \end{bmatrix} \tag{6.10}$$

$$M = \frac{EJ}{L_{el}} m_N + \frac{EJ}{L_{el}} m_{2N} + w_2 \frac{EJ}{L_{el}^2} \begin{bmatrix} \sin\theta & -\cos\theta \end{bmatrix} \begin{bmatrix} -\sin\beta & -\cos\beta \\ \cos\beta & -\sin\beta \end{bmatrix} \begin{bmatrix} p_{N+1} \\ f_{N+1} \end{bmatrix} + \\ 0.5 w_2 \begin{bmatrix} \sin\theta & -\cos\theta \end{bmatrix} \begin{bmatrix} -F_x & -F_y \end{bmatrix} \tag{6.11}$$

For both the pivot's flexures, the overall displacements and rotation at the extremities A and B (see Fig 6.4(a)) are related to the local entities δ_{xi}, δ_{yi} and α_i. Consequently, 6 constraint geometric equations must be enforced in the model. For the first flexure, which refers to $O_1 x_1 y_1$, it is possible to write:

$$\begin{bmatrix} x_B \\ y_B \end{bmatrix} = \sum_{i=1}^{N} \left[\begin{bmatrix} \cos\theta_i & -\sin\theta_i \\ \sin\theta_i & \cos\theta_i \end{bmatrix} \begin{bmatrix} L_{el}(1+\delta_{xi}) \\ L_{el}\delta_{yi} \end{bmatrix} \right] \qquad \theta_N + \alpha_N = \theta \tag{6.12}$$

and, for the second beam, by considering $O_{N+1}x_{N+1}y_{N+1}$, becomes:

$$\begin{bmatrix} x_A \\ y_A \end{bmatrix} = \sum_{i=N+1}^{2N} \left[\begin{bmatrix} \cos\theta_i & -\sin\theta_i \\ \sin\theta_i & \cos\theta_i \end{bmatrix} \begin{bmatrix} L_{el}(1+\delta_{xi}) \\ L_{el}\delta_{yi} \end{bmatrix} \right] \qquad \theta_{2N} + \alpha_{2N} = \theta \tag{6.13}$$

Note that, for i=1 and i=N+1, the local reference coincides with the fixed coordinate systems, $O_1x_1y_1$ and $O_{N+1}x_{N+1}y_{N+1}$, and thus $\theta_1 = 0$ and $\theta_{N+1} = 0$. The global displacements of the output link during the pivot deflection, Δ_x and Δ_y, can be expressed with respect to OXY by the following 2 equations:

$$\begin{bmatrix} \Delta_X \\ \Delta_Y \end{bmatrix} = 0.5 \begin{bmatrix} -\sin\beta & -\cos\beta \\ \cos\beta & -\sin\beta \end{bmatrix} \begin{bmatrix} x_A \\ y_A \end{bmatrix} + 0.5 \begin{bmatrix} \sin\beta & -\cos\beta \\ \cos\beta & \sin\beta \end{bmatrix} \begin{bmatrix} x_B \\ y_B \end{bmatrix} \tag{6.14}$$

The last 2 equations of the model provide the geometric loop closure, written as:

$$\begin{bmatrix} w_1 + w_2\cos\theta \\ w_2\sin\theta \end{bmatrix} = - \begin{bmatrix} -\sin\beta & -\cos\beta \\ \cos\beta & -\sin\beta \end{bmatrix} \begin{bmatrix} x_A \\ y_A \end{bmatrix} + \begin{bmatrix} \sin\beta & -\cos\beta \\ \cos\beta & \sin\beta \end{bmatrix} \begin{bmatrix} x_B \\ y_B \end{bmatrix} \tag{6.15}$$

The overall nonlinear system of $12N$+7 equations can be numerically solved in Matlab environment resorting to a *fsolve* routine. The algorithm provides, as a result of the single analysis, a matrix containing the values of the $12N$+7 variables for a series of r incremental substeps.

6.4.2. Contact Force

Focusing on Figs. 6.2 and 6.3, the interaction between the *Beam 2* and the contact triangular member can be modeled at nodal level by two approaches. The first approach introduces the effect by adding, on the basis of L_c, some additional constraints (i.e. $\delta_{yi} = 0$) to the nodes in the range $[N+1, N+\text{round}\,(N(L_c/L))]$, where "round" defines an operator that returns the integer number of the argument. However, two main issues arise:

1. the bonded condition on those nodes does not allow to capture the real behavior of the beam during the anti-clockwise deflection. In fact, in the contact area, the beam should manifest a limited, but not negligible, curvature. Similar results can be achieved by modeling a CAFP composed of flexures with different length, i.e. $L_1 = L$ and

$L_2 = L - Lc$;

2. the convergence is reached after a large number of numerical iterations and thus the CBCM computational efficiency is considerably decreased.

The second approach operates on nodal forces instead of nodal displacements. Taking as a reference the *Augmented Lagrangian* algorithm from the ANSYS contact library, the contact normal and tangential forces, to be expressed in the CBCM nodes, can be written as follows:

$$f_{cn,i} = -k\delta_{yi}, \quad i = N+1, .., N + \text{round}\,(N(L_c/L)) \tag{6.16}$$

$$f_{ct,i} = \mu f_{cn,i}, \quad i = N+1, .., N + \text{round}\,(N(L_c/L)) \tag{6.17}$$

where k is the contact stiffness and μ is the static friction coefficient. Note that Eq. 6.16 represents a simplified version of the penalty class algorithms [190], in which dynamic effects (e.g. damping) are usually considered. The proposed contact presents a friction force that is almost null during the CAFP deflection, and thus only Eq. 6.16 is considered in this work. From a practical standpoint, for $i = N+1, .., N + \text{round}\,(N(L_c/L))$, Eq. 6.2 becomes:

$$\begin{bmatrix} f_i \\ m_i \end{bmatrix} = \begin{bmatrix} 12 & -6 \\ -6 & 4 \end{bmatrix} \begin{bmatrix} \delta_{yi} \\ \alpha_i \end{bmatrix} + p_i \begin{bmatrix} 6/5 & -1/10 \\ -1/10 & 2/15 \end{bmatrix} \begin{bmatrix} \delta_{yi} \\ \alpha_i \end{bmatrix} + p_i^2 \begin{bmatrix} -1/700 & 1/1400 \\ 1/1400 & -11/6300 \end{bmatrix} \begin{bmatrix} \delta_{yi} \\ \alpha_i \end{bmatrix} + \begin{bmatrix} f_{cn,i} \\ 0 \end{bmatrix} \tag{6.18}$$

In the reported CBCM model, the element length, L_{el}, is constant along the beams and thus round $(N(L_c/L))$ is used to ensure the stability of the problem, i.e. to select a precise nodes interval to be considered for the contact. To achieve a major sensibility in the contact analysis, i.e. to study slight variations of L_c, a fine mesh can be defined in the model by choosing a high value for N or by adopting the unequal discretization method [65]. However, both these solutions increase the computational cost, since:

- for the single candidate, the total number of equations to be solved is $12N + 7$ for each of the r substeps;
- a variable element length $L_{el}(i), i = 1, .., 2N$ would complicate the software structure

because several additional subroutines (e.g. *for* loops and *if-else* statements) must be added.

After a series of preliminary tests, in this work, $N = 10$ is used to ensure good accuracy and high computational efficiency (note that in [22], large deflections without contact analysis are solved with $N = 4$).

6.4.3. Performance Indexes Estimation

As previously introduced in Sec. 6.3, three different outputs are considered for the study of the contact-aided CAFP, namely the pivot stiffness, parasitic shift and maximum stress in deflected state. These performance indexes are derived from the aforementioned results matrix. Considering a quasi-linear torque deflection law for medium/large deflections (i.e. $\theta < 0.883$ rad), the stiffness, to be calculated in case of $F_x = F_y = 0$, can be directly obtained as the mean value of $K = \partial M(\theta)/\partial\theta$.

Then, by considering a rigid segment $\overline{CP} = \overline{C_0P_0} = (w_2/2)/\tan\beta$ as in Fig. 6.3, the position of point P with respect to a coordinate system placed in P_0 and oriented as OXY, is given by:

$$x_P = \Delta_x + ((w_2/2)/\tan\beta)\sin\theta \tag{6.19}$$

$$y_P = \Delta_y - ((w_2/2)/\tan\beta)\cos\theta - (w_1/2)/(\tan\beta) \tag{6.20}$$

and thus the parasitic shift module and phase can be calculated as:

$$s = \sqrt{x_P^2 + y_P^2} \qquad \begin{cases} \phi = \arctan\left(\frac{y_P}{x_P}\right),\ x_P > 0 \\ \phi = \pi/2,\ x_P = 0 \\ \phi = \arctan\left(\frac{y_P}{x_P}\right) + \pi,\ x_P < 0 \end{cases} \tag{6.21}$$

Lastly, the stress acting on the i-th element can be viewed as a superposition of two components:

$$\sigma_i(x_i) = \sigma_{b,i}(x_i) + \sigma_{ax,i} \tag{6.22}$$

where $\sigma_{b,i}(x_i)$ is the bending stress along the x-coordinate of $O_ix_iy_i$, whereas $\sigma_{ax,i}$ is the

tensile stress related to the stretch of the i-th element under the axial force p_i, such that:

$$\sigma_{b,i}(x_i) = \frac{M(x_i)t/2}{J} \qquad \sigma_{ax,i} = \frac{p_i EJ/L_{el}^2}{bt} \tag{6.23}$$

While $\sigma_{ax,i}$ is uniform along the i-th element, $\sigma_{b,i}(x_i)$ requires the knowledge of $M(x_i)$, namely the dimensional moment acting along the i-th element:

$$M(x_i) = \frac{EJ}{\rho(x_i)} \tag{6.24}$$

The curvature is estimated for $x_i \in [0, 1]$ resorting to the following equation [22]:

$$\begin{cases} \frac{1}{\rho(x_i)} = \frac{1}{L_{el}} \left(\frac{\tanh(\sqrt{p_i})\cosh(x_i\sqrt{p_i}) - \sinh(x_i\sqrt{p_i})}{\sqrt{p_i}} f_i + \frac{\cosh(x_i\sqrt{p_i})}{\cosh(\sqrt{p_i})} m_i \right), & p_i \geq 0 \\ \frac{1}{\rho(x_i)} = \frac{1}{L_{el}} \left(\frac{\tan(\sqrt{-p_i})\cos(x_i\sqrt{-p_i}) - \sin(x_i\sqrt{-p_i})}{\sqrt{-p_i}} f_i + \frac{\cos(x_i\sqrt{-p_i})}{\cos(\sqrt{-p_i})} m_i \right), & p_i < 0 \end{cases} \tag{6.25}$$

At each analysis substep, the maximum stress σ_{Max} acting on the CAFP is then found as follows:

$$\sigma_{Max} = \max(\sigma_i,\ i = 0.., 2N) \tag{6.26}$$

6.5. Design Tool - Frameworks C and D

6.5.1. Software Architecture

The mechanical models are solved employing CBCM method, following the procedure reported in Sec. 6.4, and then verified by means of the FEA approach. In particular, 1D FEA is used to test the CBCM performance both in terms of results accuracy and simulation time. A full factorial selection criteria [98] is used to perform a bi-dimensional DOE (being the parameters AR and L_c), allowing the generation of the performance maps. Following Tab. 2.3, frameworks C and D are combined in a single integrated environment to allow the use of both the modeling techniques. Based on the schematic depicted in Fig. 6.6, the framework is guided by a Matlab file, which is organized in four sections as follows:

1. In the first section, the user defines the *Input Parameters*, which comprise geometrical dimensions (L or β, w_1, b and t), material properties (E and ν), external loads (F_x, F_y and M) or displacements (Δ_x, Δ_y and θ), number of elements (N), number of substeps

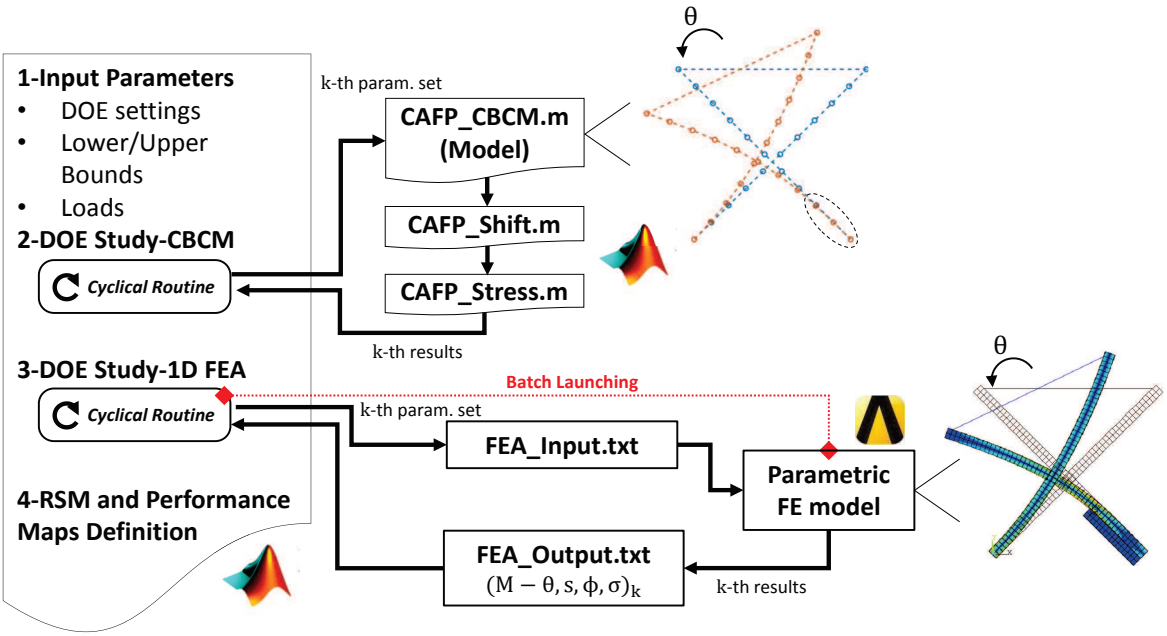

Figure 6.6: Framework C-D used for the parametric studies.

(r) and DOE spacing (number of points to be tested for each parameter, i.e. AR and L_c);

2. In the second section, a *for* loop allows to perform the *DOE CBCM* by singularly testing each of the candidates, i.e. the $AR - L_c$ combinations, thanks to an external Matlab function (*CAFP_CBCM.m*), which implements all the equations discussed in Sec. 6.4. Once the numerical results of the single simulation are available, two additional functions (*CAFP_Shift.m* and *CAFP_Stress.m*) are launched for the evaluation of the performance indexes described in Sec. 6.4.3. The stiffness evaluation is performed in the main script by means of a simple numerical derivative followed by a mean value calculation.

3. In the third section, a *for* loop is used for the *DOE FEA*. In particular, by leveraging the ANSYS interfacing capabilities, a multi-software routine that can automatically solve all the candidates is implemented. For each analysis, Matlab exports the parameters vector (composed of the entities defined at point 1) into an external file (*FEA_Input.txt*) and provides the ANSYS batch launching. The parametric FE model, updated on the basis of the information stored in the previous file, exports the results of the nonlinear (NLGEOM option) analysis into *FEA_Output.txt*, which is then processed by Matlab.

Table 6.1: CAFP parameters considered in this work.

Parameter	**Value(s)**
N	10
t	1.6 mm
b	5 mm
w_1	30 mm
r	10
$\beta = \text{const}$	
β	$\pi/4$ rad
AR	$[0.5, 3]$
L_c	$[0, 30]$ $\%L$
$L = \text{const}$	
L	50 mm
AR	$[0.8, 1.3]$
L_c	$[0, 30]$ $\%L$

4. In the last section, a *Results Comparison* is provided.

The Matlab and APDL scripts used in this work are reported in Appendix F.

6.5.2. Parametric FE model

The FE model, whose geometry is automatically re-defined for each candidate, is composed of two identical beams connected by a rigid segment, characterized by a larger cross section. The lowest node set, composed of nodes 0 in Fig. 6.4(a), is fixed to the ground. A second rigid segment is placed in proximity of the *Beam 2* so as to model the contact. To ensure consistency with the CBCM models, the number of elements N is automatically imported in ANSYS. Each of the flexible beams is discretized with N *Beam 188* elements with quadratic shape functions, whereas *Conta 176* and *Targe 170* elements are used for the contact interaction. Furthermore, the *Augmented Lagrangian* contact formulation is enforced (*Key-option(2)=0*) in all the simulations. Then, in line with the CBCM, the external loads are applied in a series of r incremental substeps. The performance indexes are computed resorting to the relations presented in Sec. 6.4.3, except for the maximum Von Mises stress, which is directly provided by ANSYS.

6.6. Results - Numerical Characterization of the Pivot

This section reports the DOE results achieved on the pivot via the proposed numerical framework. Recalling Sec. 6.2, several combinations (AR, L_c) are tested for both the configurations reported in Figs. 6.2(a) and 6.2(b). All the candidates are guided in a pure rotation $\theta = 0.7$ rad. Other load scenarios are discussed in Sec. 6.7. The adopted mate-

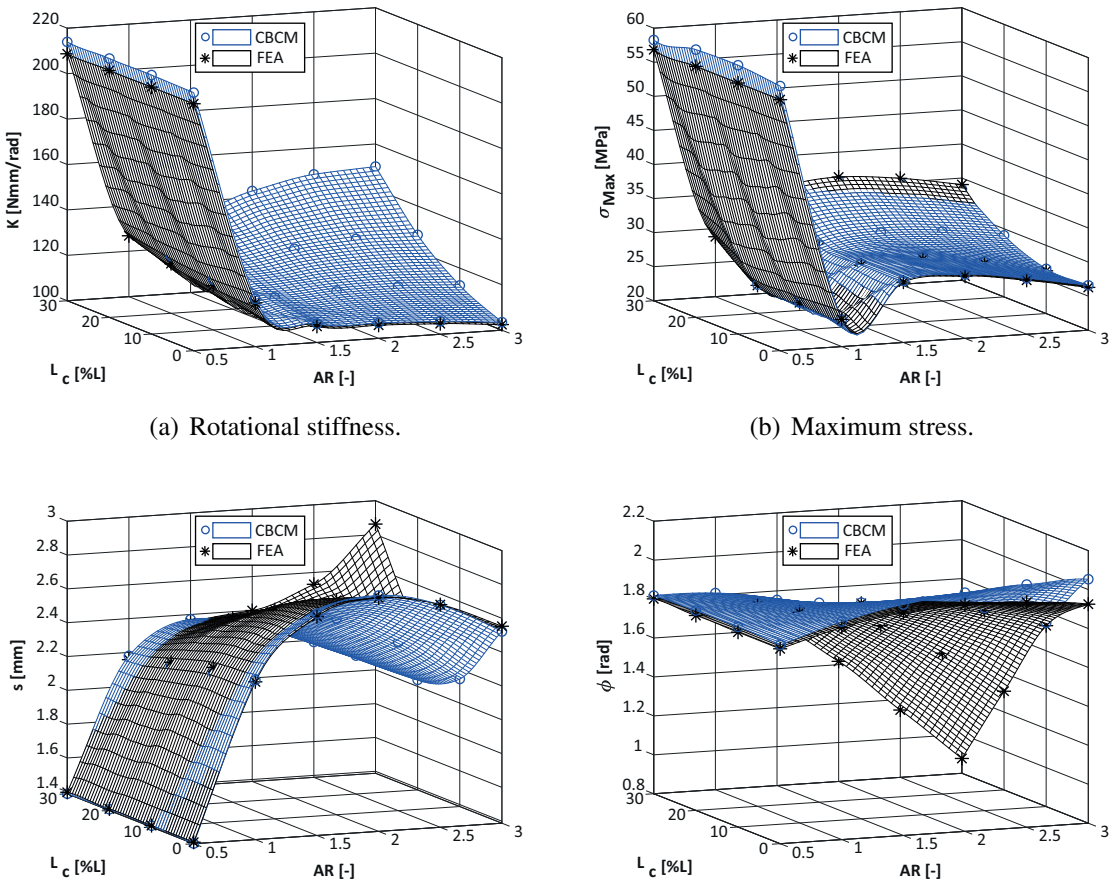

(a) Rotational stiffness.

(b) Maximum stress.

(c) Parasitic shift module.

(d) Parasitic shift phase.

Figure 6.7: DOE results for $\beta = \pi/4$ rad in a pure rotation $\theta = 0.7$ rad.

rial for the current application is Glycol-Modified Polyethylene Terephthalate (PETG). The Young's modulus and Poisson's ratio are, respectively, $E = 1400$ MPa and $\nu = 0.4$, whereas the flexural yield strength is assumed equal to $\sigma_s = 45$ MPa. Parameter set and allowed range of variation for each geometrical parameter are summarized in Tab. 6.1. Figures 6.7 and 6.8 provide a comparison between the results obtained via CBCM and 1D FEA for the $\beta =$ const and $L =$ const configurations respectively. The data show a good agreement for

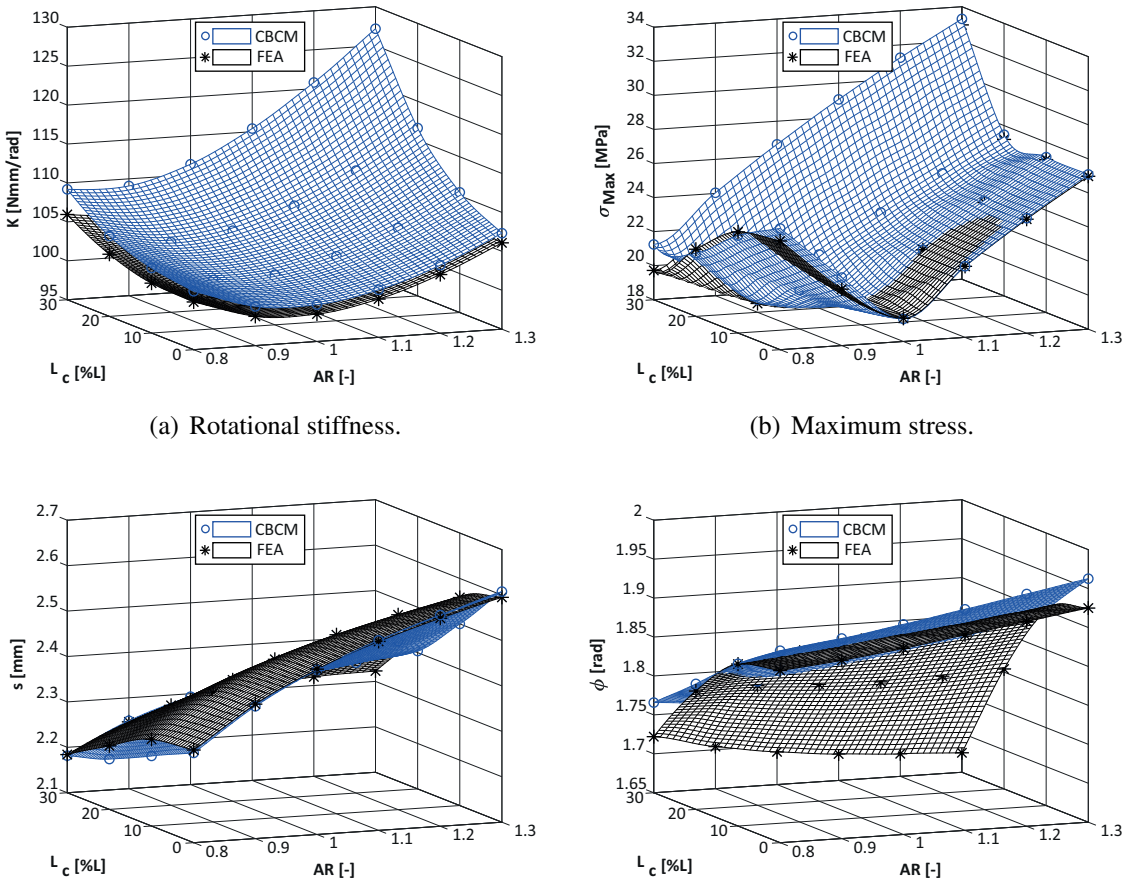

(a) Rotational stiffness.

(b) Maximum stress.

(c) Parasitic shift module.

(d) Parasitic shift phase.

Figure 6.8: DOE results for $L = 50$ mm in a pure rotation $\theta = 0.7$ rad.

each of the performance indexes, confirming the suitability of the CBCM for the analysis of large deflections and contact pairs. Moreover, as it may be seen in Fig. 6.8(a), the stiffness shows a remarkable variation in the design domain. This output highlights the possibility to exploit the $L = \text{const}$ configuration (see Fig. 6.2(b)) for designing a rotational variable stiffness joint.

As discussed in Sec. 6.4.2, restricted ranges of L_c can be investigated by changing the value of N or by adopting the unequal discretization method [65]. The major source of discrepancy between the numerical results, obtained when $L_c = 30\%L$, may be attributed to the adopted contact algorithm. In the penalty algorithms, the amount of penetration between bodies depends on the normal stiffness k. Higher values of k reduce the penetration but can lead to convergence problems. To overcome this issue, ANSYS refines the value of k during the simulations [192]. On the contrary, in the current framework, the CBCM is solved with a

constant value for k, causing differences in terms of penetration, that influence the processed results. To avoid this problem, k may be forced to be constant in ANSYS by means of a specific *Real Constant*, even though the problem convergence would be compromised, especially since r (i.e. the number of substeps) is kept constant. Alternatively, an iterative process that aims at refining the value of k can be implemented in the CBCM algorithm. In both cases, the computational efficiency of the proposed framework would be considerably decreased.

6.7. Experimental Validations

PETG physical prototypes of the configuration in Fig. 6.2(a), namely the one with a constant value of β, have been manufactured via 3D printing and tested resorting to two experimental setups. The tests aim at validating the accuracy of the proposed simulation framework for two different load scenarios: *i)* a rotation θ applied to a constrained point P_0 of the workspace that forces the CAFP to follow a circular deflection path; *ii)* a horizontal force F_x applied to the output link at point C.

6.7.1. Rotational setup

As visible from the results reported in Figs. 6.7(c), 6.7(d), 6.8(c) and 6.8(d), and in [93], the CAFP is subjected to an evident parasitic shift when a pure torque (or rotation) is applied to the outer link. The error between the resulting deflection path and an ideal circular path increases with the rotation. From a practical standpoint, this issue limits the use of a pure torque (or rotation) to the simulations. On the basis of these considerations and similarly to the previous literature [18, 67, 90], in this work, the experiments have been conducted via a standard moment-deflection test rig. The same measurement equipment as in Sec. 5.8.2 is used to conduct the experiments. The system, shown in Fig. 6.9(a), is equipped with a worm-wheel gearset that acts on a main shaft, an Omega TQ103-50 socket calibrated torque sensor, and a US Digital E2-500-375-IE-H-D-B optical encoder. A LabView interface is used to acquire the data from the sensors. The shaft is supported by bearings and is connected to the CAFP via a shape coupling, as shown in Fig. 6.9(b). Each candidate, characterized by a specific combination of AR and L_c, is fixed to the ground through a connection member (shown in blue) and it is deflected by the shaft. The experimental load scenario is depicted

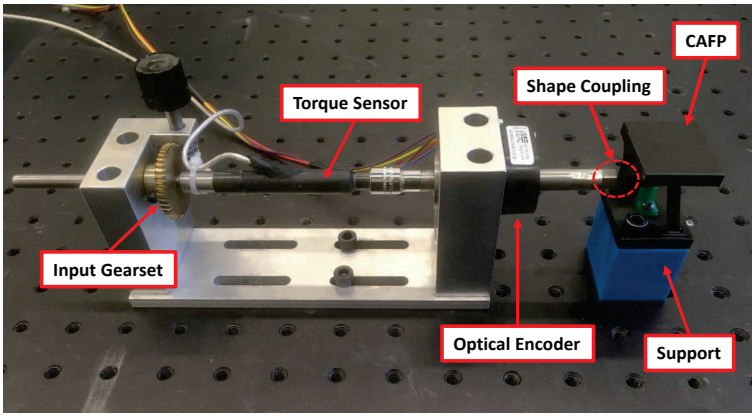

(a) Setup overview.

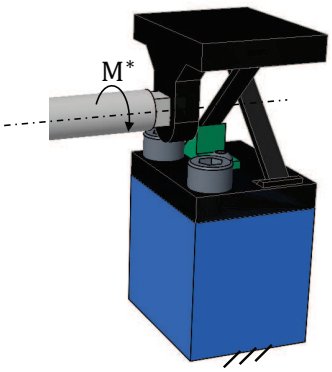

(b) Detailed view of the connection.

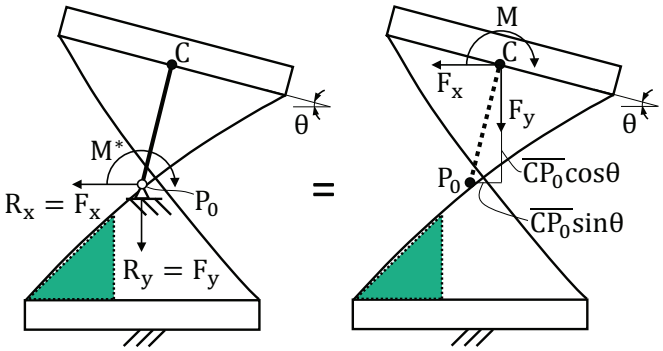

(c) Experimental load scenario.

Figure 6.9: Experimental setup for stiffness evaluation.

in Fig. 6.9(c): a moment M^* is applied by the shaft to the constrained point P_0, i.e. the initial intersection point between the CAFP beams. A rigid connection member between P_0 and C enforces a circular deflection path. As a direct consequence of the applied boundary conditions, the CAFP is not allowed to manifest the characteristic parasitic shift. The same results would be obtained by applying a set of forces F_x and F_y and moment M at point C, as shown in Fig. 6.9(c). For a deflection θ, the following relations hold:

$$R_x = F_x \qquad R_y = F_y \qquad M^* = M - F_x\overline{CP_0}\cos\theta + F_y\overline{CP_0}\sin\theta \tag{6.27}$$

To comply with the new load scenario, both CBCM and FEA models have been modified. In particular, a rigid segment connecting the output link to P_0 is used in the FE model, whereas a new global moment equilibrium, previously described by Eq. 6.11, has been de-

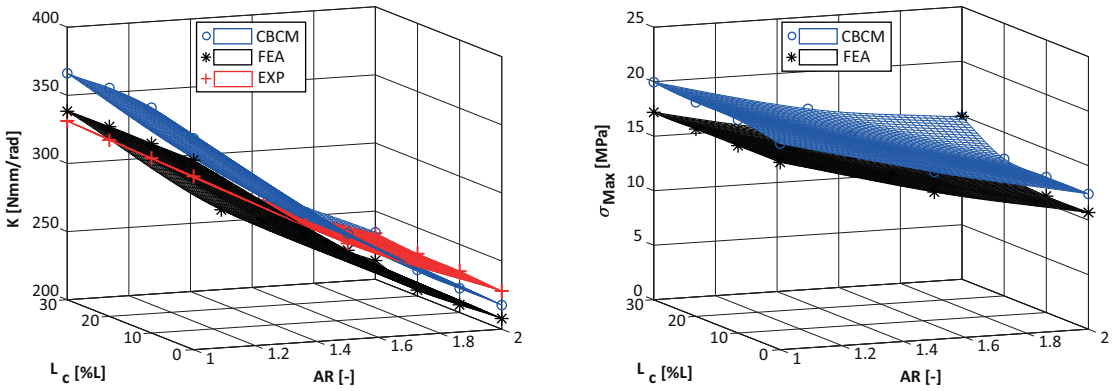

(a) Numerical and experimental stiffness.

(b) Numerical maximum stress.

Figure 6.10: Experimental and numerical results with an imposed rotation $\theta = 0.52$ rad.

fined in the CBCM with respect to P_0:

$$
\begin{aligned}
M^* = & \frac{EJ}{L_{el}} m_N + \frac{EJ}{L_{el}} m_{2N} + \\
& \frac{EJ}{L_{el}^2} \begin{bmatrix} -(Y_A - (w_1/2 \tan\beta)) & X_A \end{bmatrix} \begin{bmatrix} -\sin\beta & -\cos\beta \\ \cos\beta & -\sin\beta \end{bmatrix} \begin{bmatrix} p_{N+1} \\ f_{N+1} \end{bmatrix} + \\
& \frac{EJ}{L_{el}^2} \begin{bmatrix} -(Y_B - (w_1/2 \tan\beta)) & X_B \end{bmatrix} \begin{bmatrix} \sin\beta & -\cos\beta \\ \cos\beta & \sin\beta \end{bmatrix} \begin{bmatrix} p_1 \\ f_1 \end{bmatrix}
\end{aligned} \tag{6.28}
$$

where, by reference to Fig. 6.5(a), X_A, Y_A, X_B and Y_B are the coordinate of points A and B with respect to OXY:

$$
\begin{bmatrix} X_A \\ Y_A \end{bmatrix} = \begin{bmatrix} -\sin\beta & -\cos\beta \\ \cos\beta & -\sin\beta \end{bmatrix} \begin{bmatrix} x_A \\ y_A \end{bmatrix} + \begin{bmatrix} w_1/2 \\ 0 \end{bmatrix} \tag{6.29}
$$

$$
\begin{bmatrix} X_B \\ Y_B \end{bmatrix} = \begin{bmatrix} \sin\beta & -\cos\beta \\ \cos\beta & \sin\beta \end{bmatrix} \begin{bmatrix} x_B \\ y_B \end{bmatrix} - \begin{bmatrix} w_1/2 \\ 0 \end{bmatrix} \tag{6.30}
$$

The total deflection, $\theta = 0.52$ rad, is manually imposed to the CAFP in a series of static increments. The geometric dimensions refer to the values reported in Tab. 6.1. Figure 6.10 shows the results of the study for $AR = [1, 2]$ and $L_c = [0, 30]\%L$. The experimental stiffness, evaluated for each candidate as the mean value of $K = \partial M^*(\theta)/\partial\theta$, shows a good agreement with the numerical models. In line with the study presented in [193], the point

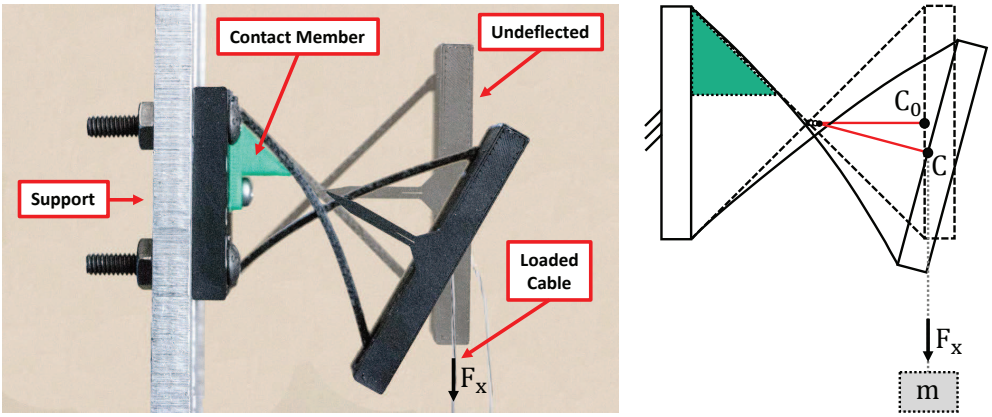

(a) Setup overview: deflected and undeflected configurations.

(b) Experimental load scenario.

Figure 6.11: Vertical experimental setup for parasitic shift evaluation.

at which the flexures cross in the undeformed state, defined by AR, strongly affects the joint stiffness. The influence of L_c is limited due to the applied boundary conditions, that guide the CAFP in an unnatural deflection, in which the contact is partially involved. Also the maximum stress, plotted in Fig. 6.10(b), shows a good overlap between CBCM and 1D FEA.

6.7.2. Vertical setup

A vertical setup [194] is used to validate the framework in case of a single force load. By considering the same AR and L_c combinations of Sec. 6.7.1, the parasitic shift is evaluated in the deflected state. As shown in Figs. 6.11(a) and 6.11(b), the CAFP, fixed to the ground via a pair of screws, is vertically loaded by means of a cable and a calibrated mass $m = 0.4$ kg, resulting in a planar force equal to $F_x = 3.92$ N. The geometry of the output link has been designed to apply the force at point C (see also Fig. 6.5(a)). A rigid member that connects the output link to the initial center of rotation has been used as a simple way to trace the parasitic shift during the deflection of the pivot. Two separate images, acquired by a Canon EOS Rebel T6s equipped with EF-S 18-135 mm IS STM Lens Kit, are scaled and overlapped in CAD environment (PTC Creo), allowing the evaluation of the shift module s and phase ϕ. The results of the experimental activity are reported in Fig. 6.12 for each combination of AR and L_c. In particular, Figs. 6.12(a) and 6.12(b) show a comparison between numerical and experimental data, whereas Fig. 6.12(c) reports the maximum numerical stress acting on

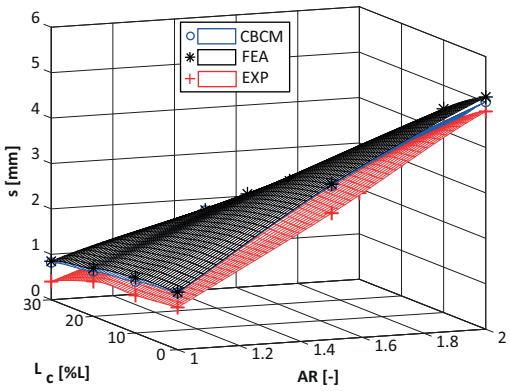

(a) Numerical and experimental parasitic shift module.

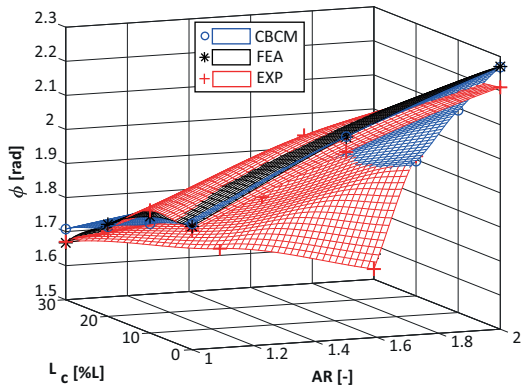

(b) Numerical and experimental parasitic shift phase.

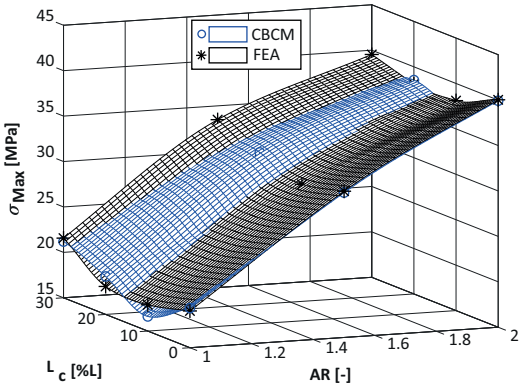

(c) Numerical maximum stress.

Figure 6.12: Experimental and numerical results with a pure force $F_x = 3.92$ N.

the pivot. Note that, as predicted by the numerical calculations providing $\sigma_{Max} < \sigma_s$, the structural integrity of each specimen has been preserved during physical testing. In line with the previous scenarios, the experimental assessment confirms the validity of the proposed numerical framework and underlines the accuracy of the CBCM for the modeling of contacts in large deflection problems.

6.8. Summary

This chapter demonstrates the suitability of the CBCM for the modeling of contact-aided CMs undergoing large deflections. A simple system comprising a standard CAFP and a purposely shaped contact member, that acts on a single flexure, is used as a test case. The contact affects several functional aspects of the CAFP. In particular, the interaction between bodies limits the free length of the flexure, allowing a remarkable increment of the overall

stiffness. The parasitic shift is also affected by the presence of the contact, as well as the stress acting on the pivot, which is an important aspect to be considered for design purposes.

Different planar load cases are investigated via an integrated software environment combining Matlab and ANSYS APDL (i.e. frameworks C and D in Tab. 2.3). Performance maps for the pivot under a pure rotation are provided, showing a good matching between CBCM and 1D FEA results for different combinations of aspect ratios and contact extensions.

By meshing each beam with 10 elements, the CBCM model is solved in Matlab in 1.5 s, whereas a single APDL batch simulation takes $5 - 7$ s to be completed. The limited computational time required to solve a single simulation confirms the suitability of the CBCM for parametric optimization studies.

At last, 3D printed specimens of the contact-aided CAFP have been tested experimentally by means of two special purpose test rigs. The acquired data show good agreement with the behavior predicted by CBCM and 1D FEA.

Chapter 7

Conclusions

This work has explored design strategies and modeling techniques for beam-based CMs. In the last decades, many impressive theories have been developed to accurately model large deflections and satisfy challenging functional requirements. The validity of such theories has been validated with numerous examples, which became standard concepts to be used for the synthesis of new mechanisms. Theoretical models provide fast and accurate results, limiting the use of FEA to the final design steps, in other words for validation purposes. Designers can resort to a wide selection of modeling techniques for analyzing and designing relatively simple CMs, characterized by straight beams with uniform cross sections and subjected to typical loads and constraints. More complex scenarios involving curved beams, variable cross sections, hybrid flexures or self/mutual contacts between the members may be approached by means of 3D FEA, though its low computational efficiency makes it inappropriate for parametric studies or optimizations. Fast behavioral models are always desirable in the initial design steps for characterizing existing concepts or synthesizing new ones.

This work compares the benefits of a selected group of computationally efficient techniques among the most used in literature (1D FEA, PRB method and CBCM) for the modeling of nonstandard beam-based CMs. Furthermore, to meet the need of a general design optimization tool, a modular multi-software environment is proposed and described. The framework exploits dedicated commercial CAE solvers that allow code-based simulations and batch run mode. These features ensure an easy linkage with Matlab and high applicability to a large variety of problems. As a result of the study, Chap. 2 reports comparative tables for the selection of the appropriate modeling technique(s) and software framework(s) on the basis of specific design requirements and intents.

In the next chapters, the considered scenarios (geometrical features or contacts between bodies) have been treated singularly by adopting specific case studies. To generalize the approaches, each demonstrative example analyzes a set of properties and proposes a design

procedure. Chapters 3, 4 and 5 describes the shape optimization of flexible members with nonstandard geometries, respectively identified by hybrid flexures, variable section beams and spline beams. The chapters illustrate possible design strategies for achieving optimal results by leveraging on computationally efficient models. The PRB method is discussed and, when possible, directly employed for design purposes. The CMs have been optimized to fulfill prescribed behaviors in terms of motion or force-deflection characteristics. Furthermore, Chaps. 4 and 5 introduces novel concepts in the field of constant force CMs and statically balanced CMs.

Chapter 6 reports the performance study carried out on a contact-aided CAFP. The proposed device can be useful for systems requiring different behaviors when deflecting clockwise or anti-clockwise. The chapter has two significant contributions. At first, it demonstrates the efficiency of the CBCM for the analysis/design of contact-aided CMs. Secondly, it provides useful performance maps that help designers in visualizing the potentialities of the concept and the influence of the geometrical parameters on the CAFP behavior.

To facilitate the reproduction of the reported results, detailed descriptions of the design tools are given throughout the thesis and many codes are reported in the Appendix. Chapters 4, 5 and 6 are also supported by experimental activities carried out with custom test equipment. The measured data is used to verify the accuracy of the predicting models. Much work has been done regarding the design and implementation of the setups as well as for the fabrication of physical prototypes and for the materials characterizations. Many details about the testing are not included in the text, which instead emphasizes the design procedures.

Bibliography

[1] Howell, L. L., 2001. *Compliant mechanisms*. John Wiley & Sons.

[2] Wang, P., and Xu, Q., 2018. "Design and modeling of constant-force mechanisms: A survey". *Mechanism and Machine Theory,* **119**, pp. 1–21.

[3] Meng, Q., Berselli, G., Vertechy, R., and Castelli, V. P., 2012. "An improved method for designing flexure-based nonlinear springs". *ASME IDETC/CIE International Design Engineering Technical Conferences and Computers and Information in Engineering Conference*, pp. 211–219.

[4] Palli, G., Berselli, G., Melchiorri, C., and Vassura, G., 2011. "Design of a variable stiffness actuator based on flexures". *Journal of Mechanisms and Robotics,* **3**(3), p. 034501.

[5] Tanık, Ç. M., Parlaktaş, V., Tanık, E., and Kadıoğlu, S., 2015. "Steel compliant cardan universal joint". *Mechanism and Machine Theory,* **92**, pp. 171–183.

[6] Parvari Rad, F., Vertechy, R., Berselli, G., and Parenti-Castelli, V., 2018. "Design and stiffness evaluation of a compliant joint with parallel architecture realizing an approximately spherical motion". *Actuators,* **7**(2), p. 20.

[7] Liang, Q., Zhang, D., Chi, Z., Song, Q., Ge, Y., and Ge, Y., 2011. "Six-DOF micromanipulator based on compliant parallel mechanism with integrated force sensor". *Robotics and Computer-Integrated Manufacturing,* **27**(1), pp. 124–134.

[8] Yun, Y., and Li, Y., 2011. "Optimal design of a 3-PUPU parallel robot with compliant hinges for micromanipulation in a cubic workspace". *Robotics and Computer-Integrated Manufacturing,* **27**(6), pp. 977–985.

[9] Verotti, M., Dochshanov, A., and Belfiore, N. P., 2017. "A comprehensive survey on microgrippers design: Mechanical structure". *Journal of Mechanical Design,* **139**(6), p. 060801.

[10] Gibson, I., Rosen, D. W., and Stucker, B., 2010. "Design for additive manufacturing". *Additive Manufacturing Technologies*, pp. 299–332.

[11] Lan, C.-C., and Wang, J.-Y., 2011. "Design of adjustable constant-force forceps for robot-assisted surgical manipulation". *IEEE ICRA International Conference on Robotics and Automation*, pp. 386–391.

[12] Dearden, J., Grames, C., Jensen, B. D., Magleby, S. P., and Howell, L. L., 2017. "Inverted l-arm gripper compliant mechanism". *Journal of Medical Devices,* **11**(3), p. 034502.

[13] Nelson, T. G., Avila, A., Howell, L. L., Herder, J. L., and Machekposhti, D. F., 2019. "Origami-inspired sacrificial joints for folding compliant mechanisms". *Mechanism and Machine Theory,* **140**, pp. 194–210.

[14] Lang, R. J., Tolman, K. A., Crampton, E. B., Magleby, S. P., and Howell, L. L., 2018. "A review of thickness-accommodation techniques in origami-inspired engineering". *Applied Mechanics Reviews,* **70**(1), p. 010805.

[15] Lobontiu, N., 2002. *Compliant mechanisms: design of flexure hinges*. CRC press.

[16] Seffen, K. A., 2012. "Compliant shell mechanisms". *Philosophical Transactions of the Royal Society A: Mathematical, Physical and Engineering Sciences,* **370**(1965), pp. 2010–2026.

[17] Satheeshbabu, S., and Krishnan, G., 2016. "Qualitative mobility analysis of wire flexure systems using load flow visualization". *Journal of Mechanisms and Robotics,* **8**(6), p. 061012.

[18] Merriam, E. G., and Howell, L. L., 2016. "Lattice flexures: Geometries for stiffness reduction of blade flexures". *Precision Engineering,* **45**, pp. 160–167.

[19] Howell, L. L., and Midha, A., 1995. "Parametric Deflection Approximations for End-Loaded, Large-Deflection Beams in Compliant Mechanisms". *Journal of Mechanical Design,* **117**(1), pp. 156–165.

[20] Campanile, L., and Hasse, A., 2008. "A simple and effective solution of the elastica problem". *Proceedings of the Institution of Mechanical Engineers, Part C: Journal of Mechanical Engineering Science,* **222**(12), pp. 2513–2516.

[21] Awtar, S., Slocum, A. H., and Sevincer, E., 2007. "Characteristics of beam-based flexure modules". *Journal of Mechanical Design,* **129**(6), pp. 625–639.

[22] Ma, F., and Chen, G., 2016. "Modeling large planar deflections of flexible beams in compliant mechanisms using chained beam-constraint-model". *Journal of Mechanisms and Robotics,* **8**(2), p. 021018.

[23] Jonker, J., and Meijaard, J., 1990. "SPACAR-computer program for dynamic analysis of flexible spatial mechanisms and manipulators". *Multibody Systems Handbook*, pp. 123–143.

[24] Turkkan, O. A., and Su, H.-J., 2016. "DAS-2D: a concept design tool for compliant mechanisms". *Mechanical Sciences,* **7**(2), pp. 135–148.

[25] Berselli, G., Guerra, A., Vassura, G., and Andrisano, A. O., 2014. "An engineering method for comparing selectively compliant joints in robotic structures". *Transactions on Mechatronics,* **19**(6), pp. 1882–1895.

[26] Zhu, B., Lu, Y., Liu, M., Li, H., and Zhang, X., 2017. "Fatigue study on the right circular flexure hinges for designing compliant mechanisms". *ASME IMECE International Mechanical Engineering Congress and Exposition*.

[27] Bharanidaran, R., and Ramesh, B., 2013. "Design of compliant mechanism based microgripper with three finger using topology optimization". *International Journal of Mechanical, Aerospace, Industrial, Mechatronic and Manufacturing Engineering,* **7**(7).

[28] Cannon, B. R., Lillian, T. D., Magleby, S. P., Howell, L. L., and Linford, M. R., 2005. "A compliant end-effector for microscribing". *Precision Engineering,* **29**(1), pp. 86–94.

[29] Howell, L. L., Magleby, S. P., Olsen, B. M., and Wiley, J., 2013. *Handbook of compliant mechanisms*. Wiley Online Library.

[30] Blanding, D. L., 1999. *Exact constraint: machine design using kinematic principles*. American Society of Mechanical Engineers.

[31] Su, H.-J., and Tari, H., 2011. "On line screw systems and their application to flexure synthesis". *Journal of Mechanisms and Robotics,* **3**(1), p. 011009.

[32] Hopkins, J. B., and Culpepper, M. L., 2010. "Synthesis of multi-degree of freedom, parallel flexure system concepts via freedom and constraint topology (FACT)-Part I: Principles". *Precision Engineering,* **34**(2), pp. 259–270.

[33] Hopkins, J. B., and Culpepper, M. L., 2010. "Synthesis of multi-degree of freedom, parallel flexure system concepts via freedom and constraint topology (FACT). Part II: Practice". *Precision Engineering,* **34**(2), pp. 271–278.

[34] Li, H., Hao, G., and Kavanagh, R. C., 2016. "Position-space-based compliant mechanism reconfiguration approach and its application in the reduction of parasitic motion". *Journal of Mechanical Design,* **138**(9), p. 092301.

[35] Li, H., and Hao, G., 2018. "Position-space-based design of a symmetric spatial translational compliant mechanism for micro-/nano-manipulation". *Micromachines,* **9**(4), p. 189.

[36] Hao, G., and Li, H., 2015. "Conceptual designs of multi-degree of freedom compliant parallel manipulators composed of wire-beam based compliant mechanisms". *Proceedings of the Institution of Mechanical Engineers, Part C: Journal of Mechanical Engineering Science,* **229**(3), pp. 538–555.

[37] Kim, C. J., Moon, Y.-M., and Kota, S., 2008. "A building block approach to the conceptual synthesis of compliant mechanisms utilizing compliance and stiffness ellipsoids". *Journal of Mechanical Design,* **130**(2), p. 022308.

[38] Jutte, C. V., and Kota, S., 2008. "Design of nonlinear springs for prescribed load-displacement functions". *Journal of Mechanical Design,* **130**(8), p. 081403.

[39] Frecker, M. I., Ananthasuresh, G. K., Nishiwaki, S., Kikuchi, N., and Kota, S., 1997. "Topological Synthesis of Compliant Mechanisms Using Multi-Criteria Optimization". *Journal of Mechanical Design,* **119**(2), 06, pp. 238–245.

[40] Lu, K.-J., and Kota, S., 2005. "Topology and Dimensional Synthesis of Compliant Mechanisms Using Discrete Optimization". *Journal of Mechanical Design,* **128**(5), 10, pp. 1080–1091.

[41] Sigmund, O., 1997. "On the design of compliant mechanisms using topology optimization". *Journal of Structural Mechanics,* **25**(4), pp. 493–524.

[42] Huang, X., Li, Y., Zhou, S., and Xie, Y., 2014. "Topology optimization of compliant mechanisms with desired structural stiffness". *Engineering Structures,* **79**, pp. 13–21.

[43] Bruns, T. E., and Tortorelli, D. A., 2001. "Topology optimization of non-linear elastic structures and compliant mechanisms". *Computer methods in applied mechanics and engineering,* **190**(26-27), pp. 3443–3459.

[44] Hao, G., 2011. "Creative design and modelling of large-range translation compliant parallel manipulators". *PhD Dissertation, Heriot-Watt University*.

[45] Xia, Q., and Shi, T., 2016. "Topology optimization of compliant mechanism and its support through a level set method". *Computer Methods in Applied Mechanics and Engineering,* **305**, pp. 359–375.

[46] Zhu, B., Zhang, X., Zhang, H., Liang, J., Zang, H., Li, H., and Wang, R., 2020. "Design of compliant mechanisms using continuum topology optimization: A review". *Mechanism and Machine Theory,* **143**, p. 103622.

[47] Mattiasson, K., 1981. "Numerical results from large deflection beam and frame problems analysed by means of elliptic integrals". *International Journal for Numerical Methods in Engineering,* **17**(1), pp. 145–153.

[48] Saxena, A., and Kramer, S. N., 1998. "A Simple and Accurate Method for Determining Large Deflections in Compliant Mechanisms Subjected to End Forces and Moments". *Journal of Mechanical Design,* **120**(3), 09, pp. 392–400.

[49] Lan, C.-C., 2008. "Analysis of large-displacement compliant mechanisms using an incremental linearization approach". *Mechanism and Machine Theory,* **43**(5), pp. 641–658.

[50] Tolou, N., and Herder, J., 2009. "A seminalytical approach to large deflections in compliant beams under point load". *Mathematical Problems in Engineering,* **2009**.

[51] Holst, G. L., Teichert, G. H., and Jensen, B. D., 2011. "Modeling and experiments of buckling modes and deflection of fixed-guided beams in compliant mechanisms". *Journal of Mechanical Design,* **133**(5), p. 051002.

[52] Zhang, A., and Chen, G., 2013. "A comprehensive elliptic integral solution to the large deflection problems of thin beams in compliant mechanisms". *Journal of Mechanisms and Robotics,* **5**(2), p. 021006.

[53] Venkiteswaran, V. K., Turkkan, O. A., and Su, H.-J., 2017. "Speeding up topology optimization of compliant mechanisms with a pseudorigid-body model". *Journal of Mechanisms and Robotics,* **9**(4), p. 041007.

[54] Chen, G., Xiong, B., and Huang, X., 2011. "Finding the optimal characteristic parameters for 3R pseudo-rigid-body model using an improved particle swarm optimizer". *Precision Engineering,* **35**(3), pp. 505–511.

[55] Su, H.-J., 2009. "A pseudorigid-body 3R model for determining large deflection of cantilever beams subject to tip loads". *Journal of Mechanisms and Robotics,* **1**(2), p. 021008.

[56] Venkiteswaran, V. K., and Su, H.-J., 2015. "A parameter optimization framework for determining the pseudo-rigid-body model of cantilever-beams". *Precision Engineering,* **40**, pp. 46–54.

[57] Tolman, K. A., Merriam, E. G., and Howell, L. L., 2016. "Compliant constant-force linear-motion mechanism". *Mechanism and Machine Theory,* **106**, pp. 68–79.

[58] Midha, A., Howell, L. L., and Norton, T. W., 2000. "Limit positions of compliant mechanisms using the pseudo-rigid-body model concept". *Mechanism and Machine Theory,* **35**(1), pp. 99–115.

[59] Berselli, G., Piccinini, M., and Vassura, G., 2011. "Comparative evaluation of the selective compliance in elastic joints for robotic structures". *IEEE ICRA International Conference on Robotics and Automation*, pp. 4626–4631.

[60] Jin, M., Yang, Z., Ynchausti, C., Zhu, B., Zhang, X., and Howell, L. L., 2019. "Large deflection analysis of general beams in contact-aided compliant mechanisms using chained pseudo-rigid-body model". *Journal of Mechanisms and Robotics*, pp. 1–14.

[61] Jensen, B. D., and Howell, L. L., 2003. "Identification of compliant pseudo-rigid-body four-link mechanism configurations resulting in bistable behavior". *Journal of Mechanical Design,* **125**(4), pp. 701–708.

[62] Boyle, C., Howell, L. L., Magleby, S. P., and Evans, M. S., 2003. "Dynamic modeling of compliant constant-force compression mechanisms". *Mechanism and Machine Theory,* **38**(12), pp. 1469–1487.

[63] Lu, T.-F., Handley, D. C., and Yong, Y. K., 2004. "Position control of a 3 DOF compliant micro-motion stage". *ICARCV International Conference on Control, Automation, Robotics and Vision,* **2**, pp. 1274–1278.

[64] Her, I., 1986. "Methodology for compliant mechanisms design.". *PhD Dissertation, Purdue University*.

[65] Chen, G., Ma, F., Hao, G., and Zhu, W., 2019. "Modeling large deflections of initially curved beams in compliant mechanisms using chained beam constraint model". *Journal of Mechanisms and Robotics,* **11**(1), p. 011002.

[66] Chen, G., and Bai, R., 2016. "Modeling large spatial deflections of slender bisymmetric beams in compliant mechanisms using chained spatial-beam constraint model". *Journal of Mechanisms and Robotics,* **8**(4), p. 041011.

[67] Dearden, J., Grames, C., Orr, J., Jensen, B. D., Magleby, S. P., and Howell, L. L., 2018. "Cylindrical cross-axis flexural pivots". *Precision Engineering,* **51**, pp. 604–613.

[68] Tummala, Y., Wissa, A., Frecker, M., and Hubbard, J. E., 2014. "Design and optimization of a contact-aided compliant mechanism for passive bending". *Journal of Mechanisms and Robotics,* **6**(3), p. 031013.

[69] Fowler, R. M., Maselli, A., Pluimers, P., Magleby, S. P., and Howell, L. L., 2014. "Flex-16: A large-displacement monolithic compliant rotational hinge". *Mechanism and Machine Theory,* **82**, pp. 203–217.

[70] Marković, K., and Zelenika, S., 2017. "Optimized cross-spring pivot configurations with minimized parasitic shifts and stiffness variations investigated via nonlinear FEA". *Mechanics Based Design of Structures and Machines,* **45**(3), pp. 380–394.

[71] Prakashah, H. N., and Zhou, H., 2016. "Synthesis of constant torque compliant mechanisms". *Journal of Mechanisms and Robotics,* **8**(6), p. 064503.

[72] Haringx, J., 1949. "The cross-spring pivot as a constructional element". *Flow, Turbulence and Combustion,* **1**(1), p. 313.

[73] Valentini, P. P., and Pennestrì, E., 2017. "Elasto-kinematic comparison of flexure hinges undergoing large displacement". *Mechanism and Machine Theory,* **110**, pp. 50–60.

[74] Zhao, H., and Bi, S., 2010. "Stiffness and stress characteristics of the generalized cross-spring pivot". *Mechanism and Machine Theory,* **45**(3), pp. 378–391.

[75] Zelenika, S., and De Bona, F., 2002. "Analytical and experimental characterisation of high-precision flexural pivots subjected to lateral loads". *Precision Engineering,* **26**(4), pp. 381–388.

[76] Hongzhe, Z., and Shusheng, B., 2010. "Accuracy characteristics of the generalized cross-spring pivot". *Mechanism and Machine Theory,* **45**(10), pp. 1434–1448.

[77] Zhao, H., Bi, S., and Yu, J., 2012. "A novel compliant linear-motion mechanism based on parasitic motion compensation". *Mechanism and Machine Theory,* **50**, pp. 15–28.

[78] Bi, S., Yao, Y., Zhao, S., and Yu, J., 2012. "Modeling of cross-spring pivots subjected to generalized planar loads". *Chinese Journal of Mechanical Engineering,* **25**(6), pp. 1075–1085.

[79] Wittrick, W., 1948. "The theory of symmetrical crossed flexure pivots". *Australian Journal of Chemistry,* **1**(2), pp. 121–134.

[80] Bi, S., Zhang, S., and Zhao, H., 2016. "Quasi-constant rotational stiffness characteristic for cross-spring pivots in high precision measurement of unbalance moment". *Precision Engineering,* **43**, pp. 328–334.

[81] Choi, Y.-j., Sreenivasan, S., and Choi, B. J., 2008. "Kinematic design of large displacement precision XY positioning stage by using cross strip flexure joints and over-constrained mechanism". *Mechanism and Machine Theory,* **43**(6), pp. 724–737.

[82] Hongzhe, Z., Shusheng, B., Jingjun, Y., and Jun, G., 2012. "Design of a family of ultra-precision linear motion mechanisms". *Journal of Mechanisms and Robotics,* **4**(4).

[83] Liu, L., Bi, S., Yang, Q., and Wang, Y., 2014. "Design and experiment of generalized triple-cross-spring flexure pivots applied to the ultra-precision instruments". *Review of Scientific Instruments,* **85**(10), p. 105102.

[84] Rundle, W. J., 1989. "Design and performance of an optical mount using cross-flexure pivots". *SPIE Proceedings,* **1167**, pp. 306–312.

[85] Martin, J., and Robert, M., 2011. "Novel flexible pivot with large angular range and small center shift to be integrated into a bio-inspired robotic hand". *Journal of Intelligent Material Systems and Structures,* **22**(13), pp. 1431–1437.

[86] Merriam, E., Jones, J., Magleby, S., and Howell, L. L., 2013. "Monolithic 2 DOF fully compliant space pointing mechanism". *Mechanical Sciences,* **4**(2), pp. 381–390.

[87] Merriam, E. G., Lund, J. M., and Howell, L. L., 2016. "Compound joints: Behavior and benefits of flexure arrays". *Precision Engineering,* **45**, pp. 79–89.

[88] Merriam, E. G., and Howell, L. L., 2015. "Non-dimensional approach for static balancing of rotational flexures". *Mechanism and Machine Theory,* **84**, pp. 90–98.

[89] Morsch, F. M., and Herder, J. L., 2010. "Design of a generic zero stiffness compliant joint". *ASME IDETC/CIE International Design Engineering Technical Conferences and Computers and Information in Engineering Conference*, pp. 427–435.

[90] Merriam, E. G., Tolman, K. A., and Howell, L. L., 2016. "Integration of advanced stiffness-reduction techniques demonstrated in a 3D-printable joint". *Mechanism and Machine Theory,* **105**, pp. 260–271.

[91] Zhao, H., Zhao, C., Ren, S., and Bi, S., 2019. "Analysis and evaluation of a near-zero stiffness rotational flexural pivot". *Mechanism and Machine Theory,* **135**, pp. 115–129.

[92] Bi, S., Li, Y., and Zhao, H., 2019. "Fatigue analysis and experiment of leaf-spring pivots for high precision flexural static balancing instruments". *Precision Engineering,* **55**, pp. 408–416.

[93] Jensen, B. D., and Howell, L. L., 2002. "The modeling of cross-axis flexural pivots". *Mechanism and Machine Theory,* **37**(5), pp. 461–476.

[94] Awtar, S., Shimotsu, K., and Sen, S., 2010. "Elastic averaging in flexure mechanisms: A three-beam parallelogram flexure case study". *Journal of Mechanisms and Robotics,* **2**(4), p. 041006.

[95] Zhou, H., and Ting, K.-L., 2006. "Shape and size synthesis of compliant mechanisms using wide curve theory". *Journal of Mechanical Design,* **128**(3), pp. 551–558.

[96] Moon, Y.-M., 2007. "Bio-mimetic design of finger mechanism with contact aided compliant mechanism". *Mechanism and Machine Theory,* **42**(5), pp. 600–611.

[97] Tummala, Y., Frecker, M. I., Wissa, A., and Hubbard Jr, J. E., 2014. "Design optimization of a twist compliant mechanism with nonlinear stiffness". *Smart Materials and Structures,* **23**(10), p. 104010.

[98] Cavazzuti, M., 2013. *Optimization Methods: From Theory to Design*. Springer.

[99] Cirone, S. A., Hayes, G. R., Babcox, B. L., Frecker, M., Adair, J. H., and Lesieutre, G. A., 2012. "Design of contact-aided compliant cellular mechanisms with curved walls". *Journal of Intelligent Material Systems and Structures,* **23**(16), pp. 1773–1785.

[100] Jin, M., Zhu, B., Mo, J., Yang, Z., Zhang, X., and Howell, L. L., 2020. "A cprbm-based method for large-deflection analysis of contact-aided compliant mechanisms considering beam-to-beam contacts". *Mechanism and Machine Theory,* **145**, p. 103700.

[101] Venkiteswaran, V. K., and Su, H.-J., 2016. "Pseudo-rigid-body models for circular beams under combined tip loads". *Mechanism and Machine Theory,* **106**, pp. 80–93.

[102] Awtar, S., and Sen, S., 2010. "A generalized constraint model for two-dimensional beam flexures: nonlinear load-displacement formulation". *Journal of Mechanical Design,* **132**(8), p. 081008.

[103] Hou, C.-W., and Lan, C.-C., 2013. "Functional joint mechanisms with constant-torque outputs". *Mechanism and Machine Theory,* **62**, pp. 166–181.

[104] Nguyen, D. N., Dao, T.-P., Chau, N. L., and Dang, V. A., 2019. "Hybrid approach of finite element method, kigring metamodel, and multiobjective genetic algorithm for computational optimization of a flexure elbow joint for upper-limb assistive device". *Complexity,* **2019**.

[105] Ho, N. L., Dao, T.-P., Le Chau, N., and Huang, S.-C., 2019. "Multi-objective optimization design of a compliant microgripper based on hybrid teaching learning-based optimization algorithm". *Microsystem Technologies,* **25**(5), pp. 2067–2083.

[106] Cheng, Z., Foong, S., Sun, D., and Tan, U.-X., 2014. "Algorithm for design of compliant mechanisms for torsional applications". *IEEE/ASME AIM International Conference on Advanced Intelligent Mechatronics*, pp. 628–633.

[107] Dang, M. P., Dao, T.-P., Chau, N. L., and Le, H. G., 2019. "Effective hybrid algorithm of taguchi method, FEM, RSM, and teaching learning-based optimization for multiobjective optimization design of a compliant rotary positioning stage for nanoindentation tester". *Mathematical Problems in Engineering,* **2019**.

[108] Cheng, Z., Foong, S., Sun, D., and Tan, U.-X., 2015. "Towards a multi-DOF passive balancing mechanism for upper limbs". *IEEE ICORR International Conference on Rehabilitation Robotics*, pp. 508–513.

[109] Simpson, T. W., Poplinski, J., Koch, P. N., and Allen, J. K., 2001. "Metamodels for computer-based engineering design: survey and recommendations". *Engineering with Computers,* **17**(2), pp. 129–150.

[110] Goldberg, D. E., 1989. *Genetic Algorithms in Search, Optimization, and Machine Learning*. Addison-Wesley.

[111] Wang, J., Niu, W., Ma, Y., Xue, L., Cun, H., Nie, Y., and Zhang, D., 2017. "A CAD/CAE-integrated structural design framework for machine tools". *International Journal of Advanced Manufacturing Technology,* **91**(1-4), pp. 545–568.

[112] Brouwer, D. M., Meijaard, J. P., and Jonker, J. B., 2013. "Large deflection stiffness analysis of parallel prismatic leaf-spring flexures". *Precision Engineering,* **37**(3), pp. 505–521.

[113] Ramirez, I. A., and Lusk, C. P., 2011. "Spatial-beam large-deflection equations and pseudo-rigid-body model for axisymmetric cantilever beams". *ASME IDETC/CIE International Design Engineering Technical Conferences and Computers and Information in Engineering Conference*, pp. 43–49.

[114] Hao, G., 2013. "Simplified prbms of spatial compliant multi-beam modules for planar motion". *Mechanical Sciences,* **4**, pp. 311–318.

[115] Timoshenko, S., and Goodier, J., 1951. *Theory of Elasticity*. McGraw-Hill Book Company.

[116] Bilancia, P., Berselli, G., Bruzzone, L., and Fanghella, P., 2019. "A cad/cae integration framework for analyzing and designing spatial compliant mechanisms via pseudo-rigid-body methods". *Robotics and Computer-Integrated Manufacturing,* **56**, pp. 287–302.

[117] Wang, J., and Liu, G., 2002. "A point interpolation meshless method based on radial basis functions". *International Journal for Numerical Methods in Engineering,* **54**(11), pp. 1623–1648.

[118] RecurDyn support. https://support.functionbay.com/en. Accessed: 2019-11-25.

[119] Zhang, X., and Xu, Q., 2019. "Design and analysis of a 2-DOF compliant gripper with constant-force flexure mechanism". *Journal of Micro-Bio Robotics*, pp. 1–12.

[120] Chen, Y.-H., and Lan, C.-C., 2012. "An adjustable constant-force mechanism for adaptive end-effector operations". *Journal of Mechanical Design,* **134**(3), p. 031005.

[121] Jenuwine, J., and Midha, A., 1994. "Synthesis of single-input and multiple-output port mechanisms with springs for specified energy absorption". *Journal of Mechanical Design,* **116**(3), pp. 937–943.

[122] Meaders, J. C., and Mattson, C. A., 2010. "Optimization of near-constant force springs subject to mating uncertainty". *Structural and Multidisciplinary Optimization,* **41**(1), pp. 1–15.

[123] Howell, L. L., and Magleby, S. P., 2006. Substantially constant-force exercise machine, June 13. US Patent 7,060,012.

[124] Weight, B. L., Magleby, S. P., and Howell, L. L., 2002. "Selection of compliant constant-force mechanisms based on stress and force criteria". *ASME IDETC/CIE International Design Engineering Technical Conferences and Computers and Information in Engineering Conference*, pp. 51–63.

[125] Liu, Y., and Xu, Q., 2017. "Design of a 3D-printed polymeric compliant constant-force buffering gripping mechanism". *IEEE ICRA International Conference on Robotics and Automation*, pp. 6706–6711.

[126] Fryman, J., and Matthias, B., 2012. "Safety of industrial robots: From conventional to collaborative applications". *7th ROBOTIK German Conference on Robotics*, pp. 1–5.

[127] Chen, Y., Yu, M., Bruck, H. A., and Smela, E., 2018. "Characterization of a compliant multi-layer system for tactile sensing with enhanced sensitivity and range". *Smart Materials and Structures,* **27**(6), p. 065005.

[128] Chen, Y., Yu, M., Bruck, H. A., and Smela, E., 2018. "Compliant multi-layer tactile sensing for enhanced identification of human touch". *Smart Materials and Structures,* **27**(12), p. 125009.

[129] Wang, J.-Y., and Lan, C.-C., 2014. "A constant-force compliant gripper for handling objects of various sizes". *Journal of Mechanical Design,* **136**(7), p. 071008.

[130] Xu, Q., 2015. "Design of a constant-force flexure micropositioning stage with long stroke". *ASME IDETC/CIE International Design Engineering Technical Conferences and Computers and Information in Engineering Conference*, pp. V05AT08A012–V05AT08A012.

[131] Liu, Y., and Xu, Q., 2016. "Design of a compliant constant force gripper mechanism based on buckled fixed-guided beam". *IEEE MARSS International Conference on Manipulation, Automation and Robotics at Small Scales*, pp. 1–6.

[132] Hao, G., Mullins, J., and Cronin, K., 2017. "Simplified modelling and development of a bi-directionally adjustable constant-force compliant gripper". *Proceedings of the Institution of Mechanical Engineers, Part C: Journal of Mechanical Engineering Science,* **231**(11), pp. 2110–2123.

[133] Liu, Y., Zhang, Y., and Xu, Q., 2017. "Design and control of a novel compliant constant-force gripper based on buckled fixed-guided beams". *Transactions on Mechatronics,* **22**(1), pp. 476–486.

[134] Liu, Y., and Xu, Q., 2016. "Design and analysis of a micro-gripper with constant force mechanism". *12th WCICA World Congress on Intelligent Control and Automation*, pp. 2142–2147.

[135] Zhang, X., Wang, G., and Xu, Q., 2018. "Design, analysis and testing of a new compliant compound constant-force mechanism". *Actuators,* **7**(4), p. 65.

[136] Lan, C.-C., Wang, J.-H., and Chen, Y.-H., 2010. "A compliant constant-force mechanism for adaptive robot end-effector operations". *IEEE ICRA International Conference on Robotics and Automation*, pp. 2131–2136.

[137] Evans, M., and Howell, L. L., 1999. "Constant-force end-effector mechanism". *IASTED Interrational Conference on Robotics and Applications*, pp. 250–256.

[138] Berselli, G., Vertechy, R., Vassura, G., and Parenti Castelli, V., 2011. "Optimal synthesis of conically shaped dielectric elastomer linear actuators: Design methodology and experimental validation". *Transactions on Mechatronics,* **16**(1), pp. 67–79.

[139] Berselli, G., Meng, Q., Vertechy, R., and Parenti Castelli, V., 2016. "An improved design method for the dimensional synthesis of flexure-based compliant mechanisms: optimization procedure and experimental validation". *Meccanica,* **51**(5), pp. 1209–1225.

[140] Cazottes, P., Fernandes, A., Pouget, J., and Hafez, M., 2009. "Bistable buckled beam: modeling of actuating force and experimental validations". *Journal of Mechanical Design,* **131**(10).

[141] McGuire, J. R., 1996. "Analysis and design of constant-torque springs used in aerospace applications". *PhD Dissertation, University of Texas at Austin.*

[142] Arakelian, V., and Ghazaryan, S., 2008. "Improvement of balancing accuracy of robotic systems: application to leg orthosis for rehabilitation devices". *Mechanism and Machine Theory,* **43**(5), pp. 565–575.

[143] Schiavi, R., Grioli, G., Sen, S., and Bicchi, A., 2008. "VSA-II: a novel prototype of variable stiffness actuator for safe and performing robots interacting with humans". *IEEE ICRA International Conference on Robotics and Automation*, May, pp. 2171–2176.

[144] Migliore, S. A., Brown, E. A., and DeWeerth, S. P., 2007. "Novel nonlinear elastic actuators for passively controlling robotic joint compliance". *Journal of Mechanical Design,* **129**(4), pp. 406–412.

[145] Boccadamo, G., Schiavi, R., Sen, S., Tonietti, G., and Bicchi, A., 2006. "Optimization and fail-safety analysis of antagonistic actuation for pHRI". *European Robotics Symposium 2006,* **22**, pp. 109 – 118.

[146] Wu, Y.-S., and Lan, C.-C., 2014. "Linear variable-stiffness mechanisms based on preloaded curved beams". *Journal of Mechanical Design,* **136**(12), p. 122302.

[147] Scirè Mammano, G., and Dragoni, E., 2014. "Elastic compensation of linear shape memory alloy actuators using compliant mechanisms". *Journal of Intelligent Material Systems and Structures,* **25**(9), pp. 1124–1138.

[148] Ma, F., and Chen, G., 2017. "Bi-BCM: A closed-form solution for fixed-guided beams in compliant mechanisms". *Journal of Mechanisms and Robotics,* **9**(1), p. 014501.

[149] Hao, G., and Mullins, J., 2016. "On the comprehensive static characteristic analysis of a translational bistable mechanism". *Proceedings of the Institution of Mechanical Engineers, Part C: Journal of Mechanical Engineering Science,* **230**(20), pp. 3803–3817.

[150] Kumar, P., Saxena, A., and Sauer, R. A., 2019. "Computational synthesis of large deformation compliant mechanisms undergoing self and mutual contact". *Journal of Mechanical Design,* **141**(1), p. 012302.

[151] Naselli, G., Rimassa, L., Zoppi, M., and Molfino, R., 2017. "A variable stiffness joint with superelastic material". *Meccanica,* **52**(4-5), pp. 781–793.

[152] Reddy, B. P., and Zhou, H., 2017. "Synthesizing bidirectional constant torque compliant mechanisms". *ASME IDETC/CIE International Mechanical Engineering Congress and Exposition*, pp. V04AT05A006–V04AT05A006.

[153] Xu, D., and Ananthasuresh, G., 2003. "Freeform skeletal shape optimization of compliant mechanisms". *Journal of Mechanical Design,* **125**(2), pp. 253–261.

[154] Wolf, S., Grioli, G., Eiberger, O., Friedl, W., Grebenstein, M., Höppner, H., Burdet, E., Caldwell, D. G., Carloni, R., Catalano, M. G., et al., 2015. "Variable stiffness actuators: Review on design and components". *Transactions on Mechatronics,* **21**(5), pp. 2418–2430.

[155] Vanderborght, B., Albu-Schaeffer, A., Bicchi, A., Burdet, E., Caldwell, D., Carloni, R., Catalano, M., Eiberger, O., Friedl, W., Ganesh, G., Garabini, M., Grebenstein, M., Grioli, G., Haddadin, S., Hoppner, H., Jafari, A., Laffranchi, M., Lefeber, D., Petit, F., Stramigioli, S., Tsagarakis, N., Damme, M. V., Ham, R. V., Visser, L., and S., 2013. "Variable impedance actuators: A review". *Robotics and Autonomous Systems,* **61**(12), pp. 1601–1614.

[156] Goris, K., Saldien, J., Vanderborght, B., and Lefeber, D., 2011. "How to achieve the huggable behavior of the social robot probo? a reflection on the actuators". *Mechatronics,* **21**(3), pp. 490–500.

[157] Au, S., Berniker, M., and Herr, H., 2008. "Powered ankle-foot prosthesis to assist level-ground and stair-descent gaits". *Neural Networks,* **21**(4), pp. 654–666.

[158] Bicchi, A., and Tonietti, G., 2004. "Fast and soft arm tactics: Dealing with the safety-performance trade-off in robot arms design and control". *Robotics and Automation Magazine,* **11**(2), pp. 22–33.

[159] Tonietti, G., Schiavi, R., and Bicchi, A., 2005. "Design and control of a variable stiffness actuator for safe and fast physical human/robot interaction". *IEEE ICRA International Conference on Robotics and Automation*, pp. 528–533.

[160] Wolf, S., and Hirzinger, G., 2008. "A new variable stiffness design: Matching requirements of the next robot generation". *IEEE ICRA International Conference on Robotics and Automation*, May, pp. 1741–1746.

[161] Groothuis, S. S., Carloni, R., and Stramigioli, S., 2016. "Single motor-variable stiffness actuator using bistable switching mechanisms for independent motion and stiffness control". *IEEE AIM International Conference on Advanced Intelligent Mechatronics*, pp. 234–239.

[162] Sardellitti, I., Palli, G., Tsagarakis, N., and Caldwell, D., 2010. "Antagonistically actuated compliant joint: Torque and stiffness control". *IEEE IROS International Conference on Intelligent Robots and Systems*, Oct, pp. 1909–1914.

[163] Jafari, A., Tsagarakis, N. G., Sardellitti, I., and Caldwell, D. G., 2012. "A new actuator with adjustable stiffness based on a variable ratio lever mechanism". *Transactions on Mechatronics,* **19**(1), pp. 55–63.

[164] Russel, D., McTavish, M., and English, C., 2009. "Mechanical issues inherent in antagonistically actuated systems". *Journal of Mechanisms and Robotics,* **1**(4), pp. 044501–8p.

[165] Palli, G., Hosseini, M., Moriello, L., and Melchiorri, C., 2015. "Modeling and identification of a variable stiffness joint based on twisted string actuators". *IEEE IROS International Conference on Intelligent Robots and Systems*, pp. 1757–1762.

[166] Migliore, S. A., Brown, E. A., and DeWeerth, S. P., 2005. "Biologically inspired joint stiffness control". *IEEE ICRA International Conference on Robotics and Automation*, pp. 4508–4513.

[167] Palli, G., Melchiorri, C., Wimböck, T., Grebenstein, M., and Hirzinger, G., 2007. "Feedback linearization and simultaneous stiffness-position control of robots with antagonistic actuated joints". *IEEE ICRA International Conference on Robotics and Automation*, April, pp. 4367–4372.

[168] Gandhi, I., and Zhou, H., 2019. "Synthesizing constant torque compliant mechanisms using precompressed beams". *Journal of Mechanical Design,* **141**(1), p. 014501.

[169] Wang, P., Yang, S., and Xu, Q., 2018. "Design and optimization of a new compliant rotary positioning stage with constant output torque". *International Journal of Precision Engineering and Manufacturing,* **19**(12), pp. 1843–1850.

[170] Brown, A., 1981. *Engineering Design Guides (Mechanical Springs) 42*. Oxford University Press.

[171] Herder, J. L., 2001. "Energy-free systems. theory, conception and design of statically". *PhD Dissertation, Delft University of Technology,* **2**.

[172] Sangamesh, D., 2012. "Static balancing of rigid-body linkages and compliant mechanisms". *Indian Institute of Science Bangalore*.

[173] Radaelli, G., Gallego, J. A., and Herder, J. L., 2011. "An energy approach to static balancing of systems with torsion stiffness". *Journal of Mechanical Design,* **133**(9), p. 091006.

[174] Stapel, A., and Herder, J. L., 2004. "Feasibility study of a fully compliant statically balanced laparoscopic grasper". *ASME IDETC/CIE International Design Engineering Technical Conferences and Computers and Information in Engineering Conference*, pp. 635–643.

[175] C-Flex Bearing Co., Inc. https://c-flex.com/. Accessed: 2020-01-05.

[176] Rubbert, L., Caro, S., Gangloff, J., and Renaud, P., 2014. "Using singularities of parallel manipulators to enhance the rigid-body replacement design method of compliant mechanisms". *Journal of Mechanical Design,* **136**(5), p. 051010.

[177] Herder, J. L., 1998. "Design of spring force compensation systems". *Mechanism and Machine Theory,* **33**(1-2), pp. 151–161.

[178] Tolou, N., Smit, G., Nikooyan, A. A., Plettenburg, D. H., and Herder, J. L., 2012. "Stiffness compensation mechanism for body powered hand prostheses with cosmetic covering". *Journal of Medical Devices,* **6**(1), p. 011004.

[179] Berselli, G., Mammano, G. S., and Dragoni, E., 2014. "Design of a dielectric elastomer cylindrical actuator with quasi-constant available thrust: modeling procedure and experimental validation". *Journal of Mechanical Design,* **136**(12), p. 125001.

[180] Timoshenko, S. P., and Gere, J. M., 2009. *Theory of elastic stability*. Courier Corporation.

[181] Knox, B. T., and Schmiedeler, J. P., 2009. "A unidirectional series-elastic actuator design using a spiral torsion spring". *Journal of Mechanical Design,* **131**(12), p. 125001.

[182] Muñoz-Guijosa, J. M., Caballero, D. F., de la Cruz, V. R., Sanz, J. L. M., and Echávarri, J., 2012. "Generalized spiral torsion spring model". *Mechanism and Machine Theory,* **51**, pp. 110–130.

[183] Scarcia, U., Berselli, G., Melchiorri, C., Ghinelli, M., and Palli, G., 2016. "Optimal design of 3D printed spiral torsion springs". *ASME SMASIS Conference on Smart Materials, Adaptive Structures and Intelligent Systems*, pp. V002T03A020–V002T03A020.

[184] Furnémont, R., Mathijssen, G., Van Der Hoeven, T., Brackx, B., Lefeber, D., and Vanderborght, B., 2015. "Torsion MACCEPA: A novel compact compliant actuator designed around the drive axis". *IEEE ICRA International Conference on Robotics and Automation*, pp. 232–237.

[185] Mankame, N. D., and Ananthasuresh, G., 2002. "Contact aided compliant mechanisms: concept and preliminaries". *ASME IDETC/CIE International Design Engineering Technical Conferences and Computers and Information in Engineering Conference*, pp. 109–121.

[186] Cannon, J. R., and Howell, L. L., 2005. "A compliant contact-aided revolute joint". *Mechanism and Machine Theory,* **40**(11), pp. 1273–1293.

[187] Neumann, D. A., 2013. *Kinesiology of the musculoskeletal system-e-book: foundations for rehabilitation*. Elsevier Health Sciences.

[188] Lee, Y.-F., Chu, C.-Y., Xu, J.-Y., and Lan, C.-C., 2016. "A humanoid robotic wrist with two-dimensional series elastic actuation for accurate force/torque interaction". *Transactions on Mechatronics,* **21**(3), pp. 1315–1325.

[189] Durand, S., Rohan, C. P.-Y., Hamilton, T., Skalli, W., and Krebs, H. I., 2018. "Passive wrist stiffness: the influence of handedness". *Transactions on Biomedical Engineering,* **66**(3), pp. 656–665.

[190] Choi, J., Rhim, S., and Choi, J. H., 2013. "A general purpose contact algorithm using a compliance contact force model for rigid and flexible bodies of complex geometry". *International Journal of Non-Linear Mechanics,* **53**, pp. 13–23.

[191] Song, Z., Lan, S., and Dai, J. S., 2019. "A new mechanical design method of compliant actuators with non-linear stiffness with predefined deflection-torque profiles". *Mechanism and Machine Theory,* **133**, pp. 164–178.

[192] ANSYS, 2016. *ANSYS Mechanical User's Guide*. ANSYS, Inc, Canonsburg, Pennsylvania.

[193] Wittrick, W., 1951. "The properties of crossed flexure pivots, and the influence of the point at which the strips cross". *The Aeronautical Quarterly,* **2**(4), pp. 272–292.

[194] Yang, M., Du, Z., Dong, W., and Sun, L., 2019. "Design and modeling of a variable thickness flexure pivot". *Journal of Mechanisms and Robotics,* **11**(1), p. 014502.

Appendix

In all the appended scripts, the red arrows are used to indicate that the command continues on the next line. All arrows should be removed from the file and the commands consolidated in a text editor so they are all on one line. This will enable the scripts to run correctly.

A. ProcessNet Code Used for the Automatic Model Generation (Chap. 3)

The proposed C# script has to be integrated in ProcessNet and then linked to the main RecurDyn environment in order to run the automatic procedure. The name of the parts ("...") must be updated to match the model. Note that the reported results (see Chap. 3) cannot be replicated without a specific set of simulation files. Therefore, the code is appended to facilitate the users with similar design problems. Users may refer to the ProcessNet manual for a detailed assistance and more examples.

A.1. Main Function

```
public void RegisterFunction()
{

// Import CAD file

string szPathName = @"C:\PhD\CAD_modification\hybrid_flexure.
   ↪ x_t";
if (false == File.Exists(szPathName))
{application.PrintMessage("File_not_found:" + szPathName);
return;}

refFrame1 = modelDocument.CreateReferenceFrame();
refFrame1.SetOrigin(0, 0, 0);

IBody HYBRID_SX = model.CreateBodyGeneral("HYBRID_SX");
HYBRID_SX.FileImport(szPathName);
IGeometry HYBRID_SX_geom = HYBRID_SX.GetEntity("HYBRID_SX")
   ↪ as IGeometry;

IBody FRAME = model.GetEntity("frame_body") as IBody;

IBody PLATFORM = model.GetEntity("platform_body") as IBody;

IBody MOTOR = model.GetEntity("motor_body") as IBody;
```

```
IBody ROD = model.GetEntity("rod_body") as IBody;

IBody CRANK = model.GetEntity("crank_body") as IBody;

// Modeling (B.C., mesh, material, etc.)

refFrame2 = modelDocument.CreateReferenceFrame();
refFrame2.SetOrigin(8.5, 0, -31);

refFrame3 = modelDocument.CreateReferenceFrame();
refFrame3.SetOrigin(8.5, 500, -31);

IJointFixed jointFixed1 = model.CreateJointFixed("FixedJoint1
   ↪ ", HYBRID_SX, PLATFORM, refFrame2);
IJointFixed jointFixed2 = model.CreateJointFixed("FixedJoint2
   ↪ ", HYBRID_SX, FRAME, refFrame3);

IFFlexToolkit fflexToolkit = model.FFlexToolkit as
   ↪ IFFlexToolkit;
IMeshMode meshMode = fflexToolkit.MeshMode as IMeshMode;
meshMode.Start(HYBRID_SX);

IMesherAssistModeling assistModeling = meshMode.
   ↪ AssistModeling(HYBRID_SX_geom);
assistModeling.TargetBody = HYBRID_SX_geom;

assistModeling.UsePreserveConstraint = true;
IAssistConstraintCollection constCollection = assistModeling.
   ↪ ConstraintCollection;

foreach (IAssistConstraint constraint in constCollection)
{

string strName = constraint.Name;
if (strName == "FixedJoint1")
{
constraint.UseFDR = true;
String[] strFaces = assistModeling.OriginalBodyFaces;
String[] arrFaceGeo = { strFaces[5], strFaces[9] };
constraint.SetGeometries(arrFaceGeo);
constraint.UseSelection = true;
}
else if (strName == "FixedJoint2")
{
constraint.UseFDR = true;
String[] strFaces2 = assistModeling.OriginalBodyFaces;
```

```
String[] arrFaceGeo2 = { strFaces2[11], strFaces2[15] };
constraint.SetGeometries(arrFaceGeo2);
constraint.UseSelection = true;
}
}

IMesherMeshOption meshOption = meshMode.MeshOption(
   ↪ HYBRID_SX_geom);
meshOption.MeshType = MeshType.MeshType_Solid8;
meshOption.FFlexProperty = meshOption.PropertyCollection["
   ↪ PSolid1"];
meshOption.MaxElementSize = 1.5;
meshOption.MinElementSize = 1;
meshOption.UseStructublackOutput = true;
meshOption.StructublackOutput = StructublackOutputType.
   ↪ StructublackOutputType_SimplePattern;
meshOption.UseCloseGaps = true;
meshOption.UseIncludeAssistModeling = true;
meshMode.Mesh();

IFFlexBody fflexBody1 = meshMode.End();

IFFlexBody HYBRID_SX_FE = model.GetEntity("HYBRID_SX_FE") as
   ↪ IFFlexBody;

IFFlexMaterialIsotropic Mat_3 = HYBRID_SX_FE.GetEntity("
   ↪ Mat_Property_3") as IFFlexMaterialIsotropic;

Assert.AreEqual("Mat_Property_3", Mat_3.Name);

Mat_3.IsotropicType = IsotropicType.NU;
Mat_3.Density.Value = 0.00000775;
Mat_3.DampingRatio.Value = 0.0001;
Mat_3.YoungsModulus.Value = 207000;
Mat_3.PoissonsRatio.Value = 0.33;

Assert.AreEqual(0.00000775, Mat_3.Density.Value);
Assert.AreEqual(0.0001, Mat_3.DampingRatio.Value);
Assert.AreEqual(207000, Mat_3.YoungsModulus.Value);
Assert.AreEqual(0.3, Mat_3.PoissonsRatio.Value);
Assert.AreEqual(IsotropicType.NU, Mat_3.IsotropicType);

}

// Start the MFBD Simulation
```

```
string szFilename = @"C:\PhD\CM\parametric_model.rdyn";

modelDocument = application.OpenModelDocument(szFilename1);

modelDocument.SettingSolverPriority(SolverPriority.
   ↪ AboveNormal);
modelDocument.ModelProperty.DynamicAnalysisProperty.
   ↪ SimulationStep.Value = 100;
modelDocument.ModelProperty.DynamicAnalysisProperty.
   ↪ SimulationTime.Value = 4;
modelDocument.Analysis(AnalysisMode.Dynamic);

// Export the Maximum Von Mises Stress

modelDocument = application.ActiveModelDocument;
model = modelDocument.Model;
IFFlexToolkit fflexToolkit2 = model.FFlexToolkit as
   ↪ IFFlexToolkit;
IContour contour = fflexToolkit.Contour;
contour.EnableView = true;
IContourTypeOption type = contour.TypeOption;
type.Type = ContourType.CT_STRESS;
type.Component = ContourComponent.CC_SMISES;
type.ContactSurfaceOnly = false;
contour.MinMaxOption.Calculation();
type.VectorDisplay = true;
type.VectorDisplayArrowSize = 3.0;
type.VectorDisplayArrowSizeUniformFlag = false;
contour.UpdateLegend();

IContourMinMaxOption minmax = contour.MinMaxOption;

minmax.Type = ContourMinMaxType.MM_Display;
minmax.Calculation();
double dMin = minmax.Min;
double dMax = minmax.Max;
minmax.Type = ContourMinMaxType.MM_UserDefined;
minmax.UserDefinedMin = dMin + 1;
minmax.UserDefinedMax = dMax - 1;
minmax.ShowMinMax = true;
minmax.UserDefinedMaxColor = true;
minmax.EnableLogScale = true;
application.PrintMessage(minmax.Max.ToString());
System.IO.TextWriter file = new System.IO.StreamWriter(@"C:\
   ↪ PhD\CM\VMISES_MAX.txt");
file.WriteLine(minmax.Max.ToString());
```

```
file.Close();

// Delete the Hybrid Flexures and Close RecurDyn

IFFlexBody del1 = model.GetEntity("HYBRID_DX_FE") as
   ↪ IFFlexBody;
IFFlexBody del2 = model.GetEntity("HYBRID_SX_FE") as
   ↪ IFFlexBody;

modelDocument.DeleteEntity(del1);
modelDocument.DeleteEntity(del2);
modelDocument.FileSave(szFilename1, true);
application.CloseModelDocument(modelDocument);
System.Diagnostics.Process.Start(@"C:\PhD\CM\
   ↪ RecurDyn_Shutdown.bat");

}
```

A.2. Batch File

The following command must be included in the batch file ("RecurDyn_Shutdown.bat") to provide the automatic software shut down.

```
taskkill/F/IM RecurDyn.exe
```

B. Matlab Code Used for the PRB Optimization and the Flexural Hinges Dimensioning (Chap. 4)

These Matlab scripts have to be stored and run in a single folder.

B.1. Main Matlab Script

Save this code in a single Matlab file.

```
%% Simulation Settings
clear all
clc

% Geometrical Parameters
e=60e-3; % Eccentricity [m]
xt=100e-3; % Initial x-position [m]
rif=1.5; % Target force [N]

lm=sqrt(e^2+xt^2); % Maximum mechanism length (crank+rod)

% Lower/Upper Bounds
K1t=1; % Spring 1: max stiffness [Nm]
```

```
K1b=0; % Spring 1: min stiffness [Nm]
K2t=1; % Spring 2: max stiffness [Nm]
K2b=0; % Spring 2: min stiffness [Nm]
K3t=1; % Spring 3: max stiffness [Nm]
K3b=0; % Spring 3: min stiffness [Nm]
r1t=0.9*e; % Max crank length
r1b=e/5; % Min crank length
t10t=pi/2; % Max theta10
t10b=asin(e/lm); % Min theta10

% Simulation Parameters
t1t=1*pi/2; % Max theta1
t1dp=deg2rad(.1); % Additional angle

nc=100; % Number of steps for the force evaluation
nd=3; % Number of points for each of the design variables

% Material
E=1800; % Young's Modulus [MPa]

%% #Step 1a: Optimal PRB Model Derivation
warning off
tic

dom=[linspace(K1b, K1t,nd)',linspace(K2b, K2t,nd)',linspace(
   ↪ K3b, K3t,nd)',linspace(r1b, r1t,nd)',linspace(t10b +
   ↪ t1dp, t10t,nd)'];

par=zeros(nd^5,5);
val=zeros(nd^5,1);

cost.e=e;
cost.xt=xt;
cost.rif=rif;
cost.nc=nc;
cost.t1dp=t1dp;
cost.t1t=t1t;

for i=1:nd
for k=1:nd
for j=1:nd
for w=1:nd
for u=1:nd
% Research of the minimum for each initial point
[par((i-1)*(nd^4)+(k-1)*(nd^3)+(j-1)*(nd^2)+(w-1)*nd+u,:),val
   ↪ ((i-1)*(nd^4)+(k-1)*(nd^3)+(j-1)*(nd^2)+(w-1)*nd+u)
```

```
   ↪ ]=...
fmincon(@(p)slider_optfun(p,cost),[dom(i,1),dom(k,2),dom(j,3)
   ↪ ,dom(w,4),dom(u,5)],[],[],[],[],...
[K1b,K2b,K3b,r1b,t10b+t1dp],[K1t,K2t,K3t,r1t,t10t],
   ↪ @slider_nonlcon,optimoptions('fmincon','Display','off')
   ↪ );
end
end
end
end
end
end
toc

% Sorting of the Results
val=val(:,1);
mi=find(val==min(val));
[val, si]=sort(val);
par=par(si,:);

% Final Values
K1f=par(1,1);
K2f=par(1,2);
K3f=par(1,3);
r1f=par(1,4);
r2f=lm-r1f;
t10f=par(1,5);
t30f=pi-asin((r1f*sin(t10f)-e)/r2f);
t20f=t30f-t10f;
[~, ~,xs,~,tm]=slider_optfun(par(1,:),cost);
dx=max(xs)-min(xs);
[res,t1,xs,obj,~]=slider_optfun(par(1,:),cost);

% Display Results
disp(['Target force: ',num2str(rif),' [N]'])
disp(['Obtained force (RMS value in the whole range of
   ↪ displacements): ',num2str(res),' [N]'])
disp('The optimal PRB parameters are as follows:')
disp(['K1: ' , num2str(K1f) , ' [Nm]; K2: ' , num2str(K2f) ,
   ↪ ' [Nm]; K3: ' , num2str(K3f) , '[Nm];' ])
disp(['r1: ' , num2str(r1f) , ' [m]; r2: ' , num2str(r2f) , '
   ↪  [m];' ])
disp(['t10: ' , num2str(rad2deg(t10f)) , ' [Â°]; t20: ' ,
   ↪ num2str(rad2deg(t20f)) , ' [Â°]; t30: ' , num2str(
   ↪ rad2deg(t30f)) , ' [Â°];' ])
disp(['dx: ' , num2str(dx*1000), ' [mm];' ])
```

```
%% #Step 1b: FLexures Hinge Dimensioning
L1_tb=min([r1f r2f].*1000)/5;
L2_tb=L1_tb;
L3_tb=L1_tb;
h1_tb=(4*1000*K1f*L1_tb/E)^(1/4);
h2_tb=(4*1000*K2f*L2_tb/E)^(1/4);
h3_tb=(4*1000*K3f*L3_tb/E)^(1/4);
b1_tb=3*h1_tb;
b2_tb=3*h2_tb;
b3_tb=3*h3_tb;

disp( 'Final hinges dimensions as follows:' )
disp([' #1 (base) h: ' num2str(h1_tb) ' [mm]; b: ' num2str(
   ↪ b1_tb) ' [mm]; L: ' num2str(L1_tb) ' [mm];']);
disp([' #2 (int.) h: ' num2str(h2_tb) ' [mm]; b: ' num2str(
   ↪ b2_tb) ' [mm]; L: ' num2str(L2_tb) ' [mm];']);
disp([' #3 (fine) h: ' num2str(h3_tb) ' [mm]; b: ' num2str(
   ↪ b3_tb) ' [mm]; L: ' num2str(L3_tb) ' [mm];']);
```

B.2. Objective Function (Behavioral Model)

Save this code in a single Matlab file and name it "slider_optfun.m".

```
function [res,t1,xs,obj,tm ]=slider_optfun(par, cost)

% Constant
xt=cost.xt;
e=cost.e;
rif=cost.rif;
t1dp=cost.t1dp;
t1t=cost.t1t;
nc=cost.nc;

% Design Variables
K1=par(1);
K2=par(2);
K3=par(3);
r1=par(4);
t10=par(5);

% Behavioral Model (Lengths and Angles)
lm=sqrt(e^2+xt^2);
r2=lm-r1;
t1b=asin(e/lm);
t1=linspace(t1b+t1dp,t1t,nc);

t3=pi-asin((r1.*sin(t1)-e)./r2);
```

```
t30=pi-asin((r1*sin(t10)-e)/r2);
t2=t3-t1;
t21=pi-t2;
tm=[max(t1)-min(t1),max(t21)-min(t21),max(t3)-min(t3)];

xs=r1.*cos(t1)-r2.*cos(t3);
alpha=atan(e./xs);

% Springs Deflections
psi1=t1-t10;
psi2=t3-t30-t1+t10;
psi3=t3-t30;

% Objective Function
F1=K1.*psi1.*cos(t3)./(r1.*sin(t3-t1));
F2=K2.*psi2.*cos(alpha)./(r1.*sin(t1-alpha));
F3=K3.*psi3.*cos(t1)./(xs.*sin(t1)-e.*cos(t1));

obj=-(F1+F2+F3);
res=sqrt(sum((obj-rif).^2 ));

end
```

B.3. Optimization Constraint

Save this code in a single Matlab file and name it "slider_con.m".

```
function [c,ceq]=slider_con(par)

c(1)=abs(par(2)-par(1))/par(1)-0.25;
c(2)=abs(par(3)-par(1))/par(1)-0.25;
ceq=[];

end
```

C. ANSYS Code Used for the Analysis of the Beam-Based Constant Force CM (Chap. 4)

This APDL script simulates the optimal beam-based configuration (i.e. the one found through GA optimization). Simple changes can be made to the script for modeling the lumped compliance configuration.

```
fini
/cle

eps=1e-6
mm=1e-3
```

```
MPa=1e6
pg=acos(-1)

xS1=0*mm $ yS1=0*mm
xS2=8.37*mm $ yS2=6.36*mm
xS3=43.64*mm $ yS3=31.78*mm
xS4=52.85*mm $ yS4=37.41*mm
xS5=99.10*mm $ yS5=60.75*mm
xS6=108.74*mm $ yS6=65.61*mm

B=5.14*mm

t1=0.997*mm
t2=0.929*mm
t3=1.356*mm
t4=1.339*mm
t5=0.996*mm
t6=0.920*mm
t7=1.440*mm
t8=1.434*mm
t9=0.968*mm
t10=1.046*mm
Tin=0.927*mm
Tfin=0.947*mm

a1 =0.285
a2 = 0.803
a3 = 0.582
a4 = 0.851
a5 = 0.254
a6 = 0.842
a7 = 0.578
a8 = 0.798
a9 = 0.231
a10 = 0.765

E=1800*MPa
nu=0.4
siz=0.5*mm
deltax=20*mm
substeps=10

/prep7

xp1=xS1+a1*(xS2-xS1)
yp1=yS1+a1*(yS2-yS1)
```

```
xp2=xS1+a2*(xS2-xS1)
yp2=yS1+a2*(yS2-yS1)

xp3=xS2+a3*(xS3-xS2)
yp3=yS2+a3*(yS3-yS2)

xp4=xS2+a4*(xS3-xS2)
yp4=yS2+a4*(yS3-yS2)

xp5=xS3+a5*(xS4-xS3)
yp5=yS3+a5*(yS4-yS3)

xp6=xS3+a6*(xS4-xS3)
yp6=yS3+a6*(yS4-yS3)

xp7=xS4+a7*(xS5-xS4)
yp7=yS4+a7*(yS5-yS4)

xp8=xS4+a8*(xS5-xS4)
yp8=yS4+a8*(yS5-yS4)

xp9=xS5+a9*(xS6-xS5)
yp9=yS5+a9*(yS6-yS5)

xp10=xS5+a10*(xS6-xS5)
yp10=yS5+a10*(yS6-yS5)

k,1,xS1,yS1
k,2,xp1,yp1
k,3,xp2,yp2
k,4,xp3,yp3
k,5,xp4,yp4
k,6,xp5,yp5
k,7,xp6,yp6
k,8,xp7,yp7
k,9,xp8,yp8
k,10,xp9,yp9
k,11,xp10,yp10
k,12,xS6,yS6

*do,i,1,11
l,i,i+1
*enddo

et,1,188
```

```
keyopt,1,3,2
keyopt,1,7,2
keyopt,1,9,2

mp,ex,1,E
mp,nuxy,1,nu

sectype,1,beam,rect
secdata,Tin,B

sectype,2,beam,rect
secdata,t1,B

sectype,3,beam,rect
secdata,t2,B

sectype,4,beam,rect
secdata,t3,B

sectype,5,beam,rect
secdata,t4,B

sectype,6,beam,rect
secdata,t5,B

sectype,7,beam,rect
secdata,t6,B

sectype,8,beam,rect
secdata,t7,B

sectype,9,beam,rect
secdata,t8,B

sectype,10,beam,rect
secdata,t9,B

sectype,11,beam,rect
secdata,t10,B

sectype,12,beam,rect
secdata,Tfin,B

sectype,13,taper
secdata,1,xS1,yS1
secdata,2,xp1,yp1
```

```
sectype,14,taper
secdata,2,xp1,yp1
secdata,3,xp2,yp2

sectype,15,taper
secdata,3,xp2,yp2
secdata,4,xp3,yp3

sectype,16,taper
secdata,4,xp3,yp3
secdata,5,xp4,yp4

sectype,17,taper
secdata,5,xp4,yp4
secdata,6,xp5,yp5

sectype,18,taper
secdata,6,xp5,yp5
secdata,7,xp6,yp6

sectype,19,taper
secdata,7,xp6,yp6
secdata,8,xp7,yp7

sectype,20,taper
secdata,8,xp7,yp7
secdata,9,xp8,yp8

sectype,21,taper
secdata,9,xp8,yp8
secdata,10,xp9,yp9

sectype,22,taper
secdata,10,xp9,yp9
secdata,11,xp10,yp10

sectype,23,taper
secdata,11,xp10,yp10
secdata,12,xS6,yS6

*get,nli,line,,num,max
*do,i,1,nli
lsel,s,line,,i
lsum
*get,lun,line,0,leng
```

```
lesi,i,,,lun/siz
secnum,i+12
lmesh,i
alls
*enddo

nsel,s,loc,x,0-eps,0+eps
d,all,all
alls

ksel,s,kp,,12
nslk,s
*get,nvinc,node,,num,max
d,all,ux,-deltax
d,all,uy,0
d,all,rotz,0
alls

fini

/solu
nlgeom,on
autots,off
nsubst,substeps
outre,all,all
solve
fini

/post1

*get, nstep,active,,solu,NCMSS
*dim,res,table,nstep+1,3

set,first
*do,i,1,nstep

*get,force,node,nvinc,rf,fx
*get,disp,node,nvinc,ux
*get,sigma,secr,,s,eqv,max

res(1,1)=0
res(1,2)=0
res(1,3)=0
res(i+1,1)=-disp*1000
res(i+1,2)=-force
res(i+1,3)=sigma/MPa
```

```
set,next
*enddo

*cfopen,FEA_CF_Output,txt
*vwrite,res(1,1),res(1,2),res(1,3)
(F8.3,' ',F8.3,' ',F8.3,' ')
*cfclose

/eshape,1
set,last
plns,s,eqv,2,1
```

D. ANSYS Code Used for the Analysis of the Torsional Springs (Chap. 5)

This APDL script simulates the optimal CTE (i.e. the one found through GA optimization) for the antagonistic VSA. By changing the input parameters (refer to the results in Chap. 5), also the nonlinear compensation spring can be simulated.

```
fini
/cle

eps=1e-6
mm=1e-3
MPa=1e6
pg=acos(-1)
RTOD=180/pg

Rin=10*mm
Rext=41*mm

b_Sb=3.41*mm
t_Sb=1.00*mm

Rp1=11.33*mm
Rp2=23.19*mm
Rp3=25.50*mm
Rp4=35.36*mm

phi_p1=1.33
phi_p2=1.70
phi_p3=1.37
phi_p4=1.71

phi_p_in=1.27
phi_p_ext=1.73
```

```
E=1800*MPa
nu=0.4
siz=Rin/50
theta=15
substeps=5

/prep7

csys,1

k,1,Rin,phi_p_in*RTOD,0
k,2,Rp1,phi_p1*RTOD,0
k,3,Rp2,phi_p2*RTOD,0
k,4,Rp3,phi_p3*RTOD,0
k,5,Rp4,phi_p4*RTOD,0
k,6,Rext,phi_p_ext*RTOD,0

bspli,1,2,3,4,5,6

mp,ex,1,E
mp,nuxy,1,nu

et,1,188
keyopt,1,3,2

sectype,1,beam,rect
secdata,t_Sb,b_Sb

esiz,siz
lmesh,all

et,2,184
keyopt,2,1,1
keyopt,2,2,1
type,2

*get,Numax,node,,num,max
n,Numax+1,0,0

ksel,s,kp,,1
nslk,s,1
*get,slave,node,,num,max
alls

e,Numax+1,slave
```

```
ksel,s,kp,,6
nslk,s,1
d,all,all
alls

d,Numax+1,ux,0
d,Numax+1,uy,0

fini

/solu

antype, static
nlgeom,on
autots,off
nsubst,substeps
outre,all,all

d,Numax+1,rotz,theta/RTOD
solve

fini

/post1

*get,nstep,active,,solu,NCMSS
*dim,res,table,2*nstep+1,3

set,first
*do,i,1,nstep

*get,rot,node,Numax+1,rot,z
*get,Mom,node,Numax+1,rf,mz

*get,sigma,secr,,s,eqv,max

res(nstep+1-i,1)=-rot
res(nstep+1-i,2)=-4*Mom/mm
res(nstep+1-i,3)=sigma/MPa

set,next
*enddo

res(nstep+1,1)=0
res(nstep+1,2)=0
res(nstep+1,3)=0
```

```
fini

/solu

antype, static
nlgeom,on
autots,off
nsubst,substeps
outre,all,all

d,Numax+1,rotz,-theta/RTOD
solve

fini

/post1

set,first
*do,i,1,nstep

*get,rot,node,Numax+1,rot,z
*get,Mom,node,Numax+1,rf,mz

*get,sigma,secr,,s,eqv,max

res(nstep+1+i,1)=-rot
res(nstep+1+i,2)=-4*Mom/mm
res(nstep+1+i,3)=sigma/MPa

set,next
*enddo

*do,i,1,nstep

*cfopen,FEA_VSA_Output,txt
*vwrite,res(1,1),res(1,2),res(1,3)
(F8.3,' ',F8.3,' ',F8.3,' ')
*cfclose

/eshape,1
set,last
plns,s,eqv,2,1
```

E. ANSYS Code Used for the Analysis of the Zero Torque CM (Chap. 5)

This APDL script simulates the overall zero torque CM (combination between negator and compensation spring).

```
fini
/cle

eps=1e-6
mm=1e-3
MPa=1e6
pg=acos(-1)
RTOD=180/pg

Rin=10*mm
Rext=50*mm

b_N=2.12*mm
t_N=0.26*mm
L_N=0.2*(Rext-Rin)

b_Sb=3.81*mm
t_Sb=0.80*mm

Rp1=13.29*mm
Rp2=25.00*mm
Rp3=28.21*mm
Rp4=35.00*mm

phi_p1=1.61
phi_p2=1.56
phi_p3=1.40
phi_p4=1.13

phi_p_in=1.77
phi_p_ext=1.75

ESteel=190000*MPa
nuSteel=0.33
EPlastic=1450*MPa
nuPlastic=0.4
siz=Rin/50
theta=40
substeps=10

/prep7
```

```
n,1,0,0
n,2,-Rin,0,0

k,1,-Rin,0,0
k,2,-(Rext+L_N)/2,0,0
k,3,-(Rext+L_N),0,0

csys,1
n,3,Rin,phi_p_in*RTOD,0

k,4,Rin,phi_p_in*RTOD,0
k,5,Rp1,phi_p1*RTOD,0
k,6,Rp2,phi_p2*RTOD,0
k,7,Rp3,phi_p3*RTOD,0
k,8,Rp4,phi_p4*RTOD,0
k,9,Rext,phi_p_ext*RTOD,0

csys,0

l,1,2
l,2,3

bspli,4,5,6,7,8,9

mp,ex,1,ESteel
mp,nuxy,1,nuSteel

mp,ex,2,EPlastic
mp,nuxy,2,nuPlastic

et,1,188
keyopt,1,3,2

sectype,1,beam,rect
secdata,5*t_Sb,b_Sb

sectype,2,beam,rect
secdata,t_N,b_N

sectype,3,beam,rect
secdata,t_Sb,b_Sb

mat,2
secnum,1
e,1,2
e,1,3
```

```
esiz,siz

mat,1
secnum,2
lmesh,1
lmesh,2

mat,2
secnum,3
lmesh,3

et,2,184,6
keyopt,2,4,1

sectype,4,JOIN,REVO,REVO
type,2

nsel,s,loc,x,-Rin-eps,-Rin+eps
nsel,r,loc,y,0-eps,0+eps
*vget,Nodesel,node,,nlist
alls

secnum,4
e,Nodesel(1),Nodesel(2)

csys,1
nsel,s,loc,x,Rin-eps,Rin+eps
nsel,r,loc,y,phi_p_in*RTOD-eps,phi_p_in*RTOD+eps
numm,all
alls

ksel,s,kp,,2
nslk,s,1
*get,NodePerturb,node,,num,max
alls

dk,3,uy,0
dk,3,uz,0
dk,3,roty,0
dk,3,rotx,0

d,1,ux,0
d,1,uy,0
d,1,uz,0
d,1,roty,0
```

```
d,1,rotx,0

dk,9,all

fini

/solu
nlgeom,on

outre,all,all

dk,3,ux,0.1*L_N
f,NodePerturb,fy,3
d,1,rotz,0

solve

dk,3,ux,L_N
f,NodePerturb,fy,0
solve

autots,off
nsub,substeps
d,1,rotz,theta/RTOD
solve
fini

/post1

set,3,
*get,nsub,active,,solu,NCMSS
*dim,res,table,nsub+1,2

res(1,1)=0
res(1,2)=0

set,3,1
*do,i,1,nsub

*get,rot,node,1,rot,z
*get,Mom,node,1,rf,mz

res(i+1,1)=rot*RTOD
res(i+1,2)=Mom/mm

set,next
```

```
*enddo

*vplot,res(1,1),res(1,2)

*cfopen,FEA_Output,txt
*vwrite,res(1,1),res(1,2)
(F8.3,' ',F8.3,' ')
*cfclose
```

F. Code Used for the Analysis of the Contact-Aided CAFP (Chap. 6)

This package allows to simulate the contact-aided CAFP. To simplify the implementation, the following Matlab/APDL codes must be stored and run in a single folder. To avoid issues with the batch analysis, the paths have to be updated in the Matlab and in the batch files.

F.1. Main Matlab Script

Save this code in a single Matlab file.

```
%% Simulation Settings
clear all
clc

global t L Beta w1 w2 L_el E I N N_step Lc Numc K

%Geometrical Parameters

%%% The script accepts 'L' OR 'Beta' as input. Please comment
   ↪ one of
%%% the following rows and modify the script in the next
   ↪ sections
%%% (where specified by **) according to the selection.
   ↪ Please modify also
%%% the APDL script in the initial section.

%L=45; % Flexure length [mm]
Beta=45*pi/180; % Semi-angle between flexures [rad]
t=1.6; % Flexure thickness [mm]
b=5; % Flexure width [mm]
w1=30; % Ground link width [mm]

%DOE Settings
AR_min=1; % Min. Aspect Ratio
AR_max=2; % Max. Aspect Ratio
Lc_min=0.0; % Min. Contact Extension
Lc_max=0.3; % Max. Contact Extension
AR_intervals=3; % DOE intervals for AR variable
```

```
Lc_intervals=4; % DOE intervals for Lc variable

%Material Properties
E= 1400; % Young's Modulus [MPa]
nu=0.4; % Poisson's Ratio [-]

%Additional Parameter
N=10; % Number of elements in each flexure

%Load Case Scenario

%%%In case of negative rotations (i.e. with Mmax<0 and/or
   ↪ Fxmax>0) please
%%%deactivate the contact by imposing Lc=0

N_step=10;
Fxmax=-3.92; % External x Force [N]
Fymax=0; % External y Force [N]
Mmax=0; % External Moment [Nmm]

if (Fxmax ~=0)
Fx=(0:Fxmax/N_step:Fxmax);
else
Fx=zeros(1,N_step+1);
end

if (Fymax ~=0)
Fy=(0:Fymax/N_step:Fymax);
else
Fy=zeros(1,N_step+1);
end

if (Mmax ~=0)
M=(0:Mmax/N_step:Mmax);
else
M=zeros(1,N_step+1);
end

fullfac=fullfact([AR_intervals,Lc_intervals]);
matrix_AR_Lc(:,1)=(fullfac(:,1)-1)/(AR_intervals-1);
matrix_AR_Lc(:,2)=(fullfac(:,2)-1)/(Lc_intervals-1);
size_fullfac=size(fullfac);
N_sampling=size_fullfac(1,1);
vect_AR=zeros(1,N_sampling);
vect_Lc=zeros(1,N_sampling);
```

```
for y=1:1:N_sampling
vect_AR(y)=AR_min+(AR_max-AR_min)*matrix_AR_Lc(y,1);
vect_Lc(y)=Lc_min+(Lc_max-Lc_min)*matrix_AR_Lc(y,2);
end

figure ('Name','Tested Samplings')
plot(vect_AR,vect_Lc,'MarkerSize',10,'Marker','x','LineWidth
   ↪ ',1,'LineStyle','none','Color',[1 0 0])
str1=sprintf('Number of samples = %d', N_sampling);
xlim([AR_min, AR_max]);
ylim([Lc_min, Lc_max])
xlabel('AR [-]','FontSize',15,'FontWeight','bold','FontName
   ↪ ','Cambria Math');
ylabel('L_{c} [%L]','FontSize',15,'FontWeight','bold','
   ↪ FontName','Cambria Math');
title(str1)
%% DOE With CBCM Technique
tic
disp('Starting DOE with CBCM technique')
Theta_CBCM = zeros(N_sampling,N_step+1);
Stiff_CBCM = zeros(N_sampling,N_step);
Stiffness_CBCM=zeros(N_sampling,1);
MaxVon_CBCM = zeros(N_sampling,1);
MaxShift_CBCM = zeros(N_sampling,1);
PhaseShift_CBCM = zeros(N_sampling,1);
Thetamax_CBCM = zeros(N_sampling,1);

I=b*(t)^3/12;

for i=1:1:N_sampling
disp(i)

AR=vect_AR(i);
Lc=vect_Lc(i);
w2=AR*w1;

%%%** Please comment one of the following rows according to
   ↪ the previous
%%%input **

%Beta=asin((w1+w2)/(2*L)); % "L" INPUT
L=((w1+w2)/2)/(sin(Beta)); % "Beta" INPUT

L_el=L/N;
Numc=round(N*Lc);
K=1000;
```

```
CollectRes=zeros(12*N+7,N_step+1);

IP=1;
for j=1:N_step+1

Loads=[Fx(1,j);Fy(1,j);M(1,j)];

if IP==1
InitialPoints=zeros(12*N+7,1)+0.01;
else
InitialPoints=CollectRes(:,IP-1);
end

options=optimset('Display','off','MaxFunEvals',1e20,'MaxIter
   ↪ ',1e20,'TolFun',1e-8,'TolX',1e-20);
[Res,exitflag]=fsolve(@CAFP_CBCM,InitialPoints,options,Loads)
   ↪ ;

CollectRes(:,IP)=Res;
IP=IP+1;
end

Theta_CBCM(i,:) = CollectRes(12*N+7,:);

if (Mmax ~=0)
Stiff_CBCM(i,1:N_step) = diff(M(1,1:N_step+1))./diff(
   ↪ Theta_CBCM(i,1:N_step+1));
Stiffness_CBCM(i,1)=mean(Stiff_CBCM(i,:));
end

StressCAFP=CAFP_Stress(CollectRes);
MaxVon_CBCM(i,1)=max(StressCAFP);

indexmax=find(StressCAFP(1,:) == max(StressCAFP(1,:)));
Thetamax_CBCM(i,1)= Theta_CBCM(i,indexmax);

ShiftCAFP=CAFP_Shift(CollectRes);
MaxShift_CBCM(i,1) = max(ShiftCAFP(3,:));
PhaseShift_CBCM(i,1) = max(ShiftCAFP(4,:));

end
toc
%% DOE With Batch FEA Technique
tic
disp('Starting DOE with batch FEA technique')
```

```
Theta_FEA = zeros(N_step+1,N_sampling);
Moment_FEA = zeros(N_step+1,N_sampling);
Stiff_FEA = zeros(N_step,N_sampling);
Stiffness_FEA=zeros(N_sampling,1);
MaxVon_FEA = zeros(N_sampling,1);
MaxShift_FEA = zeros(N_sampling,1);
PhaseShift_FEA = zeros(N_sampling,1);
Thetamax_FEA = zeros(N_sampling,1);

for i=1:1:N_sampling
disp(i);

AR=vect_AR(i);
Lc=vect_Lc(i);

%%%** Please comment one of the following rows according to
   ↪ the previous
%%%input **

%input = [E;nu;AR;L;w1;t;b;Lc;Fxmax;Fymax;Mmax;N_step;N]; % "
   ↪ L" INPUT
input = [E;nu;AR;Beta;w1;t;b;Lc;Fxmax;Fymax;Mmax;N_step;N]; %
   ↪  "Beta" INPUT

dlmwrite('FEA_Input.txt',input,'precision','%.4f','newline','
   ↪ pc','delimiter',' ');

[sta, cmd] = dos('CAFP_FEA.bat','-echo');

filename = 'FEA_Output.txt';
formatSpec = '%8f%9f%9f%9f%9f%9f%9f%[^\n\r]';
fileID = fopen(filename,'r');
dataArray = textscan(fileID, formatSpec, 'Delimiter', '', '
   ↪ WhiteSpace', '', 'TextType', 'string', 'ReturnOnError',
   ↪  false);
fclose(fileID);
FEAOutput = [dataArray{1:end-1}];
clearvars filename formatSpec fileID dataArray ans;

siz=size(FEAOutput);

Theta_FEA(1:siz(1),i) = FEAOutput(:,1);

if (Mmax ~=0)
Moment_FEA(1:siz(1),i) = FEAOutput(:,2);
Stiff_FEA(1:siz(1)-1,i) = diff(Moment_FEA(1:siz(1),i))./diff(
```

```
   ↪ Theta_FEA(1:siz(1),i)*pi/180);
Stiffness_FEA(i)=mean(Stiff_FEA(:,i));
end

MaxVon_FEA(i) = max(FEAOutput(:,3));
MaxShift_FEA(i) = max(FEAOutput(:,6));
PhaseShift_FEA(i) = max(FEAOutput(:,7));

indexmax=find(FEAOutput(:,3) == max(FEAOutput(:,3)));
Thetamax_FEA(i)= FEAOutput(indexmax,1);

delete('FEA_Input.txt');
delete('FEA_Output.txt');

end

delete('file.DSP');
delete('file.esav');
delete('file.ldhi');
delete('file.mntr');
delete('file.rdb');
delete('file.rst');
delete('file0.err');
delete('file0.esav');
delete('file0.full');
delete('file0.log');
delete('file0.r001');
delete('file0.rst');
delete('file0.stat');
delete('file1.err');
delete('file1.esav');
delete('file1.full');
delete('file1.out');
delete('file1.r001');
delete('file1.rst');
delete('cafp_fea.out');

toc
%% PLOT RESULTS
warning off;

%Stress
ft = 'cubicinterp';
[xstressC, ystressC, zstressC] = prepareSurfaceData( vect_AR,
   ↪ vect_Lc*100, MaxVon_CBCM );
fitStressCBCM = fit( [xstressC, ystressC], zstressC, ft, '
```

```
   ↪ Normalize', 'on' );

[xstressF, ystressF, zstressF] = prepareSurfaceData( vect_AR,
   ↪  vect_Lc*100, MaxVon_FEA );
fitStressFEA = fit( [xstressF, ystressF], zstressF, ft, '
   ↪ Normalize', 'on' );

figure( 'Name', 'Von Mises Stress' );
p1=plot( fitStressCBCM, [xstressC, ystressC], zstressC );
hold on
colormap(jet);
p2=plot( fitStressFEA, [xstressF, ystressF], zstressF );
xlabel('AR [-]','FontSize',15,'FontWeight','bold','FontName
   ↪ ','Cambria Math');
ylabel('L_{c} [%L]','FontSize',15,'FontWeight','bold','
   ↪ FontName','Cambria Math');
zlabel('{\sigma}_{Max} [MPa]','FontSize',15,'FontWeight','
   ↪ bold','FontName','Cambria Math');
grid on
view([-22.3 11.2]);

set(p1(1), 'FaceColor', 'white','edgecolor','black');
set(p1(2), 'MarkeblackgeColor', 'black','Marker','x','
   ↪ MarkerSize',10,'LineWidth',1);
set(p2(1), 'FaceColor', 'white','edgecolor','black');
set(p2(2), 'MarkeblackgeColor', 'black','Marker','*','
   ↪ MarkerSize',10,'LineWidth',1);

legend( [p1(1) p2(1)], 'CBCM', 'FEA' );
set(legend,'Location','north','FontWeight','bold','FontSize
   ↪ ',10,'FontName','Calibri');

%Shift Module
[xshiftC, yshiftC, zshiftC] = prepareSurfaceData( vect_AR,
   ↪ vect_Lc*100, MaxShift_CBCM );
fitShiftCBCM = fit( [xshiftC, yshiftC], zshiftC, ft, '
   ↪ Normalize', 'on' );

[xshiftF, yshiftF, zshiftF] = prepareSurfaceData( vect_AR,
   ↪ vect_Lc*100, MaxShift_FEA );
fitShiftFEA = fit( [xshiftF, yshiftF], zshiftF, ft, '
   ↪ Normalize', 'on' );

figure( 'Name', 'Shift Module' );
h1=plot( fitShiftCBCM, [xshiftC, yshiftC], zshiftC );
hold on
```

```
h2=plot( fitShiftFEA, [xshiftF, yshiftF], zshiftF);
xlabel('AR [-]','FontSize',15,'FontWeight','bold','FontName
   ↪ ','Cambria Math');
ylabel('L_{c} [%L]','FontSize',15,'FontWeight','bold','
   ↪ FontName','Cambria Math');
zlabel('s [mm]','FontSize',15,'FontWeight','bold','FontName
   ↪ ','Cambria Math');
grid on
view([-22.3 11.2]);

set(h1(1), 'FaceColor', 'white','edgecolor','black');
set(h1(2), 'MarkeblackgeColor', 'black','Marker','x','
   ↪ MarkerSize',10,'LineWidth',1);
set(h2(1), 'FaceColor', 'white','edgecolor','black');
set(h2(2), 'MarkeblackgeColor', 'black','Marker','*','
   ↪ MarkerSize',10,'LineWidth',1);

legend( [h1(1) h2(1)], 'CBCM', 'FEA');
set(legend,'Location','north','FontWeight','bold','FontSize
   ↪ ',10,'FontName','Calibri');

%Shift Phase
[x1shiftC, y1shiftC, z1shiftC] = prepareSurfaceData( vect_AR,
   ↪  vect_Lc*100, PhaseShift_CBCM );
fit1ShiftCBCM = fit( [x1shiftC, y1shiftC], z1shiftC, ft, '
   ↪ Normalize', 'on' );

[x1shiftF, y1shiftF, z1shiftF] = prepareSurfaceData( vect_AR,
   ↪  vect_Lc*100, PhaseShift_FEA );
fit1ShiftFEA = fit( [x1shiftF, y1shiftF], z1shiftF, ft, '
   ↪ Normalize', 'on' );

figure( 'Name', 'Shift Phase' );
h1=plot( fit1ShiftCBCM, [x1shiftC, y1shiftC], z1shiftC );
hold on
h2=plot( fit1ShiftFEA, [x1shiftF, y1shiftF], z1shiftF);

xlabel('AR [-]','FontSize',15,'FontWeight','bold','FontName
   ↪ ','Cambria Math');
ylabel('L_{c} [%L]','FontSize',15,'FontWeight','bold','
   ↪ FontName','Cambria Math');
zlabel('{\phi} [rad]','FontSize',15,'FontWeight','bold','
   ↪ FontName','Cambria Math');
grid on
view([-22.3 11.2]);
```

```
set(h1(1), 'FaceColor', 'white','edgecolor','black');
set(h1(2), 'MarkeblackgeColor', 'black','Marker','x','
   ↪ MarkerSize',10,'LineWidth',1);
set(h2(1), 'FaceColor', 'white','edgecolor','black');
set(h2(2), 'MarkeblackgeColor', 'black','Marker','*','
   ↪ MarkerSize',10,'LineWidth',1);

legend( [h1(1) h2(1) ], 'CBCM', 'FEA' );
set(legend,'Location','north','FontWeight','bold','FontSize
   ↪ ',10,'FontName','Calibri');

%Stiffness
if (Mmax ~=0)
[xstiffC, ystiffC, zstiffC] = prepareSurfaceData( vect_AR,
   ↪ vect_Lc*100, Stiffness_CBCM );
fitStiffCBCM = fit( [xstiffC, ystiffC], zstiffC, ft, '
   ↪ Normalize', 'on' );

[xstiffF, ystiffF, zstiffF] = prepareSurfaceData( vect_AR,
   ↪ vect_Lc*100, Stiffness_FEA );
fitStiffFEA = fit( [xstiffF, ystiffF], zstiffF, ft, '
   ↪ Normalize', 'on' );

figure( 'Name', 'Stiffness' );
s1=plot( fitStiffCBCM, [xstiffC, ystiffC], zstiffC );
hold on
s2=plot( fitStiffFEA, [xstiffF, ystiffF], zstiffF);
colormap(jet);
xlabel('AR [-]','FontSize',15,'FontWeight','bold','FontName
   ↪ ','Cambria Math');
ylabel('L_{c} [%L]','FontSize',15,'FontWeight','bold','
   ↪ FontName','Cambria Math');
zlabel('K [Nmm/rad]','FontSize',15,'FontWeight','bold','
   ↪ FontName','Cambria Math');
grid on
view([-22.3 11.2]);

set(s1(1), 'FaceColor', 'white','edgecolor','black');
set(s1(2), 'MarkeblackgeColor', 'black','Marker','x','
   ↪ MarkerSize',10,'LineWidth',1);
set(s2(1), 'FaceColor', 'white','edgecolor','black');
set(s2(2), 'MarkeblackgeColor', 'black','Marker','*','
   ↪ MarkerSize',10,'LineWidth',1);

legend( [s1(1) s2(1)], 'CBCM', 'FEA' );
set(legend,'Location','north','FontWeight','bold','FontSize
```

```
   ↪ ',10,'FontName','Calibri');
end
```

F.2. Matlab Script for the CBCM Equations

Save this code in a single Matlab file and name it "CAFP_CBCM.m".

```
function Eq=CAFP_CBCM(Unknown,Loads)
global t Beta w1 w2 L_el E I N Numc K

Fx=Loads(1);
Fy=Loads(2);
M=Loads(3);

p = Unknown(1:6:end-7);
f = Unknown(2:6:end-7);
m = Unknown(3:6:end-7);
delta_x = Unknown(4:6:end-7);
delta_y = Unknown(5:6:end-7);
alpha = Unknown(6:6:end-7);

xA = Unknown(end-6);
yA = Unknown(end-5);
xB = Unknown(end-4);
yB = Unknown(end-3);

Delta_X = Unknown(end-2);
Delta_Y = Unknown(end-1);
Delta_theta = Unknown(end);

Eq=zeros(12*N+7,1);
j = 1;

% CBCM Eqs.(3N)x2
for i=1:(2*N)

if (N<i) && (i<=N+Numc)
Eq(j) = [12 -6]*[delta_y(i);alpha(i)] + p(i)*[6/5 -1/10]*[
   ↪ delta_y(i);alpha(i)] + p(i)^2*[-1/700 1/1400]*[delta_y(
   ↪ i);alpha(i)] - K* delta_y(i)- f(i);
else
Eq(j) = [12 -6]*[delta_y(i);alpha(i)] + p(i)*[6/5 -1/10]*[
   ↪ delta_y(i);alpha(i)] + p(i)^2*[-1/700 1/1400]*[delta_y(
   ↪ i);alpha(i)] - f(i);
end
Eq(j+1)= [-6 4]*[delta_y(i);alpha(i)] + p(i)*[-1/10 2/15]*[
   ↪ delta_y(i);alpha(i)] + p(i)^2*[1/1400 -11/6300]*[
```

```
   ↪ delta_y(i);alpha(i)] - m(i);
Eq(j+2)= t^2*p(i)/(12*L_el^2) - 0.5*[delta_y(i) alpha(i)
   ↪ ]*[6/5 -1/10;-1/10 2/15]*[delta_y(i);alpha(i)]- p(i)*[
   ↪ delta_y(i) alpha(i)]*[-1/700 1/1400;1/1400 -11/6300]*[
   ↪ delta_y(i);alpha(i)] - delta_x(i);
j = j+3;
end

% Static equilibrium Eqs. between 1st and i-th elements (
   ↪ first beam, i=2,..,N) 3(N-1)
th1=zeros(N-1,1);
xx1=zeros(N-1,1);
yy1=zeros(N-1,1);
for i=2:N
if i==2
th1(i) = alpha(1);
else
th1(i) = sum(alpha(1:i-1));
end
Eq(j) = [cos(th1(i)) -sin(th1(i))]*[p(i); f(i)]*(E*I/L_el^2)
   ↪ - p(1)*(E*I/L_el^2);
Eq(j+1) = [sin(th1(i)) cos(th1(i))]*[p(i); f(i)]*(E*I/L_el^2)
   ↪  - f(1)*(E*I/L_el^2);
Eq(j+2) = m(i)*(E*I/L_el) + (1 + delta_x(i))*f(i)*(E*I/L_el)
   ↪ - delta_y(i)*p(i)*(E*I/L_el) - m(i-1)*(E*I/L_el);
j = j + 3;
% For the next step, i.e. Geometric constraint Eqs.
xx1(i) = cos(th1(i))*(L_el*delta_x(i)+L_el)-sin(th1(i))*L_el*
   ↪ delta_y(i);
yy1(i) = sin(th1(i))*(L_el*delta_x(i)+L_el)+cos(th1(i))*L_el*
   ↪ delta_y(i);
end

% Static equilibrium Eqs. between 1st and i-th elements (
   ↪ second beam, i=N+2,..,2N) 3(N-1)
th2=zeros(N-1,1);
xx2=zeros(N-1,1);
yy2=zeros(N-1,1);
for i=(N+2):(2*N)
if i==N+2
th2(i) = alpha(N+1);
else
th2(i) = sum(alpha(N+1:i-1));
end
Eq(j) = [cos(th2(i)) -sin(th2(i))]*[p(i); f(i)]*(E*I/L_el^2)
   ↪ - p(N+1)*(E*I/L_el^2);
```

```
Eq(j+1) = [sin(th2(i)) cos(th2(i))]*[p(i); f(i)]*(E*I/L_el^2)
   ↪  - f(N+1)*(E*I/L_el^2);
Eq(j+2) = m(i)*(E*I/L_el) + (1 + delta_x(i))*f(i)*(E*I/L_el)
   ↪ - delta_y(i)*p(i)*(E*I/L_el) - m(i-1)*(E*I/L_el);
j = j + 3;
% For the next step, i.e. Geometric constraint Eqs.
xx2(i) = cos(th2(i))*(L_el*delta_x(i)+L_el)-sin(th2(i))*L_el*
   ↪ delta_y(i);
yy2(i) = sin(th2(i))*(L_el*delta_x(i)+L_el)+cos(th2(i))*L_el*
   ↪ delta_y(i);
end

% Geometric constraint Eqs. (first beam) (3)
th1(1) = 0;
xx1(1) = L_el*(delta_x(1)+1);
yy1(1) = L_el*delta_y(1);
Eq(j)=sum(xx1)-xB;
Eq(j+1)=sum(yy1)-yB;
Eq(j+2)=th1(N)+alpha(N)-Delta_theta;
% Geometric constraint Eqs. (second beam) (3)
th2(1) = 0;
xx2(1) = L_el*(delta_x(N+1)+1);
yy2(1) = L_el*delta_y(N+1);
Eq(j+3)=sum(xx2)-xA;
Eq(j+4)=sum(yy2)-yA;
Eq(j+5)=th2(2*N)+alpha(2*N)-Delta_theta;

% Output link Displacements (2)
XA=[-sin(Beta) -cos(Beta)]*[xA;yA]+w1/2;
YA=[cos(Beta) -sin(Beta)]*[xA;yA];
XB=[sin(Beta) -cos(Beta)]*[xB;yB]-w1/2;
YB=[cos(Beta) sin(Beta)]*[xB;yB];
Eq(j+6)=Delta_X-(XA+XB)/2;
Eq(j+7)=Delta_Y-(YA+YB)/2;

% Loop closure (2)
Eq(j+8)=[sin(Beta) -cos(Beta)]*[xB;yB]-[-sin(Beta) -cos(Beta)
   ↪ ]*[xA;yA]-w1-w2*cos(Delta_theta);
Eq(j+9)=[cos(Beta) sin(Beta)]*[xB;yB]-[cos(Beta) -sin(Beta)
   ↪ ]*[xA;yA]-w2*sin(Delta_theta);

% Global Equilibrium Eqs.(3)
Eq(j+10)=[sin(Beta) -cos(Beta)]*[p(1);f(1)]*(E*I/L_el^2)+[-
   ↪ sin(Beta) -cos(Beta)]*[p(N+1);f(N+1)]*(E*I/L_el^2)-Fx;
Eq(j+11)=[cos(Beta) sin(Beta)]*[p(1);f(1)]*(E*I/L_el^2)+[cos(
   ↪ Beta) -sin(Beta)]*[p(N+1);f(N+1)]*(E*I/L_el^2)-Fy;
```

```
Eq(j+12)=m(N)*E*I/L_el+m(2*N)*E*I/L_el+w2*[sin(Delta_theta) -
   ↪ cos(Delta_theta)]*[-sin(Beta) -cos(Beta);cos(Beta) -sin
   ↪ (Beta)]*[p(N+1);f(N+1)]*(E*I/L_elˆ2)+0.5*w2*[sin(
   ↪ Delta_theta) -cos(Delta_theta)]*[-Fx;-Fy]-M;
```

F.3. Matlab Script for the Shift Evaluation

Save this code in a single Matlab file and name it "CAFP_Shift.m".

```
function y=CAFP_Shift(IN)
global Beta w1 w2 N_step

Delta_X = IN(end-2,:);
Delta_Y = IN(end-1,:);
Delta_theta = IN(end,:);

for j=1:1:N_step+1

X=Delta_X(1,j);
Y=Delta_Y(1,j);
Theta=Delta_theta(1,j);

xloc= (w2/2)/(tan(Beta));
%yloc=0;
xlocrot=xloc*sin(Theta);
ylocrot=-xloc*cos(Theta);
xICR(1,j)=xlocrot+X;
yICR(1,j)=ylocrot+Y-(w1/2)/(tan(Beta));

if j==1

Dev(1,j)=0;
Phi(1,j)=0;

else
Dev(1,j)=(xICR(1,j)ˆ2+yICR(1,j)ˆ2)ˆ0.5;

if xICR(1,j)>0
Phi(1,j)=atan(yICR(1,j)/xICR(1,j));
end

if xICR(1,j)==0
Phi(1,j)=pi/2;
end

if xICR(1,j)<0
Phi(1,j)=atan(yICR(1,j)/xICR(1,j))+pi;
```

```
end

end

end
y=[xICR; yICR; Dev; Phi];
```

F.4. Matlab Script for the Stress Evaluation

Save this code in a single Matlab file and name it "CAFP_Stress.m".

```
function y=CAFP_Stress(x)
global t L_el N_step N E Numc

p = x(1:6:end-7,:);
f = x(2:6:end-7,:);
m = x(3:6:end-7,:);

for j=1:N_step+1
for i=1:(2*N)

P=p(i,j);
F=f(i,j);
M=m(i,j);

k=1;
for x=0:0.1:1
if (N<i) && (i<=N+Numc)
Stb(k)=0;
else
if P<0
r=sqrt(-P);
Stb(k)=[(tan(r)*cos(r*x)-sin(r*x))/r cos(r*x)/cos(r)]*[F;M];
else
r=sqrt(P);
Stb(k)=[(tanh(r)*cosh(r*x)-sinh(r*x))/r cosh(r*x)/cosh(r)]*[F
   ↪ ;M];
end
end
k=k+1;
end
Stress_bend(i,j)=max(Stb);
Stress_tot(i,j)=Stress_bend(i,j)*t*E/(2*L_el) + abs(P)*E*t
   ↪ ^2/(12*L_el^2);
end
Stress_max(j)=max(Stress_tot(:,j));
end
```

```
y=Stress_max;
```

F.5. ANSYS Script

Save this code in a single text file and name it “CAFP_FEA.txt”.

```
fini
/cle

!** 1 Constants

eps=1e-6
mm=1e-3
MPa=1e6
pg=acos(-1)

!** 2 Simulation Selector

BATCH=1 !1-->Batch input 0-->Manual input
CONT=1 !1-->Contact Aided 0-->No Contact Aided

!** 3 Parameters Definition

!%%%%%%%%%%%%%%%%%%%%%%%%
*if,BATCH,eq,1,then
CONT=1

*DIM,input_data,array,13,2
*VREAD,input_data,FEA_Input,txt,,,13,1
(1F7.3)

E=input_data(1,1)*MPa $ nu=input_data(2,1)

!************Please comment one of the following rows
   ↪ according to the input imposed in Matlab************

!AR=input_data(3,1) $ L=input_data(4,1)*mm
AR=input_data(3,1) $ Beta=input_data(4,1)

w1=input_data(5,1)*mm $ t=input_data(6,1)*mm
b=input_data(7,1)*mm $ Lc=input_data(8,1)
Fx=input_data(9,1) $ Fy=input_data(10,1)
M=input_data(11,1)*mm $ substeps=input_data(12,1)
N=input_data(13,1)

*else !Manual input
```

```
E=1400*MPa $ nu=0.4
AR=1.5 $ Beta=45*pg/180 !or L=__*mm
w1=30*mm $ t=1.60*mm
b=5*mm $ Lc=0.2
Fx=0 $ Fy=0
M=0 $ substeps=10
N=10

*endif
!%%%%%%%%%%%%%%%%%%%%%%%%%

!%%%%%%%%%%%%%%%%%%%%%%%%%
*if,Lc,eq,0,then
CONT=0
*endif
!%%%%%%%%%%%%%%%%%%%%%%%%%

w2=AR*w1

!************Please comment one of the following rows
   ↪ according to the input imposed in Matlab************

!Beta=asin((w1+w2)/(2*L))
L=((w1+w2)/2)/(sin(Beta))

L_el=L/N
L_el2=L/(N+1)
LCA=Lc*L
tblo=3*t
bblo=b
Erig=1000*E
dx=0.0001*w1

!** 4 FE Model Definition

/prep7
x1=0
y1=0
x2=w1
y2=0
x3=(w1/2)+(w2/2)
y3=((w1/2)/tan(Beta))+((w2/2)/tan(Beta))
x4=(w1/2)-(w2/2)
y4=((w1/2)/tan(Beta))+((w2/2)/tan(Beta))
xLoad=(w1/2)
yLoad=((w1/2)/tan(Beta))+((w2/2)/tan(Beta))
```

```
xICR=(w1/2)
yICR=((w1/2)/tan(Beta))

k,1,x1,y1
k,2,x2,y2
k,3,x3,y3
k,4,x4,y4
k,5,xLoad,yLoad

l,1,3
l,3,5
l,5,4
l,4,2

*if,CONT,eq,1,then
xCI=w1-((t/2)/(cos(Beta)))-dx
yCI=-((t/2)/(sin(Beta)))
xCF=w1-((t/2)/(cos(Beta)))-LCA*sin(Beta)-dx
yCF=LCA*cos(Beta)-((t/2)/(sin(Beta)))

k,6,xCI,yCI
k,7,xCF,yCF

l,6,7
*endif

et,1,188
keyopt,1,3,2

mp,ex,1,E
mp,nuxy,1,nu

mp,ex,2,Erig
mp,nuxy,2,nu

sectype,1,beam,rect
secdata,t,b

sectype,2,beam,rect
secdata,tblo,bblo

mat,1
esiz,L_el
secnum,1
lmesh,1
```

```
esiz,L_el2
lmesh,4

secnum,2
lmesh,2
lmesh,3

!%%%%%%%%%%%%%%%%%%%%%%%%%
*if,CONT,eq,1,then
mat,2
secnum,1
lmesh,5

et,2,170

r,1,

et,3,176
keyopt,3,2,0
keyopt,3,3,0
keyopt,3,5,3
keyopt,3,6,2
keyopt,3,9,1

type,2
real,1
tshape,line
lsel,s,line,,5
nsll,s,1
esln
esurf
esurf,,reverse
alls

type,3
real,1
tshape,line
lsel,s,line,,4
nsll,s,1
esln
esurf
alls
*endif
!%%%%%%%%%%%%%%%%%%%%%%%%%

ksel,s,kp,,1
```

```
ksel,a,kp,,2
nslk,s,1
d,all,all
alls

*if,CONT,eq,1,then
ksel,s,kp,,6
ksel,a,kp,,7
nslk,s,1
d,all,all
alls
*endif

ksel,s,kp,,5
nslk,s,1
*get,NodeLoad,node,,num,max

*if,Fx,ne,0,then
f,all,fx,Fx
*endif

*if,Fy,ne,0,then
f,all,fy,Fy
*endif

*if,M,ne,0,then
f,all,mz,M
*endif

alls

fini

!** 5 FEA Simulation

/solu
antype, static
nlgeom,on
autots,off
nsubst,substeps
outre,all,all
solve
fini

!** 6 FEA Post-Processing and Results Export
```

```
/post1
*get,nstep,active,,solu,NCMSS
*dim,res,table,nstep+1,7
res(1,1)=0
res(1,2)=0
res(1,3)=0
res(1,4)=0
res(1,5)=0
res(1,6)=0
res(1,7)=0

set,first

*do,i,1,nstep

*get,rot,node,NodeLoad,rot,z
*get,sig,secr,,s,eqv,max
*get,ux,node,NodeLoad,u,x
*get,uy,node,Nodeload,u,y

xShift=(((w2/2)/tan(Beta))*sin(rot))+ux
yShift=(-((w2/2)/tan(Beta))*cos(rot))+uy+((w2/2)/tan(Beta))

Dev=((xShift)**2+(yShift)**2)**0.5

*if,xShift,gt,0,then
phi=atan(yShift/xShift)
*endif

*if,xShift,eq,0,then
phi=pg/2
*endif

*if,xShift,lt,0,then
phi=atan(yShift/xShift)+pg
*endif

mom=i*M/nstep

res(i+1,1)=rot*180/pg
res(i+1,2)=mom/mm
res(i+1,3)=sig/MPa
res(i+1,4)=xShift/mm
res(i+1,5)=yShift/mm
res(i+1,6)=Dev/mm
res(i+1,7)=phi
```

```
set,next
*enddo

*cfopen,FEA_Output,txt
*vwrite,res(1,1),res(1,2),res(1,3),res(1,4),res(1,5),res(1,6)
   ↪ ,res(1,7)
(F8.3,' ',F8.3,' ',F8.3,' ',F8.3,' ',F8.3,' ',F8.3,' ',F8.3,'
   ↪  ')
*cfclose

!set,last
!*vplot,res(1,1),res(1,2)
!plns,s,eqv,2,1
!/contour,,,0,,50*MPa
```

F.6. Batch File

Save this code in a single batch file and name it "CAFP_FEA.bat".

```
SET KMP_STACKSIZE=2048k
"C:\Program Files\ANSYS Inc\v193\ansys\bin\winx64\MAPDL.exe"
   ↪ -p aa_t_a -dis -mpi INTELMPI -np 2 -lch -dir "C:\Users\
   ↪ Pietro Bilancia\Documents\PhD_USA\BYU_Research\CBCM\PB\
   ↪ DOE" -j "file" -s read -l en-us -b -i "C:\Users\Pietro
   ↪ Bilancia\Documents\PhD_USA\BYU_Research\CBCM\PB\DOE\
   ↪ CAFP_FEA.txt" -o "C:\Users\Pietro Bilancia\Documents\
   ↪ PhD_USA\BYU_Research\CBCM\PB\DOE\CAFP_FEA.out"
```